Re-evaluating Scattering Mechanisms in Snow-Covered Freshwater Lake Ice Containing Bubbles Using Polarimetric Ground-based and Spaceborne Radar Data

by

Grant E. Gunn

A thesis
presented to the University of Waterloo
in fulfillment of the
thesis requirement for the degree of
Doctor of Philosophy
in
Geography

Waterloo, Ontario, Canada, 2015

AUTHOR'S DECLARATION

This thesis consists of material all of which I authored or co-authored: see Statement of Contributions included in the thesis. This is a true copy of the thesis, including any required final revisions, as accepted by my examiners.

I understand that my thesis may be made electronically available to the public.

Statement of Contributions

This thesis contains introductory chapters in addition to four articles that are collaborative efforts of multiple researchers that have been submitted or accepted into peer-reviewed journals. The first paper, presented as chapter 4 in this thesis has been accepted into *IEEE Journal of Selected Topics in Applied Earth Observations and Remote Sensing (JSTARS)*. The second paper (chapter 5) has been submitted to the journal *Cold Regions Science and Technology (CRST)* with submission reference CRST-D-15-00093 and is currently under review. The third paper (chapter 6) has been submitted to the journal *IEEE Transactions on Geoscience and Remote Sensing (TGRS)* with submission reference TGRS-2014-01296. The final paper is included in the Appendix to provide context to the reader regarding the evolution of thought of the presented research. The paper was accepted into *IEEE Transactions on Geoscience and Remote Sensing* and is currently in press.

With the exception of the paper in the Appendix, all materials in composition of the original journal articles provided in the thesis are the sole production of the primary investigator listed as first author in journal publication. The research presented in this thesis is the direct result of collaboration of the listed co-authors, with the specific contributions listed below.

In chapter 4, the collection and interpretation of in-situ and scatterometer observations were a direct collaboration between Grant Gunn and co-authors Claude Duguay, Joshua King and Andrew Kasurak. The field methodology was developed by Grant and Claude, while in-situ snow and ice measurements and scatterometer observations were conducted by Grant, Joshua, Claude and Andrew. The scatterometer hardware including RF-head, positioner base and processing software was developed and manufactured by Prosensing Inc., in Amherst Massachusetts, with modifications to the processing software completed by Joshua. The dense media radiative transfer (DMRT) model was conceived with collaboration from Grant, Claude, Marco Brogioni and Giovanni Macelloni. The subsequent development and model runs were completed by Marco and Giovanni using in-situ measurements as the model inputs. The written portions of the manuscript and production of diagrams was completed in its entirety by Grant and edited by coauthors.

Chapter 5 was a collaborative effort between Grant Gunn and co-authors Claude Duguay, Laura Brown, Don Atwood, Joshua King and Andrew Kasurak. The collection of in-situ data was consistent with chapter 4 (Grant, Claude, Joshua, and Andrew). Interpretation of the scatterometer observations was completed by Grant with collaboration from Don Atwood to provide a further understanding and confirming multiple interactions within the range profiles of scans. Simulated ice

thickness for Malcolm Ramsey Lake was produced using the Canadian Lake Ice Model (CLIMo), with model runs completed by Laura. Additionally, ice thickness observations from the Shallow Water Ice Profiler (SWIP) were quality-controlled and interpreted by Laura. The written portions of the manuscript and production of diagrams was completed in its entirety by Grant, and edits by coauthors.

Chapter 6 was a collaborative effort between Grant Gunn and coauthors Claude Duguay, Don Atwood, Joshua King, Andrew Kasurak and Peter Toose. The collection of in-situ data was consistent with chapter 4 (Grant, Claude, Joshua, and Andrew), with additional ice stratigraphy photography, information and in-situ measurements provided by Peter Toose. The interpretation and polarimetric decomposition results was a product of direct collaboration with Don Atwood and an extension of the hypothesis presented in paper in the Appendix. The written manuscript and production of polarimetric parameters, decompositions and figures in chapter 6 was completed by Grant and edited by coauthors.

The paper provided in the Appendix was a direct result of collaboration between Don Atwood, Grant Gunn, Chris Roussi, Jianfeng Wu, Claude Duguay and Kamal Sarabandi. The in-situ snow and ice measurements and scatterometer observations were provided by Grant, with interpretation a collaborative effort between Don, Grant and Claude. The scattering simulation of and ice layer over water with modified surface roughness was developed and run by Jianfeng under the supervision of Kamal. The written manuscript was produced in its entirety by Don Atwood. Tables and figures pertaining to the University of Waterloo scatterometer (UW-Scat) was produced by Grant, and the scattering simulation results were produced by Jianfeng. All remaining figures were produced by Don Atwood. The manuscript was edited for content and composition by co-authors.

The undersigned are in agreement with the evaluation of contribution and roles of the authors stated in the Statement of Contributions:

_____	_____23/6/2015_____
Claude Duguay	Date
_____	_____22/6/2015_____
Joshua King	Date
_____	_____23/6/2015_____
Marco Brogioni	Date
_____ _____	_____23/6/2015_____
Giovanni Macelloni	Date
_____	_____
Andrew Kasurak	Date
_____ _____	_____28/6/2015_____
Laura Brown	Date
_____	_____22/6/2015_____
Don Atwood	Date

_____	_____22/6/2015_____
Peter Toose	Date

Abstract

Lakes are a prominent feature of the sub-Arctic and Arctic regions of North America, covering up to 40% of the landscape. Seasonal ice cover on northern lakes afford habitat for several flora and fauna species, and provide drinking water and overwintering fishing areas for local communities. The presence of lake ice influences lake-atmosphere exchanges by modifying the radiative properties of the lake surface and moderating the transfer of heat to the atmosphere. The thermodynamic aspects of lakes exhibit a pronounced effect on weather and regional climate, but are also sensitive to variability in climate forcings such as air temperature and snow fall, acting as proxy indicators of climate variability and change. To refine the understanding of lake-climate interactions, improved methods of monitoring lake ice properties are needed. Manual lake ice monitoring stations have dropped significantly since the 1990s and existing stations are restricted to populated and coastal regions. Recently, studies have indicated the use of radar remote sensing as a viable option for the monitoring of small lakes in remote regions due to its high spatial resolution and imaging capability independent of solar radiation or cloud cover. Active microwave radar in the frequency range of 5 – 10 GHz have successfully retrieved lake ice information pertaining to the physical status of the ice cover and areas that are frozen to bed, but have not been demonstrated as effective for the derivation of on-ice snow depth. In the 10 – 20 GHz range, radar has been shown to be sensitive to terrestrial snow cover, but has not been investigated over lakes.

Utilizing a combination of spaceborne and ground-based radar systems spanning a range of 5 – 17 GHz, simulations from the Canadian Lake Ice Model (CLIMo), and ice thickness information from a shallow water ice profiler (SWIP), this research aimed to further our understanding of lake ice scattering sources and mechanisms for small freshwater lakes in the sub-Arctic. Increased comprehension of scattering mechanisms in ice advances the potential for the derivation of lake ice properties, including on-ice snow depth, lake ice thickness and identification of surface ice types.

Field observations of snow-covered lake ice were undertaken during the winter seasons of 2009-2010 and 2010-2011 on Malcolm Ramsay Lake, near Churchill Manitoba. In-situ snow and ice observations were coincident with ground-based scatterometer (UW-Scat) and spaceborne synthetic aperture radar (SAR) acquisitions. UW-Scat was comprised of two fully polarimetric frequency modulated continuous wave (FMCW) radars with centre frequencies of 9.6 and 17.2 GHz (X- and Ku-bands, respectively). SAR observations included fine-beam fully polarimetric RADARSAT-2 acquisitions, obtained coincident to UW-Scat observations during 2009-2010. Three experiments

were conducted to characterize and evaluate the backscatter signatures from snow-covered freshwater ice coincident to in-situ snow and ice observations.

To better understand the winter backscatter (σ°) evolution of snow covered ice, three unique ice cover scenarios were observed and simulated using a bubbled ice σ° model. The range resolution of UW-SCAT provided separation of microwave interaction at the snow/ice interface (P1), and within the ice volume (P2). Ice cores extracted at the end of the observation period indicated that a considerable σ° increase at P2 of approximately 10 – 12 decibels (dB) HH/VV at X- and Ku-band occurred coincident to the timing of tubular bubble development in the ice. Similarly, complexity of the ice surface (high density micro-bubbles and snow ice) resulted in increased P1 σ° at X- and Ku-band at a magnitude of approximately 7 dB. P1 observations also indicated that Ku-band was sensitive to snowpack overlying lake ice, with σ° exhibiting a 5 (6) dB drop for VV (HH) when ~ 60 mm SWE is removed from the scatterometer field of view. Observations indicate that X-band was insensitive to changes in overlying snowpack within the field of view. A bubbled ice σ° model was developed using the dense medium radiative transfer theory under the Quasi-Crystalline Approximation (DMRT-QCA), which treated bubbles as spherical inclusions within the ice volume. Results obtained from the simulations demonstrated the capability of the DMRT model to simulate the overall magnitude of observed σ° using in-situ snow and ice measurements as input. This study improved understanding of microwave interaction with bubble inclusions incorporated at the ice surface or within the volume.

The UW-Scat winter time series was then used to derive ice thickness under the assumption of interactions in range occurring at the ice-snow and ice-water interface. Once adjusted for the refractive index of ice and slant range, the distance between peak returns agreed with in-situ ice thickness observations. Ice thicknesses were derived from the distance of peak returns in range acquired in off-nadir incidence angle range 21 - 60°. Derived ice thicknesses were compared to in-situ measurements provided by the SWIP and CLIMo. Median ice thicknesses derived using UW-Scat X- and Ku-band observations agreed well with in-situ measurements (RMSE = 0.053 and 0.045 m), SWIP (RMSE = 0.082 and 0.088 m) and Canadian Lake Ice Model (CLIMo) simulations using 25% of terrestrial snowpack scenario (RMSE = 0.082 and 0.079), respectively.

With the launch of fully polarimetric active microwave satellites and upcoming RADARSAT Constellation Mission (RCM), the utility of polarimetric measurements was observed for freshwater bubbled ice to further investigate scattering mechanisms identified by UW-Scat. The 2009-2010 time series of UW-Scat and RADARSAT-2 (C-band) fully polarimetric observations coincident to in-situ

snow and ice measurements were acquired to identify the dominant scattering mechanism in bubbled freshwater lake ice. Backscatter time series at all frequencies show increases from the ice-water interface prior to the inclusion of tubular bubbles in the ice column based on in-situ observations, indicating scattering mechanisms independent of double-bounce scatter, contrary to the longstanding hypothesis of double-bounce scatter off tubular bubbles and the ice-water interface. The co-polarized phase difference of interactions at the ice-water interface from both UW-Scat and SAR observations were centred at 0°, indicating a scattering regime other than double bounce. A Yamaguchi three-component decomposition of the time series suggested the dominant scattering mechanism to be single-bounce off the ice-water interface with appreciable surface roughness or preferentially oriented facets.

Overall, this work provided new insight into the scattering sources and mechanisms within snow-covered freshwater lake ice containing spherical and tubular bubbles.

Acknowledgements

My sincere appreciation is extended to my supervisor, Dr. Claude Duguay for his insight, guidance, direction, unlimited support and patience throughout the years it took to complete this research. I am extremely appreciative of the opportunities that you have given me to study and research the Arctic and sub-Arctic, both in the lab and in the "mild" conditions in Churchill, Resolute and Inuvik. I hope to replicate your direction, trust and enthusiasm in the field in the coming years. It was truly amazing to be part of "Team Duguay"!

I would also like to extent my appreciation to Dr. Richard Kelly (GEM, University of Waterloo), Dr. Stephen Howell (Environment Canada) and Dr. Andrea Scott (Systems Design Engineerin, University of Waterloo) for serving as my committee members on this thesis. Your continued support and advice has helped make this thesis possible. Thank you to Dr. Christian Haas (York University) for serving as my external thesis examiner, and for your role in improving this thesis.

The Canadian Foundation for Innovation, the Natural Sciences and Engineering Research Council of Canada (NSERC), the University of Waterloo and the European Space Agency are also gratefully acknowledged for their financial support. I would also like to thank the Churchill Northern Studies Centre for providing accommodation and a home base for field operations in Churchill, Manitoba.

I would like to thank all my friends I have met during my time at the University of Waterloo. In particular, Alec Casey, Kevin Kang, Homa KheyrollahPour, Cristina Surdu, Laura Brown, Ryan Sim, Joshua King, and Andrew Kasurak. A special thanks to all those friends outside of academics who have actively supported my career through their genuine interest in my research, and wearing my field gear as party decorations, including: Scott Sobering, Rob Lanteigne, Brendan Murphy, Kevin Bond, and Bogdan Kiedrowski.

Most importantly, I would like to thank my family for their unwavering support and faith in me during this journey. I am extremely grateful to my wife, Michelle, for being my sounding board, my emotional support and proposal proof-reader. Thank you to my family, especially my parents, who have helped me enormously in getting to this point academically. A special note for my nieces: thank you for keeping me grounded and making me realize that everything can be fixed by colouring inside the lines.

Dedication

This thesis is dedicated to Michelle. It's a magical world – let's go exploring!

Also – Chicka: You kept your promise through not one, but two dissertations. Thanks for your company while writing.

Table of Contents

List of Figures

List of Tables

List of Symbols and Abbreviations

A	Radar illuminated area
Å	Unit of length (10^{-10}m)
α	Albedo
c	Speed of light (299 297 458 m s^{-1})
c_i	Speed of light in ice (168 102 199 m s^{-1})
C_p	Specific Heat Capacity
$[C_3]$	Covariance matrix
d_s	Slant distance within ice volume obtained by UW-Scat
d_{meas}	Slant distance within ice volume derived from in-situ measurements
ε (CLIMo)	Emissivity
ε (Dielectrics)	Permittivity
ε_0	Permittivity of free space (8.8542 x $10^{-12}C^2N^{-1}m^{-2}$)
ε_r	Relative Permittivity
ε'	Real component of complex relative permittivity
ε"	Imaginary component of complex relative permittivity
ε_∞	High frequency limiting value
ε_s	Static dielectric constant
f	Frequency (Hz)
f_0	Relaxation frequency (Hz)
F_0	Net heat flux
F_{lat}	Latent heat flux
F_{lw}	Downwelling longwave radiative energy flux
F_{sens}	Sensible heat flux
F_{sw}	Downwelling shortwave radiative energy flux
G	Sensor gain
I_0	Fractional shortwave radiation flux
K	Bulk extinction coefficient
k_{eff}	Effective thermal conductivity
λ	Wavelength (m)

n	Refractive index
ρ	Density
ϕ	Phase
ϕ_{HHVV}	Co-polarized phase difference
P_r	Backscatter power from scene
P_t	Transmitted power
R (Radar)	Range (m)
R	Reflection coefficient
r_{min}	Minimum range resolution of radar sensor
RMS	Root mean square
σ	Root mean square of height deviations relative to surface mean height
σ (Radar)	Radar cross-section
σ°	Normalized radar cross-section
σ (CLIMo)	Stefan-Boltzmann constant (5.67×10^{-8} W m^{-2} K^{-4})
$[S]$	Scatting matrix
Γ	Transmission coefficient
T	Temperature (°K)
t	Time (seconds)
$[T_3]$	Coherency matrix
τ	Relaxation time
ω	Angular frequency
χ	Electrical susceptibility
ACP	Alaskan Coastal Plain
BW	Bandwidth
CASIX	Canadian Snow and Ice Experiment
CLIMo	Canadian Lake Ice Model
dB	Decibel
DMRT	Dense Medium Radiative Transfer
DMRT-ML	Multi-Layered Dense Medium Radiative Transfer
EOP	Extended Observation Period
FMCW	Frequency Modulated Continuous Wave
FQ	Fine Beam Quad Mode

IEEE	Institute of Electrical and Electronics Engineers
IOP	Intensive Operation Period
IMS	Interactive Multisensor Snow and Ice Mapping System
MBE	Mean Bias Error
MDA	McDonald, Dettwiler and Associates, Ltd. (MDA)
MSC	Meteorological Service of Canada
MODIS	MOderate Resolution Imaging Spectroradiometer
NEST	Next ESA SAR Toolbox
NRCS	Normalized Radar Cross-Section
NSA	North Slope of Alaska
QCA	Quasi-Crystalline Approximation
Radar	Radio detection and ranging
RMSE	Root Mean Square Error
SAR	Synthetic Aperture Radar
SLAR	Side Looking Airborne Radar
SLC	Single Look Complex
SNR	Signal-to-Noise Ratio
SP	Sum of Peaks
SWE	Snow Water Equivalent
SWIP	Shallow Water Ice Profiler
UTM	Universal Transverse Mercator
UW-Scat	University of Waterloo Scatterometer

Chapter 1
General Introduction

1.1 Motivation

Lake ice thickness and ice cover phenology (freeze-up, break-up and duration) have been regarded as indicators of variability in regional and global climate (Livingstone, 1997). A total of approximately 2% of the Earth's surface is occupied by lakes, mainly situated in the Northern Hemisphere. Sub-Arctic and Arctic lakes located in boreal and tundra ecozones dominate the landscape, covering between 15 – 45% of the land topography (Brown and Duguay, 2010). Seasonal ice cover on sub-Arctic and Arctic lakes afford habitat for several flora and fauna species, and is a source of drinking water and overwintering fishing areas for local communities. Significant ice cover can be utilized as ice roads, which provides more direct transportation corridors to remote locations during the winter season (Key et al., 2007). Apart from economic benefits, the thermodynamic aspects of lakes exhibit a pronounced effect on weather and climate, but are also sensitive to variability in climate forcing (air temperature, snow fall patterns).

The availability of observational snow and ice properties is hindered by the remoteness of sub-Arctic lakes, and the severe decrease of manual lake ice monitoring stations since the late 1980s, shown in Figure 1-1 (Duguay et al., 2006). Existing monitoring stations are geographically restricted to coastal or populated regions, omitting remote regions of the Arctic. Remote sensing observations can provide information of ice properties and phenology absent of in-situ measurements. Products that combine data from multiple sources to produce daily products like the Interactive Multisensor Snow and Ice Mapping System (IMS) provide the opportunity to map snow and ice extent for larger lakes with a spatial resolution of 4 km. However, small lakes and ponds are typical of sub-Arctic regions but are not resolved by low resolution data products. Moderate to high resolution optical data such as the MOderate Resolution Imaging Spectroradiometer (MODIS) or Landsat are able to resolve smaller lakes but rely on reflected solar radiation during clear sky scenarios, restricting its use in polar darkness conditions during the winter. Active microwave remote sensing presents the most viable option for the observation of small lakes and ponds due to its high spatial resolution (e.g. 9 x 10m for RADARSAT-2 Fine Beam Mode) and imaging capability independent of solar radiation or cloud cover.

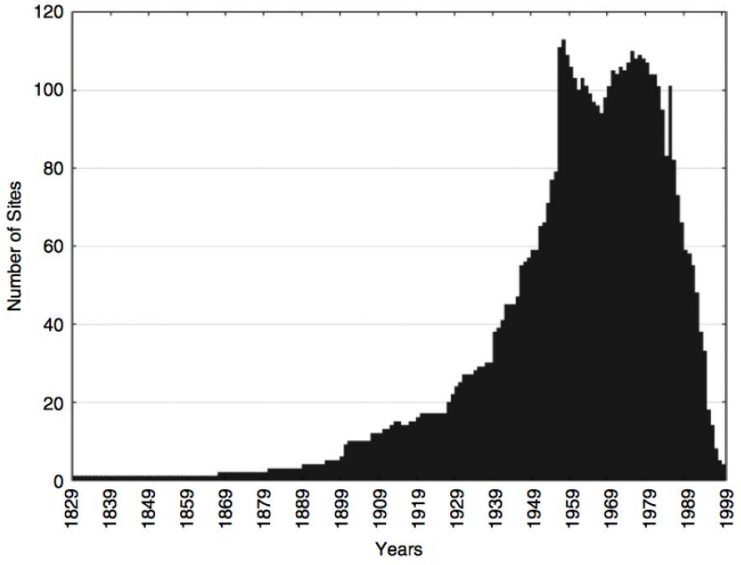

Figure 1-1: Frequency of manual monitoring stations recording in-situ observations in the Canadian Ice Database (1829-1999) (Duguay et al., 2006)

Several studies have identified the utility of active microwave systems for the observation of fresh water lake ice. Side looking airborne radar (SLAR) was operated in the late 1970s and early 1980s, creating the general basis of backscatter links to physical parameters of snow-covered lake ice, which has been utilized in the formulation of several bubbled ice backscatter models (Elachi et al., 1976; Weeks et al., 1981)**.** The classic dominant scattering mechanisms for bubbled ice in shallow Arctic/Sub-Arctic lakes are as follows:

(1) Lakes with ice afloat: High backscatter late in the winter season is the result of double-bounce off tubular bubbles in the ice volume and the ice-water interface (e.g. Sellmann et al., 1975; Elachi et al., 1976; Weeks et al., 1981; Jeffries et al., 1994; Duguay et al., 2002).

(2) Lakes with ice afloat: Overlying snowpack contributes to overall backscatter, but the influence of bubbles is greater (Onstott et al., 1982).

(3) Lakes Frozen to Bed: Low backscatter late in the winter season is the result of ice that has frozen to the lake bed due to the removal of the high-dielectric contrast ice-

water interface (e.g. Sellmann et al., 1975; Elachi et al., 1976; Weeks et al., 1981; Jeffries et al., 1994; Duguay et al., 2002).

Weeks et al. (1981) identified the potential for X-band acquisitions to provide bathymetric maps for shallow lakes based on areas of low backscatter within the lake extent, extended with the successful mapping of multiple lakes on the North Slope of Alaska by Mellor (1982). Bathymetric observations have been repeated using spaceborne C-band sensors (Jeffries et al., 1996; Duguay et al., 2003), using the bathymetric technique to infer ice growth and thickness from a time series of observations. Ice thickness has also been derived using ground-based Frequency Modulated Continuous Wave (FMCW) scatterometers pointed at nadir, measuring the distance to the reflection from the ice-snow and ice-water interface (Yankielun et al., 1992; Leconte et al., 2009).

Recent developments in active microwave synthetic aperture radar (SAR) technology permit the use of fully polarimetric observations at C-, X-, and L-band (RADARSAT-2, TerraSAR-X, and PALSAR-2, respectively), with the ability to extract the target scattering matrix and phase information. The extended polarimetric information allows for the decomposition of each pixel into the contribution of the main scattering components. Polarimetric decomposition of lakes with large methane ebullition bubbles on the Alaskan North Slope and Alaskan Coastal Plain (Engram et al., 2013a; Engram et al., 2013b) indicates that contrary to the long-held double bounce theory in bubbled ice, the dominant scattering mechanism is caused by surface roughness (odd-bounce) regime. Fully polarimetric observations of bubbled lake ice at wavelengths corresponding to C-, X- and Ku-bands are necessary to assess the true scattering mechanisms within bubbled ice to improve the theoretical basis of bubbled ice backscatter models.

1.2 Objectives

The primary goal of this thesis is to further the understanding of microwave interaction with physical components of snow-covered freshwater shallow lakes and ponds in sub-Arctic and Arctic environments. The unique C-, X- and Ku-band fully polarimetric dataset was used to answer the following questions: (1) Can backscatter from lake ice be decomposed into interactions near the snow-ice and ice-water interface using ground-based scatterometer observations? (2) What influence does the presence of bubble inclusions near snow-ice and ice-water interface have on observed backscatter, and by what scattering mechanism is the signal returned to the sensor? (3) Do ground-

based observations provide the potential to identify the influence of the evolving snowpack overlying lake ice?

These questions were addressed with the following objectives:

(1) Demonstrate that backscatter response from lake ice is a combination of multiple returns in range with the deployment of ground-based dual frequency scatterometer system on snow-covered fresh water lake ice.
(2) Identify and characterize scattering centres in range using repeated scatterometer observations of an undisturbed footprint coincident with detailed in-situ snow and ice observations to assess the influence of the evolution of the ice cover.
(3) Develop and test a lake ice backscatter model that incorporates the influence of scattering mechanisms within lake ice identified in objective (1).
(4) Identify and evaluate polarimetric parameters of the returned signal using SAR acquisitions to corroborate scatterometer observations and provide an improved understanding of lake ice backscatter.

1.3 Structure

This manuscript-based thesis is comprised of seven chapters which provide background information for each of the subsequent chapters that address the objectives identified in the previous section. This chapter provides the motivation and context relevant to the remote sensing of lake ice in the sub-Arctic and identifies the need for improvement in the understanding of microwave interactions within snow and ice volume. Chapter two provides a review of physical processes and thermodynamics involved with freshwater ice and snow development. Chapter three introduces the electrical and physical properties of snow and ice relevant to active microwave remote sensing. Additionally, Chapter 3 introduces relevant radar theory and measurement principles of ground- and spaceborne sensors.

Chapter 4 addresses the first three objectives of the thesis, using ground-based scatterometers to identify backscatter returns from near the ice-snow and ice-water interface and their associated hypothesized scattering mechanisms. A lake ice backscatter model is introduced using the dense-medium radiative-transfer (DMRT) theory that includes spherical bubbles within the ice volume. This chapter has been published in the peer-reviewed journal *IEEE Journal of Selected Topics in Applied Earth Observations and Remote Sensing* (JSTARS):

Gunn, G. E., Brogioni, M., Duguay, C. R., Macelloni, G., Kasurak, A., and King, J. (2015). Observation and Modeling of X- and Ku-band Backscatter of Snow-Covered Freshwater Lake Ice. *IEEE Journal of Selected Topics in Applied Earth Observations and Remote Sensing*, DOI 10.1109/JSTARS.2015.2420411.

Chapter 5 addresses the second objective of the thesis using the results established in Chapter 4. Chapter 5 uses the range of the returns from the two interfaces to successfully derive ice thickness from scatterometer measurements at an observed range of 0.4 to 1.3 m (compared to modeled ice thicknesses and validated by in-situ measurements). Chapter 5 has been submitted to the journal *Cold Regions Science and Technology*:

Gunn, G. E., Duguay, C. R., Brown, L., Atwood, D., King, J., Kasurak, A. (2015). Freshwater Ice Thickness Derived using X- and Ku-band FMCW Scatterometers in the Hudson Bay Lowlands Near Churchill, Manitoba. *Cold Regions Science and Technology*, in review, CRST-D-15-00093.

Chapter 5 is written under the assumption of the validity of consistently published hypothesis of backscatter returned from the ice-water interface to be the result of double-bounce interaction of electromagnetic waves off of vertical tubular bubbles within the ice volume, and reflected off the ice-water interface. However, sites that had not yet developed tubular bubbles (thicknesses <0.5 m) exhibited defined returns, leading to collaboration with Dr. Donald Atwood at the Michigan Technological University: Research Institute. The collaboration with Dr. Atwood regarding scattering mechanisms at the ice-water interface led to a paper submission in the peer reviewed journal *Transactions on Geoscience and Remote Sensing*, which has been accepted for publication. The paper in full is presented in Appendix A, and laid the groundwork for Chapter 6:

Atwood. D., Gunn, G. E., Roussi, C. Wu, J., Duguay, C., Sarabandi, K. (2015). Microwave Backscatter from Arctic Lakes and Polarimetric Implications. *IEEE Transactions on Geoscience and Remote Sensing*, DOI: TGRS-2014-01296.

Chapter 6 addresses the final objective of the thesis presenting a time-series of derived polarimetric parameters and decomposition of ground-based scatterometer and spaceborne SAR data to identify the dominant scattering mechanism, in conjunction with coincident in-situ snow and ice observations at four static sites. This chapter identifies that the dominant scattering mechanism within bubbled ice is caused by surface roughness at the ice-water interface, opposing the long-held hypothesis of double-bounce being the dominant scattering mechanism. Chapter 6 was submitted to the journal *IEEE Transactions on Geoscience and Remote Sensing*.

> Gunn, G. E., Duguay, C. R., Atwood, D., King, J., Kasurak, A. and Toose, P. (2015). Examining Scattering Mechanisms within Bubbled Freshwater Lake Ice Using a Time-Series of RADARSAT-2 (C-band) and UW-Scat (X-, Ku-band) Polarimetric Observations. *IEEE Transactions on Geoscience and Remote Sensing*, in review, TGRS-2015-00477.

The final chapter of the thesis provides a summary of the findings presented, as well as limitations and suggested directions for further research within this field of study. Chapters that contain published material or material that is currently under review are provided in their original format and are subject to copyright. The manuscripts are included in their original format, resulting in some duplication of equations, sensor descriptions and methodologies between chapters.

Chapter 2
Freshwater Ice Fundamentals

2.1 Introduction

The scientific objectives introduced in Chapter 1 require a great deal of knowledge in several areas of research. Chapter 2 provides necessary background information regarding the physical processes that influence freshwater ice development, specifically: a) the molecular structure of the water molecule and ice crystal lattice with respect to its importance for ice formation and thermodynamics, b) variable ice type formation processes characteristic of sub-Arctic environments, c) typical snow properties observed on sub-Arctic lakes, and d) the method of modeling the thermodynamic properties of the lake ice system to simulate one-dimensional ice growth, melt and overall ice thickness.

2.2 Freshwater Ice Development

2.2.1 The Water Molecule

Water molecules are comprised of one oxygen and two hydrogen elements – H_2O. The H_2O molecule is of a triangular orientation, with the oxygen atoms separated from the hydrogen atoms at a distance of 0.958 Å and from each other at an H-O-H angle of 104.5° (Figure 2-1) (Hobbs, 1974; Petrenko, 1993a). The bond between oxygen and hydrogen atoms is referred to as *covalent,* resulting from the nationalization (sharing) of electrons. The default arrangement of the H_2O molecule depicted in Figure 2-1 is not the only arrangement as excitation can cause stretching and movement of the OH bond, altering the bond's length and angle (Hobbs, 1974). A contributing factor that governs the overall shape of H_2O is the structure of the electron cloud, which is depicted in Figure 2-2. The electron cloud of a hydrogen atom is comprised of a single electron in its first shell orbital, while the oxygen atom has two electrons in the 1s orbital, two at the 2s orbital and four electrons within the outer 2p orbital (Hobbs, 1974; Petrenko, 1993a).

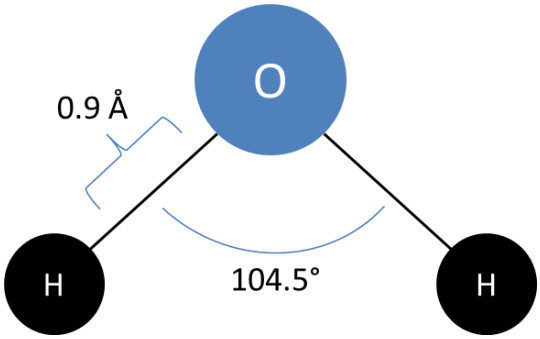

Figure 2-1: Molecular arrangement of oxygen and hydrogen nuclei within H_2O.

According to the modern valence theory, the attachment of two hydrogen atoms to a single oxygen atom is viewed to be the combination of three nuclei, resulting in the *delocalization* of the ten electrons, which are split up among the H_2O orbitals. Two electrons remain in the 1s orbital of the oxygen atom and the remaining eight electrons are divided evenly into pairs within the four directional orbitals (Hobbs, 1974; Petrenko, 1993a; Ladd, 1998). The two orbitals extending towards the hydrogen atoms are termed the *bonding* orbitals, while the other two orbitals, which extend out of the other side of the oxygen molecules are termed the *lone-pair* orbitals. The formation of the orbitals is generally tetrahedral, where the orbitals point in the direction of tetrahedral vertices (the angle of a tetrahedron is 109.467° while the H-O-H angle is 104°) (Figure 2-2).

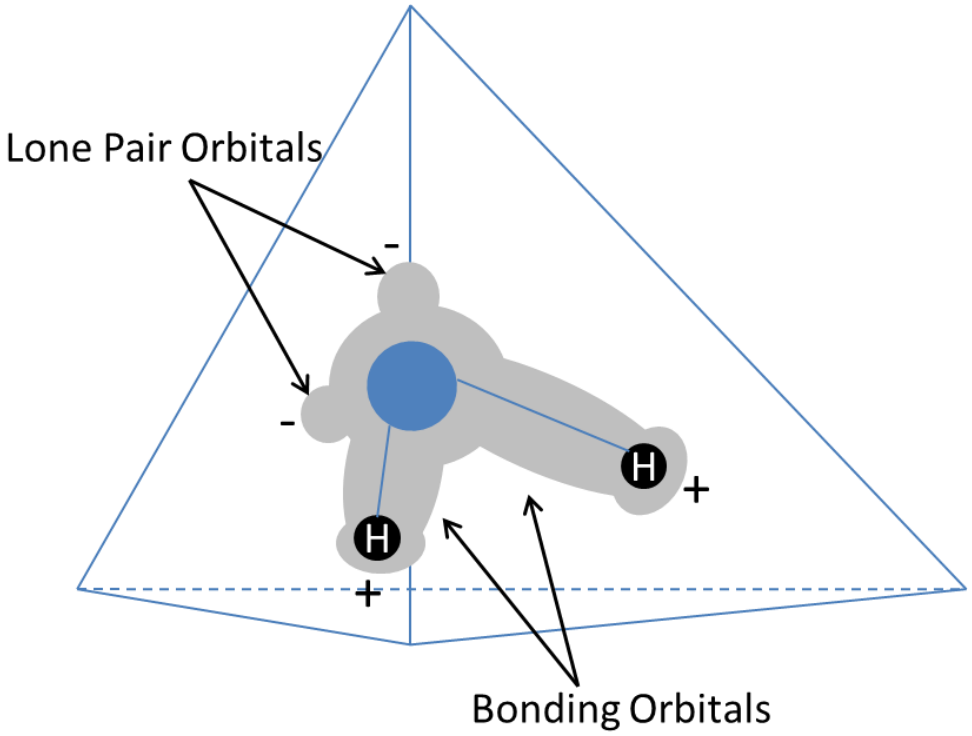

Figure 2-2: Electron density "cloud" of an H2O molecule to depict electron behaviour (after Petrenko, 1993a).

The nationalization of electrons in H_2O contributes a portion of the electron cloud to the oxygen atom and causes oxygen and hydrogen atoms to take on negative and positive charges (respectively), resulting in the formation of a polar molecule (Petrenko, 1993a). Through experiment and theory, the dipole moment of H_2O has been derived as 6.1 +/- 0.002 x 10^{-30} C m. The significance of H_2O as a polar molecule will be revisited, as it has implications for microwave remote sensing.

The water molecule is the building block by which ice formation will occur at temperatures below 273.15 °K, or 0 °C. The following section will discuss the formation of hydrogen bonds and its subsequent formation of the hexagonal ice lattice structure.

2.2.2 The Hydrogen Bond / Ice Formation

The hydrogen bond exhibited between H_2O molecules in ice is electrostatic in nature. H_2O has four electron orbitals with opposite electrostatic charges with positive charges in the bonding orbitals surrounding the hydrogen atoms, and negative charges in the lone pair orbitals (Petrenko, 1999). Based on these electrostatic properties, each H_2O molecule forms bonds with four neighbouring molecules as depicted in Figure 2-3. The lone pair orbitals of the oxygen atom with position *O* exert

an attractive force on an adjacent molecule's (O^{II}) hydrogen atom, which will align a proton along the line $O^{II}HO$. This process is similar for the other oxygen atoms O^{I}, O^{III} and $O^{IV,}$ where the lone pair orbitals attraction of adjacent hydrogen protons forms the hydrogen bond between H_2O molecules (Hobbs, 1974). The attraction exerted on hydrogen atoms stretches the valence bond between oxygen and hydrogen atoms from 0.9 Å to 1.011 Å (Hobbs, 1974; Ladd, 1998). Once the hydrogen bond has been established the distance between two oxygen atoms is determined by the sum of the atomic radii for oxygen (1.4 Å x 2, = 2.8 Å), with the influence of the hydrogen atom negated. This distance is approximately equal to that of laboratory measurements (2.76 Å) and results in an open, low density lattice structure compared to that of water (Ashton, 1986; von Hippel, 1988),

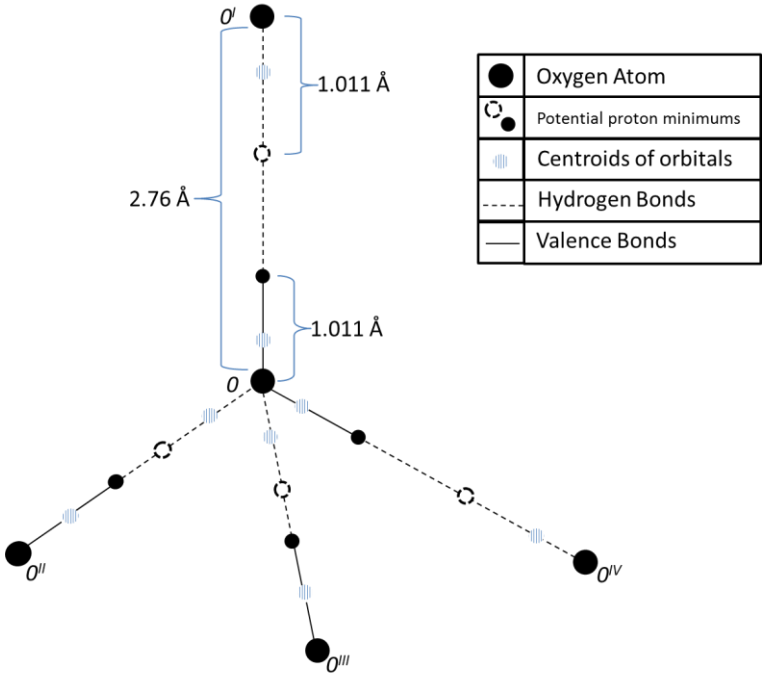

Figure 2-3: Point Charge model of hydrogen bonds between H_2O molecules (after Hobbs, 1974).

2.2.3 Ice Crystal Lattice Structure

Based on the Bernal-Fowler laws and the tetrahedral structure of ice identified in Figure 2-3, the overall structure of multiple H_2O molecules attached through a hydrogen bond will take on a hexagonal symmetry about the c-axis. The oxygen molecules are arranged on basal planes (a-axis), situated perpendicular to the c-axis in an open structure (Figure 2-4) (Ashton, 1986; Fletcher, 1970). The symmetrical lattice is characterized by the space group $P6_3/mmc$. The notation "P" refers to a primitive lattice cell and "6_3" denotes that the principle symmetry axis is a hexagonal screw axis. The

space group defines the size and orientation of the unit cell, shown in Figure 2-5**.** Each point in Figure 2-5 represents the location of an oxygen atom, with all atoms at the corners and sides of the unit cell being shared with adjacent cells. Note the angle of the vertex STQ is 120°, indicative of a hexagonal building block.

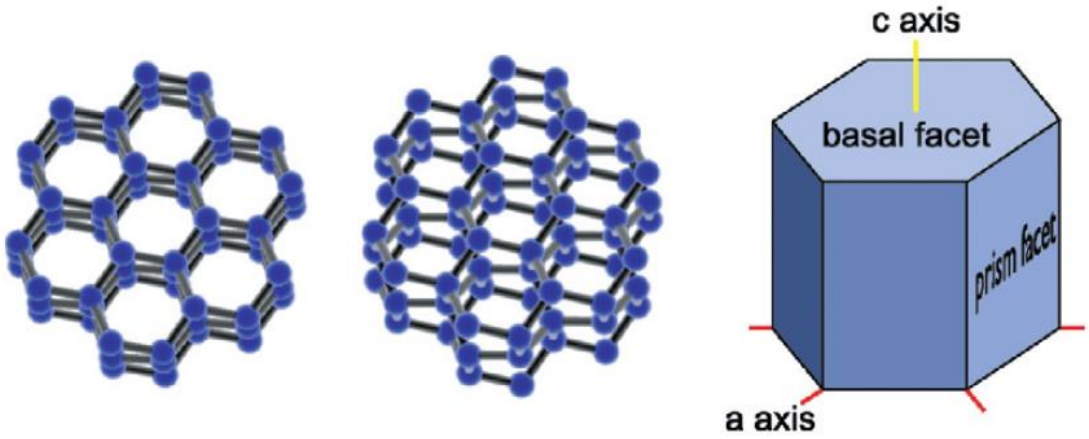

Figure 2-4: Crystal structure of Ice Ih (hexagonal) (From Libbrecht, 2005).

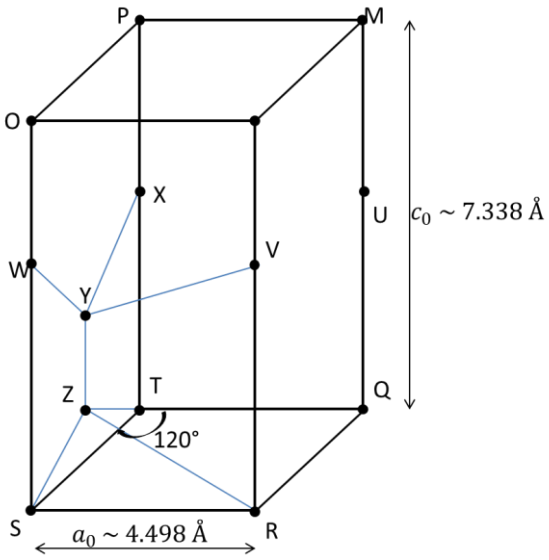

Figure 2-5: Unit Cell for Ice Ih of the space group $P6_3/mmc$ (from Hobbs, 1974).

2.2.4 Freeze-up and Ice Growth

Ice cover formation from the liquid phase in lakes and ponds is subject to many formation conditions, such as molecular (impurities from gas, dissolved salts, etc), atmospheric (air temperature, wind

speed, precipitation, cloud cover) and topographic (sheltered or open orientation of the lake, location of runoff from river inlets or outflows). This section only considers the formation of ice cover on freshwater lakes, while a thorough review of saline ice development and properties is provided by Weeks and Ackley (1982) and Petrich and Eicken (2010). Three types of freshwater ice have been identified by Michel and Ramseier (1971), defined by the depth and formation method of each type: Primary ice, Secondary ice and Superimposed ice.

2.2.4.1 Primary Ice Development

Primary ice is considered to be the first 10 – 20mm of skim ice developed on the surface of a freshwater river or lake. Under cooling conditions a heat deficit in the atmosphere elicits energy transfer from the water body (Brown and Duguay, 2010). Stratification within the water body becomes unstable, causing convective forces to transfer warm water to the surface, replacing cooled surface water which approaches maximum density at 4 °C. Once the mixing layer is sufficiently cooled and becomes stratified (commonly the entire water column in shallow lakes), sub-freezing temperatures cause the release of the latent heat of freezing associated with the formation of hydrogen bonds upon spontaneous nucleation (80 cal g^{-1}). Initial nucleation generally occurs near the shoreline, as the water column is shallower and therefore requires less time to stratify (Michel and Ramseier, 1971).

Upon spontaneous nucleation in the laboratory setting, ice crystals resembling needles form as the initial ice cover (Michel and Ramseier, 1971; Müller-Stoffels et al., 2009). The needles have optical c-axes perpendicular to the geometric molecular c-axis but are oriented randomly across the water surface (Schumskii, 1964). As the needles thicken the c-axis may rotate to become oriented vertically, which is classified as “P1” ice development (Michel and Ramseier, 1971). Concurrently, if a strong temperature gradient is present during ice formation the rapid increase in ice crystal size causes a randomly oriented c-axis, or “P2” ice.

If ice nucleation is seeded by heterogeneous nucleation (snow precipitation) the initial ice cover will be comprised of completely randomly oriented crystals. Heterogeneous nucleation is more likely in a natural setting, as seeding events caused by super-cooled nuclei interacting with H_2O molecules through precipitation or deposition from aeolian processes is more likely. In windy or turbulent conditions snow deposition events on open water can result in floating “snow slush”, which when frozen exhibits randomly oriented c-axis and high density of spherical bubble inclusions, commonly classified as “P4” or “grey ice” (Michel and Ramseier, 1971).

2.2.4.2 Secondary Ice Development

Secondary ice development occurs after primary ice development, when open water is no longer exposed to atmospheric elements. Secondary ice development rates are governed by the conductive heat flux through ice from the water to the atmosphere (thermal conductivity of pure ice = 2.24 $Wm^{-2}K^{-1}$). The conductive heat transferred to the atmosphere can be altered by an overlying snowpack, as snow has a lower thermal conductivity than ice (0.08 – 0.54 $Wm^{-2}K^{-1}$) (Brown and Duguay, 2010). The lowered thermal conductivity from the ice to the atmosphere results in slower ice growth rates related to the effective thermal conductivity of snow (k_{eff}), which is a function of depth and density (ρ). Snowpack conductivity increases with density through the empirical relationship from Sturm et al. (1997):

$$k_{eff} = \begin{cases} 0.138 - 1.01\rho + 3.233\rho^2 & [0.156 \leq \rho \geq 0.6 \text{ g cm}^{-3}] \\ 0.023 + 0.234\rho & [\rho < 0.156 \text{ g cm}^{-3}] \end{cases} \quad (2.1)$$

A detailed review of snowpack thermal conductivity measurements is provided by Sturm et al. (1997), and Jeffries and Morris (2006).

Secondary ice development involves crystal growth at the ice cover basal plane. Consequently, ice crystals with a preferential growth angle oriented off normal are "wedged" out by those with a vertical orientation. The preferred crystal grain axis orientation during ice growth is (a) perpendicular to the ice-water interface (c-axis), because the thermal conductivity is 5% greater parallel to the c-axis (termed "congelation ice"), or (b) parallel to the interface, because of increased growth velocity along the a-axis (Fletcher, 1970). The process of growing ice crystals in congelation ice results in the wedging out of crystals that are slightly off-vertical (and therefore exhibit lower thermal conductivity) is referred to as "geometric selection" (Shumskii, 1964) (Figure 2-6). The size of ice crystals in Secondary Ice are much larger than Primary Ice, with crystal sizes in a mature ice cover varying from 0.02 m to greater than 0.1m in length (Barns and Laudise, 1985; Gow, 1986; Ilescu and Baker, 2007). Ice crystal formation in Secondary Ice also exhibits an inverse relationship with ice growth rate, whereby slower growth rates lead to the development of larger crystals (Gow, 1986).

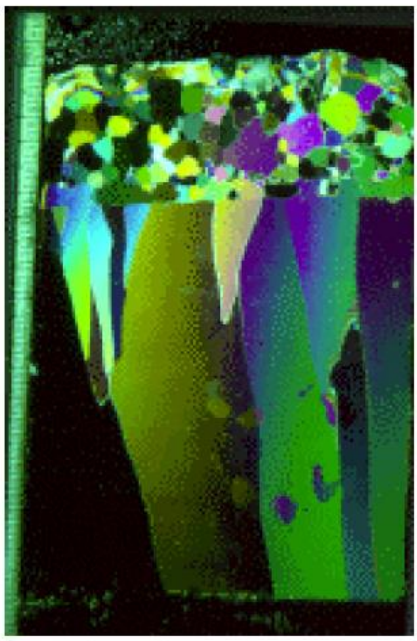

93 (0-10.5 cm)

Figure 2-6: Ice crystal geometric selection in upper 0.1m of an ice core extracted from Lake Pääjärvi viewed under polarized light. The upper layer is snow ice with randomly oriented c-axis, and the lower layer is congelation ice (Leppäranta and Kosloff, 2000).

2.2.4.3 Superimposed Surface Ice Types

Superimposed ice (snow ice) of classification "T1" is caused by (a) flooding of snow overlying the ice, or (b) by liquid precipitation events that cause percolation of water to the ice surface (Michel and Ramseier, 1971). The eventual freeze of the slush is of lower density than that of congelation ice with a randomly oriented c-axis, and can range in colour and bubble density based on snowpack properties (Adams and Roulet, 1980; Bengtsson, 1986; Lepparanta, 2000; Brown and Duguay, 2010). The common spatial distribution of snow ice is at lake edges or areas of considerable snow deposition.

In the flooding scenario, the weight of snow overlying ice depresses the ice past the hydrostatic water level. Flooding generally occurs near shore, but can infiltrate through pressure cracks throughout the ice surface. The potential and quantification of the flooding scenario is given through Archimedes Law of buoyancy,

$$h_w = \left(1 - \frac{\rho_i}{\rho_w}\right) h_i - \left(\frac{\rho_s}{\rho_w}\right) h_s \quad (2.2)$$

where h_w is the height of the snow-ice interface relative to the hydrostatic water level (freeboard), ρ denotes density, *h* represents the height for the subscripts *s, w, and i*, which denote snow, water and ice, respectively.

2.2.4.4 Bubble Inclusions

As secondary (congelation) ice thickens, dissolved gases within the water at the edge of the encroaching ice-water interface are expelled into the water below through the ice lattice formation process. When the water column becomes supersaturated with gases, bubbles are nucleated ahead of the ice-water interface, (depending on the rate of ice growth), and are incorporated into the ice (Carte, 1961; Hobbs, 1974; Morris et al., 1995; Duguay et al., 2003). The bubble shape and density depends on the rate of ice growth and level of gas saturation of the water column. For a growth rate of 3.3 μm s^{-1}, a gas supersaturation ratio for water of approximately 30 is sufficient for the nucleation of bubbles at the ice-water interface. Slower ice growth rates allow for the nucleation of bubbles at lower saturation levels, while faster growth rates require high saturation for bubble incorporation into ice (Hobbs, 1974; Nolan et al., 2002). Also, slower growth rates cause the incorporation of larger bubbles, whereas faster growth rates cause bubbles to be smaller in diameter, as depicted in Figure 2-7 (Hobbs, 1974). Tubular air bubbles were noticed at ice growth rates between 2.5 – 25 μm s^{-1}, while oval bubbles were incorporated for growth rates of 5 μm s^{-1} and higher (Bari and Hallet, 1974; Morris et al., 1995). The terminus of the bubble is not incorporated into the ice volume so long as the source of the supersaturation of gases is maintained, forming large ellipsoids or tubular shaped bubbles.

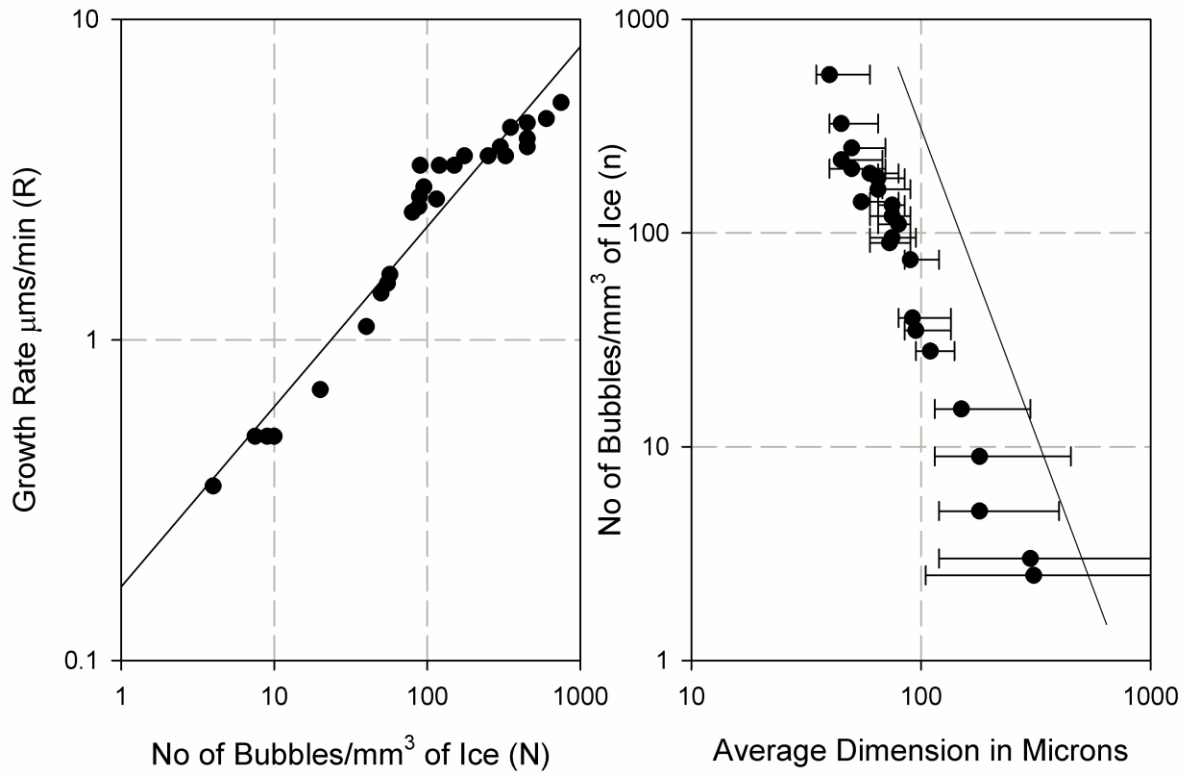

Figure 2-7: Experimental results for the number of bubbles and associated radii recorded for various ice growth rates (modified from Carte, 1961).

2.2.4.5 Snow on Lake Ice

In terms of ice thermodynamics, the addition of an appreciable snowpack retards ice growth rate as the low thermal conductivity of a snowpack insulates the underlying ice cover (Brown and Duguay, 2010). The thermal conductivity of snow is a function of heat conduction within the pore space between grains, and the transport of latent heat within the pore space (Yen, 1962). Individual grains within the snowpack are subject to metamorphosis as a function the snowpack temperature gradient. In isothermal conditions, sublimation of individual grains is caused by the natural thermodynamic process to minimize surface free energy, therefore reducing the ratio of surface area/volume to a minimum (a sphere).

For snowpack with steep temperature gradients in Subarctic and Arctic conditions, the transfer of water vapour from high pressure (warmer snow) to low pressure (colder snow) occurs across the

pore space of individual grains, increasing grain size near the ice surface. Grain growth is oriented vertically in the preferential direction of vapour transport (LaChapelle, 1969). This form of metamorphosis (temperature-gradient metamorphism) results in weak bonds between snow grains termed depth hoar, with a structure very prone to collapse. The presence of depth hoar also increases interstitial pore space, increasing the insulative properties of the snowpack, thereby lowering the conductive heat flux and decreasing ice growth rates (Adams 1976; Jeffries and Morris, 2006). This brief overview of snow metamorphosis does not include snow melt (firnification) (Albert et al., 2004) or the formation of ice lenses (Derksen et al., 2009) as it is outside the scope of this research.

2.2.4.6 Snow in Subarctic Environments

Local climate and topographic conditions influence snowpack formation and properties, as discussed in Sturm et al. (1995). Snowpack in tundra environments exhibit typical depth ranges of 10 – 75 cm, with a bulk density of 0.285 g cm^{-3} and multiple wind slab layers overlying high fractions of depth hoar. However, snowpack over lakes exhibits marked differences in composition compared to tundra snow due to unrestricted wind redistribution and erosion. The snow is characteristically thinner (7-30 cm), denser (0.344 g cm^{-3}), and comprised of less snow water equivalent (SWE) with fewer stratigraphic layers than snow on land, with a more pronounced slab-to-hoar fraction (Sturm and Liston, 2003; Derksen et al., 2009). Accumulation drifts tend to occur near shore, as shoreline vegetation acts as catchment troughs (Sturm and Liston, 2003).

2.3 The Canadian Lake Ice Model (CLIMo)

Several thermodynamic lake ice models have been developed to model the heat flux components to isolate the effects of single components within the lake ice system (surface air temperature, snow depth, etc.) or provide phenological products including ice thickness, freeze up and break-up dates (Brown and Duguay, 2010). The numerical model presented by Maykut and Untersteiner (1971) originally intended for sea-ice is the basis for several thermodynamic ice models in lake ice studies (Ebert and Curry, 1993; Flato and Brown, 1996; Vavrus et al., 1996; Duguay et al., 2003). The Flato and Brown (1996) landfast sea ice model was modified by Duguay et al., (2003) to become the Canadian Lake Ice Model (CLIMo). Several studies have utilized CLIMo to simulate ice thickness and phenology with a high level of accuracy when reliable forcing variables are available from meteorological stations or atmospheric reanalyses (Ménard et al., 2002; Duguay et al., 2003; Morris et al., 2005; Brown and Duguay, 2011a; Brown and Duguay 2011b; Surdu et al., 2014).

CLIMo models heat fluxes at the surface, bottom and ice interior. It is based on the unsteady heat conduction equation originally presented by Maykut and Untersteiner (1971):

$$\rho C_p \frac{\partial T}{\partial t} = \frac{\partial}{\partial z} k \frac{\partial T}{\partial z} + F_{sw} I_0 (1 - \alpha) K e^{-Kz} \quad (2.3)$$

where ρ is the density (kg m^{-3}), C_p is the specific heat capacity (J kg^{-1} K^{-1}), T is the temperature (K) of the ice or snow, t is time (s), z is the vertical coordinate (m), F_{sw} is the downwelling shortwave radiative energy flux (W m^{-2}), I_0 is the fractional shortwave radiation flux that penetrates through surface, α is the surface albedo and K is the bulk extinction coefficient for penetrating shortwave radiation (m^{-1}) (Duguay et al., 2003).

From Equation 2.3, the surface energy budget can be computed through:

$$F_0 = F_{lw} - \varepsilon \sigma T_s^4(0,t) + (1 - \alpha)(1 - I_0) F_{sw} + F_{lat} + F_{sens} \quad (2.4)$$

where F_0 is the net heat flux that is absorbed at the surface, ε is the emissivity at the surface, σ is the Stefan-Boltzmann constant (5.67 x 10^{-8} Wm^{-2} K^{-4}), and F_{lw}, F_{lat}, and F_{sens} are the downwelling longwave, latent and sensible heat flux (W m^{-2}), respectively (Duguay et al., 2003), shown graphically in Figure 2-8.

CLIMo also simulates snow ice development at the snow-ice interface. Internally, increase in ice thickness is computed through the differences between the rate of conductive heat flux at the ice-water interface and the ice-air or snow-air interfaces. In totality, total ice thickness is a combination of ice growth at the ice top (snow ice) and bottom (congelation ice). Further descriptions of CLIMo are provided Duguay et al. (2003), with the addition of albedo parameterizations discussed in Svacina et al. (2014).

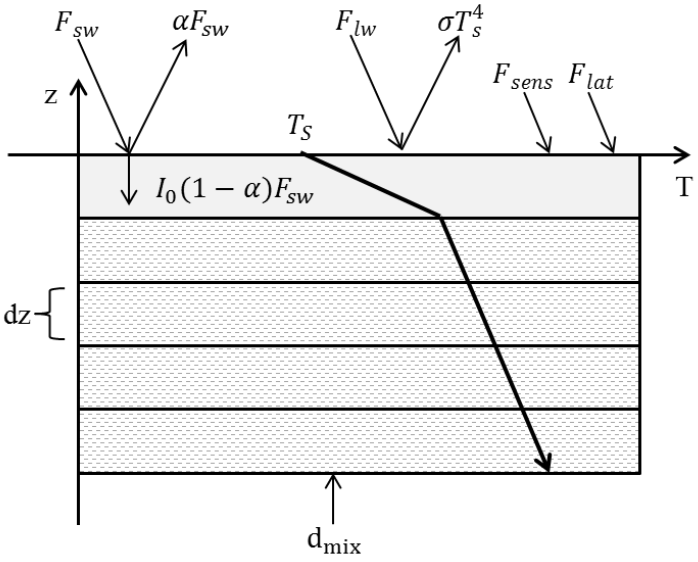

Figure 2-8: Schematic of energy flux components in CLIMo for ice covered lakes. The grey layer represents the snow surface, the dashed layer represents ice, and the thick line within the layers represents the temperature profile (modified from Duguay et al., 2003).

To simulate annual freezing and thawing cycles CLIMo includes a fixed-depth mixing layer. During ice-on conditions, the temperature of the mixed layer is kept at the freezing point. In the absence of ice, the mixed layer temperature is computed using the surface energy balance. Shallow lakes are typically well mixed with an isothermal temperature profile during ice-free conditions, resulting in the mixed-layer depth to provide a good approximation of the effect of lake depth on the timing of freeze-up in the autumn months. For the scope of this thesis, the mixing depth was set at 2 m, which approximates the mean depth of the lake observed.

Growth at the bottom of the ice cover is computed as the difference between the conductive heat flux into the underside of the ice and out of the surface of the prescribed mixed layer by:

$$\left.\frac{\partial h_i}{\partial h_t}\right|_{z=h} = \left(k\left.\frac{\partial T}{\partial z}\right|_{z=h} - \int_h^{\infty} F_{SW} I_0(1-\alpha) K e^{-Kz} dz\right)\frac{1}{L_{fi}} \qquad (2.5)$$

where h_i is the ice thickness. The last term in Equation (2.5) is the fraction of shortwave radiation that penetrates through the ice column, assumed to be absorbed at the mixing layer and returned to the ice underside, maintaining a 0 °C temperature. Ice melt at the surface is computed as the difference between the conductive heat flux and the net surface heat flux. CLIMo incorporates the creation of snow ice when the weight of the snow is such that it depresses the ice below the water level. The mass of the slush is added to the ice thickness, and freezes at the surface prior to further freezing at

the ice base. During melt conditions, ice melt at the surface occurs only after the overlying snowpack has melted.

In addition, CLIMo accounts for variation in surface energy exchanges using a surface albedo parameterization, which includes the surface ice type (ice, snow and open water), surface temperature and ice thickness as variables (Duguay et al., 2003). CLIMo has variable surface albedo parameterizations for ice under freezing and melting conditions, taken from Maykut (1982) and Heron and Woo (1994), respectively. The surface albedo parameterization is provided through:

$$\alpha = \begin{cases} \alpha_{ow} & h_i < h_{\min} \\ \min\left[\alpha_s, \alpha_i + \frac{h(\alpha_s - \alpha_i)}{c_i}\right] & h_i \geq h_{min}\ h_i \leq c_1 \\ \alpha_s & h_i \geq h_{min}\ h_s \geq c_1 \end{cases} \quad (2.6)$$

$$\alpha_i = \begin{cases} c_2 h_i^{0.28} + 0.08 & T(0,t) < T_m \\ \min\left(\alpha_{mi}, c_3 h_i^2 + \alpha_{ow}\right) & T(0,t) = T_m \end{cases} \quad (2.7)$$

$$\alpha_s = \begin{cases} 0.75 & T(0,t) < T_m \\ 0.65 & T(0,t) = T_m \end{cases} \quad (2.8)$$

where α is the surface albedo, α_{ow} is the open water albedo (0.05), α_s is the snow albedo, α_{mi} is the melting ice albedo (0.55), h is the total thickness of the ice and snow (m), $h_{\min}$ is the minimum ice thickness before open water is assumed (0.001 m), h_s is the thickness of the snow layer (m), $T(0,t)$ is the internal temperature of the ice or snow layer at time t (s), T_m is the melting temperature at the surface (273.15 K), and c_1, c_2 and c_3 are parameters derived by Maykut (1982) equal to 0.1 m, 0.44 $m^{-0.28}$ and 0.075 m^{-2}. Equation (2.6) determines which albedo equation to use depending on the snow and ice thickness, while equations (2.7) and (2.8) provide the criteria for albedo snow and ice largely depending on temperature conditions (Duguay et al., 2003).

In this thesis, CLIMo ice thickness simulations are utilized to evaluate and corroborate that scatterometer-derived ice thicknesses were within the range of possible ice thicknesses. CLIMo was forced with atmospheric data collected from a shoreline automatic weather station operating Campbell Scientific sensors, including wind speed (RM Young Wind Monitor), air temperature and relative humidity (HC-SC-XT temperature and relative humidity probe). Additional cloud cover and snow depth data (with constant density of 259 kg m^{-3}) was obtained from the Meteorological Service of Canada's Churchill weather station located at the Churchill airport.

Chapter 3
Radar Remote Sensing of Freshwater Ice

3.1 Electromagnetic Waves

3.1.1 Polarization

The polarization of a wave describes the direction and amplitude of the electromagnetic field in Cartesian coordinate systems, with variations in x and y representing the horizontal and vertical linear dimensions, respectively. As a plane wave propagates through space away from the antenna the locus of the tip of the combined electromagnetic field shifts in coordinates tracing an ellipse as a function of time. If the locus of the wave is only represented by variations in *x* or *y* planes the wave is described as propagating under "horizontal" or "vertical" linear polarizations, respectively.

In the event that the signal is scattered back to the sensor, the returned electromagnetic field propagating through space can also be described as a function of the locus of the amplitude. The properties of the locus and the amplitude provide information about the scattering target – forming the basis of the information used in Radar remote sensing.

Sensors have the capability to generate linearly polarized waves that are horizontally and vertically polarized, with emerging technology producing circularly polarized locus. When a sensor generates a vertically polarized electromagnetic field and subsequently receives vertically polarized energy, the returned signal is referred to as "co-polarized", or *VV*. Co-polarized backscatter also applies to horizontally-polarized energy generated and received (*HH*). Conversely, if energy observed at the sensor is of the opposite polarization relative to the initial signal (i.e. vertical send – horizontal return), the backscatter is referred to as "cross-polarized", (*VH or HV*). Cross-polarized returns indicate the amount of incident radiation that becomes "depolarized" (switches polarizations) during interaction with targets within a medium with anisotropic scattering centres, such as bubbles within ice, or ice grains within snowpack (Ulaby and van Zyl, 1990).

The polarization nomenclature describes the observation capability of Radar sensors. Single co-polarized sensors send and receive energy with either vertical or horizontal polarization (*VV*, or *HH*). Dual-pol sensors can send and receive with either vertical or horizontal polarizations (*VV* and *VH* or HH and HV). Quad-pol sensors are able to measure at all possible linear polarization combinations (*VV, HH, VH, HV*) and are referred to as "polarimetric" or "fully-polarimetric". This thesis utilizes

fully-polarimetric ground-based scatterometer (*UW-Scat*) and spaceborne synthetic aperture radar (SAR) (*RADARSAT-2*) observations.

3.1.2 Phase

The phase (ϕ) of a returned electromagnetic field is recorded by polarimetric sensors, which contains information about the timing of waveforms relative to one another, quantified by the difference in phase (in degrees) of co-polarized signals, termed the *co-polarized phase difference* ($\Delta\phi_{HHVV}$). The electromagnetic field generated at the sensor produces waves that are *in phase* ($\Delta\phi_{HHVV} = 0$). If a polarization is delayed upon return or changes in phase as a result of interaction with the target, the polarizations of the returned signal are no longer in phase and the sensor records the difference ($\Delta\phi_{HHVV} \neq 0$) (Figure 3-1).

Co-polarized phase differences can be caused by many scattering mechanisms, including (1) backscatter from the interface surfaces, (2) bistatic, or "double-bounce" backscatter from vertical structures and off a surface (or the reverse), and (3) interaction with scattering centres within a volume (Ulaby et al., 1987). The total quantity of backscatter observed at the sensor is a combination of these three components, the easiest to compute being scatter from (1) the interface surfaces, and (2) the double-bounce components. Scatter from a surface, governed by Fresnel equations (discussed in Section 3.2.2) produces virtually no difference in phase, therefore surface scatter results in $\Delta\phi_{HHVV} = 0$. Conversely, bistatic or "double-bounce" scatter off of vertical cylinders results in monotonic increases in phase difference to a maximum of ~150° (Ulaby et al., 1987).

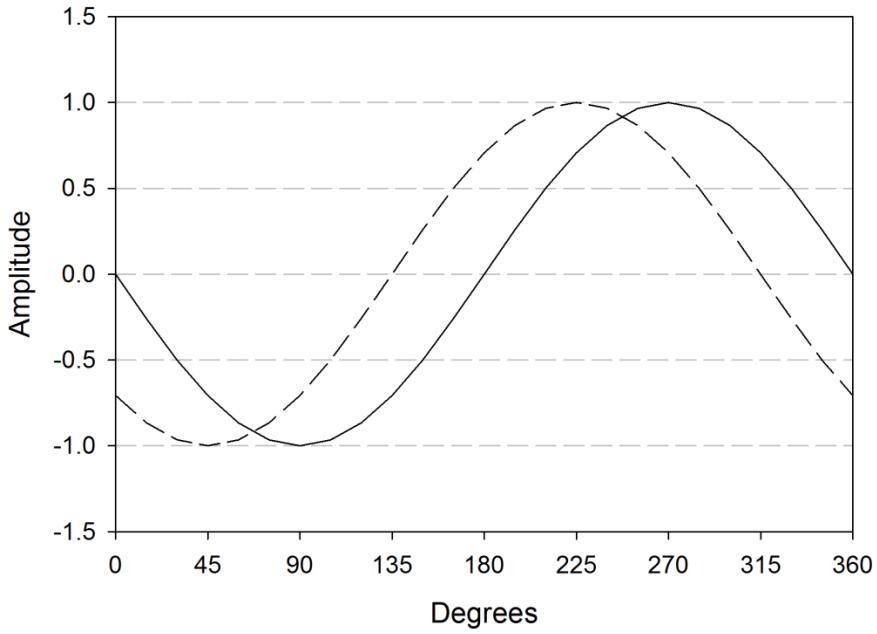

Figure 3-1: Co-pol phase difference ($\Delta\phi_{HHVV}$) of 45° between vertical (solid) and horizontally (dashed) polarized radiation observed at the sensor.

3.1.3 Dielectric Properties

3.1.3.1 Dielectrics

As discussed in Section 2.2.1, H_2O is electrically neutral, however the separability of the positive and negative charges results in a polar molecule with a permanent dipole moment (Frölich, 1958). The separability of the charges allow for H_2O to easily become polarized, leading to the reference of H_2O as a dielectric material.

Dielectrics are electrical insulators, whereby an incident electromagnetic field is not conducted through the media, but causes reorientation of molecules (dielectric polarization) (Petrenko and Whitworth, 1994). The polarizability of a molecule from the permanent dipole state is referred to as dielectric susceptibility, given through

$$D = \varepsilon E \tag{3.1}$$

where D is the displacement current vector, E is the electromagnetic field vector and ε is the permittivity of the medium (Fletcher, 1970; Stiles and Ulaby, 1980; Ellison, 1996). ε is the property of note for determining the polarizability of a medium, and is given through

$$\varepsilon = \varepsilon_r \varepsilon_0 = (1 + \chi)\varepsilon_0 \quad (3.2)$$

where ε_r is the relative permittivity, ε_0 is the permittivity of free space (8.8542 x $10^{-12}C^2N^{-1}m^{-2}$) and χ is a measure of the medium's electrical susceptibility, which determines the readiness of the material to be polarized. The permittivity is independent of field strength but is affected by the frequency of the applied field and the temperature, density and chemical impurities of the media. ε is commonly represented in complex form to represent the magnitude and relative phase of the angular frequency,

$$\varepsilon_r = \varepsilon' - j\varepsilon'' \quad (3.3)$$

where ε' is the real part of the relative permittivity which quantifies the medium's ability to be polarized, and $j\varepsilon''$ is the measure of the dielectric loss factor, presented in imaginary form.

3.1.3.2 Permittivity of Air/Atmosphere

In the case of low frequency microwaves, the relative permittivity of air is assumed to be independent of frequency in the microwave range, and is therefore assumed to be equal to the permittivity of free space ($1.0 < \varepsilon < 1.001$) (Mätzler, 1987). Outside of frequencies commonly used in microwave remote sensing, atmospheric absorption bands exist above 20 GHz caused by suspended water vapour, and precipitation. In the 60 GHz range, oxygen absorption bands dominate, thereby reducing ability of electromagnetic propagation to the surface (Mätzler, 1987).

3.1.3.3 Permittivity of Liquid Phase H_2O

The liquid phase of H_2O is comprised of weakly oriented discontinuous hydrogen bonds, allowing for a greater electrical susceptibility to dielectric polarization. When an electrical field is incident upon liquid H_2O, the dipole molecules become polarized to the direction of the field vector until the field is removed and the molecules return to their resting state. Molecular reorientation is not instantaneous, and the amount of time elapsed between polarization and a rest state is referred to as the *relaxation time* (τ) (Debye, 1929). The dielectric constant in relation to frequency proposed by the Debye dispersion equation is given by,

$$\varepsilon = \varepsilon_\infty + \frac{\varepsilon_s - \varepsilon_\infty}{1 + j\omega\tau} \quad (3.4)$$

$$\varepsilon' = \varepsilon_\infty + \left(\frac{\varepsilon_s - \varepsilon_\infty}{1 + \omega^2\tau^2}\right) \quad (3.5)$$

$$\varepsilon'' = \frac{\varepsilon_s - \varepsilon_\infty \omega\tau}{1 + \omega^2\tau^2} \quad (3.6)$$

where ε_∞ is the high frequency limiting value of the applied field, ε_s is the static dielectric constant as the frequency of the applied field approaches 0, and ω is the angular frequency.

The Debye dispersion equation has been used in a considerable amount of studies for H_2O throughout the EMR spectrum from Hz to THz. The static permittivity of liquid water ($\varepsilon_s, \omega \rightarrow 0$) is 78.3 at 25 °C, and Debye dispersion does not occur until the microwave region where the relaxation frequency is centred at approximately 10 GHz (Figure 3-2) (Evans, 1965; Fletcher, 1970). This is of note for microwave studies, as the loss factor ε'' for water is also centred at approximately 10 GHz. Therefore, any incident electromagnetic field will be subject to increased absorption and decreased penetration.

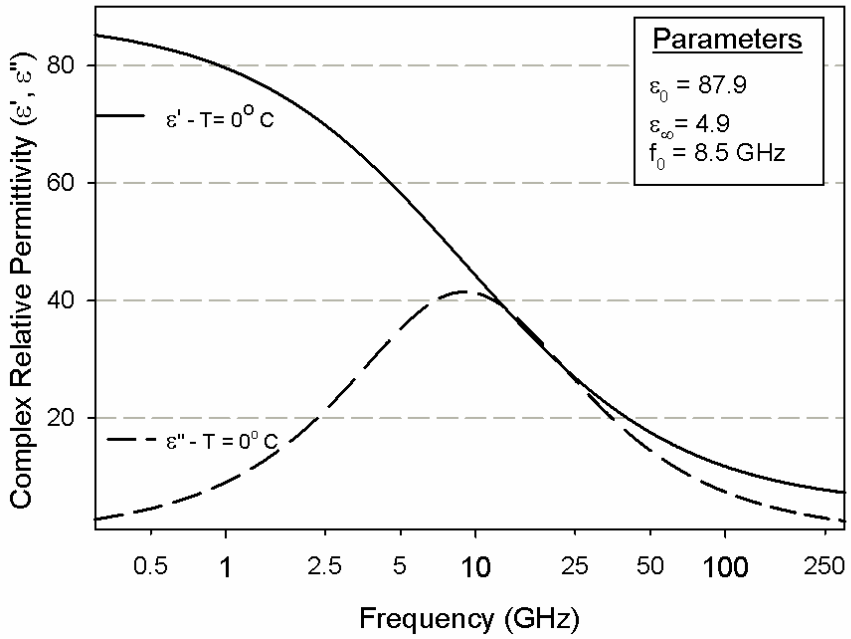

Figure 3-2: Complex relative permittivity of water at 0 °C using the Debye dispersion equation (modified from Ulaby et al., 1986).

The graphical representation of the Debye equation in Figure 3-2 is somewhat misleading because it implies the existence of an asymptotic high frequency limit ($\boldsymbol{\varepsilon_\infty}$). However, the high frequency range of Figure 3-2 does not approach a plateau; the dielectric constant will be influenced by the low frequency tails of atomic dispersion, lowering $\boldsymbol{\varepsilon}$ to an optical permittivity of $\boldsymbol{\varepsilon = 1.77}$, which is equivalent to the square of the refractive index at optical frequencies ($\boldsymbol{\varepsilon = n^2}$).

3.1.3.4 Permittivity of Solid Phase H_2O (Ice)

The dielectric permittivity of ice contrasts that of water due to the highly bonded molecular structure of the lattice. In solid phase H_2O dipole molecules are restricted in the amount of rotation and movement that occurs when an electromagnetic field is applied, and as a result, the relaxation frequency for ice is in the kilohertz region (kHz).

The high frequency relative permittivity (ε_∞) exists in ice between the high frequency tails of Debye dispersion and the low frequency tails of lattice vibration dispersion (Mätzler, 1987; Matsuoka et al., 1997a). The range of ε_∞ is approximately 10 MHz to 300 GHz and is slightly temperature dependent (Figure 3-3) (Mätzler, 2006).

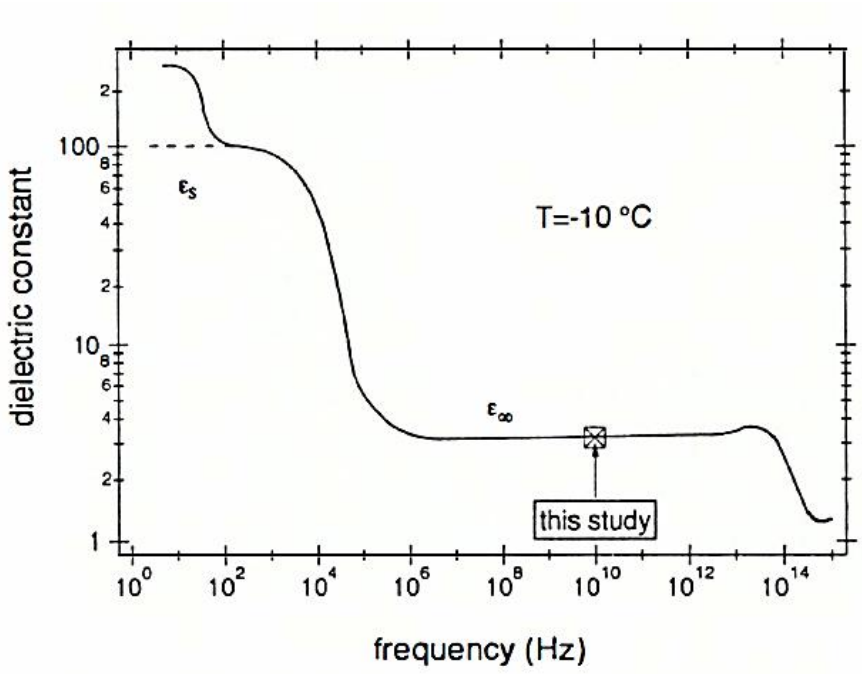

Figure 3-3: Relative permittivity of ice at -10 °C from kHz through the THz range (from Fujita et al., 1993).

Several experiments have investigated the value of ε' for freshwater ice, utilizing wave guides (Cumming, 1952; Vant et al., 1974) and cavity resonators (Lamb, 1946; Mätzler and Wegmüller, 1987). Permittivity measurements across studies agree that $\varepsilon' \cong 3.17 \pm (\varepsilon'' < 0.01)$,

with a slight temperature dependence**.** Mätzler and Wegmuller (1987) also derive relative permittivity of ice through a relation between the complex refractive index ($n = n' - jn"$) and the relative permittivity ($\varepsilon^* = \varepsilon' - j\varepsilon"$), in the microwave region through equations (3.7) – (3.9).

$$\varepsilon = n^2 \tag{3.7}$$

$$\varepsilon' = n'^2 \tag{3.8}$$

$$\varepsilon" = 2n'n" \tag{3.9}$$

The influence of $\boldsymbol{\varepsilon}"$ in microwave frequencies is small in magnitude, unless liquid water is introduced through melt.

3.1.3.5 Permittivity of Snow

Snow is a composition of ice crystals and air, each with distinct dielectric properties. A snowpack covering lake ice is unique in that it is exposed to the wind redistribution, whereas terrestrial snow can accumulate based on vegetation catchments, relief features or in areas of shelter (beneath a tree canopies) (Sturm and Wainwright, 2010). Snow on lake ice is commonly shallower, denser, has a higher slab-to-hoar fraction and fewer layers than snow on land due to wind-scouring from aeolian processes (Sturm and Liston, 2003). In terms of dielectrics, snow has been treated as a homogenous medium for empirical algorithms (Cumming, 1952; Ambach and Denoth, 1980; Tiuri et al., 1984) and as a heterogeneous mix of ice crystals and free space for dielectric mixing models (Polder and van Santeen, 1946; Evans, 1965; Tinga et al., 1973).

When treated as a homogenous medium, the permittivity of dry snow is generated in much the same way as for pure ice; for example, the use of a waveguide (Cumming, 1952) or cavity resonator (Tiuri et al., 1984). The real component of relative permittivity of dry snow, (ε'_{ds}) is independent of temperature or frequency, and is dependent on grain shape and the fractional volume of ice particles within the media (density), with the latter the more influential of the two (Mätzler, 1996). Several studies have produced empirical relationships for ε'_{ds} and $\varepsilon"_{ds}$ for snowpack based on density, given through:

$$\varepsilon'_{ds} = 1 + 2_{\rho_d} \tag{3.10}$$

$$\varepsilon'_{ds} = 1 + 2.2_{\rho_d} \tag{3.11}$$

$$\varepsilon'_{ds} = 1 + 1.91_{\rho_d} \tag{3.12}$$

where $\rho_d$is the density of the snowpack. Equations 3.12 – 3.14 are linear models fit to experimental permittivity data, proposed by Tiuri et al. (1984), Ambach and Denoth (1980) and Hallikainen et al. (1982), respectively. Values for ε'_{ds} for dry snowpacks are commonly found in the 1 – 2 range, with extremely dense snowpacks occasionally exceeding $\varepsilon'_{ds} = 2$. The imaginary part of the relative permittivity (ε''_{ds}), is displayed as a ratio to that of pure ice ε''_i as the magnitude of ε''_{ds} is on the order of 1.0x10^{-3},

$$\frac{\varepsilon''_d}{\varepsilon''_i} = 0.52_{\rho_d} + 0.62_{\rho_d}{}^2 \tag{3.13}$$

Alternatively, the complex relative permittivity can be derived through empirical or physics based dielectric mixing models. Mixing models operate under the assumption that there are inclusions within a medium that have distinct relative permittivities. The inclusions are modeled with a specific grain shape, commonly spheroids or ellipsoids (Polder and van Santen, 1946; Tinga, 1973). For spherical ice inclusion in an air host media, Tinga's (1973) two phase mixing model is given by:

$$\varepsilon_{ds} = 1 + \frac{3v_i(\epsilon_i - 1)}{(2+\varepsilon_i) - V_1(\epsilon_i - 1)} \tag{3.14}$$

where v_i is the volume of the inclusions within the medium, and ϵ_i is the relative permittivity of the inclusions. In this case, the relative permittivity of the host medium is air, and reduces the argument for the host medium 1 (Ulaby et al., 1986). Substituting ε'_{ds} = 3.15 (relative permittivity of ice), Equation 3.14 reduces to:

$$\varepsilon'_{ds} = \frac{1+0.835v_i}{1-0.417v_i} \tag{3.15}$$

$$\varepsilon''_{ds} = \frac{0.34v_i\varepsilon''_i}{(1-0.417v_i)^2} \tag{3.16}$$

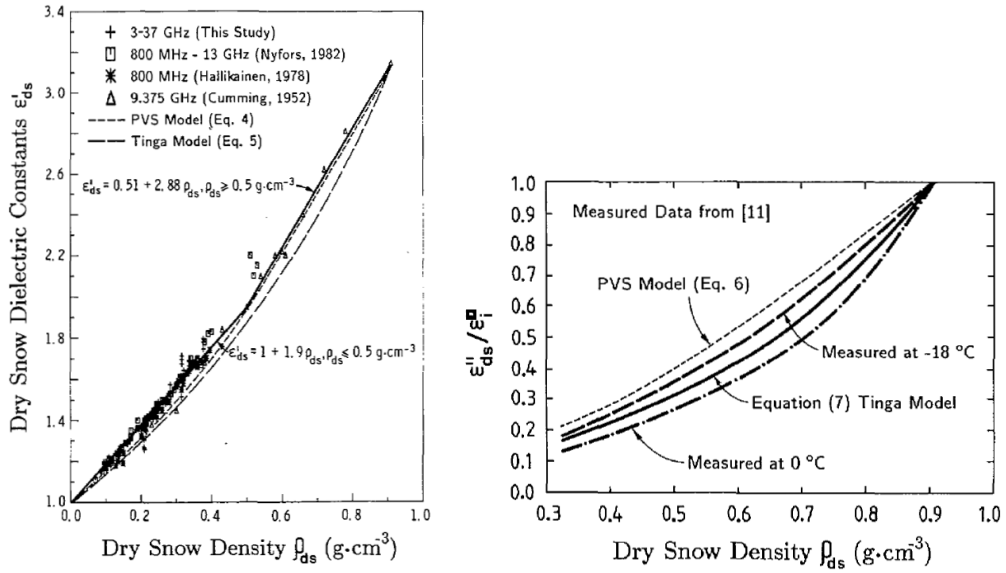

Figure 3-4: ε'_{ds} and ε''_{ds} output from Tinga et al., (1973) relative to permittivities measured with a free-space transmitter (from Hallikainen et al., 1986).

3.2 Behaviour of Electromagnetic Waves in Freshwater Ice System (Boundaries)

In the observation of freshwater lake ice, the generated microwave wave front propagating through space interacts with boundary interfaces and mediums with variable dielectric properties, described in Section 3.1.3. Knowledge of the behaviour of the electromagnetic waves across the boundary layer and through the medium is imperative to deduce the scattering mechanisms responsible for returned backscatter observed at the sensor.

3.2.1 Refraction

Microwaves impingent upon a boundary layer undergo transmission, with modifications to the wave's velocity (υ) and direction (θ) related to the dielectric properties of the medium on either side of the boundary. The angle of transmission into a medium with variable dielectric properties is described by Snell's Law:

$$\sin\theta_1 = \frac{n_1 \sin\theta_2}{n_2} \tag{3.17}$$

where n is the refractive index of the medium identifying the ratio of the velocity of light in a medium relative to a vacuum, θ is the incidence angle and the subscript $_1$ and $_2$ denote the medium in which the signal is traveling through before and after interaction at the interface, respectively. n is also related to the complex relative permittivity of a medium (ε^*), where

$$n = \sqrt{\varepsilon^*} \tag{3.18}$$

Variable refractive indices of media also modify the incident wavelength (λ) in metres and speed of light in a medium (c_t), given through equation 3.19 and 3.20, respectively.

$$\lambda = \frac{1}{\sqrt{\varepsilon^*}} \cdot \frac{c}{f} \tag{3.19}$$

$$c_t = \frac{c}{n_2} \tag{3.20}$$

where c and f are the speed of light (299 792 458 m s^{-1}) and the frequency in Hz, respectively. According to equation 3.19, greater permittivity properties result in greater reduction of wavelength within the medium, with implications as to the potential scatter of incident wavelengths caused by smaller inclusions than if scatterers were observed in a vacuum.

3.2.2 Reflection and Transmission

Microwave radiation incident to a smooth boundary of mediums with a contrast in dielectrics will elicit some change of the electromagnetic waves. Incoming waves at an incidence angle θ_i will have a proportion of the energy scattered coherently in the specular direction with an angle equal to the incident wavefront (θ_r), known as reflection. Part of the incident energy will enter the second medium at a speed and angle dependent on the refractive indices of the boundary mediums, termed transmission.

The resultant proportion of transmission and reflection of microwaves incident upon a smooth boundary are described using power reflection coefficients for non-conducting layered media modeled after Fresnel reflection coefficients (Lorrain et al., 1998):

$$R_{VV} = \left[\frac{-\cos\theta + \left(\frac{\sqrt{\varepsilon_1^*}}{\sqrt{\varepsilon_2^*}} \right) \cos\theta'}{\cos\theta + \left(\frac{\sqrt{\varepsilon_1^*}}{\sqrt{\varepsilon_2^*}} \right) \cos\theta'} \right]^2 \tag{3.21}$$

$$R_{HH} = \left[\frac{\left(\frac{\sqrt{\varepsilon_1^*}}{\sqrt{\varepsilon_2^*}}\right)\cos\theta - \cos\theta'}{\left(\frac{\sqrt{\varepsilon_1^*}}{\sqrt{\varepsilon_2^*}}\right)\cos\theta + \cos\theta'}\right]^2 \tag{3.22}$$

The reflectivity value (R) ranges from 0 to 1, representing the inverse relationship of reflectivity and transmissivity (Γ), where transmission is equivalent to $\Gamma = 1 - R$. The magnitude of reflection (or transmission) is dependent on the degree of the contrast in dielectrics of the mediums. The larger the contrast in dielectrics, the greater reflection coefficient of the interface. For example, the dielectric contrast at boundaries between air ($\varepsilon^* = 1$) and ice ($\varepsilon^* = 3.17$) or air and water ($\varepsilon^* = 80 + i40$) is quite large, which is illustrated in reflection coefficients shown in Figure 3-5.

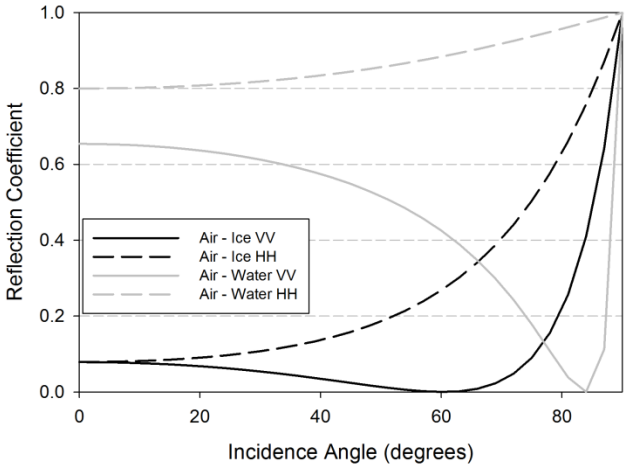

Figure 3-5: Fresnel reflection coefficients for a) a smooth air-ice ($\varepsilon^* = 3.17$) and b) air-water ($\varepsilon^* = 80 + i40$) interface. The solid line represents reflection at vertical polarizations and the dashed line is reflection at horizontal polarizations.

Horizontal reflective coefficient exhibits a monotonic increase with incidence angle in both the ice and water examples, with higher contrast in permittivity resulting in higher reflectivity. Vertical wave fronts exhibit lesser reflectivity, or greater transmissivity compared to horizontally polarized waves. Reflectivity of vertically polarized waves decreases until a minimum is reached, called the Brewster angle where no reflection is observed. The Brewster angle is modified by the

permittivity of the two mediums, as shown in Figure 3-5. Reflection of vertically polarized waves then increases to 1 nearing the grazing angle.

3.3 Radar Remote Sensing of Snow Covered Freshwater Lake Ice

The energy returned to an active microwave sensor by a target after the initial generation of the wave front is termed the backscatter, which provides information as to the magnitude of energy returned, as well as polarimetric considerations (co-polarized phase difference, depolarization, etc.). The magnitude of backscatter is dependent on the sensor parameters (frequency/wavelength), variability in permittivity at the surface/interfaces as well as the physical properties of the targets (surface roughness of interfaces, size/shape of scatterers) (Ulaby et al., 1981). In the context of snow-covered lake ice, backscatter sources include a combination of a) surface and b) volume interaction. Surface interfaces in the propagation path of incident microwaves are the air-snow, snow-ice and ice-water interface, each with unique permittivity properties. Additional volume interaction is possible with inclusions in the snow (ice grains) and ice (air bubble) volumes (Bernier, 1987). The discussion of scattering caused by constituents within snow-covered lake ice is limited to the range of C- to Ku-band (5 – 17.2 GHz) in this section.

3.3.1 The Radar Equation

Active microwave sensors obtain a measurement of the intensity of the signal that is returned to the sensor. In the case of monostatic radar systems, the transmitting antenna also functions as the receiving antenna. The power returned to the sensor (P_r) is described by the radar equation:

$$P_r = \frac{P_t G^2 \lambda^2 \sigma}{(4\pi)^3 R^4} \tag{3.23}$$

where P_t is the transmitted power by an antenna with a gain of G, λ is the transmitted wavelength, σ is the scattering cross-section of the target and R is the distance traveled by the electromagnetic field. Variables in Equation 3.23 other than σ are provided by the radar system parameters, therefore solving for σ provides the target influence on the magnitude of power scattered back to the sensor. The power observed at the sensor antenna is normalized by the radar illuminated area (A) to produce the *radar backscatter coefficient* (σ°) through:

$$\sigma^\circ = \frac{\sigma}{A} \tag{3.24}$$

The radar backscattering coefficient (σ°) is related to the radar equation through

$$\sigma^\circ = \frac{\sigma}{A} = P_r \frac{(4\pi)^3 R^4}{A P_t G^2 \lambda^2} \tag{3.25}$$

Increasing range to the target reduces the power received at the sensor by a factor of the fourth power of the range. As a result, linear returned power, or σ°, can vary over several orders of magnitude and is best expressed as a logarithm with units of decibels, related by Equations 3.26 and 3.27. Further information on the derivation of components of the radar equation are provided in Ulaby et al., (1986b).

$$\sigma^\circ{}_{dB} = 10 \cdot \log_{10} \sigma^\circ{}_{power} \tag{3.26}$$

$$\sigma^\circ{}_{power} = 10^{\sigma^\circ{}_{dB}/10} \tag{3.27}$$

3.3.2 Penetration Depth

For active microwave remote sensing of fresh-water lake ice, observed σ° is dependent on the frequency and look angle of the sensor. Relatively low frequencies in this study (5 – 10 GHz) exhibit penetration depths of up to approximately 10 m in low-loss dielectric mediums (pure ice). The incident wavelengths are sufficient to transmit through the ice and interact with the ice-water interface as a function of the low loss tangent of ice, resulting in low attenuation rates (A_i) for freshwater ice (Royer, 1973).

$$A_i \ (\mathrm{T} = -1°\mathrm{C}) = 3.2 \mathrm{dB/m} \tag{3.28}$$

$$A_i \ (\mathrm{T} = -18°\mathrm{C}) = 1 \ \mathrm{dB/m} \tag{3.29}$$

3.3.3 Microwave Interaction with Snow-Covered Lake Ice Properties

3.3.3.1 Surface Interactions

Surface scatter depends on the physical roughness of a surface, characterized by the root mean square (RMS) of height deviations relative to a mean height of the surface (Woodhouse, 2006). The surface is considered rough when reflectivity becomes increasingly incoherent as height deviations approximate the size of incident wavelengths, causing diffuse scatter and increased depolarization of the incident signal. Scatter is considered to remain coherent when phase differences caused by height deviations satisfy the Rayleigh or Fraunhoffer smooth surface criteria:

$$RMS_{smooth} < \frac{\lambda}{32 \cos \theta} \quad (3.30)$$

In the context of lake ice, the composition and roughness of boundary layers continuously evolve during the winter season. Prior to ice development, calm open water is a specular reflector due to high contrast in dielectrics of the air and water mediums, with σ^O typically below the noise floor of radar sensors. The largest contribution to σ^O over open water is surface roughness attributed to waves caused by wind events (Hall et al., 1994; Morris et al., 1995). Upon H_2O crystallization the relative permittivity significantly reduces and allows transmission of microwave EMR into the ice medium (Bernier, 1987; Woodhouse, 2006). Early season ice cover (skim ice) exhibits efficient specular reflection, as incident EMR penetrates the air/ice interface and reflects off the ice/water interface due to high contrast in dielectrics (as seen in Section 3.2.2).

With continued ice development linear deformation features such as cracks or ridges can cause localized height deviations and increase σ^O, however the majority of boundary layer interactions occur at the ice/water interface (Weeks et al., 1978; Leconte and Klassen, 1991; Nghiem et al., 1998).

3.3.3.2 Volume Interactions (Ice)

As discussed in Section 3.3.2, freshwater ice is a low-loss dielectric, allowing for transmission of incident microwaves to the ice-water interface. Microwave interaction within the ice volume is related to bubble size, shape and density – combined with the status of if the ice is floating or frozen to bed (Jeffries et al., 1994). Tubular bubble inclusions near the ice-water interface have been identified as discrete scatterers, resulting in forward scatter of the incident signal. The unique geometry has been theorized to cause in a double-bounce effect, whereby incident microwaves first reflect off the ice-water interface and then off bubbles (or vice-versa), returning a significant proportion of the incident energy back to the sensor (Figure 3-6). A high concentration of tubular bubbles near the ice/water interface has been shown to correlate with a pronounced increase in σ^O at both VV and HH polarizations (Weeks et al., 1978; Wakabayashi et al., 1993; Morris et al., 1995; Duguay et al., 2002; Lindenschmidt, 2010).

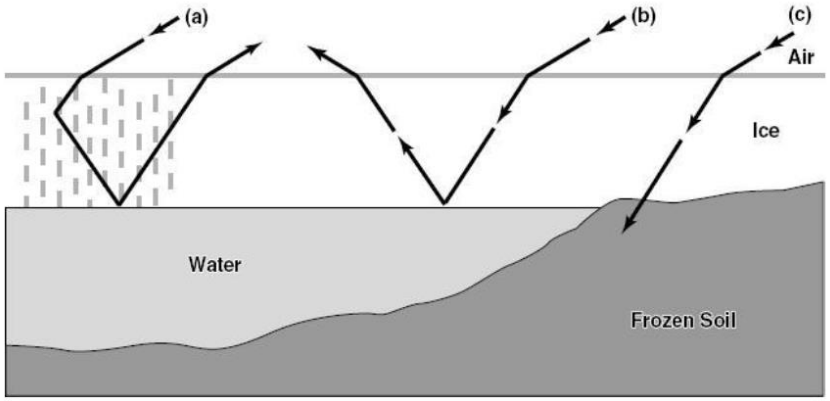

Figure 3-6: Propagation of microwaves incident upon (a) vertically oriented bubbles, (b) clear congelation ice, and (c) ice that is frozen to bed. Source: Duguay et al. (2002).

Studies have correlated the timing of bubble inclusion in the ice column coincident to σ^O increases up to a maximum, where the sensitivity of the signal becomes saturated. Jeffries et al. (1994) exhibited signal saturation at C-band for thin, tubular bubble-dense ice over shallow lakes in Alaska, similar to apparent backscatter saturation observed in Duguay et al. (2002) (Figure 3-7). The presence of high density spherical microbubbles has also been observed to be a source of volume scatter in lake ice. Signal depolarization has been observed to be spatially coincident to surface ice types (snow ice, grey ice) at frequencies <10 GHz (Leconte and Klassen, 1991; Hall et al., 1994; Morris et al., 1995).

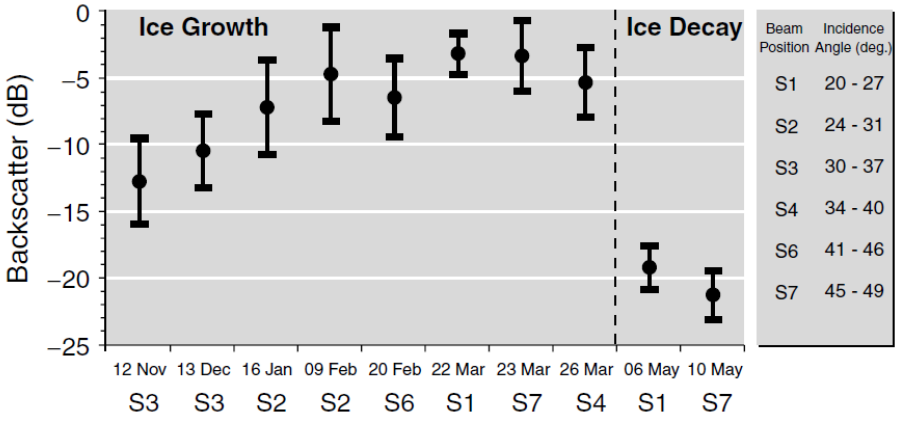

Figure 3-7: RADARSAT-1 C-band (HH) σ^O plateau for shallow, Subarctic lakes. Notice σ^O maximum reached on 09 Feb despite continued ice growth until the end of March (Source: Duguay et al., 2002).

If ice growth rates over shallow lakes are sufficient to freeze to the bed, the high contrast in dielectrics at the ice-water interface is removed. The relative permittivity of the frozen lake sediment ($\varepsilon' = 8$) is significantly lower than that of liquid water, absorbing incident microwave radiation resulting in a σ^O drop in areas that are frozen to bed (Figure 3-8) (Jeffries et al., 1994; Duguay et al., 2002; Hirose et al., 2008).

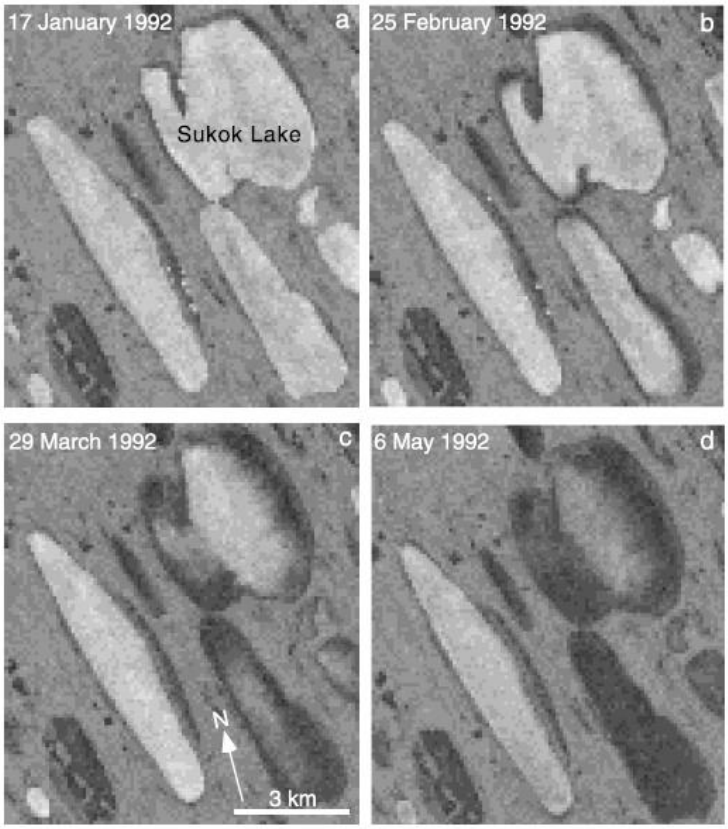

Figure 3-8: Time series of ERS-1 C-band (VV) SAR exhibiting σ^O drop as ice freezes to bottom of shallow lakes in Barrow Alaska (Source: Jeffries et al., 1996).

3.3.3.3 Volume Scatter (Snow)

The density of ice crystals within snowpack varies, with ice crystals comprising approximately 10-20% of the volume in a fresh snowpack, and up to 40% once sublimation and metamorphosis occurs (Woodhouse, 2006). The magnitude of volume scatter in a snowpack is dependent on the incident wavelength, snow density, depth, grain size and snow water equivalent

(SWE). As the ratio of incident wavelengths and ice grains approach unity, incident microwaves are scattered more efficiently through the Mie scattering regime (Woodhouse, 2006).

Metamorphic processes over tundra lakes cause increases in grain size during winter months, resulting in greater σ^O at shorter wavelengths (> 10 GHz) and the initiation of scattering for longer wavelengths (e.g. 9 GHz) (Figure 3-9) (Bernier, 1987). Snowpack density and depth are components in deriving bulk SWE properties. An increase in either component or an overall increase in SWE increases the likelihood of microwave interaction with the overlying snowpack and the potential for depolarizing scatter within the volume. Backscatter at frequencies > 10 GHz have been reported to be sensitive to SWE increases over terrestrial landcover (Stiles and Ulaby 1980; Ulaby and Stiles, 1980; Shi and Cline, 2003; Morrison et al., 2007; Yueh et al., 2009). Frequencies below 10 GHz are considered to be unable to resolve snowpack information except in cases with extremely dense or high SWE conditions (Figure 3-10). In such conditions (e.g. SWE > 40cm), the sensitivity of frequencies > 10 GHz is minimal, necessitating the use of lower frequencies for high SWE snowpacks (Bernier, 1987). It is important to note that the previously reported relationships have been derived over terrestrial sites only, as few studies have investigated microwave interactions with snow overlying lake ice (Kontu et al., 2008).

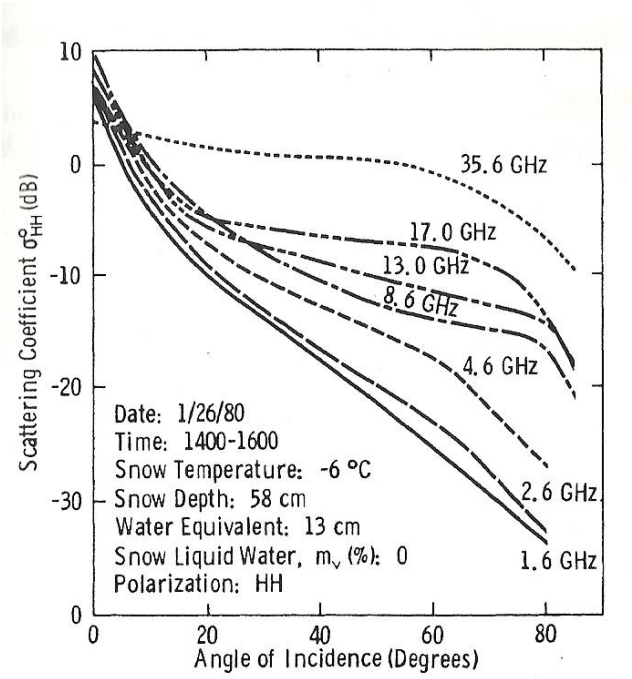

Figure 3-9: Angular response for σ^O of dry snow at a frequency range of 1 - 36 GHz (Stiles et al., 1981).

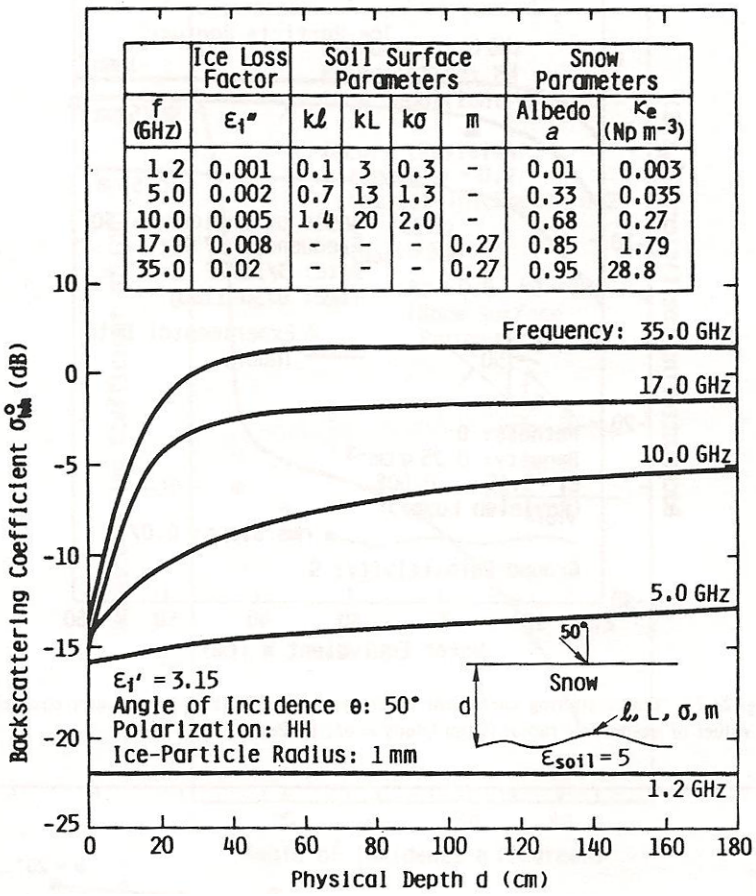

Figure 3-10: Example of σ^o response for terrestrial dry snow at a frequency range of 5 - 35 GHz. Note the high sensitivity of 17 and 35 GHz to shallow snowpack and saturation of signal at ~50cm (Source: Ulaby et al., 1986b).

3.4 Polarimetric Decomposition

Recent developments in active microwave synthetic aperture radar (SAR) have resulted in the spaceborne observation of fully-polarimetric quad-pol data, allowing for the examination of the full target scattering matrix.

3.4.1 Scattering, Covariance, and Coherency Matrix Derivation

Microwaves incident on a target or surface exhibit change in phase and/or polarization states. The energy that is re-radiated by the target has a response in both the vertical and horizontal polarizations, and is expressed in the form of a 2 x 2 scattering matrix in SAR polarimetry:

$$[S] = \begin{bmatrix} S_{HH} & S_{HV} \\ S_{VH} & S_{VV} \end{bmatrix} \tag{3.31}$$

where each element in the matrix represents the backscatter response of the target at a specific polarization. The diagonal elements of the matrix represent the co-polarized scattering information, and the off-diagonal terms represent the cross-polarized information. The scattering matrix provides first order statistics which describe the scattering information of a pure target that exhibits a specific scattering mechanism, but is often insufficient to describe the scattering response of complex distributed targets in nature. Therefore, second-order statistics of the backscatter response are obtained through the covariance or coherency matrices that are derived from the vectorized form of the scattering matrix from the Pauli and Lexicographic basis (Verma, 2012). The vectorized version of the scattering vector, or covariance vector (k_c) assumes reciprocity in the monostatic case ($S_{HV} = S_{VH}$) and is obtained through

$$k_C = \begin{pmatrix} S_{HH} \\ \sqrt{2}S_{HV} \\ S_{VV} \end{pmatrix} \tag{3.32}$$

The scattering properties are represented in the power domain through the covariance matrix $[C]$, derived through $k_c \times k_c^+$:

$$[C] = \begin{pmatrix} S_{HH}S_{HH}^* & \sqrt{2}S_{HH}S_{HV}^* & S_{HH}S_{VV}^* \\ \sqrt{2}S_{HV}S_{HH}^* & 2|S_{HV}|^2 & \sqrt{2}S_{HV}S_{VV}^* \\ S_{VV}S_{VV}^* & \sqrt{2}S_{VV}S_{HV}^* & |S_{VV}|^2 \end{pmatrix} \tag{3.33}$$

where + is representative of the complex conjugate and transpose, and * represents the complex conjugate.

The coherency matrix is similarly derived as a vectorized version of the scattering matrix, again assuming reciprocity of cross-polarized scattering elements.

$$k_T = \frac{1}{\sqrt{2}} \begin{pmatrix} S_{HH} + S_{VV} \\ S_{HH} - S_{VV} \\ 2S_{HV} \end{pmatrix} \tag{3.34}$$

The vectorized scattering matrix in Equation 3.34 is useful for target decomposition because the elements present a physical interpretation (surface, double or volume bounce). The scattering properties of Equation 3.34 is converted to the coherency matrix $[T]$ in the power domain using the product of $k_T \times k_T^+$:

$$[T] = \begin{pmatrix} |S_{HH} + S_{VV}|^2 & \langle (S_{HH} + S_{VV})(S_{HH} - S_{VV})^* \rangle & 2\langle (S_{HH} + S_{VV}) S_{HV}^* \rangle \\ \langle (S_{HH} - S_{VV})(S_{HH} + S_{VV})^* \rangle & |S_{HH} - S_{VV}|^2 & 2\langle (S_{HH} - S_{VV}) S_{HV}^* \rangle \\ 2\langle S_{HV}(S_{HH} + S_{VV})^* \rangle & \sqrt{2} S_{VV} S_{HV}^* & 4\langle |S_{HV}|^2 \rangle \end{pmatrix} \quad (3.35)$$

The sum of the diagonal elements of the covariance matrix $[T]$ represents the total power of the scattered wave returned to the sensor.

3.4.2 Coherent and Incoherent Decompositions

Polarimetric decompositions utilize the target scattering matrix to extract the scattering components for each observed pixel based on either the scattering matrix [S] or the covariance/coherency matrices ($[C]$, $[T]$). Polarimetric decompositions using the [S] matrix are categorized as *Coherent*, with decompositions using $[C]$ and $[T]$ categorized as *Incoherent*. Coherent target decompositions are useful for pure target geometry within a single pixel that returns completely polarized backscatter, synonymous with man-made objects (e.g. buildings, bridges, corner reflectors). Incoherent target decompositions statistically characterize the complex scattering behaviour of naturally occurring distributed targets, which return a complex scattering response due to the speckle noise inherent in SAR observations. It is therefore more appropriate to utilize the incoherent target decomposition method for the types of scattering media in lake ice environments.

Incoherent polarimetric decompositions model the second-order polarimetric representations of the $[C]$ or $[T]$ matrices; the most notable contribution being the three component scattering model proposed by Freeman and Durden (1998) which describes the polarimetric response of naturally distributed targets through surface bounce, double bounce, and volume scatter (Figure 3-11), without the use of ground measurements. The surface bounce component is modeled by a first-order Bragg scattering surface assuming zero depolarization/cross-polarization. The double-bounce component is modeled as a dihedral reflector that exhibits Fresnel-style reflection at multiple surfaces. The volume scatter component is modeled as a uniform distribution of a probability density function to describe the orientation of cylinder-like dipoles in an air host, similar to a vegetation canopy. The three component model was extended by Yamaguchi, with the incorporation of a helical component (developed by Krogager and Freeman (1994)) to account for co-polarized and cross-polarized responses typically observed in complex urban environments, which is typically unobserved in natural distributed targets. In addition, multiple polarimetric decompositions have been proposed using experimental datasets, with multiple fully-polarimetric sensors and acquisitions becoming increasingly available (Freeman and Durden, 1998; Yamaguchi, 2006; Cloude, 2010).

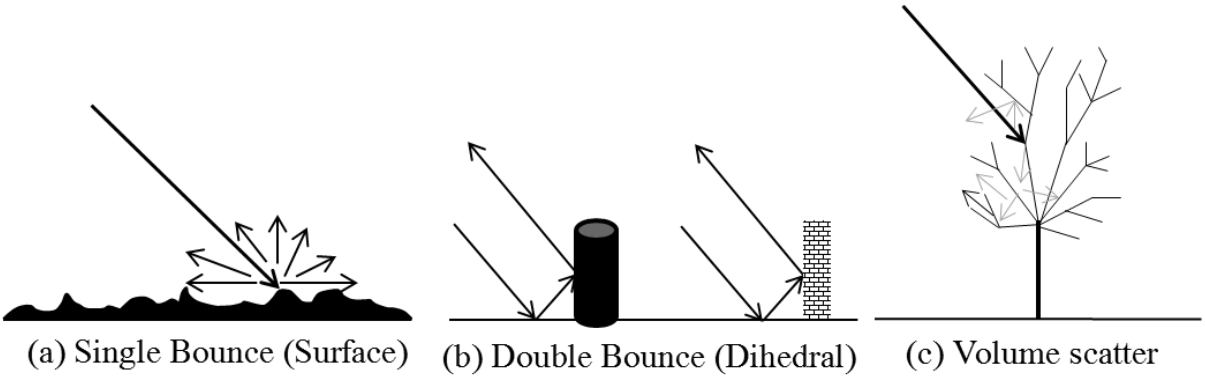

Figure 3-11: Polarimetric decomposition scattering mechanisms as proposed by Freeman and Durden (1998): (a) Surface bounce from a rough surface, (b) double bounce scatter from ground and a tree trunk or wall, and (c) volume scatter from tree branches.

Few polarimetric decompositions have been conducted for fresh-water lake ice. Van der Sanden and Drouin (2011) developed polarimetric parameters for freshwater river ice, determining that the Pauli double-bounce component exhibited the highest correlation when categorizing various ice types. However, the study did not report the power parameters of the $[C]$ or $[T]$ matrices. Engram et al. (2013a, 2013b) observed a positive correlation with large methane ebullition (0.01 – 1m) bubbles and the Pauli single-bounce component using multiple low-frequency L-band (1.2 GHz) SAR acquisitions within a single spring season. The increases in the Pauli single-bounce component was hypothesized to be the result of modification of the surface at the ice-water interface by methane ebullition bubbles to produce large-scale roughness features to produce increasingly diffuse scatter (Engram et al., 2013a). Model-based polarimetric decomposition of SAR acquisitions over tubular-bubbled freshwater lake ice not associated with methane ebullition with has currently not yet been observed.

3.5 Radar Datasets

The research within this thesis utilized two fully polarimetric radar datasets acquired using ground-based and spaceborne observation platforms. Ground-based observations were acquired at 9.6 (X-band) and 17.2 GHz (Ku-band) during the 2009-2010 and 2010-2011 winter seasons using UW-Scat, a fully polarimetric sledborne FMCW. Spaceborne scenes were acquired from RADARSAT-2 (C-band, 5.6 GHz) temporally and spatially coincident to UW-Scat observations to provide multi-frequency polarimetric observations of backscatter mechanisms within lake ice. This section describes the technology and collection parameters of radar acquisitions that are utilized in the

manuscripts within this thesis. Description of data products and procedures using UW-Scat and RADARSAT-2 are described in Section 3.5.1 and 3.5.2, respectively.

3.5.1 FMCW Dataset – UW-Scat

Scatterometer observations were conducted on Malcolm Ramsay Lake near Churchill, Manitoba, for the winter seasons of 2009-2010 and 2010-2011 at static and roving sites to capture local snow and ice variability. In both observation periods the static sites were positioned in a N/S transect. Observations were conducted monthly in 2009-2010 due to limited intensive observation periods, and bi-weekly in 2010-2011. The University of Waterloo Scatterometer system (UW-Scat) is comprised of two frequency modulated continuous wave (FMCW) radars that operate with a bandwidth of 500 MHz with centre frequencies of 9.6 (X-band) and 17.2 GHz (Ku-band). UW-Scat functions using a switched transmit-receive antenna mode, obtaining fully polarimetric observations (VV, HH, VH, HV). Each scan is conducted by mounting the radio frequency (RF) units on supports that were maneuvered by a stationary Kipp and Zonen 2ap Suntracker unit (Figure 3-12).

Figure 3-12: Sled-borne UW-Scat field set up during Ku-band scan of undisturbed static site on Malcolm Ramsay Lake near Churchill, Manitoba.

Each scan was comprised of a 60° azimuth sweep for an incidence angle range of 21 - 60° at 3° increments, resulting in a total of 20 scan lines. Data blocks that are collected by the scatterometer are translated to the range domain via a fast Fourier Transform. Transmit leakage is estimated by coherently subtracting averaged sky observations from each scan. The range profiles for each incidence angle are then averaged in azimuth (Geldsetzer et al., 2007). Additional relevant UW-Scat sensor parameters are provided in Table 3-1, with a further description of the calculation of normalized radar cross section (NRCS) in King et al. (2013) and Section 3.3.1.

Table 3-1: UW-Scat Sensor Specifications

Parameter	X-band	Ku-band
Output Frequency (GHz)	9.35-9.85	16.95 - 17.45
Transmit Bandwidth (GHz)	0.5	0.5
Transmit Power (dB)	-11.8	-8.0

Range Resolution (m)	0.3	0.3
Cross-polarization isolation (dB)	>30	>30
Sensitivity/Noise Floor (dB m2/m2)	-50	-50
Antenna Beam width (°)	4.3	5.6
Transmit/Receive polarizations	VV/VH/HH/HV	VV/VH/HH/HV

3.5.2 Synthetic Aperture Radar (SAR)

Synthetic aperture radar (SAR) systems are commonly mounted on a moving platform (airborne/spaceborne) and operate using a side-looking geometry that illuminates ground targets perpendicular to the direction of flight. Active microwave observations from space are independent of reflected solar radiation and penetrate through cloud cover, enabling year-round observations of ground targets in Arctic and sub-Arctic regions. SAR systems transmit a linear chirp over a specific frequency range and combine and record subsequently returned echoes. SAR systems achieve high spatial resolution in the azimuth (along-track resolution) through the application of Doppler principles to process returned radar echoes, achieving high spatial resolution independent of target distance or antenna length (Ulaby et al., 1982a).

SAR acquisitions, or complex images, are formed of a 2-D array of pixels that represent a complex number (amplitude and phase information) associated with the radar return from all the scatterers present in the pixel's ground footprint (Lee and Pottier, 2009). The derivation to the returned power to the normalized backscatter coefficient is provided in Section 3.3.1.

RADARSAT-2 is a fully-polarimetric SAR with centre frequency of 5.405 GHz, and is jointly owned between government (Canadian Space Agency (CSA)) and industry (McDonald, Dettwiler, and Associates Ltd. (MDA)). The satellite was launched in December 2007 as a follow-on mission to RADARSAT-1 (co-pol HH) (launched 1995) to continue legacy operations with improvements to high resolution imaging (3 x 3 m) while providing additional polarizations and beam modes, shown in Table 3-2. RADARSAT-2 was the first operational SAR to provide fully-polarimetric quad-pol capabilities. The satellite's mission is to monitor the environment and natural resources, with numerous applications in the observation of the Cryosphere (Geldsetzer et al., 2010; Lindenschmidt et al., 2010; van der Sanden and Drouin, 2011; Cable et al., 2014).

RADARSAT-2 is polar orbiting in a time-offset identical orbit to RADARSAT-1 at an inclination of 98.6° with a repeat pass of 24 days, with potential coverage north of 48° every 1-2 days. The fully polarimetric beam modes are of reduced nominal swath (25 km) but offer the potential for polarimetric decomposition through the scattering [S] or covariance [C_3] and coherency [T_3] matrices. This thesis utilizes Fine-Beam Quad Polarization observations acquired over an incidence angle range of 19.4 – 39.35°, more specifically FQ1 (19.4), FQ11 (31.4°) and FQ18 (38.35°).

Table 3-2: RADARSAT-2 Beam Mode Characteristics

Polarization	Beam Mode	Swath Width (nominal) (km)	Incidence Angle Range	Ground Resolution (m)
Dual Pol HH, HV VV, VH	Standard	100	20 - 49	25 x 28
	Wide	150	20 - 45	25 x 28
	Low Incidence	170	10 - 23	40 x 28
	High Incidence	70	50 - 60	20 x 28
	Fine	50	37 - 49	10 x 9
	ScanSAR Wide	500	20 - 46	100 x 100
	ScanSAR Narrow	300	20 - 49	50 x 50
Polarimetric HH, HV, VV, VH	Standard Quad-Pol	25	20 - 41	25 x 28
	Fine Quad-Pol	25	20 - 41	11 x 9
Selective Single Polarization HH, VV	Multi-Look Fine	50	30 - 40	11 x 9
	Ultra-fine	20	30 - 50	3 x 3

3.6 Summary

Microwave backscatter observations of snow-covered fresh-water lake ice are the result of a combination of interactions within the snow and ice volumes and interfaces, governed by the physical and dielectric status of the media. Snow-covered lakes present a unique combination of multi-layered targets for incident electromagnetic waves, as the scattering potential continuously evolves throughout the winter season with changes to the overlying snowpack (grain size metamorphosis,

depth modification), surface ice types (snow, grey ice), ice volume (tubular bubble inclusions) and the roughness at the associated boundary layers. A wide range of σ° is observed both spatially and temporally as the medium's physical and dielectric properties fluctuate. Table 3-3 presents a summary of the snow and ice properties that influence backscatter in fresh-water environments.

The contribution of scatter from physical parameter near the ice surface (snow and ice types) and within the ice volume (double-bounce caused by tubular bubbles) have been hypothesized and modeled, but not quantified through field observations. SLAR and SAR do not possess the required range resolution to provide quantitative information regarding the scattering contribution from components near the snow-ice and ice-water interface.

The current interpretation of lake ice backscatter evolution is analogous to the hypothesis first presented by Sellmann et al. (1975) whereby bright regions (high σ°) are related to increases in bubble content within the ice. Concurrently, studies that have observed scattering from ice have typically been restricted to single polarizations (Jeffries et al., 1993; Wakabayashi et al., 1993; Matsuoka et al., 1999), which typically provided the basis for validating backscatter models that incorporated tubular bubbles into the volume.

Quantification of scattering components within lake ice is needed to further future research endeavors into: a) modeling backscatter from snow-covered lake ice, and b) the observation and monitoring of lake ice using increasingly advanced technology, including the development of full- and compact-polarimetric spaceborne sensors. Both of the gaps identified will be examined in the next three chapters.

Table 3-3: Influence of seasonal snow and ice properties on observed backscatter for fresh-water environments.

Parameter	Influence
Permittivity	Incident electromagnetic fields penetrate both snow and ice to a significant depth in sub-freezing scenarios. During melt scenarios, the high-relative permittivity of liquid water absorbs incident microwaves, significantly reducing penetration through the overlying snowpack, effectively restricting the observation of the ice volume.
	Snow
Depth	Thicker snow increases the path length of incident microwave radiation, promoting increased potential for interaction with snow grains.
Density	Increased snow density exhibits a relationship with bulk snow permittivity and thermal conductivity, modifying scattering potential.
Grain Size	Grain size increases approaching the wavelength of the incident electromagnetic field causes increased scatter. Continuous metamorphosis and snow redistribution in lake environments produces significant variability in snow grain size, influencing overall backscatter.
	Ice
Interface Roughness	Interfaces with significant contrast in relative permittivity (ice-water) serve as specular reflectors when smooth. Modification of roughness at the ice-water interface during ice growth increases σ° potential.
Thickness	Analogous to snow, thicker ice presents a greater potential for the inclusion of tubular or spherical bubbles in the ice volume. Additionally, thicker ice presents greater separation from interactions near the snow-ice and ice-water interface.
Tubular Bubbles	Tubular bubble inclusions present a significant source of double-bounce scatter, with increasing bubble density causing saturation of the signal returned to the sensor.
Surface Ice Types	An increase in spherical microbubble density near the snow-ice interface presents depolarizing scattering potential, influencing cross-polarized σ° and limiting penetration into the ice volume.
Frozen to Bed	Upon freezing to bed the high permittivity contrast ice-water interface is removed and replaced with a lower contrast ice-ground interface, thereby lowering the reflection coefficient of the interface, and therefore, observed σ°.

Chapter 4
Observation and Modeling of X- and Ku-band Backscatter of Snow-Covered Freshwater Lake Ice

4.1 Introduction

Lakes, in their open water or frozen state, comprise 2% of the Earth's surface and are an important thermodynamic component in the global cryosphere. In arctic and subarctic boreal/tundra environments lakes can occupy 15-45% of the landscape (Brown & Duguay, 2010). The presence of lake ice influences lake-atmosphere exchanges by modifying the radiative properties of the lake surface and moderating the transfer of heat to the atmosphere (Brown & Duguay, 2010; Melling, 2012). Through these effects, ice cover serves to influence local/regional weather and climate patterns including but not limited to thermal moderation and lake-effect snow (Rouse et al., 2008).

The timing of snow deposition and snow density overlying lake ice is a dominant factor influencing lake ice growth. The lower thermal conductivity of snow ($0.08 – 0.54\ Wm^{-2}K^{-1}$) compared to that of ice ($2.24\ Wm^{-2}K^{-1}$) serves to insulate the underlying media, limiting heat flux from the water through the ice to the atmosphere, thereby reducing the ice growth rate (Sturm & Benson, 1997; Jeffries & Morris, 2006). Snow mass can also modify the ice composition and thickness through the development of snow ice (Brown and Duguay, 2010).

Thermodynamic models have been successful in simulating ice thickness and phenology when snow depth and distribution information is known, either from shoreline monitoring or field sampling (Duguay et al., 2002). Sensitivity analyses of input parameters reveal that the presence and depth of snow overlying the ice column exerts a greater influence on ice growth rates than air temperature, necessitating accurate snow cover knowledge over lakes for modeling ice thickness and composition (Brown and Duguay, 2010).

The network of manual lake ice monitoring stations in the Arctic has been severely reduced since the late 1900s (Duguay et al., 2002). Existing monitoring stations are confined to either populated regions or relatively accessible coastal areas, with few stations in remote regions of the Arctic. Satellite remote sensing can improve monitoring of snow and ice conditions in remote arctic environments. Active microwave remote sensing has been identified as useful for retrieving both snow and ice properties, as wavelengths within the microwave spectrum interact with the snow and/or ice volume, providing the potential for snow mass (density, SWE) (Mätzler et al., 1982) and ice

thickness/composition estimates. Active microwave sensors are also able to obtain measurements independent of solar radiation and cloud cover, allowing for measurements throughout the winter season. Several studies have investigated the backscatter response of evolving lake ice cover at relatively low microwave frequencies (C-, X-band), inferring lake ice composition characteristics (Duguay et al., 2002; Elachi et al., 1976; Weeks et al., 1981; Leconte & Klassen, 1991). Ku-band has been observed to interact with the thermodynamic state of snow overlying freshwater lake ice, and exhibits sensitivity to snow mass in terrestrial snow (King et al., 2013).

This study presents the winter evolution of backscatter observations for snow covered lake ice at X- (9.6 GHz) and Ku-band (17.2 GHz) collected within the Canadian Snow and Ice Experiment (CASIX) during the winter of 2010-11 near Churchill, Manitoba. Additionally, a model based on the multi-layer dense media radiative transfer (DMRT–ML) under the quasi-crystalline approximation (QCA) is used to simulate backscatter response from snow and lake ice in order to interpret observational data. The model treatment of bubbled ice uses the reciprocity theorem in replacing the real component of the relative permittivity (ε') of the host medium (ε'=1) and its inclusions (ε'=3.14) that are used for snow to a host medium (ε'=3.14) with air (ε'=1) inclusions.

The goal of this study is to observe the coincident backscatter response for various ice cover types (clear, tubular bubbles, grey surface ice, etc) at X- and Ku-band to produce a backscatter evolution through the winter observation period. In addition, this study aims to identify and model the physical components that contribute to overall backscatter within the lake ice system (i.e. snow, surface ice types, and tubular bubbles within the ice volume). In-situ snow and ice properties with coincident scatterometer observations are described in Section 4.3. Section 4.4 presents the formulation and simulations of the bubbled-ice model, with conclusions in Section 4.5.

4.2 Background

Many studies examine the backscatter response from freshwater ice using various frequencies (C-, X-, Ku-band) on airborne (Elachi et al., 1976; Weeks et al., 1981; Leconte & Klassen, 1991) and spaceborne (Duguay et al., 2002; Jeffries et al., 1996; Howell et al., 2009) platforms. Frequencies within this range of the electromagnetic spectrum (5 – 17 GHz) are sensitive to the presence of liquid water within the snowpack or ice surface due to the contrasting dielectric properties of water and ice. The relative complex permittivity of a media is given by

$$\varepsilon^* = \varepsilon' + j\varepsilon'' \tag{4.1}$$

where ε' is real and $\varepsilon^{"}$ are the real and imaginary components of ε^{*}, respectively. The permittivity of pure water varies across the microwave region of the electromagnetic spectrum due to temperature and frequency dependencies associated with Debye-style dispersion (Ulaby et al., 1986). The dielectric constant of water is $\varepsilon' \sim 40$ and $\varepsilon' \sim 20$ for pure water at 0 ^{0}C at X- and Ku-bands, respectively (Meissner & Wentz, 2004). Conversely, the real component of the relative permittivity of ice is $\varepsilon_i' = 3.15$ and is considered independent of temperature (below 0 ^{0}C) or frequency across the microwave spectrum (Ulaby et al., 1986). The contrasting dielectric properties of water and ice form the basis of physical property retrieval within the lake ice system associated with the presence of liquid water, such as ice phenology, ice volume, and grounded ice areas.

Studies examining winter season backscatter evolution for shallow ponds and lakes with spaceborne SAR reveal a seasonal pattern during ice growth (Duguay et al., 2002; Jeffries & Morris, 1994; Morris et al., 1995). Ice that is free of bubbles or impurities early in winter results in low backscatter due to the lack of volume scatter and to the specular reflection of incident radiation at the ice-water interface (so long as the snow-ice and ice-water interfaces remain smooth). Interfaces become rough when height deviations relative to the mean (h) are greater than $\frac{\lambda}{8 \cos \theta_i}$, known as the Rayleigh criterion. Larger height deviations result in increasingly diffuse scatter (Woodhouse, 2006).

As ice thickens, tubular and teardrop-like bubbles can be incorporated into the ice volume, oriented parallel to the direction of ice growth. The density and shape of bubble inclusions are dependent on gas concentration in the water and the ice growth rate (Bari & Hallet, 1974; Yoshimura et al., 2008). The inclusion of tubular bubbles in the ice volume is thought to cause "double-bounce" of incident microwaves; a combination of forward scatter off bubble inclusions and reflection off the high contrast in permittivity at the ice-water interface (Duguay et al., 2002). The double-bounce effect returns a substantial portion of the initial signal transmission relative to other interactions, resulting in a considerable overall increase in backscatter relative to clear ice. Figure 1 shows an idealized portrayal of the potential propagation paths of incident microwave radiation.

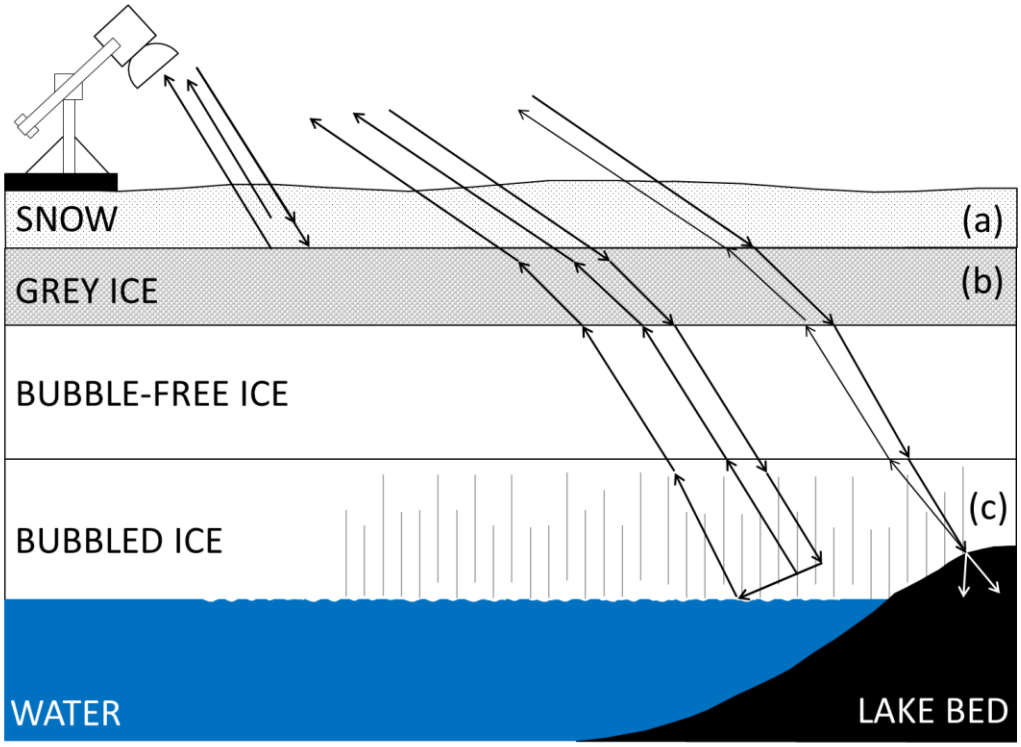

Figure 4-1: Propagation path of microwaves within (a) snowpack overlying lake ice, (b) spherical micro-bubbles in grey ice, and (c) tubular bubbled ice layer that is either floating or grounded. This represents a typical bubbled-ice situation at maximum ice thickness on Malcolm Ramsay Lake (modified from Duguay et al., 2002).

High density spherical micro-bubbles can form within surface ice layers when: (a) ice formation is nucleated by snow precipitated on calm or turbulent water, forming an initial ice cover with a randomly oriented c-axis commonly referred to as "grey ice" (Michel & Ramseier, 1971); (b) the weight of snowpack is sufficient to depress the ice cover below the hydrostatic water level, flooding the surface at the ice edge or via infiltration through cracks in ice, forming a superimposed layer of "snow ice", or "white ice" (Michel & Ramseier, 1971). The resulting media, with high density spherical bubbles on the order of 0.5 – 1mm has been noted as a potential source of volume scatter (Leconte et al., 2009; Hall et al., 1994; Nolan et al., 2002). Larger methane ebullition bubbles on the order of 0.1 – 1m distributed throughout the ice cover have also been identified as a source of backscatter when observed using low frequency active microwave sensors (C-, L-bands) (Walter et al., 2008; Engram et al., 2013; Haijang et al., 2009).

If the ice cover is sufficiently thick to freeze to bed, the high contrast in relative permittivity at the ice-water interface is removed and replaced by the lower-contrast ice-ground interface. The lower contrast in permittivity associated with the ground interface serves to absorb incident microwave radiation (at various efficiencies depending on the substrate composition), reducing overall backscatter magnitude (Jeffries et al., 1996; Duguay & Lafleur, 2003; Grunblatt & Atwood, 2013).

A number of studies have modeled the scattering properties of snow covered ice, with a dominant focus on sea ice (Tjuatja et al., 1992; Fung, 1994; Nghiem et al., 1995; Redmuund & Long, 2003; Albert et al., 2012), while few have investigated freshwater lake or river ice (Gherboudj et al., 2010; Wakabayashi et al., 1994; Matsuoka et al., 1999). Backscatter models used for sea ice commonly separate ice into saline (first year) and de-salinated (multi-year) ice. De-salinated multi-year ice is commonly likened to freshwater lake ice due to the low brine content and air pockets (drained brine channels) throughout the ice column. In contrast to multi-year ice, tubular bubbles within lake ice are commonly incorporated into the lower depths of the ice column during secondary ice development, modifying the scattering potential. Further, observed surface roughness of multi-year ice is exaggerated compared to lake ice by the annual formation of melt ponds, facilitating differential backscatter characteristics at the ice surface (Gogineni et al., 1992)..

Modeling studies that are specific to freshwater ice are commonly formulated at C-band due to the availability of spaceborne observations that can be used as training or validation data (Gherboudj et al., 2010; Wakabayashi et al., 1994). Bubbles within ice have commonly been modeled as spherical using a distribution function of bubble density under the Mie scattering theory (Matsuoka et al., 1999), or a combination of spherical and cylindrical bubbles using radiative transfer theory (Gherboudj et al., 2010; Wakabayashi et al., 1994). The overall contribution of the overlying snow layer is generally assumed to be transmissive or relatively insignificant at C-band by observational (Leconte & Klassen, 1991; Weber et al., 2003) and modeling studies (Gherboudj et al., 2010; Matsuoka et al., 1999). However, snowpack overlying lake ice presents an increasingly effective scattering media at higher frequencies such as Ku-band, with σ^0 differences of up to 8 dB between observations of smooth bare ice and snow covered lake ice (Onstott et al., 1982).

4.3 Lake Ice Scatterometer Observations

4.3.1 Study site

Malcolm Ramsay Lake (formerly Lake 58) is situated 20 km east of Churchill, Manitoba (58.7221^{0}N, 93.7845^{0}W) in the Hudson Bay Lowlands region (Figure 4-2). The lake covers an area of approximately 2 km^2, with a lake bed comprised of organics and sediment, and has a mean depth of 2.4 m, with maximum depths of 3.2 m (Duguay & Lafleur, 2003).

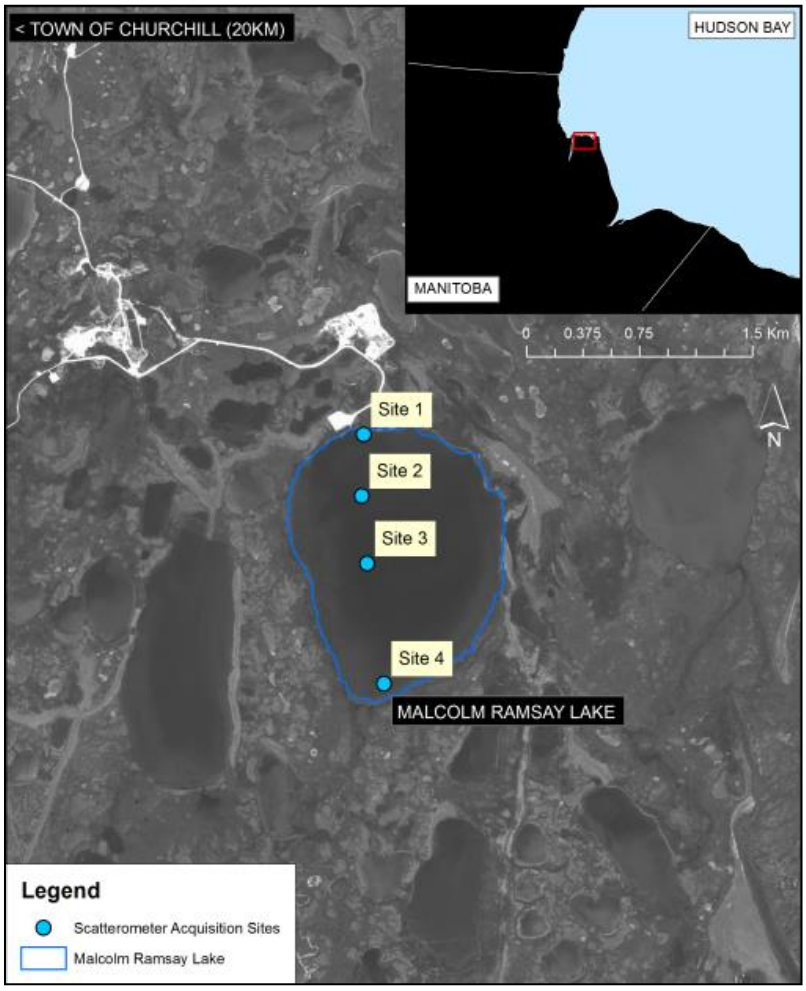

Figure 4-2: Distribution of static scatterometer observation sites on Malcolm Ramsay Lake, near Churchill, Manitoba, Canada.

The region is characterized by the intersection of three ecological zones; the boreal forest, the forest-tundra transition, and tundra, with the boundaries between zones running parallel to the coast (Scott et al., 1987). The Hudson Bay Lowlands are typified by high lake fraction, comprising 40% of

the landscape (Bello & Smith, 1990). Lakes and ponds in the area surrounding Malcolm Ramsay Lake most commonly occur in tundra regions (32% of total surface area), compared to tundra-boreal forest (24%) and forest ecozones (7%) (Lafleur et al., 1997). The regional relief is relatively flat, with major formations and associated overburden the result of glacial deposits.

The mean annual air temperature at Churchill airport (58.7392 ^{0}N. 94.0664 ^{0}W) is -6.9 ^{0}C, with positive mean monthly temperatures occurring from June through September. The total water-equivalent precipitation is 432 mm, of which 1.91 m falls as snow. The situation of Churchill also lends to its high annual sustained wind average (20.5 km/h), influencing ice stratigraphy and snowpack development.

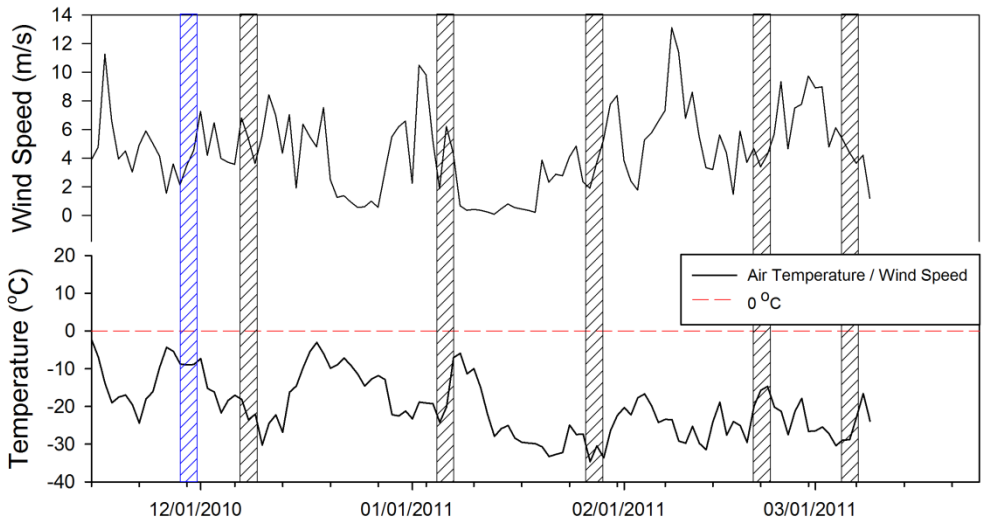

Figure 4-3: Wind speed and temperature collected using an automated weather station on the north shore of Malcolm Ramsay Lake from 1-10-2010 to 25-3-2011. Scatterometer observations begin 28-11-2010, with dates indicated by hashed columns. The blue column indicates that only Site 1 was visited due to thin ice conditions at other sites.

Meteorological variables measured on the north shoreline of Malcolm Ramsay Lake include air temperature, relative humidity, and wind speed/direction (Figure 4-3). Ambient air temperature did not exceed 0 °C during the period of scatterometer observations, maintaining dry snowpack conditions. Measured winds during the observation period originated dominantly from the northwest, with sustained mean wind speeds of 17.42 km/h with a standard deviation of 9.94 km/h. Events with sustained winds of 50.18 km/h recorded on the shoreline were common and are requisite for the formation of the tundra-lake classification of snow (Sturm & Liston, 2003).

4.3.2 UW-Scat

Scatterometer observations were conducted on Malcolm Ramsay Lake from 28-11-2010 to 6-3-2011 at four sites positioned to capture local ice conditions (floating, frozen to bed). The sites were positioned along a N/S transect (Figure 2) and observed on a bi-weekly basis with the exception of December, 2010.

The scatterometer system (UW-Scat) is comprised of two frequency modulated continuous wave (FMCW) radars operated over a bandwidth of 500 MHz at centre frequencies of 9.6 (X-band) and 17.2 GHz (Ku-band). The switched transmit and receive functionality allowed for fully polarimetric observations (VV, VH, HH, HV). UW-Scat radio frequency units were mounted on supports maneuvered by a Kipp & Zonen 2AP Suntracker across an azimuth of 60° for an incidence angle range of 21^0 - 81° at 3° intervals.

Data blocks collected by the scatterometer during scans are converted to the range domain by means of a fast Fourier Transform. The range-dependent transmit leakage is estimated by obtaining a sky observation at the beginning of each scan. Range profiles from the sky observations are averaged and coherently subtracted from the target range bin. Once the transmit leakage removal has been completed, the range profiles for each polarization state and elevation angle are averaged in azimuth (Geldsetzer et al., 2007). The normalized radar cross-section (NRCS) (σ^0) is obtained through

$$\sigma^o = \frac{8\ln(2)R_t^2\sigma_c\cos(\phi_{inc})}{\pi R_c^4\theta_{3\,dB}^2}\left(\frac{\acute{P}_r}{\acute{P}_{rc}}\right) \tag{4.2}$$

where R_t is the target range, σ_c is the corner reflector's radar cross section, ϕ_{inc} is the incidence angle, R_c is the corner reflector range, $\theta_{3_{dB}}$ is the observing antenna's one-way half-power beamwidth, $\acute{P}_r$ and $\acute{P}_{rc}$ are the recorded power for the scene and the corner reflector, respectively (King et al., 2013).

UW Scat signal to noise ratio (SNR) is high across all incidence angles, with decreasing SNR trend at higher incidence angles (King et al., 2013). The minimum Ku-band SNR observed for an ice target averaged over ten scans is 10.67 dB with $\sigma^0{}_{HH}$ of -25.69 dB at an incidence angle of 81^0. Concurrently, averaged X-band SNR of the same ice target produces a minimum of 11.26 dB at 81^0 with $\sigma^0{}_{HH}$ of -25.62 dB. Cross-polarized returns at an incidence angle of 75^0 remained above the noise floor for both frequencies with SNR above 10 dB. Observed SNR for Ku-band was 11.81 dB with $\sigma^0{}_{HV}$ of -28.85, with an X-band SNR of 12.10 dB and $\sigma^0{}_{HV}$ of -31.21 at 75°. Conservative error estimates for processed normalized radar cross section (NRCS) are within +/- 2 dB of systematic

error with an additional +/- 0.5 dB of random error. Other pertinent UW-Scat sensor parameters are provided in Table 4-1**,** and an extended sensor design description is provided in King et al., 2013).

Table 4-1: UW-Scat sensor specifications modified from (King et al., 2013).

Parameter	X-band	Ku-band
Output Frequency (GHz)	9.35-9.85	16.95 - 17.45
Transmit Bandwidth (GHz)	0.5	0.5
Transmit Power (dBm)	-11.8	-8
Range Resolution (m)	0.3	0.3
Sensitivity (dB m^2/m^2)	-50	-50
Antenna Beam width (Flood, Narrow, °)	5.8, 4.3	7.3, 5.6
Transmit/Receive polarizations	VV/VH/HH/HV	VV/VH/HH/HV

4.3.3 Observed Snow and Ice Properties

Correlative datasets, including in-situ snow and ice properties, were collected adjacent to the scatterometer footprint, allowing for scatterometer observation of the natural winter evolution of the lake ice system (Figure 4-4). Traditional snow pits were conducted in the "pit farm" near the undisturbed footprint (Fierz et al., 2009). Measurements included snow stratigraphy, grain size/type using a Sear grain size card and hand lens, density obtained using 100 cm^3 density cutter, hardness, and temperature profiles using digital thermometer. Additionally, a 100 m transect was established parallel to zero azimuth of the scatterometer where ice thickness and surface ice types were measured at 25 m intervals. Ice thickness and stratigraphy presented in Figure 4-5 are averaged from transect observations. At the end of the observation period, the snow and ice sampling procedure was completed both within and adjacent to the scatterometer footprint to characterize the snowpack and ice conditions in the direct field of view. In addition, an ice core was extracted three metres from 0^0 azimuth to identify ice stratigraphy and bubble content.

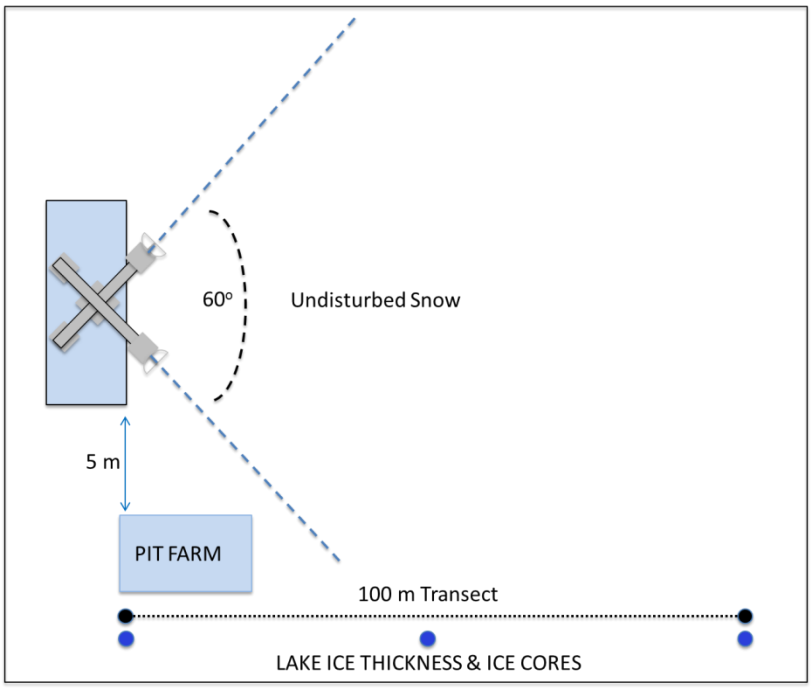

Figure 4-4: Snow and ice sampling layout. Snow stratigraphy, grain size, density, etc. are collected within the "pit farm". A 100 m transect is established parallel to the scatterometer zero azimuth where lake ice thickness/type measurements were recorded (not to scale).

Table 4-2: Summary of snow and ice properties collected adjacent to the scatterometer footprint.

Snow			Ice		
Parameter	**Unit**	**Meas. Device**	**Parameter**	**Unit**	**Meas. Device**
Depth	m	SnowHydro© Magnaprobe (Sturm & Holmgren, 1999)	Thickness	m	10 cm ice auger
Density	kg/m^3	100 cm^3 density cutter/ ESC-30 snow core tube	Surface Types/ Thickness	m	Avalanche Probe
Grain size	mm	Sear grain size card (labelled 1-3 mm)	Layering (Core)	m	Kovaks© Mark II 9 cm Coring system
Hardness	Knife/ Pencil/ Finger/ Fist				
Temp	^0C	Digital Thermometer			

Snow and ice properties collected at Sites 1 – 4 are shown in Figure 4-5, showing snow stratigraphy, layer thickness and grain type (new snow, faceted, depth hoar, etc.), as well as bulk snowpack density on the right y-axis. Figure 4-5 also provides ice thickness and stratigraphy averaged over the 5 measurements collected adjacent to the scatterometer footprint. The depth associated with the extent of tubular bubble inclusions within the ice column was obtained from ice cores extracted within the footprint at the end of the observation period (using Kovacs © Mark II 90 mm coring system) with the exception of Site 4, where the ice froze to bed.

The snow conditions at Sites 1 – 4 were that of higher density wind slab comprised of wind-rounded and faceted grains underlain by moderate density depth hoar grains that retained wind slab hardness characteristics, similar to the slab-to-hoar snow classification discussed in (Sturm & Liston, 2003). The observed snow grain size of the wind slab and depth hoar layers increased during the observation period as a function of the high thermal gradient within the snowpack. Average snow

depths on the lake were approximately 0.1 m, and were governed by sustained wind from the northwest. Local deviations in snow depth were related to snow drift topography and situation on the lake.

Ice column stratigraphy at Sites 1-4 varied depending on the relative location on Malcolm Ramsay Lake (e.g. proximity to shore, local bathymetry), reaching a maximum thickness of 1.2 m. Sites 1-3 exhibited tubular bubble inclusion into the ice volume at depths between 0.53 and 0.70 m parallel to the direction of ice growth, with increased bubble density at greater depths (Figure 4-5). Observed bubble inclusions were up to 0.15 m in length and appeared as elongated tear drops, whereby the bubble origin appeared as a semi-circle (~8 mm) which reduced to a column 5 mm in diameter until termination. Bubble content within the ice volume at Site 4 was not available as ice in that region froze to bed before the conclusion of the observation period.

Surface ice types composed of high-density spherical micro-bubbles were noticed at all sites with the exception of Site 1, where predominately clear ice was observed. Observations at Sites 2 and 3 indicated similar surface ice type development to each other while Site 4 exhibited relatively thick surface ice development. Sites 2 and 3 exhibit the development of 0.07 and 0.17 m of grey ice respectively, consistent with variable ice crystal c-axis orientation and high density of spherical bubble inclusions near the surface. Conversely, the ability to measure the grey ice layer at Site 4 exceeded observable depths, and could not be estimated via ice core due to the site freezing to bed. The measurement protocol estimated grey ice development at Site 4 of at least 0.57 m, which was likely caused by the build-up of slush and rafted ice pushed to the southern end of the lake by high sustained wind speeds originating from the northwest during ice formation.

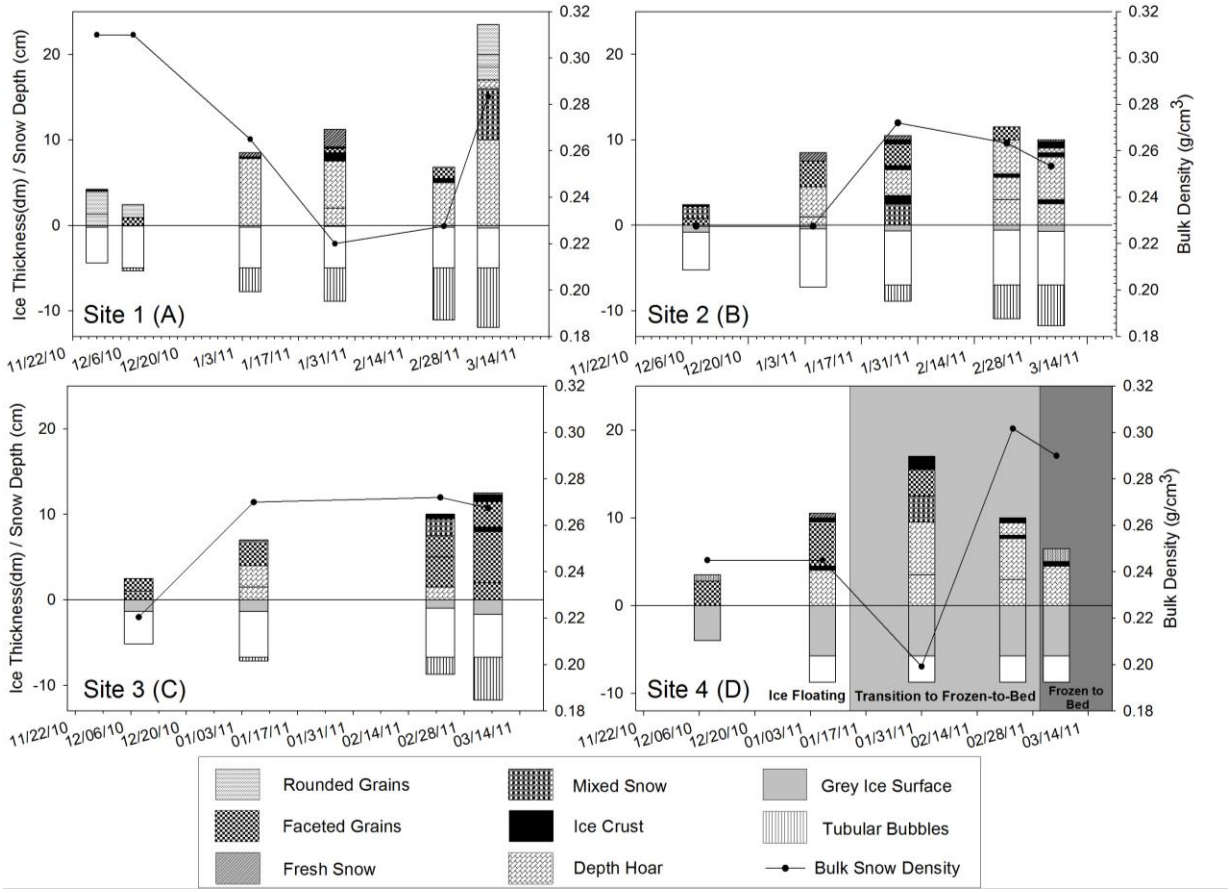

Figure 4-5: In-situ snow and ice stratigraphy for Sites 1 - 4 (A – D). Snow stratigraphy is derived from snowpit observations adjacent to scatterometer footprint. Ice stratigraphy is obtained from ice cores extracted at the end of season. Ice thickness and surface ice types (represented in decimeters) are averaged from measurements along the 100 m transect.

4.3.4 Scatterometer Observations

Within the UW-Scat processing procedure, co- and cross-polarized received signal power was averaged across all potential range profiles for a given incidence angle. The procedure allowed for automatic or manual selection of the peak signal return, depending on the complexity of the target. In the case of lake ice, the media underlying the snowpack continually thickened throughout the observation period, increasing the distance to the high permittivity-contrast ice-water interface. The range resolution of UW-Scat (0.3 m) was sufficient to resolve signal return from snow-ice and ice-water interfaces based on the distance from the sensor, shown in Figure 4-6**.** When thin ice was present a single peak was noticed, whereas the observation of thick ice resulted in two peaks. The

multiple peaks were observed to be the result of scatter at the surface (snow volume, snow-ice interface), within the ice volume (double-bounce off tubular bubbles) and the ice-water interface, and potentially from multiple scattering events.

Two methods to obtain returned power were implemented in this study; sum of peaks, and individual peaks. 1) The "Sum of Peaks" (SP) return was produced to identify the summation of power returned from interactions near the snow-ice and the ice-water interface. SP was calculated by summing the power coefficients of the peaks in range to obtain the returned power from interactions near the ice surface and ice-water interface, including possible double-bounce from tubular bubbles. 2) The individual peaks statistics were the σ^0 produced from the UW-Scat processing software for the first (P1) and second (P2) peak in range, hypothesized to be interactions near the ice surface, and ice-water interface, respectively.

This section examines the backscatter evolution of the SP return and individual peaks separately as an average of the incidence range of 39 - 45^{O}. The averaging of multiple azimuth sweeps serves to reduce the backscatter fluctuations caused by snowpack and ice surface micro-topography, potential for in-scene cracks and system noise. At the end of the observation period, snow and ice sampling was completed within the footprint. An additional scan was completed after snow was removed from a 15 x 15 m area within the scatterometer field of view using snow shovels (Figure 4-7).

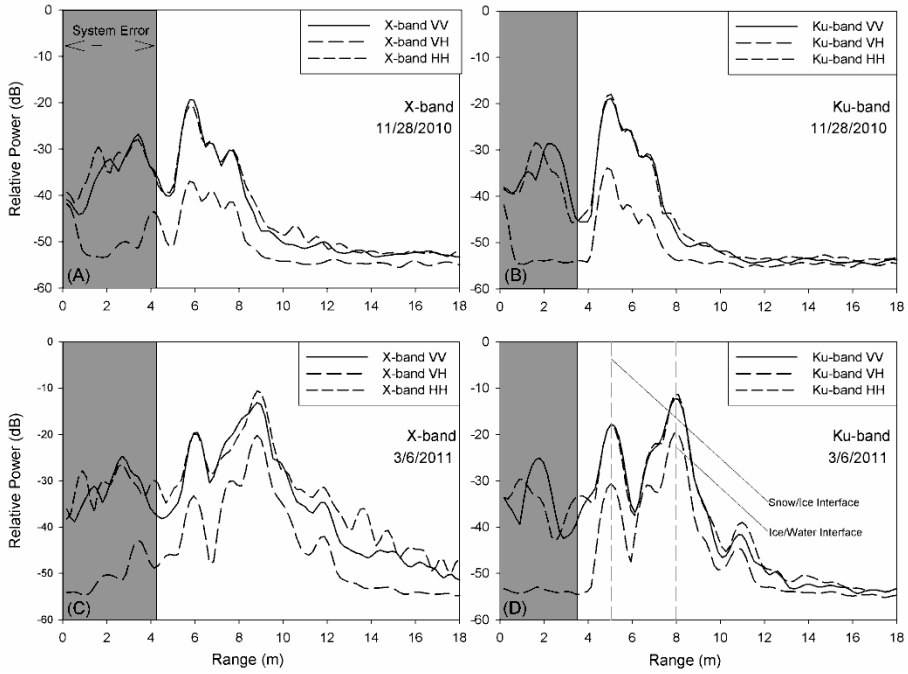

Figure 4-6: Average slant range profiles for X- and Ku-band at 39^{O} for the first (28-11-2010) (A-B) and last (6-3-2011) (C-D) observations at Site 1. Note the single peak associated with thin ice in A-B. In C-D the first peak remains at the same distance within the range gate (snow volume and snow-ice interface), while the second peak (double bounce off tubular bubbles & ice-water interface) is easily discernable.

Figure 4-7: Procedure of snow removal from the scatterometer field of view at completion of the observation period at Site 1 (March 5, 2011).

The winter evolution of X- and Ku-band backscatter observed at Site 1 using the SP method is presented in Figure 4-8. Both X- and Ku-band exhibit a similar seasonal evolution in both VV and VH (HH, HV not shown), but have similar seasonal patterns), except for the end of the observation period. The removal of the 0.24 m snowpack results in a drop in Ku-band SP of 2 dB, while the X-band return exhibited a slight increase (within measured system error). This indicates that a portion of Ku-band backscatter is returned by a component within the snowpack, however, it is apparent that another physical component of the lake ice system facilitates the increases in backscatter noticed throughout the observation period. A large increase (~10 dB) at both frequencies coincides with the inclusion of tubular bubbles within the ice volume, consistent with previous studies that examined winter backscatter evolution at C-band from synthetic aperture radar (SAR) systems aboard satellite platforms (Duguay et al., 2002; Jeffries et al., 1996).

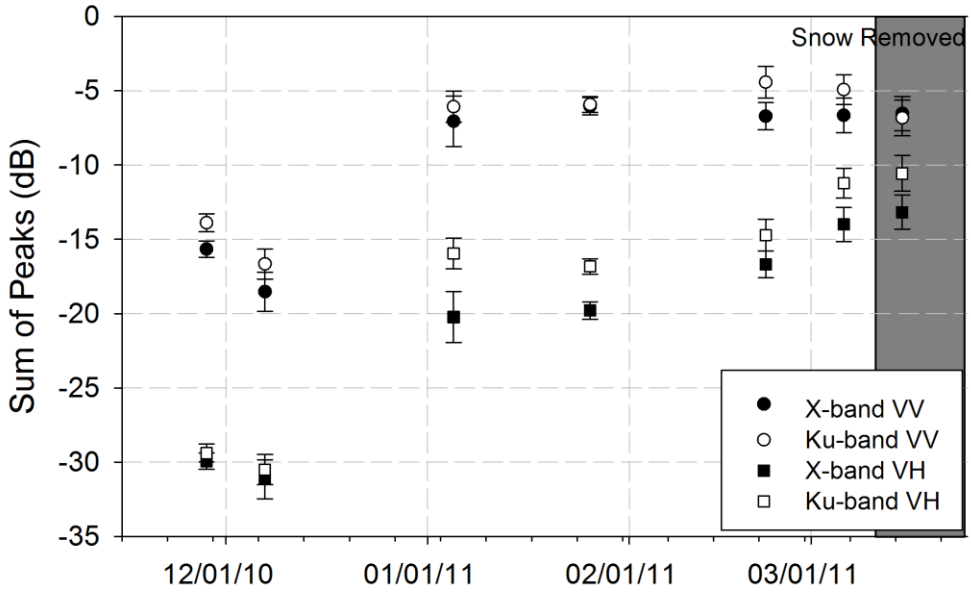

Figure 4-8: X- and Ku-band (39-45^0 average) sum of peaks evolution (VV and VH) at Site 1 with error bars denoting standard deviation within averaged incidence angle range. Note slight drop in Ku-band VV (2 dB) when snow is removed (grey box) Error bars represent the standard deviation of observations.

When peaks within the range gate are processed separately, the backscatter evolution associated with the first peak (P1) and second peak (P2) provides a more promising avenue to observe the various physical components of the lake ice system. Figure 4-9 exhibits the different σ^0 patterns

associated with P1 and P2 when processed separately. X-band σ^0 for P1 remains consistently low throughout the season because the snowpack is nearly transparent, and the ice surface is devoid of ice types. Upon snow removal, the co-polarized X-band P1 σ^O drops ~2 dB, which is within UW-Scat error range, while the cross-polarized σ^O drops 4.1 dB indicating that the thick snowpack (0.24 m) may contribute to P1 returns. X-band σ^O for P2 increases incrementally throughout the season at all polarizations, coinciding with the increase in density of tubular bubble inclusions.

Ku-band P1 σ^O remains relatively constant throughout the season, however upon snow removal, P1 σ^O drops considerably at a magnitude of 5.5 dB (Figure 4-9). The increase in the drop of P1 magnitude associated with snow removal compared to that of Figure 4-8 suggests that Ku-band is sensitive to snow overlying ice. However, the presence of tubular bubbles within the ice volume and roughness at the ice-water interface may saturate the signal, limiting the sensitivity to the snowpack when the SP method is considered. P2 σ° at Ku-band also indicates that the signal is efficiently returned to the sensor, possibly via double bounce off vertical tubular bubbles and the ice-water interface, returning a high fraction of incident energy to the sensor.

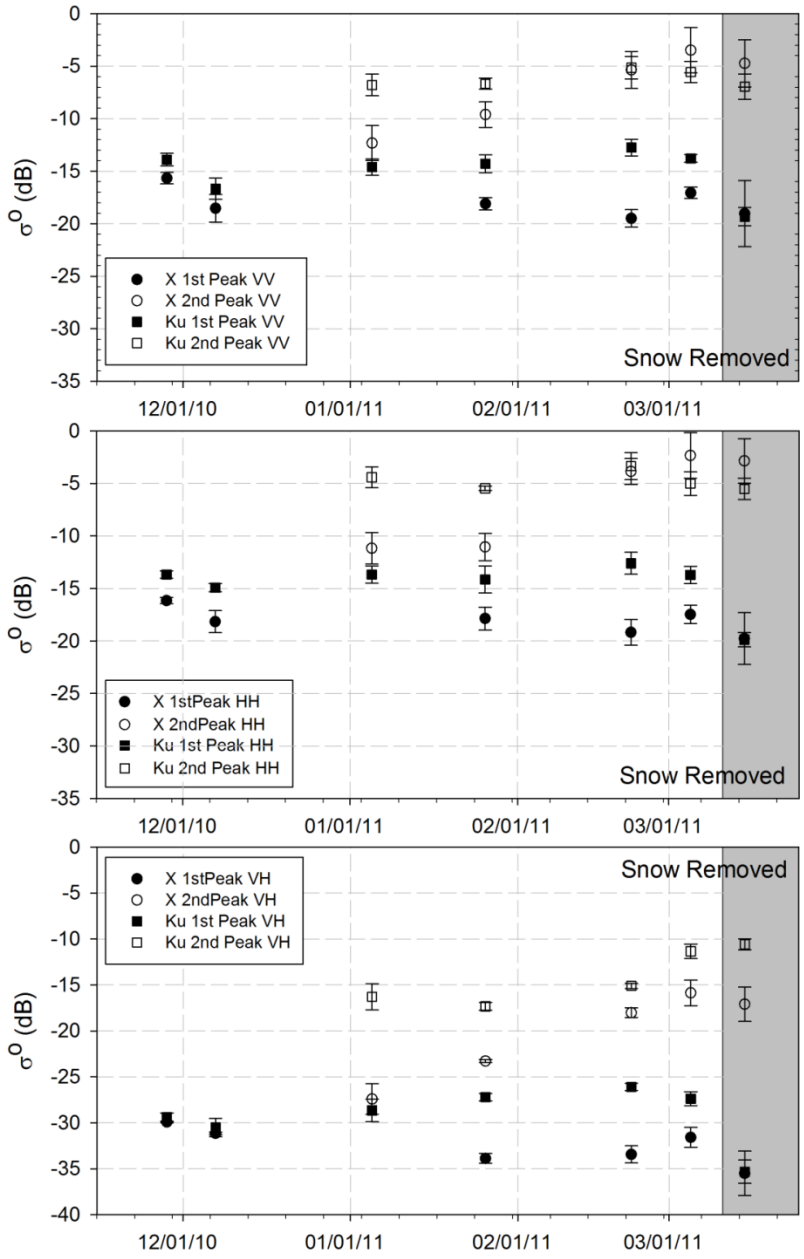

Figure 4-9: X- and Ku-band (39 – 45^{O} average) σ^{0} evolution for P1 and P2 at Site 1 (VV, HH and VH). The processing of peaks individually exhibit differential backscatter magnitude associated with physical properties of the snow and ice volume. No 2nd peak observation is available for initial observations because of a lack of tubular bubbles within the ice volume. Upon snow removal, Ku-band σ^{O} drops 5.5 and 6.2 dB at VV/HH, respectively.

Sites 2 and 3 exhibit similar snow and ice properties to each other, exhibiting considerable snow ice thickness development at the surface (Figure 4-5B, C). The backscatter evolution for both the SP and separated peaks for Sites 2 and 3 are also similar in both backscatter magnitude and pattern, therefore only Site 2 is shown in Figures Figure 4-10 and Figure 4-11.

When the SP is observed, the return at Sites 2 and 3 are initially high with NRCS on the order of -8 dB at X-band and -6 dB at Ku-band (VV). Backscatter at both frequencies increase incrementally throughout the observation period and reach a maximum at -3 dB. When the overlying snow (0.1 m) is removed, Ku-band VV drops by 2.6 dB and X-band VV drops by 1.1 dB, similar to the effect of snow removal at Site 1 (Figure 4-10). The incremental increase in SP return is observed coincident to the inclusion of tubular bubbles near the ice-water interface beginning in late January 2011 (Figure 4-5B), but it does not account for the initially high SP return observations during December 2010. Scatter caused by surface ice types contribute to the SP return prior to the inclusion of tubular bubbles in the ice volume.

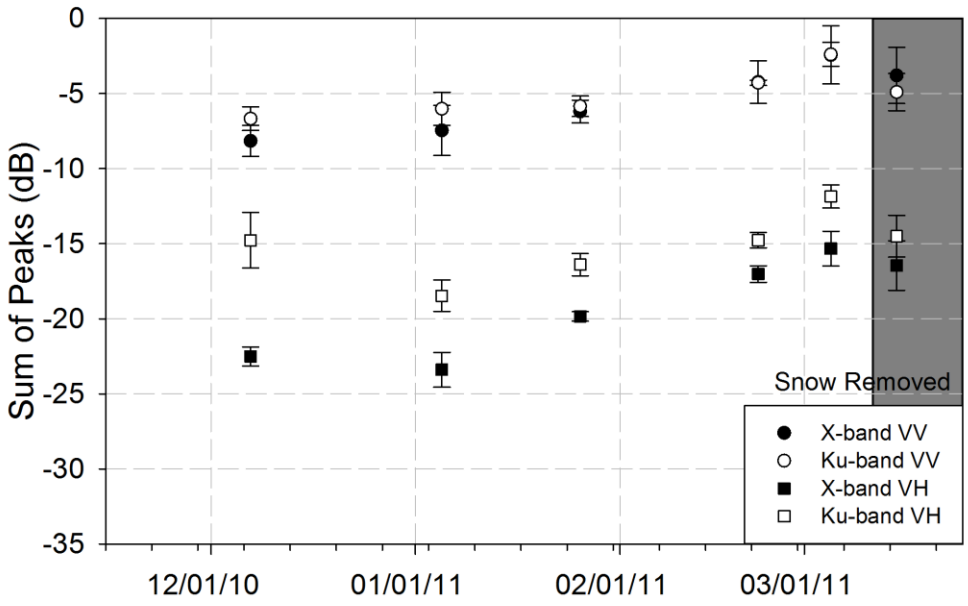

Figure 4-10: X- and Ku-band (39-45^0 average) sum of peaks evolution (VV and VH) at Site 2 with error bars denoting standard deviation within averaged incidence angle range. Note slight drop in Ku-band VV (2 dB) when snow is removed (grey box).

Individually processed peaks for Site 2 exhibit consistent P1 σ^O of approximately -10 dB and -8 dB for X- and Ku-band (VV), respectively, throughout the observation period (Figure 4-11). P1 σ^O at Site 2 contrasts with that of Site 1 (clear ice), where the P1 peak σ^O is much lower at approximately -18 and -15 dB for X- and Ku-band, respectively. The contrast between sites with and without surface ice types indicates that surface ice types are a source of scatter at both X- and Ku-band prior to tubular ice development, consistent with (Hall et al., 1994). Similar to Site 1, snow removal results in a drop in Ku-band σ^O of 2.8 dB (3.7 dB) at VV (HH) polarizations at Site 2, and 5.1 dB (4.8 dB) at VV (HH) polarizations at Site 3 (Figure 4-11).

Tubular bubbles incorporated into the ice volume during secondary ice development at Site 2 prior to January 2011 result in increases in P2 σ^O throughout the season from approximately -14 to -3 dB at X- and Ku-bands (VV, HH), respectively (Figure 4-11). P2 becomes the dominant component within the returned σ^O upon tubular bubble inclusion, with both X- and Ku-band increasing to approximately -5 dB on 22-2-2011. In terms of the SP, returned power associated with tubular bubble inclusions results in a masking of scatter associated with the presence of grey surface ice (Figure 4-10).

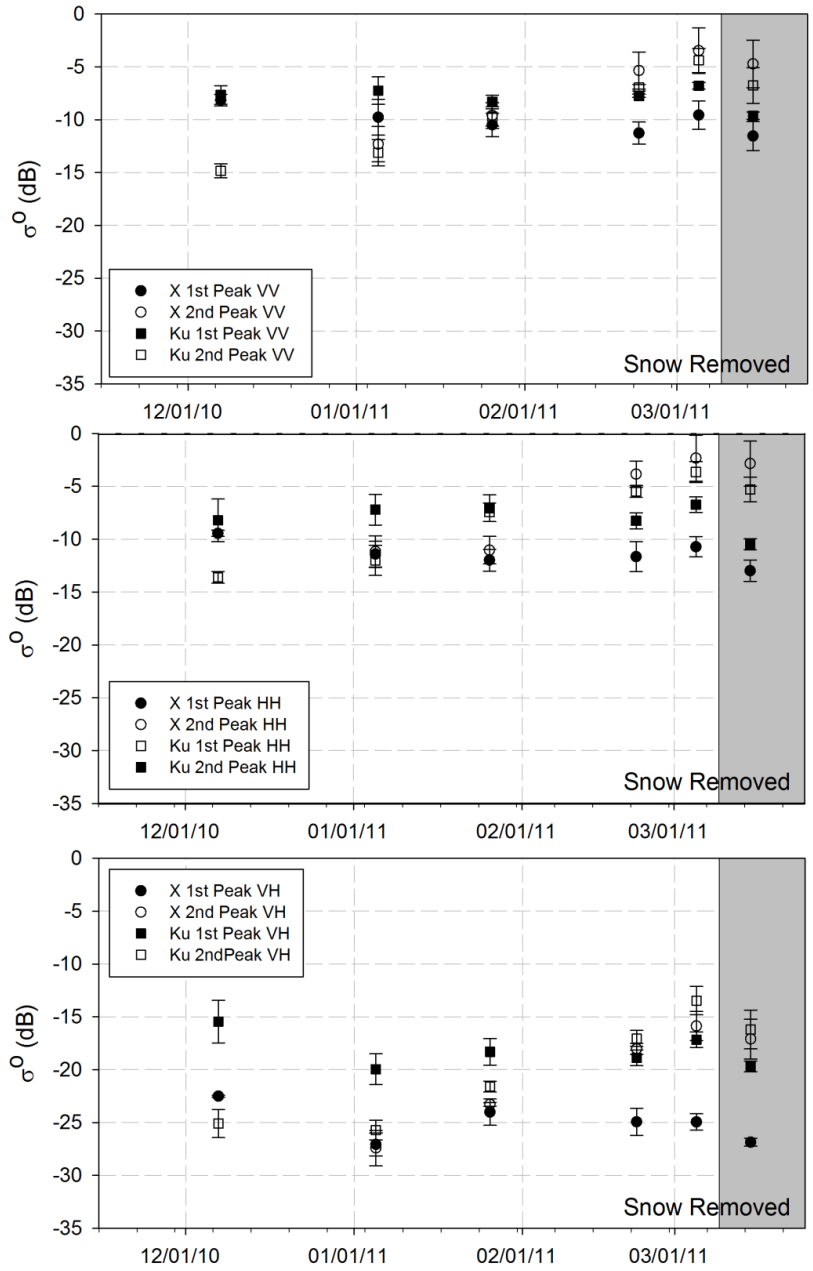

Figure 4-11: X- and Ku-band (39 – 45^{O} average) σ^{0} evolution for P1 and P2 at Site 2 (VV, HH and VH). No 2nd peak observation is available for initial X-band because of a lack of tubular bubbles within the ice volume. P1 for both X- and Ku-band exhibits high σ° throughout the observation period as a result of snow ice development. Upon snow removal, Ku-band σ^{O} also drops 2.8 and 3.7 dB for VV and HH, respectively.

Site 4 was the only site to freeze to bed during the observation period. Variable ice formation processes resulted in the thickest observed grey ice surface layer (0.57 m), and the thinnest sustained snowpack. Site 4 presents a unique scenario whereby no information is available for the ice volume, so the date of tubular bubble inclusion is observed from ice cores extracted at the other sites. Consistent with Sites 2 and 3, X- and Ku-band returns for SP remains relatively constant between -9 and -6 dB throughout the observation period (Figure 4-12), indicating the presence of surface ice types due to the similarities with Figure 4-10. There is also an incremental increase at X-band (VV, VH) potentially associated with increases in bubble density within the ice volume, however the exact timing of bubble inclusion is not known as tubular bubble information is inferred from ice cores. Based on scatterometer observations, the true timing of Site 4 freezing to bed occurs just prior to the final measurement of the observation period (5-3-2011), when σ^{O} dropped approximately 2 dB for X- and Ku-band (VV, VH).

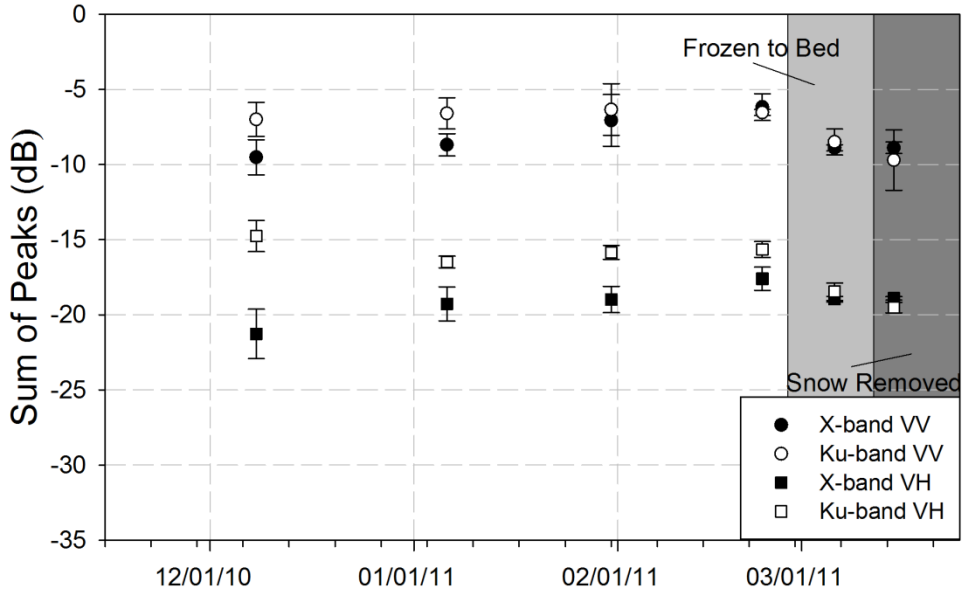

Figure 4-12: X- and Ku-band (39-45^{0} average) sum of peaks evolution (VV and VH) at Site 4 with error bars denoting standard deviation within incidence angle range. Note the slight drop in X- and Ku-band VV/VH (~4 dB) when the ice freezes to bed (light grey box).

Ice formation processes at Site 4 results in a physically complex combination of potential scattering media including thick grey ice surface, tubular bubble inclusions and the grounding of the ice cover. However, the separation of the returned signal into P1 and P2 exhibits similar σ^{0} patterns

associated with surface and ice volume contributions compared to Sites 1 – 3. Figure 4-13 shows P1 σ^0 at X- and Ku-band at approximately -10 and -8 dB, respectively, similar to other sites where a surface ice types are observed. Concurrently, X- and Ku-band P2 σ^O increases of approximately 5 – 7 dB during the observation period are consistent with the timing of tubular bubble inclusions at all other sites on the lake (Figure 4-13).

The P2 σ^0 drop associated with the ice freezing to bed is much greater in magnitude compared to the SP; 7 dB for X-/Ku-band at P2 compared to 2 dB in Figure 4-12. The disparity between P2 and the SP is potentially due to the increased scatter caused by the substantially thicker surface ice type layer.

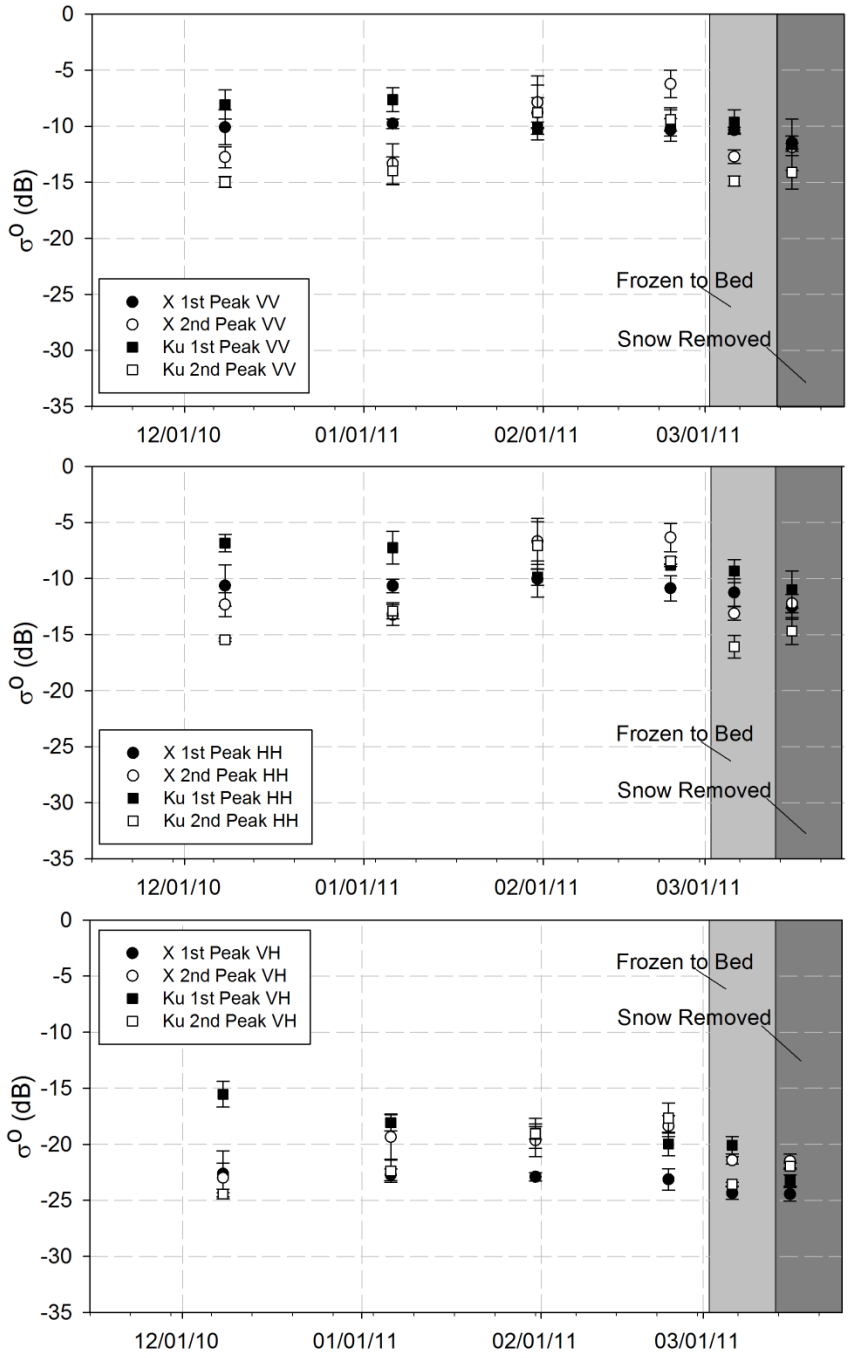

Figure 4-13: X- and Ku-band (39 – 45^{O} average) σ^0 evolution for P1 and P2 at Site 4 (VV, HH and VH). Note the 7 dB backscatter drop for P2 when the ice freezes to bed at both X- and Ku-bands.

Table 4-3 summarizes the σ^O difference at X- and Ku-band when snow is removed from the field of view. Ku-band exhibits sensitivity of up to 5.55 and 6.17 dB for VV and HH (respectively) to the snow volume with increasing absolute differences coincident to snow depth, while X-band exhibits negligible change, within the UW-Scat system-derived error.

Table 4-3: Relative P1 σ^O (dB) difference for snow-on and snow-off ice conditions at maximum ice thickness. Bolded values indicate differences larger than UW-Scat error estimates (+/- 2.5 dB) and are therefore significant.

	Snow Depth	Bulk Density	SWE	Ku-band			X-band		
	(m)	(kg/m^3)	(mm)	VV	HH	VH	VV	HH	VH
Site 4	0.065	290	18.85	2.03	1.63	**3.14**	1.10	1.27	0.10
Site 2	0.100	250	25.33	**2.81**	**3.75**	**2.53**	1.98	2.26	1.91
Site 3	0.125	270	33.44	**5.12**	**4.80**	**3.85**	0.03	0.55	**2.53**
Site 1	0.235	270	63.89	**5.55**	**6.17**	**7.96**	1.97	2.30	**4.10**

4.4 Model Formulation and Simulations

To support the interpretation of scatterometer observations, identify and evaluate the scattering mechanisms which occur in freshwater lake ice, a dedicated electromagnetic model is used. Since the scene is composed of a temporally evolving multilayer media comprised of snow and ice with and without air inclusions of appreciable size (e.g. 1mm wide and up to 0.15m in length at the end of the season) overlying water (or soil when the lake is frozen to bed), an appropriate model is chosen that accounts for both surface and volume scattering in floating and grounded ice scenarios. Volume scatter takes place whenever the medium in which electromagnetic waves travels through is not homogeneous. Snow can be considered as a bulk of air with ice inclusions, and bubbled or grey ice as pure ice hosting air bubbles. Volume scattering is simulated using the Dense Medium Radiative Transfer theory under the Quasi-Crystalline Approximation (DMRT-QCA) (Tsang et al., 2007). This model is based on Mie scattering theory (occurs when the size of the scatterer is of the same order as the wavelength), and simulates the scattering of densely packed spherical scatterers embedded in a host medium that comprise a percentage of the total volume. The phase matrix used in the DMRT-QCA accounts for multiple scattering among the densely-packed inclusions in the medium, the formulation of which is described in (Tsang et al., 2007; Tsang & Kong, 2001). Using this approach,

the model applies the reciprocity theorem to invert the permittivity of the host and inclusion media (ice and air) without stickiness effects to account for scatter in both the snow and ice volumes. Albeit the shapes of the real scatterers are not spherical lower in the ice volume, this assumption retains computational and theoretical simplicity. The model accounts for the multi-layered structure of the media based on the formulation presented in (Liang et al., 2008; Liang et al., 2008).

Surface scattering occurs at the interface between two different media (e.g. air-snow, snow-ice, ice-water and whenever there is a discontinuity between layers) and depends mainly on the difference between the permittivity of the contiguous media and the roughness of the boundary interface. In some cases the discontinuity between two adjacent layers is small and the contribution is negligible (e.g. air-snow or snow-ice). In order to simulate surface scattering, the Oh model (Oh et al., 2002) is applied, which provides backscatter at both co- and cross-polarization. The Oh model relies on semi-empirical relationships between the roughness characteristics of the ice or ground interface and the backscattering.

The inputs to the multilayer electromagnetic model for each layer are: thickness, temperature, density, size of the scatterers (snow grains or bubbles) if present, and roughness of the top interface. Moreover, the roughness of the lowest layer bottom interface and the permittivity of underlying medium (which is usually water but can be soil if the lake is frozen to bed) are required. All inputs except the roughness and the size of bubble inclusions in ice are derived from ground measurements, assuming a fixed ice density of 850 kg m^{-3} (Adams, 1976). The roughness between the layers is assumed to be smooth with a fixed height standard deviation of 1 mm. The roughness of the ice-water interface (which plays a major role in the surface scattering) and bubble size inputs are obtained by fitting the angular backscatter measurements for each observation starting from the first survey. In the following dates the fitting parameters are constrained by the ones already founded on prior observations. The fitting is performed by minimizing the following cost function:

$$C_{site,date}(h, r_1, .., r_n) == \frac{1}{N_{pol} N_{freq} N_\theta} \sum_{pol=VV,VH} \sum_{freq=9.6,17.2} \sum_\theta \begin{bmatrix} \sigma^o_{Model}(pol, freq, \theta, h, r_1, .., r_n) \\ -\sigma^o_{Measured}(pol, freq, \theta \end{bmatrix}^2 \quad (4.3)$$

which is equivalent to the mean standard error. In Equation (4.3), *h* is the height standard deviation of ice-water interface, $r_1 \ldots r_n$ are the radius of the bubbles in the *1..n-th* ice layers (*r* is zero in case of

clear ice), N_{pol}=2 is the number of polarizations, N_{freq}=2 is the number of frequencies, N_θ is the number of angular measurements which depends on the survey considered.

The fitting procedure starts at the first observation that presented the simplest ice properties. For example, at Site 1 it is composed of a very thin snowpack (0.04 m) comprised of rounded grains with an average long-axis grain size of 0.2 mm above a shallow layer of grey ice and 0.4 m clear ice. The fitting parameters are in this case, the tiny bubbles within the grey ice, and the ice-water interface roughness.

It is worth noting that the angular trend is mainly dependent on the surface scattering (i.e. ice-water roughness) while the volume scattering (i.e. snow and air bubbles) affects the magnitude. For the first date the volume scattering is almost negligible due to the thin snow and grey ice layers, and the roughness value determined the measured backscatter.

The following step is the minimization for the second date assuming that the physical properties of the snow and ice did not exhibit dramatic changes between the two dates. This implies that for the pre-existing layers the parameters remain almost the same and the fitting is performed for the new ones. The procedure is then applied for the whole observation period.

Figure 4-14 shows the angular trends of backscatter measured and simulated at Site 1 on 28-11-2010 and 5-3-2011. At X-band the model is in good agreement with UW-Scat observations at both VV and VH with a cumulative Root Mean Square Error (RMSE) (i.e. VV+VH) of 2.78 and 2.62 dB for the early and late winter scene, respectively. An underestimation of 3-5 dB is observed at low incidence angles (i.e. <30°). At Ku-band the model is able to reproduce the angular trend at the beginning of the season and the backscatter increase between the two dates. However, the model overestimates the data for 5-3-2011 and does not reproduce the trend effectively. The RMSE for Ku-band is 3.5 dB for the early winter scene and 5.2 dB for the late winter scene. The discrepancy is due to the overestimation of the volume scattering, which is relevant at Ku-band and for the thick ice bubble layer of 0.683 m observed at Site 1, produced by the model that considers spheres instead of tubular bubbles (Figure 4-14-D). As an example, the parameters used in the model for Site-1 on 28-11-2010 and 5-3-2011 are summarized in Table 4-4.

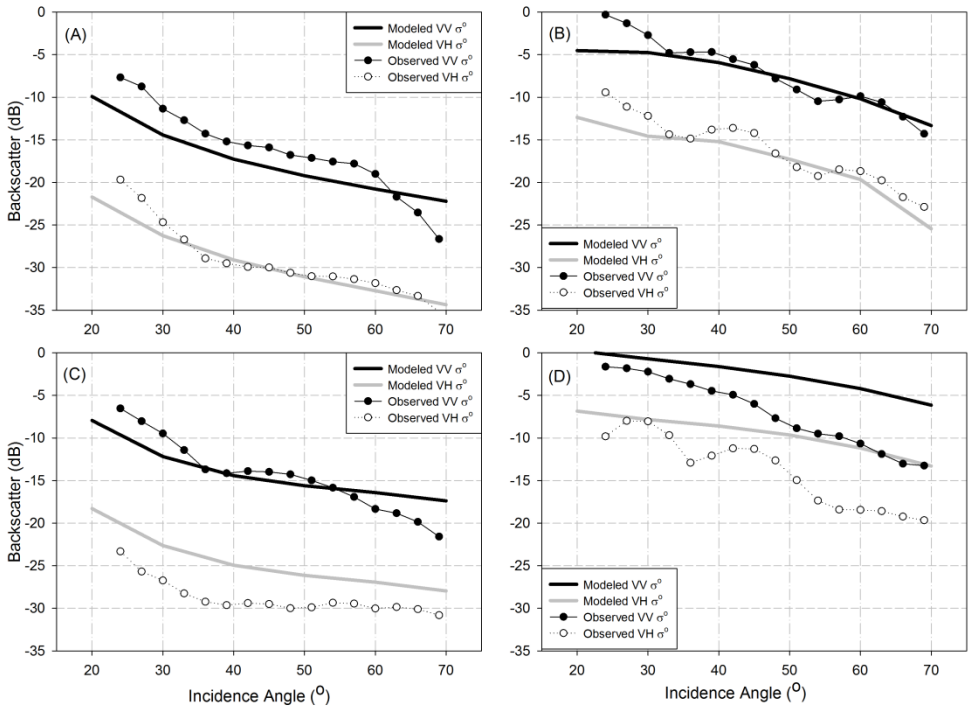

Figure 4-14: Comparison of observed SP (dashed lines) and modeled backscatter (continuous lines) obtained for Site 1 on 28-11-2010 (A, C) and on 5-3-2011 (B, D) for X- (A,B) and Ku-band (C,D).

Table 4-4: Input backscatter model parameters for early (28-11-2010) and late (5-3-2011) winter scenarios derived from in-situ measurements, with assumed values for ice density, stickiness and roughness.

Date: 28-11-2010	Layer 1	Layer 2	Layer 3	Layer 4	Layer 5
Type	Snow	Hoar	Grey Ice	Clear Ice	Bubble Ice
Thickness (m)	.06	.17	.064	.443	.683
Density (kg/m^3)	250	300	850	850	850
Temperature (°C)	-25	-20	-15	-10	-5
Grains Radius (mm)	0.3	1.25	0.1	-	0.4
Stickiness	0.1	1	0.3	-	1
Roughness (mm)	1	1	1	1	5

Date: 5-3-2011	Layer 1	Layer 2	Layer 3
Type	Snow	Grey Ice	Clear Ice
Thickness (m)	.042	.02	.438
Density (kg/m^3)	310	850	850
Temperature (°C)	-8.9	-5	-2.5
Grains Radius (mm)	0.1	0.1	-
Stickiness	0.1	0.3	-
Roughness (mm)	1	1	15

4.4.1 Modeled Time Series

Figure 4-15 shows the comparison between SP observed and simulated time series for Site 1 (A, B) and 4 (C, D). Sites 1 and 4 are chosen to illustrate model performance for sites that exhibit contrasting ice regimes; clear bubbled ice (Site 1), and grounded bubble ice with a thick surface grey ice layer (Site 4).

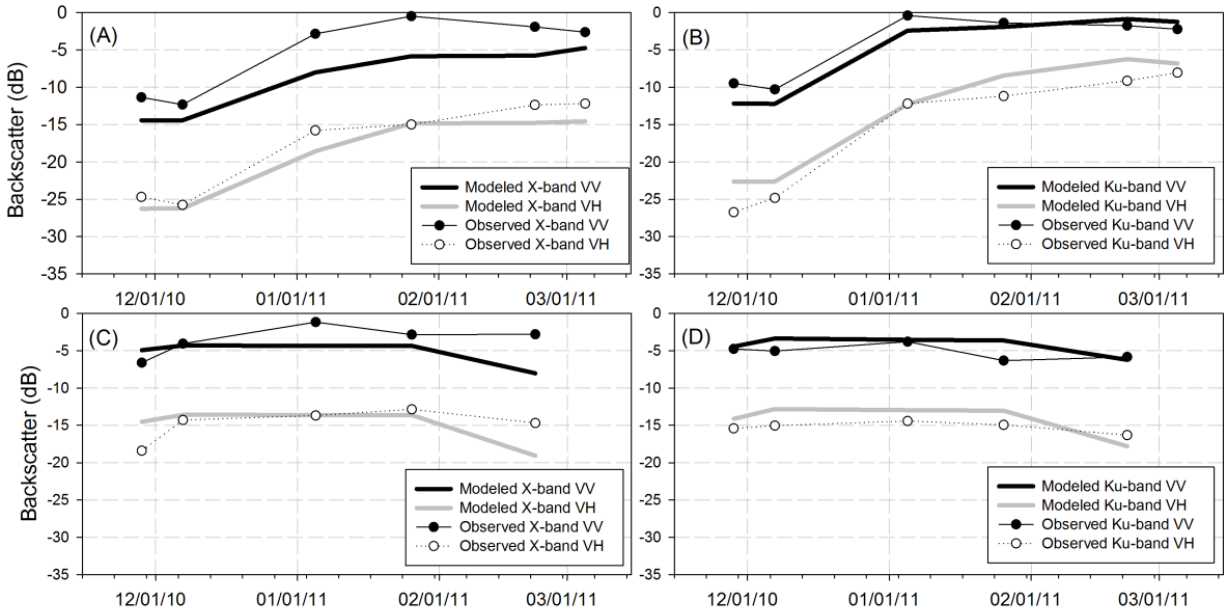

Figure 4-15: Comparison between observed SP and simulated backscatter time series at Site 1 (A, B) and Site 4 (C, D) at 30^0 incidence angle for X- (A, C) and Ku-band (B, D).

Figure 4-15 illustrates the potential for the model to reproduce the temporal trend observed by scatterometer measurements. At Site 1, modeled σ° increases monotonically throughout the season (approximately 9-10 dB at both frequencies and polarizations), while Site 4 remains relatively constant, similar to backscatter of specific sites presented in (Jeffries & Morris, 1994). Model runs indicate that the increasing backscatter at Site 1 was the result of the development of bubbles within the ice. It is worth noting that this is caused by the increase of both volume (due to the bubbles' formation) and surface scattering because of the increase of roughness at the ice-water interface. Conversely, backscatter variations are relatively minute at Site 4 (from -4.3 to -4.9 until frozen to bed at -8 dB), where the ice composition at the surface (0.57 m of grey ice) remains relatively constant throughout the season.

4.4.2 Modeled Effects of Bubbles

In order to assess the backscatter sensitivity to the bubbled ice layer, model runs are performed with and without the presence of bubbles for grounded and floating ice scenarios (Figure 4-16) keeping all other input parameters (i.e. snow, ice and layers roughness) fixed. Figure 4-16 indicates that σ^0 simulations including spherical bubbles within the ice volume results in increased σ° at all

frequencies and polarizations due to an increase in volume scattering. The σ^0 increase is more pronounced at Ku-band than X-band (with VV increases of 4.77 dB vs. 0.88 dB, respectively), which is a function of the size of the bubble scatterer relative to the incident wavelength. Simulations of grounded ice result in lower σ^0 than in floating ice scenarios as a result of the reduced permittivity of the ice substrate (ground vs. ice), and therefore, contrast in permittivity between the two media.

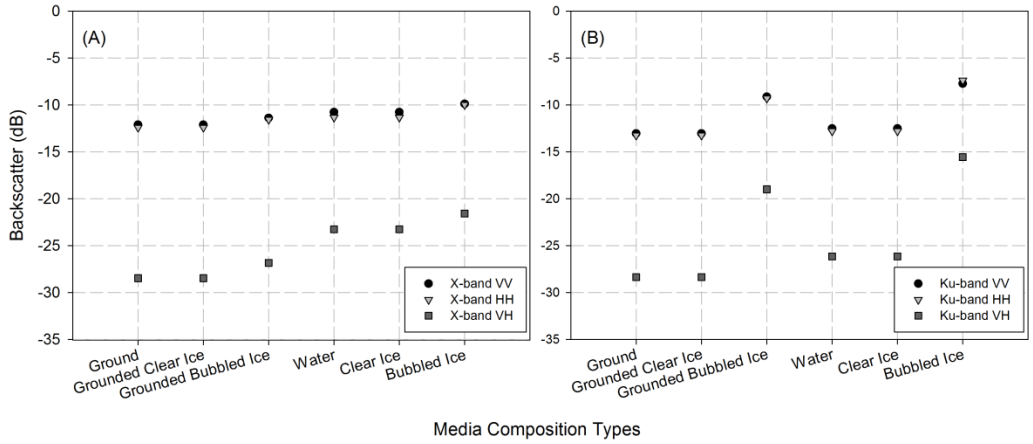

Figure 4-16: Model runs (incidence angle = 40°) indicating the influence of various ice scenarios on overall backscatter at X- (A) and Ku-band (B). The incorporation of spherical bubbles in the ice volume increases overall modeled backscatter.

Figure 4-17 shows angular trends for observed and simulated σ^0 for the end-of-season scenario at Site 1, when maximum ice thickness is observed. The dashed and solid lines represent simulations that consider the ice layer as clear and bubbled, respectively. Modeled X-band σ^0 indicates that the backscatter contribution of bubbles within the ice volume is less than that of Ku-band. Modeled Ku-band σ^0 exhibit sensitivity to the presence of bubble inclusions; VV increases 2 – 3 dB and VH increases 3 – 5 dB, depending on incidence angle observed. The modeled results illustrate that the size of the spherical inclusions (radius = 1mm) scatter incident microwaves more efficiently when the wavelength is shorter (Ku-band), resulting in increased backscatter.

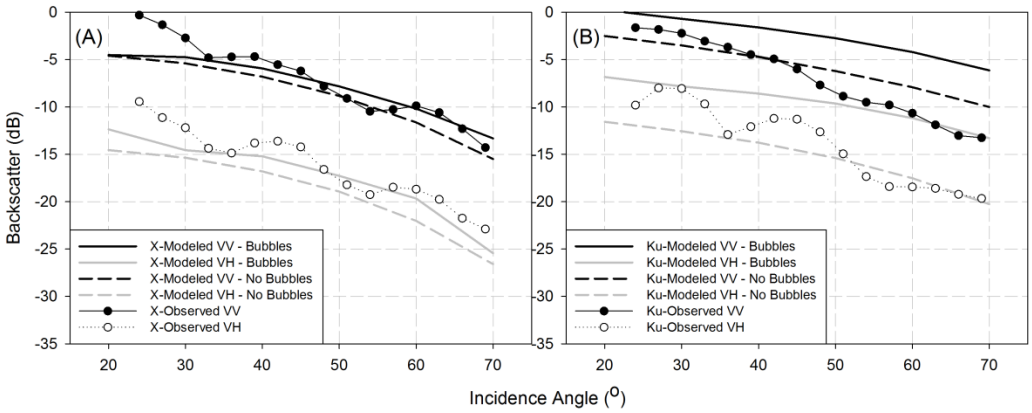

Figure 4-17: Effect of removing bubbles within the ice volume on modeled backscatter at X- (A) and Ku-band (B) compared to observed SP for maximum ice thickness at Site 1 (5-3-2011). Inclusion of spherical bubbles result in sharp σ° increase at Ku-band, but are negligible at X-band.

4.4.3 Modeled Effects of Overlying Snowpack

Figure 4-18 shows the modeled and observed effects of snow removal from the scatterometer field of view on the SP return to the sensor at Site 1 and 4, respectively, with a summary of RMSE and Mean Bias Error (MBE) shown in Table 4-5. Sites 1 and 4 are shown because of their contrasting clear and grey surface ice regimes. In Figure 4-18A modeled and observed VV, VH X-band returns exhibit little deviation when the snow is removed from the scene. The lack of observed or modeled change at X-band is consistent with previous observations in this study; minimal scatter is caused by the overlying snowpack due to X-band wavelengths penetrating through the snowpack. RMSE for X-band for snow-covered and snow-free ice are 1.65 and 1.96 dB (VV) at Site 1 and 5.57 and 5.44 dB (VV) at Site 4, indicating that modeled X-band has little influence to overlying snow cover. However, X-band RMSE and MBE indicate that backscatter is underestimated at Site 4, as a result of the influence of the thick grey ice layer at the surface (Table 4-5).

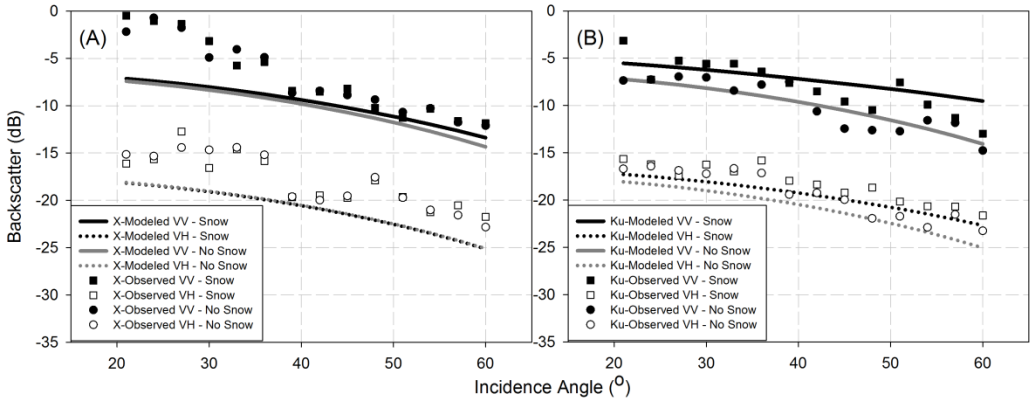

Figure 4-18: Effect of removing snow layer on modeled backscatter at X- (A) and Ku-band (B) compared to observed SP for maximum ice thickness at Site 4 (6-3-2011). The model underestimates X-band returns, and agrees for Ku-band upon snow removal (see Table 4-5 for statistics).

Table 4-5: RMSE and MBE (dB) for modeled backscatter at Sites 1 and 4 with and without the presence of snowpack overlying the ice, shown in Figs 18 and 19. RMSE indicates that the model performed better for both X- and Ku-band at Site 1, while the presence of a thick grey ice layer at Site 4 resulted in underestimation.

		X-band				Ku-band			
		VV		VH		VV		VH	
		Snow	No Snow	Snow	No Snow	Snow	No Snow	Snow	No Snow
Site 1	RMSE	1.65	1.96	2.43	2.43	1.48	1.53	3.33	2.78
Site 1	MBE	-0.19	-0.21	-0.32	0.07	-0.81	0.27	-2.50	-1.95
Site 4	RMSE	5.57	5.44	3.96	4.01	1.68	2.82	1.44	2.08
Site 4	MBE	5.36	5.30	3.65	3.93	-0.60	0.13	1.31	1.58

Modeled Ku-band for snow-covered and snow-free conditions agree with in-situ observations (Table 4-5), showing a drop in backscatter with greater magnitude at increasing incidence angles (Figure 4-18B). Modeled Ku-band VV and VH at Site 4 exhibit a larger drop in return upon snow removal (2.37 dB VV) compared to Site 1 (1.27 dB VV), with a shallower snowpack (0.065m at Site 4 compared to 0.235 m at Site 1) and comparatively smaller grain sizes (1.3 mm bulk average at Site

4 compared to 2.3 mm at Site 1). Based on in-situ observations, Site 4 should have exhibited larger σ^0 differences, but other confounding factors such as the presence of thick grey ice at the surface and the ice freezing to bed may influence overall simulated σ^0.

4.5 Conclusions

This study investigated the backscatter response from a variety of snow and ice scenarios (clear ice, tubular bubbles, grey surface ice, and the presence/absence of overlying snowpack with ice afloat and frozen to bed) and identified the dominant σ^0 source as tubular bubbles within the ice, and surface ice types. In situ snow and ice conditions at Sites 1 – 4 provided excellent examples of the complexity associated with microwave interaction with lake ice. Additionally, Ku-band exhibited sensitivity to the overlying snowpack when it was removed from the scatterometer field of view with the maximum σ° drop at VV (5.55 dB), HH (6.17 dB) and VH (7.96 dB) at Site 1 with a snow depth of 0.235 m. The σ° drop is similar to the magnitude of Ku-band backscatter increases noticed in observations of terrestrial snow of the same depth (Yueh et al., 2009).

Scatterometer measurements complemented with field observations of snow and ice properties showed that: a) the observations provided by the SP is a combination of the surface snow and ice volumes near the snow-ice interface, and forward double-bounce scatter within the ice volume and ice-water interface; and b) while Ku-band exhibited a potential relation to snow depth as demonstrated by snow-removal experiments, the magnitude and variability of backscatter contribution from spherical and tubular bubble inclusions serve to confound the potential for on-ice SWE estimation. The low number of snow removal observations (n = 4) restricted any statistical analysis of the influence of snow overlying freshwater lake ice on Ku-band σ^0 to a more qualitative analysis. The observation of σ^O associated with scattering sources is a necessity for further understanding of microwave interaction with snow-covered lake ice, and can be addressed through Dense Media Radiative Transfer (DMRT) modeling.

The backscatter model was used to simulate volume scatter contributions from the snowpack and bubbled ice volume, whereby the reciprocity theorem is applied to invert host and inclusion media without stickiness effects. The modification to include bubbles within the ice volume agreed with X-band in-situ observations but overestimated at Ku-band, demonstrating the need for further model modification including the addition of tubular bubbles and roughness considerations at the ice-water interface, which is currently under development.

Simulations for snow-covered and snow-free conditions indicated that the overlying snowpack was a potential σ^0 source at Ku-band, and predominantly transparent at X-band with the snow depths observed and modeled in this study. However, the difference in modeled Ku-band σ^0 magnitude associated with the snowpack between Sites 1 and 4 was confounded by other factors such as differential surface ice types and Site 4 being frozen to the lake bed. Signal interaction associated with grey ice has been shown to increase overall σ^0 by a magnitude of approximately 6 dB at VV and 7 dB at HH for ~0.6 m layer, and is a required variable in future model iterations.

The observation of surface and volume returns separately provided an important analysis of scattering sources in the lake ice system. The influence of spherical microbubbles within surface ice types has been observed as a component of overall backscatter at X- and Ku-bands, especially prior to tubular bubble inclusions at the base of the ice cover. The separation of surface and volume returns also provided an avenue to improve future modeling development of specific components within the lake ice system (surface ice types, on-ice snowpack, bubble inclusions). This study also identifies the existence of Ku-band sensitivity to on-ice snowpack, although a larger sample size is required to further quantify the potential for snow property retrieval or the presence of ice types at various thicknesses.

4.6 Acknowledgements

This research was made possible with financial support from the European Space Agency (ESTEC Contracts No. 4000103590/11/NL/FF/fk and 4000106960/12/NL/BJ/lf) and the Natural Sciences and Engineering Research Council of Canada (NSERC) to C. Duguay and G. Gunn. Logistics for field data collection was provided by the Churchill Northern Studies Centre. The authors thank all those who assisted in field data collection, notably R. Kelly, A. Silis, S. Howell, K. Kang, J. Oldham, N. Svacina and A. Casey. UW-Scat was developed and manufactured by J. Mead of ProSensing Inc. with funding provided by grants from the Canadian Foundation for Innovation and the Ontario Ministry of Research and Innovation to C. Duguay and R. Kelly.

Chapter 5

Freshwater Lake Ice thickness Derived Using X- and Ku-band FMCW Scatterometers in the Hudson Bay Lowlands Near Churchill, Manitoba

5.1 Introduction

The presence of freshwater lake ice constitutes an important component of the biological, chemical and physical processes of the cold regions freshwater cycle. Lakes cover approximately 2% of the Earth's land surface, with the majority located in the Northern Hemisphere (Brown and Duguay, 2010). In the Arctic and sub-Arctic, lakes can occupy up to 40% of the land surface. The presence or absence of freshwater lake ice affects local and regional weather and climate, influencing evaporative and sensible heat fluxes to the atmosphere as well as weather events (e.g. thermal moderation or lake-effect snow) (Rouse et al., 2008; Brown and Duguay, 2010). Knowledge of the status of ice-covered lakes is crucial for numerical weather prediction and regional climate modeling in regions where a significant fraction of land cover is comprised of lakes (Kheyrollah Pour et al., 2012; Martynov et al., 2012). Freshwater lake ice phenology and thickness also has many economic implications ranging from hydroelectricity to winter ice road transportation used to supply remote northern settlements (Prowse et al., 2009). In addition to its significant influence on weather, climate and socio-economic systems, freshwater ice is also an important indicator of climate change. Increasingly warm temperatures (Overland et al., 2014), increased snow precipitation (Arp et al., 2012) and sea ice extent reductions (Serreze et al., 2007) have become enhanced in recent years (Walsh et al., 2011). The response of lakes to changes in climate may vary due to variations in areal extent, depth, volume and latitudinal position.

Historically the observation of changes in lake ice cover, phenology (frequency, break-up and duration) and thickness was collected through manual measurements in conjunction with the weather observation, which has drastically reduced over the last two decades (Lenormand et al., 2002; Prowse et al., 2011). Recent studies have identified and demonstrated the use of remote sensing to produce observations of ice parameters, including lake ice phenology (Latifovic et al., 2007; Howell et al., 2009) and ice thickness (directly or indirectly) (Jeffries et al., 1996; Arcone et al., 1997; Kang et al., 2010; Kang et al., 2012; Surdu et al., 2014). Previous studies indicate that the use of active microwave observations was most suitable for lake ice observation as a result of the ability of active

microwave sensors to resolve small lakes due to its high spatial resolution compared to that of passive microwave instruments (meters vs kilometers) and the ability to acquire observations independent of incoming solar radiation or cloud cover.

Spaceborne C-band synthetic aperture radar (SAR) (Mueller et al., 2009; Cook and Bradley, 2010; Surdu et al., 2014), X-band SAR (Sobiech and Dierking, 2013) and Ku-band scatterometer (Howell et al., 2009) measurements have been used for tracking ice phenology, focusing largely on the observation of freeze-up and break-up dates. Active microwave observations of ice thickness have been restricted to shallow lakes, where ice thickness values have been inferred when a floating ice cover thickens sufficiently to become grounded, subsequently resulting in a drop in backscatter ($\sigma°$) (Mellor, 1982; Hirose et al., 2008). Mellor (1982) tracked X-band $\sigma°$ departures using multi-temporal airborne acquisitions and referencing previously produced bathymetric charts, successfully mapping bathymetry for multiple lakes on the Alaskan North Slope. The method was repeated using C-band ERS-1 SAR acquisitions with the successful mapping of bathymetric elevations (Mellor, 1994). Jeffries et al. (1996) extended this methodology by applying predicted ice thickness values derived from a one-dimensional thermodynamic lake ice model to areas that were identified as frozen to bed from ERS-1 SAR acquisitions. Jeffries et al. (2005a) repeated this methodology, assigning ice thickness values to pixels at the edge of the floating ice and interpolating bathymetry at increments of 0.25 m. While independent of bathymetric charts, the method presented by Kozlenko and Jeffries (2000) could only predict a maximum ice thickness of areas that are frozen to bed, restricting the application to shallow lakes. Duguay and Lafleur (2003) remotely observed lake depth using Landsat Band-2 (0.52 – 0.6 μm) and determined ice thickness by tracking backscatter over a time-series of ERS-1 acquisitions.

Ground based Frequency Modulated Continuous Wave (FMCW) radars operating at C- and X-band have been utilized to observe the snow-ice and ice-water interface with the sensor normally angled at nadir incidence angle (0°), resulting in a coherent reflection from the horizontal interfaces (Yankielun et al., 1992; Arcone et al., 1997; Leconte et al., 2009). Leconte et al., (2009) utilized a FMCW radar with a linear chirp over a bandwidth of 2 GHz (4 – 6 GHz) in laboratory observations of artificially grown bubble-free freshwater ice, and obtained a coefficient of determination (R^2) of 0.989 for ice thicknesses < 0.26 m. This study utilizes two ground-based FMCW radar systems with center frequencies at X- (9.6 GHz) and Ku-band (17.2 GHz) (UW-Scat) with a smaller bandwidth of 500 MHz to extend the framework of the laboratory experiments of Leconte et al. (2009) using field-based scatterometer observations of snow-covered freshwater lake ice, near Churchill, Manitoba. The

goal of this study was to identify the ability of X- and Ku-band scatterometers to derive ice thicknesses of floating freshwater lake ice that exhibits heterogeneous snow depth and surface ice types. Verification of snow and ice thicknesses were provided by in-situ snow and ice measurements adjacent to scatterometer scans, an upward facing SONAR on the lake bed, and a one-dimensional thermodynamic lake ice model; the Canadian Lake Ice Model (CLIMo) (Duguay et al., 2003). The use of two frequencies also provides potential for increased information of targets within range, as the difference in wavelengths may potentially interact with discrete scatterers within the snow and ice volume.

5.2 Study Site

Scatterometer observations were acquired at four undisturbed sites with repeated observations ("static sites") and 12 sites where sampling occurred within the footprint immediately after the completion of the scan ("roving sites"). Static sites were selected to resolve differential snow and ice conditions based off the lake bathymetry, while roving sites were selected to collect observations with variable snow depths. Observations were acquired from 28/11/2010 to 6/3/2011 on Malcolm Ramsay Lake (formerly known as Lake 58) within the Canadian Snow and Ice Experiment (CASIX). Malcolm Ramsay Lake is situated 20 km east of Churchill, Manitoba (58.7221°N, 93.7845°W) in the Hudson Bay Lowlands region (Figure 5-1). The lake bed is comprised of sediment and organics with a mean depth of 2.4 m and maximum of 3.2 m (Duguay and Lafleur, 2003).

The Hudson Bay Lowlands region is typified by the intersection of three ecological zones; tundra, tundra-boreal forest transition, and boreal forest, the separation of which runs parallel to the coast (Scott et al., 1987). The relief of the region surrounding Malcolm Ramsay Lake is relatively flat with a high lake fraction (32% of surface area), with formations of overburden the result of glacial deposits (Lafleur et al., 1997).

According to the 1981-2010 climate average obtained from Environment Canada the mean annual temperature recorded at the Churchill airport (58.7392°N. 94.0664°W) is -6.9 °C, with negative monthly average temperatures occurring from October to May. During the observation period the average observed temperature was -20.9° C. The normal water equivalent precipitation is 452.5 mm, with 2.01 m falling as snow. Churchill is situated on the south-western shoreline of Hudson Bay, contributing to its high annual sustained average wind speeds of 20.7 km/h, influencing

ice stratigraphy and is requisite for the formation of the tundra-lake snow classification, as discussed in Sturm and Liston (2003).

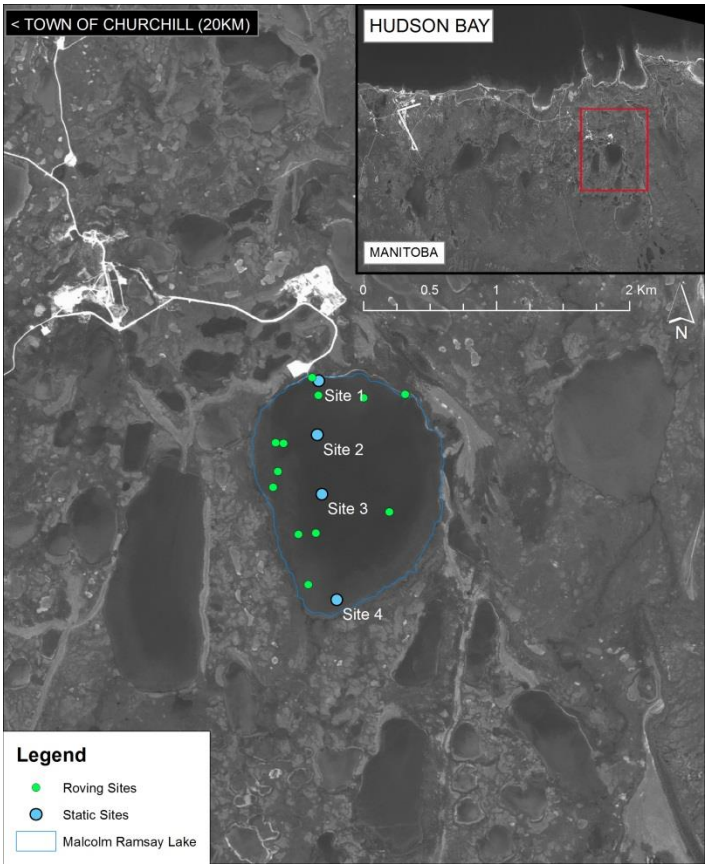

Figure 5-1: Location of Static and Roving sites on Malcolm Ramsay Lake, near Churchill, MB. UW-Scat observations were conducted during the winter of 2010-2011 within the Canadian Snow and Ice Experiment (CASIX).

5.3 Data & Methods

5.3.1 UW-Scat

The University of Waterloo Scatterometer (UW-Scat) is comprised of two frequency-modulated continuous wave (FMCW) radars that are operated at a bandwidth of 500 MHz with center frequencies of 9.6 and 17.2 GHz (X- and Ku-band, respectively) (manufactured by ProSensing Inc.). UW-Scat functions in a switched transmit and receive mode, obtaining fully-polarimetric data (VV,

HH, HV, VH). Scans are conducted by mounting the radar units to supports, which are maneuvered using a Kipp and Zonen 2ap Suntracker. Each scan is comprised of 60° azimuth sweep across and incidence angle range of 21° – 60° at 3° intervals (incidence angles >60° exhibited marked reduction in overall SNR). Additional relevant UW-Scat sensor parameters are provided in Table 5-1, with an extended sensor properties and description of the calculation of normalized radar cross section (NRCS) provided in King et al. (2013).

Table 5-1: UW-Scat Sensor Specifications

Parameter	X-band	Ku-band
Output Frequency (GHz)	9.35-9.85	16.95 - 17.45
Transmit Bandwidth (GHz)	0.5	0.5
Transmit Power (dB)	-11.8	-8
Range Resolution (m)	0.3	0.3
Cross-polarization isolation (dB)	>30	>30
Sensitivity/Noise Floor (dB m^2/m^2)	-50	-50
Antenna Beam width (°)	4.3	5.6
Transmit/Receive polarizations	VV/VH/HH	VV/VH/HH

Raw data blocks observed by the scatterometer are converted to range domain using a Fast Fourier Transform. Range-dependent transmit leakage was estimated within–scene by acquiring an average of sky observations and coherently subtracting them from the target range bin. The range profiles for each incidence angle are then averaged in azimuth (Geldsetzer et al., 2007).

Figure 5-2 shows an average range profile for observed polarizations at X- and Ku-band at 45° for floating lake ice at the beginning and end of the observation period. The profiles are binned to steps of 0.16 m to highlight peak returns within range. The minimum distance in range r_min that can be resolved by an FMCW is influenced by the refractive index of the media (n_{ice}) and the bandwidth (BW) in Hz (Yankielun, 1992; Marshall et al., 2007) where:

$$r_{min} = \frac{c}{(2n_{ice})(BW)} \tag{5.1}$$

where c is the speed of light (2.998 x 10^8 m/s). Therefore, the theoretical r_min in slant range for UW-Scat which utilizes a bandwidth of 500 MHz is 0.168 m. The nominal range resolution of UW-

Scat in air is 0.3 m (King et al., 2013) which implies that observations of thin ice (<0.4 m) will not elicit a discernable difference between returns originating from either the snow-ice or ice-water interface.

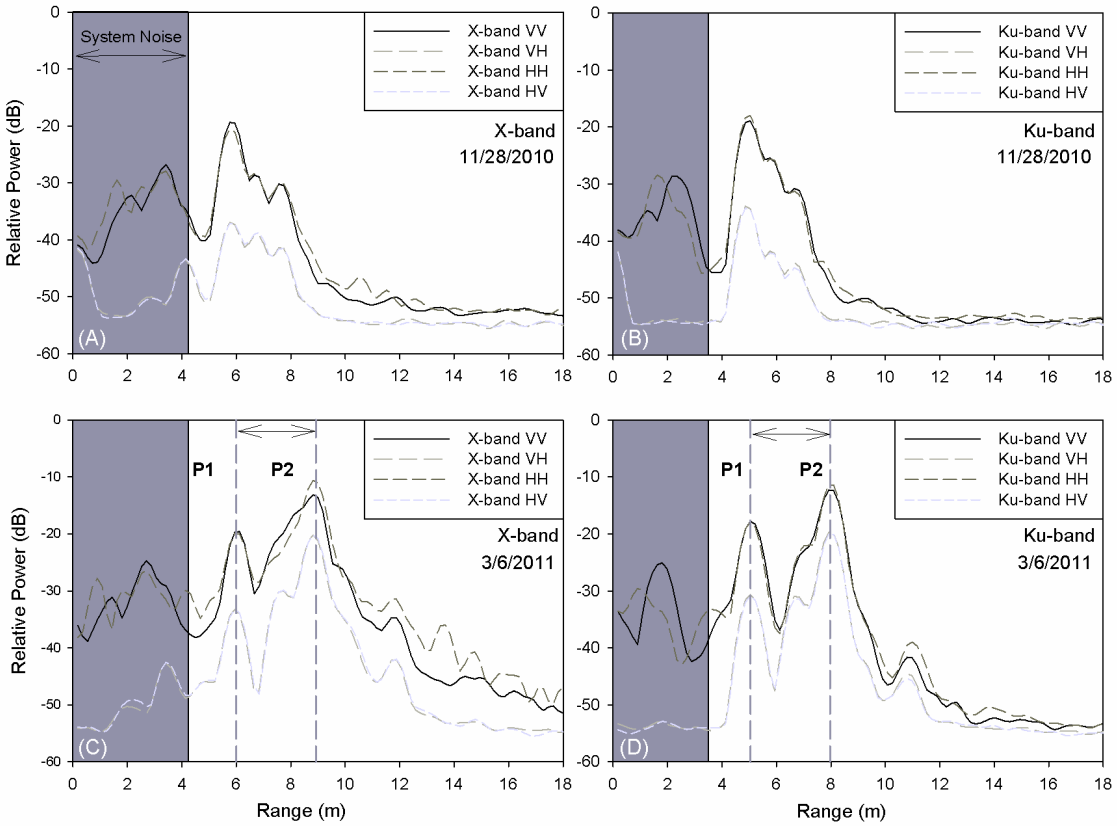

Figure 5-2: Fitted UW-Scat range profiles for X- (A, C) and Ku-bands (B, D) representing an early (A, B) and late season (C, D) observation. The second peak in C and D was not present in early season observations (A, B) due to thin ice (0.4 m). The distance between the two peaks (P2 – P1) was considered to be the distance the signal traveled within the ice volume.

5.3.2 Derivation of Ice Thickness

Ice thickness retrievals from both X- and Ku-band are achieved by first identifying returns within range that are associated with the snow-ice and ice-water interface, and second by computing the distance and geometry between the two peaks in slant range to derive a final ice thickness for each incidence angle.

5.3.2.1 Dielectric Properties of Media

The identification of the snow-ice and ice-water interface when viewed at slant range is influenced by: a) differences in the permittivity of the media, and b) sources of scatter at the media interfaces or within the media itself. The direct field of view of the scatterometer is comprised of a combination of water, freshwater ice, and snow, which is comprised of H_2O in either solid or liquid states. The separability of the positive and negative charges allow for H_2O to easily become polarized which is related to the relative permittivity of the media compared to that of air in a vacuum (ε_r) (Stiles and Ulaby, 1980), given by

$$\varepsilon_r = \varepsilon' - j\varepsilon'' \tag{5.2}$$

where ε' is the real part of the permittivity which quantifies the medium's ability to become polarized, and $j\varepsilon''$ is the dielectric loss factor, presented in complex form.

The liquid phase of H_2O is comprised of discontinuous weakly oriented hydrogen bonds that become polarized in the direction of an incident electrical field and return to their resting state once the field is removed. The amount of time elapsed between polarization and rest state is termed the relaxation time (τ), which can also be expressed in frequency, given by

$$f_0 = (2\pi\tau)^{-1} \tag{5.3}$$

The relaxation frequency (f_0) of water is temperature dependent (approximately 9 GHz at 0 °C), where Debye style dispersion is observed (Evans, 1965). Therefore, incident electromagnetic energy will be subject to increased absorption and limited penetration depth (Evans, 1965).

The relative permittivity of solid state H_2O contrasts that of the liquid state due to the highly bonded molecular structure of the lattice. The lattice structure bonds restrict the movement of molecules upon the application of an electric field limiting the relaxation time, thereby resulting in the relaxation frequency of ice to be in the kilohertz (kHz) region. The relative permittivity of freshwater ice has been experimentally measured by many studies to be independent of range from ε' = 3.11 – 3.18, with a commonly accepted value of ε' = 3.17 with negligible ε'' of 0.00065 (Lamb, 1946; Cumming, 1952).

Snow consists of a combination of ice crystals and air, which possess unique dielectric properties. At sub-freezing temperatures the permittivity of snow is independent of frequency or temperature but varies according to the grain size/shape and fractional volume of ice crystals. Studies have either treated snow as a homogenous medium with a bulk relative permittivity obtained through empirical regression using experimental datasets (Cummings, 1952; Stiles and Ulaby, 1980), or

empirical and physically-based dielectric mixing models (Polder and Van der Sanden, 1946; Evans 1965; Tinga et al., 1973; Hallikainen et al., 1986). According to experimental datasets collected by Hallikainen et al. (1986) $\varepsilon' = 1.5$ for a dry snowpack with a density of 250 kg/m^3, across a range of 3 – 37 GHz.

The differences in permittivity of media in the scatterometer field of view influence the amount of incident radiation transmitted through the boundary layer, which governs the reflection and transmission coefficients through Fresnel equations. Assuming that the horizontal interfaces are smooth and below both the critical angle and Brewster angle (where reflection reaches a minimum for vertically polarized radiation), the transmission coefficient (Γ) for perpendicular ($\Gamma_\perp$) and parallel waves ($\Gamma_\parallel$) is equal to one minus the absolute value of the Fresnel Reflection coefficient (R) (Equation 5.4) (Ulaby et al., 1982a; Barber, 2005).

$$R_\perp = \frac{\varepsilon_2^* cos\theta_1 - \varepsilon_1^* cos\theta_2}{\varepsilon_2^* cos\theta_1 + \varepsilon_1^* cos\theta_2} \tag{5.4}$$

$$R_\parallel = \frac{\varepsilon_1^* cos\theta_1 - \varepsilon_2^* cos\theta_2}{\varepsilon_1^* cos\theta_1 + \varepsilon_2^* cos\theta_2} \tag{5.5}$$

$$\Gamma = (1 - |R|) \tag{5.6}$$

where ε and θ are the relative permittivity and incidence angle for the medium in which the radiation is transmitting through and incident upon the snow-ice ($_1$) and ice-water ($_2$) interfaces.

As discussed previously, the low-loss permittivity of freshwater ice allows for transmission across the snow-ice interface to the ice-water interface, where the high contrast in permittivity results in near-specular reflection of the incident signal. The fraction of energy that is transmitted across the ice-water interface is reduced as it is attenuated in the conductive medium. The specular reflection of the signal at the ice-water interfaces typically produces a larger return in range, and the attenuation of the signal by the water results in the absence of returns associated with horizontal interfaces further in the scatterometer field of view.

5.3.2.2 Scattering Sources

Sources of scatter downrange of the scatterometer field of view can be summarized by the combination of surface and volume interactions near the snow-ice and ice-water interface due to the 0.3 m range resolution of UW-Scat, shown in Figure 5-3. The reflectivity of a horizontally or vertically polarized electric field is given by the Fresnel equations, which describe the magnitude of radiation scattered in the specular direction by a smooth surface, referred to as the coherent scattering

component (Ulaby et al., 1982b, vol 2). A surface is considered smooth when it satisfies the Rayleigh criterion, expressed as

$$\sigma < \frac{\lambda}{8 \cos \theta} \tag{5.7}$$

where σ is the root mean square of height deviations relative to the surface mean height (RMS), and λ is the incident wavelength. The magnitude of the incident signal scattered back to the sensor from an interface depends on the surface roughness, characterized by the root mean square of the height deviations relative to a mean height of the surface (Woodhouse, 2006). As height deviations approximate the size of the wavelength the reflectivity becomes increasingly incoherent (diffuse), resulting in greater backscatter magnitude. In the context of lake ice, the roughness of boundary layers continually evolve, however the majority of backscatter return occurs at the ice/water interface, consistent with Weeks et al. (1978) and Leconte and Klassen (1991).

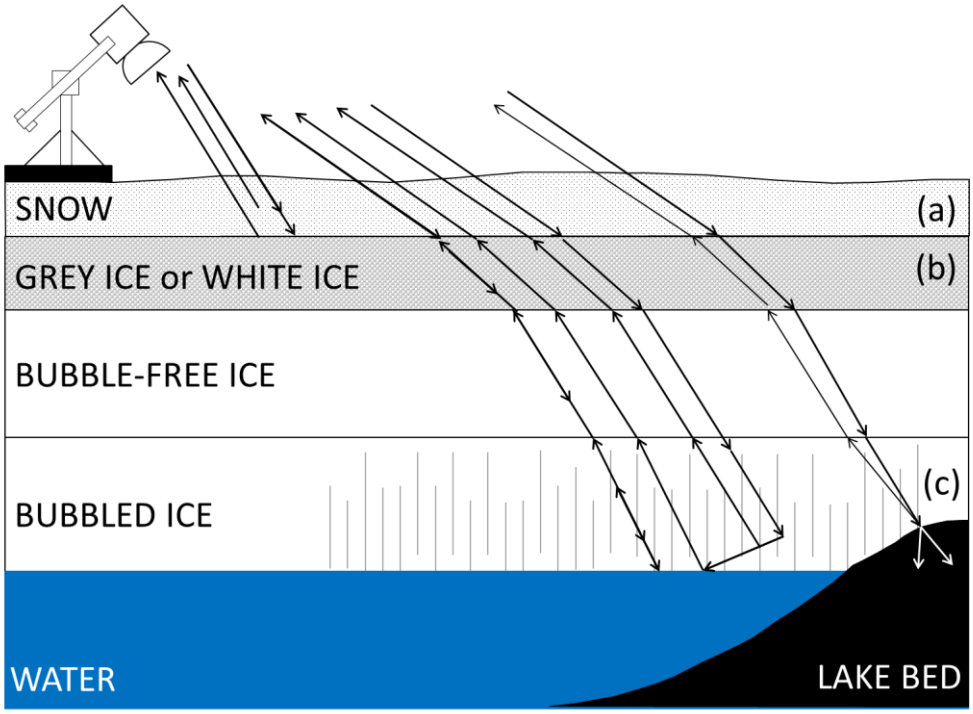

Figure 5-3: Representation of idealized scattering scenario for floating and grounded lake ice. The sources of scatter are summarized to (a) the snow volume and snow-ice interface, (b) superimposed ice (snow ice) or surface ice types composed of spherical microbubbles, and (c) incoherent double bounce off tubular bubbles within the ice volume and off the ice-water interface (modified from Duguay et al., 2002).

The physical properties contributing to volume scatter near the snow-ice interface are the snow volume and surface ice types. The magnitude of volume scatter in a snowpack is dependent on the incident wavelength, snow depth, density and grain size. Backscatter at frequencies > 10 GHz have been reported to be sensitive to terrestrial snow water equivalent (SWE) variability, which is a product of snow depth and density (Morrison et al., 2007; Yueh et al., 2009). Frequencies < 10 GHz are considered to be insensitive to snowpack variability with the exception of extreme snow density or SWE conditions (Ulaby et al., 1982b). Surface ice types, including snow-ice and grey-ice, have been noted as a potential contributor to volume scatter near the snow-ice interface due to the presence of high-density spherical micro-bubbles on the order of 0.5 – 1 mm (Hall et al., 1994; Leconte et al., 2009).

Freshwater ice is a low-loss dielectric, allowing for the transmission of incident electric fields to the ice-water interface. However, if the water becomes super-saturated with dissolved gases, tubular or tear-drop like bubbles can be incorporated into the ice volume parallel to the direction of ice growth. It is thought that the dielectric contrast of the ice and bubbles result in a "double-bounce" of incident microwave radiation whereby "forward" or coherent scatter occurs from tubular bubble inclusions and the ice-water interface, returning a large portion of incident radiation back to the sensor (Weeks et al., 1978; Jeffries et al., 1994; Duguay et al., 2002; Surdu et al., 2014). The coherent scatter occurring as a result of tubular bubbles and/or reflection off the ice-water interface leads to the determination of its distance to the sensor and forms the basis of deriving ice thickness.

5.3.2.3 Radar Processing and Derivation of Ice Thickness

The averaged azimuth range profile produced in the time delay domain using UW-Scat was dominated by two peaks once adequate separability of peaks was achieved (ice thicknesses > 0.4 m), representing return from near the snow-ice and ice-water interface, Peak-1 and Peak-2 respectively (Figure 5-2). Theoretically, the distance between the two peaks in slant range should represent the in-situ distance between the top and bottom of the ice cover when the effect of refraction on incidence angle and propagation speed is accounted for. The speed of light in an ice medium (c_i) is defined as

$$c_i = \frac{c}{n_i} \tag{5.8}$$

where c is the speed of light in a vacuum and n_i is the refractive index of ice in the microwave region, defined as the square root of the real part of the relative permittivity ($n_i = \sqrt{3.17}$) (Mätzler and Wegmüller, 1987; Woodhouse, 2006). The refracted angle which the wave front propagates through the ice medium was accounted for through Snell's Law,

$$\frac{\sin\theta_i}{\sin\theta_t} = \frac{n_2}{n_1} \tag{5.9}$$

where θ_i and θ_t are the incidence angles for the incident and transmitted wave, and n_1 and n_2 are the values of the refractive index for the free space and material medium, respectively.

Based on the contrast in complex permittivity of ice and water ($\varepsilon^*_{water} \sim 40, \varepsilon^*_{ice} \sim 3.17$), the second peak signal return was assumed to be the result of coherent reflection off the ice-water interface in the specular direction, consistent with Arcone et al. (1997) and Leconte et al, (2009). The reflected component is thought to have been returned to the sensor via incoherent double bounce mechanism caused by the presence of tubular bubble inclusions incorporated into the ice at the ice-water interface (Jeffries et al., 1994; Duguay et al., 2003). Therefore, the distance traveled by the incident wave (d_s) within the ice volume would be equivalent to

$$d_s = \frac{2d_{meas}}{\cos\theta_t} \tag{5.10}$$

where d_{meas} is the average measured in-situ ice thickness and $\theta_t$is the angle of incidence adjusted for refraction within the ice volume from Equation 5.9.With the transmission angle θ_t and the adjusted slant range distance from the ice surface to bottom (d_{si}) computed from Equation 5.8, trigonometry was used to calculate the total ice thickness ($d_{UW-Scat}$) through

$$d_{UW-Scat} = \sin C \times d_{si} \tag{5.11}$$

where $= 90° - \theta_t$, shown in Figure 5-4**.** Ice thickness ($d_{UW-Scat}$) were derived for coincident X- and Ku-band scans which included an incidence angle range of 21° - 60° at 3° intervals for each observation. The median value from the range of incidence angles from each frequency was obtained and compared to validation datasets.

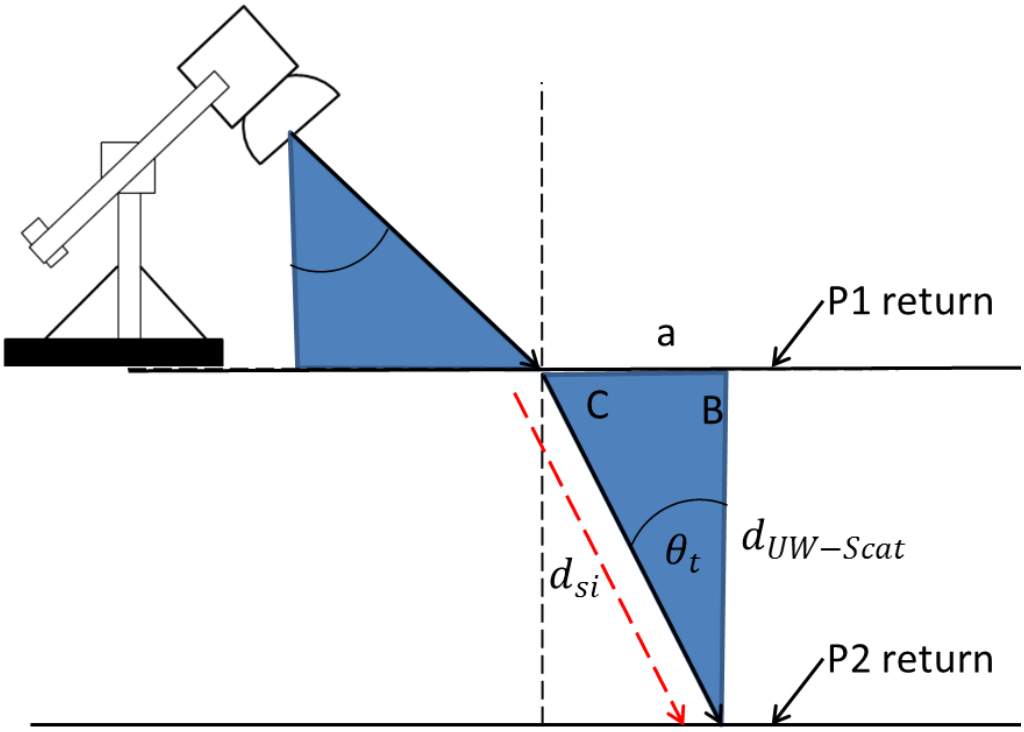

Figure 5-4: Geometry of ice thickness derivation using UW-Scat.

5.3.3 In-Situ Data Collection

Scatterometer observations were conducted at four "static" sites and several "roving" sites during the winter of 2010-11 (Figure 5-1). The "static" sites were revisited a minimum of five times at approximately 2 week intervals, while "roving" sites were observed at a minimum of once per month, with no predetermined static location. Site 4 was omitted from the analysis as a result of it freezing to bed early in the observation period, resulting in the removal of the high dielectric contrasting ice-water interface. The total number of UW-Scat observations at static and roving sites coincident to verification datasets is provided in Table 5-2.

Table 5-2: Number of UW-Scat and coincident observations during CASIX (2010-11).

	Static Sites	Roving Sites	Total Observations
X-band	14	8	22
Ku-band	14	12	26
In-situ measurements	14	12	26
SWIP observations	14	10	24

UW-Scat X- and Ku-band observations were completed facing east to ensure that snow redistribution did not deposit artificial drifts in the field of view. Correlative data including snow and ice properties were collected adjacent to the UW-Scat (Figure 5-5). Traditional snow pits were conducted in the "pit farm" outside of UW-Scat field of view according to Fierz et al. (2009), containing stratigraphy, snow depth, density, hardness and temperature profiles. Surface ice type and ice thickness measurements were collected at 25 m intervals along a 100 m transect parallel to UW-Scat zero azimuth and averaged for comparison to UW-Scat derived ice thickness. Snow depths were also collected along the 100 m transect at 0.5 m intervals using a SnowHydro® Magnaprobe (Sturm and Holgrem, 1999).

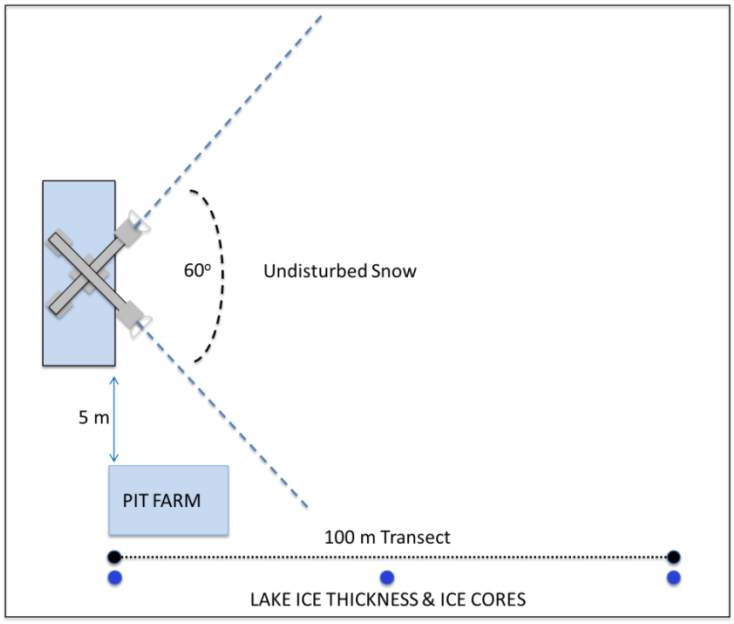

Figure 5-5: Static and roving site sampling layout. Snow pit data are collected in the "pit farm". Additional snow depths, lake ice thickness and ice stratigraphy are measured on a 100 m transect parallel to 0° azimuth of UW-Scat.

5.3.3.1 Shallow Water Ice Profiler (SWIP)

Further verification of the derived ice thickness results was provided by the placement of a Shallow Water Ice Profiler, an upward-looking acoustic sonar device manufactured by ASL Environmental Systems, Inc, within 500 m of Site 1. The SWIP is comprised of an acoustic transducer with a center frequency of 546 kHz, pressure transducer (in combination with barometric pressure from a nearby weather station to determine water level), thermometer, two axial tilt sensors

and a battery pack. The SWIP scans for targets within its field of view, collecting acoustic backscatter to isolate the ice-water interface averaged to daily ice thickness values with a vertical resolution of 0.02 m (Marko et al., 2006). Details describing the accuracy assessment for variability in ice type cover (frazil or slush on the surface) are provided in Marko et al (2006), and the nature of prior SWIP deployments in Malcolm Ramsay Lake are provided in Brown and Duguay, (2011a).

5.3.3.2 The Canadian Lake Ice Model (CLIMo)

The Canadian Lake Ice Model (CLIMo) is a one-dimensional thermodynamic model that has been utilized in simulating ice cover for many fresh water ice studies (Duguay et al., 2003; Morris et al., 2005; Brown and Duguay, 2011a). The model is capable of producing ice phenology, composition (snow ice, clear ice) and total thickness. CLIMo is based on a modification of a one-dimensional model originally conceived for sea ice (Flato and Brown, 1996), which is based on the unsteady heat conduction equation presented by Maykut and Untersteiner (1971) expressed in Equation 10**.**

$$\rho C_p \frac{\partial T}{\partial t} = \frac{\partial}{\partial z} k \frac{\partial T}{\partial z} + F_{sw} I_0 (1 - \alpha) K e^{-Kz} \tag{5.12}$$

where ρ is the density (kg m^{-3}), C_p is the specific heat capacity (J kg^{-1} K^{-1}), T is the temperature (K) of the ice or snow, t is time (s), z is the vertical coordinate (m), F_{sw} is the downwelling shortwave radiative energy flux (W m^{-2}), I_0 is the fractional shortwave radiation flux that penetrates through surface, $\alpha$is the surface albedo and K is the bulk extinction coefficient for penetrating shortwave radiation (Duguay et al., 2003).

The surface energy budget can be expressed as:

$$F_0 = F_{lw} - \varepsilon \sigma T^4(0,t) + (1 - \alpha)(1 - I_0) F_{sw} + F_{lat} + F_{sens} \tag{5.13}$$

where F_0 is the net heat flux that is absorbed at the surface, ε is the emissivity at the surface, σ is the Stefan-Boltzmann constant (5.67 x 10^{-8} Wm^{-2} K^{-4}), and F_{lw}, F_{lat}, and F_{sens} are the downwelling longwave, latent and sensible heat flux (W m^{-2}), respectively (Duguay et al., 2003).

To simulate full ice-on/ice-off seasonality, CLIMo includes a fixed-layer depth, which is set at the freezing point during ice-on and is computed from the surface energy budget in the absence of an ice cover, representing the measure of heat storage of the lake. Typically shallow lakes are well mixed with an isothermal temperature profile during ice-free conditions, resulting in the mixed-layer depth to provide a good approximation of the effect of lake depth when entering freeze-up in the autumn months (Duguay et al., 2003).

Growth at the bottom of the ice cover is computed as the difference between the conductive heat flux into the underside of the ice and out of the surface of the prescribed mixed layer by:

$$\left.\frac{\partial h_i}{\partial h_t}\right|_{z=h} = \left(k\left.\frac{\partial T}{\partial z}\right|_{z=h} - \int_h^{\infty} F_{SW} I_0 (1-\alpha) K \mathrm{e}^{-Kz} \mathrm{d}z\right) \frac{1}{L_{fi}} \quad (5.14)$$

where h_i is the ice thickness. The last term in Equation (5.14) is the shortwave radiation that penetrates through the ice column that is absorbed at the mixing layer and subsequently sent to the ice underside, keeping the temperature of the mixing layer at 0 °C.

Ice melt at the surface is computed as the difference between the conductive heat flux and the net surface heat flux. In melt conditions, the ice is melted only after the overlying snowpack has been first. Ice growth and melt at the bottom of the ice are computed as the difference between the conductive heat flux into the ice from the ice bottom, and the heat flux out of the upper portion of the mixed layer. Any shortwave radiation that penetrates through the ice is assumed to be absorbed by the mixed layer and returned to the underside of the ice, maintaining the temperature of the mixed layer at the freezing point. The model incorporates the creation of snow ice when the weight of the snow is such that it depresses the ice below the water level. The mass of the slush is added to the ice thickness, and freezes at the surface prior to further freezing at the ice base. Many other factors affect ice thickness simulations such as albedo parameterizations, which are more extensively discussed in Duguay et al., (2003) and Svacina et al., (2014).

CLIMo was run using a mixing depth of 2m (which approximates the mean depth of Malcolm Ramsay Lake) and atmospheric data collected in the vicinity of the lake using an automatic weather station (AWS) operating Campbell Scientific sensors. Inputs include wind speed (RM Young Wind Monitor), air temperature and relative humidity (HC-SC-XT temperature and relative humidity probe). Additional input including cloud cover data was acquired from the Meteorological Service of Canada's (MSC) Churchill weather station, approximately 16 km to the west of Malcolm Ramsay Lake. Consistent daily snow depth data was compiled from records at the Churchill weather stations obtained from Environment Canada, with a constant dry snow density of 259 kg m^{-3} used in simulations, obtained by averaging on-ice snowpits observed throughout the winter season.

Snow depths measured at the weather station were compared to on-ice median snow depth collected from Magnaprobe transects on the dates of scatterometer acquisitions (Figure 5-6). The on-ice snow depths have an average ratio of approximately 30% of the MSC's station obtained from snow depth transects at each static site, with a relatively consistent standard deviation and no apparent seasonal variation when averaged across the lake (dashed line in Figure 5-6). However, there is a slight increase in the standard deviation of snow depths on the lake compared to the station observations on 22/2/2011, which is reduced on 6/3/2011. The disparity between the on-ice and MSC

snow depths is due to the combination of variability in situation, and snow redistribution caused by exposure to high winds on the lake (Sturm and Liston, 2003).

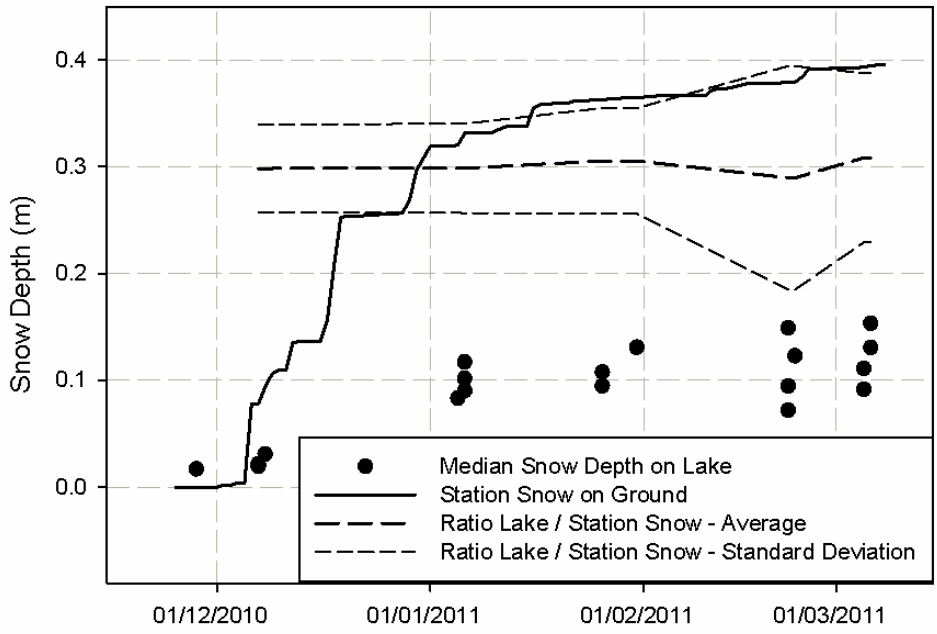

Figure 5-6: In-situ on-ice median snow depth measurement on the 100m transect at Static and Roving sites compared to terrestrial snow depths recorded at the Churchill weather station. The hashed line indicates the ratio of lake snow related to station snow at approximately 30% for the duration of CASIX observation period.

5.4 Results

5.4.1 In-situ Measurements and CLIMO Simulations

Figure 5-7 shows the average derived two-way distance traveled within the ice medium relative to the distance between Ku- and X-band peaks (Peak-2 – Peak-1) which were adjusted using Snell's law relative to output of Equation 5.10. The derived two-way distance was nearly equivalent to slant range calculated using in-situ ice thickness measurements with R^2 of 0.96 (n = 22) and 0.90 (n = 25) for X- and Ku-band, respectively. Deviations from the 1:1 relationship line were the result of the rounding of the target distance due to the range resolution of UW-Scat (0.3 m).

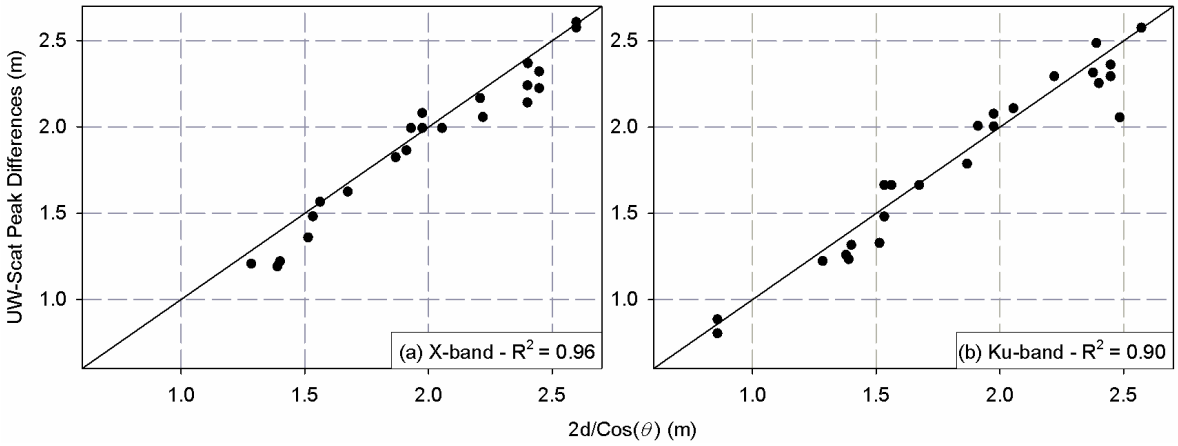

Figure 5-7: Validating the assumption of interactions at the snow-ice and ice-water interface represented by Peak 1 and 2 in range. The Peak 2 – Peak 1 differences for X- (a) and Ku-band (b) tracked the calculated slant range from the refracted incident angle and measured ice thickness with a near 1:1 relationship.

Ice growth was observed using the SWIP and modeled with CLIMo for the winter season of 2010-11, with a total of 25 in-situ thickness measurements collected from 28/11/10 to 6/3/2011 for validation (Figure 5-8). Snow depth is quite variable from the beginning to the end of the season, with increased variability later in the observation period. However, March snow depth was averaged from measurements conducted during two dates at the beginning of the month, potentially artificially reducing monthly snow depths compared to in-situ. The maximum average snow depth observed (0.21 m) was in the central portion of the lake at a roving site on 21/1/2011. Snow density increases throughout the season at all static sites up to a maximum of 451 kg m^{-3}, consistent with measurements of snow density on tundra lakes by Sturm and Liston (2003). The roving sites do not exhibit a similar increase in snow density as a result of the diverse snowpack observed at various sites across the lake.

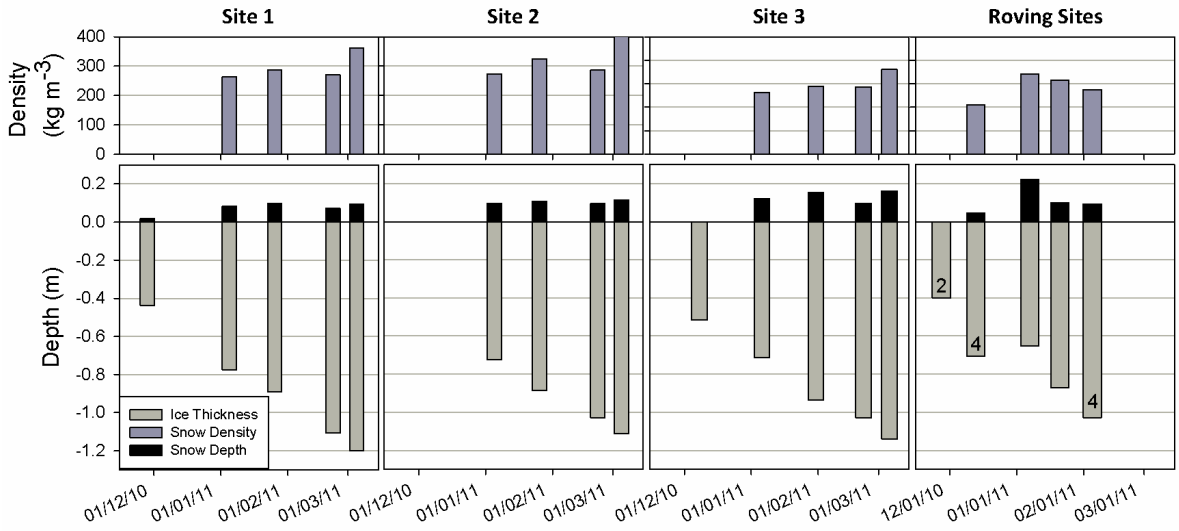

Figure 5-8: Average ice thickness (m), snow depth (m) and density (kg m^{-3}) for 100 m transect adjacent to UW-Scat. Numbers on ice thickness roving sites indicate the number of sites observed on the specified dates.

The ice cover at Site 4 was observed to freeze to bed early in the observation period, and was removed from analysis due to the inability for UW-Scat to derive ice thickness due to the removal of the high-contrast in permittivity at the ice-water interface. All other ice thickness measurements indicated that the ice remained afloat during the observation period with a maximum average observation of 1.20 m on 3/5/2011 at Static site 1. Averaged monthly ice thickness values are provided in Table 5-3.

Table 5-3: Monthly average and standard deviation of snow and ice measurements on 100 m transect adjacent to UW-Scat.

	Ice Thickness (m)		Snow Depth(m)		Snow Density (kg m^{-3})	
	Avg.	St. Dev.	Avg.	St. Dev.	Avg.	St. Dev.
November	0.41	0.02	0.02	0.01	n/a	n/a
December	0.60	0.04	0.04	0.02	220	7.21
January	0.82	0.03	0.12	0.03	290	5.22
February	1.00	0.04	0.11	0.04	280	4.35
March	1.08	0.08	0.12	0.04	390	6.65

Ice thickness simulations were produced using proportional snow cover scenarios, whereby 0, 25, 30, and 100% of reported snow depth at the Churchill weather station was used as input for CLIMo snow depth (Figure 5-9). The 0% (no snow on ice) and 100% (same amount as measured inland at the weather station) snow depth scenarios essentially show the range of potential ice thicknesses relative to input parameters, assuming minimal snow ice development. The 25 and 30% snow depth scenario simulations are nearly identical to the 0% snow depth scenario before 12/1/10, which is coincident with the absence of a consistent snowpack. The 25% snow depth scenario simulation tracks in-situ ice thickness measurements extremely well, producing a root mean square error (RMSE) and mean bias error (MBE) of 0.083 m and -0.022 m, respectively, consistent with previous studies investigating the use of CLIMo for ice thickness simulation on Malcolm Ramsay lake (Duguay et al., 2003; Brown and Duguay, 2011a). Conversely, the 30% snow depth scenario produces a thinner ice cover compared to in-situ measurements beginning 21/1/2011, with RMSE and MBE of 0.1 m and -0.057 m, respectively. The SWIP-measured ice thickness is consistently lower than values measured in-situ and simulated using 25 and 30% snow depth scenario until 2/1/11, which was likely influenced by static placement of the SWIP (located within 50 m of Site 1) relative to in-situ measurements which reflected the greater spatial variability of ice thickness across the lake, which was influenced by local snow depth and density.

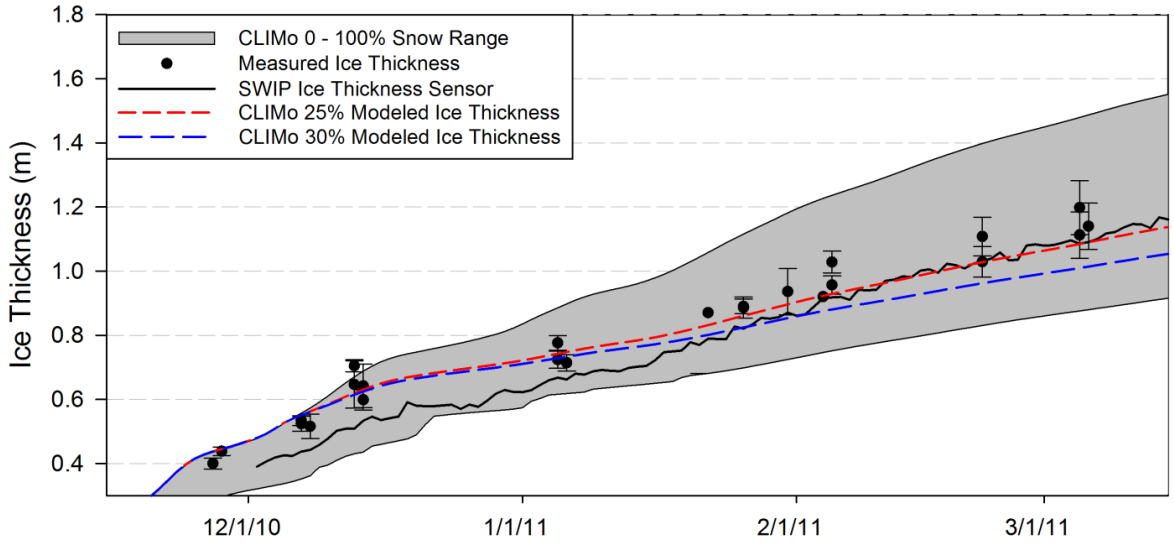

Figure 5-9: In-situ averaged ice thickness measurements relative to SWIP-measured and CLIMo simulated ice thicknesses using 0, 25, 30, and 100% snow depth scenarios.

5.4.2 Derived Ice Thickness

The methodology described in Section 3.2.3. assumed that Peak 1 and Peak 2 in the range profile are associated with interactions near the snow-ice and ice-water interface, therefore the range at Peak 1 would remain constant and would increase at Peak 2 as the ice thickened during the season. Figure 5-10 shows the range evolution for Peak 1 and 2 at X- and Ku-bands at an incidence angle of 39°. Peak 1 remains relatively constant throughout the season (+/- 1 range bin) while the range for peak 2 increases steadily, indicating that the distance to the ice-water interface is increasing as a result of ice thickening. Peak 1 range at X-band is slightly further than Ku-band, a result of the differential placement of the transmit/receive antennas on UW-Scat. Figure 5-10b shows the relationship of observed distances between peaks to be nearly equivalent to each other, and also related to ice thickness shown by CLIMo 25% snow depth scenario simulations. The constant distance at Peak 1 also indicates that changes in snow depth/density did not alter the target distance, resulting in a consistent benchmark for the duration of the observation period.

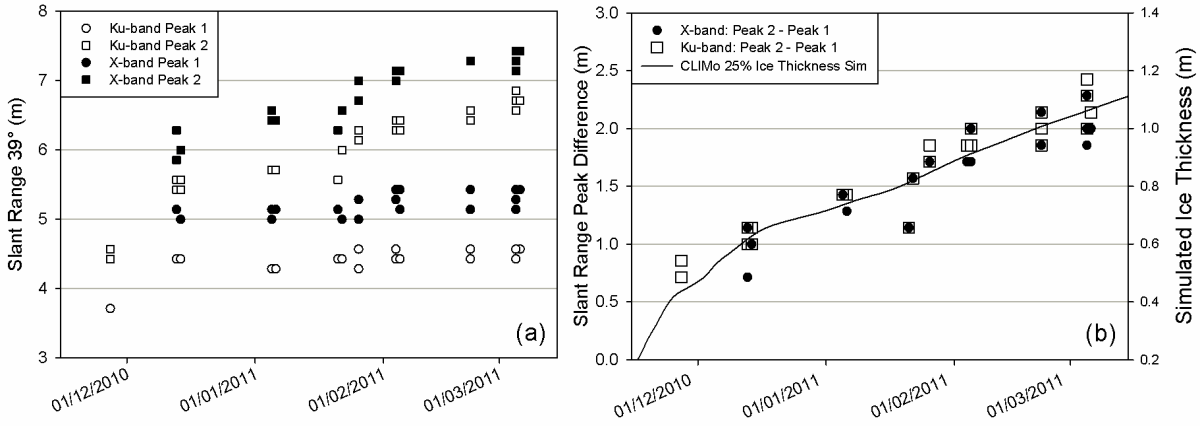

Figure 5-10: X- and Ku-band Peak 1 target range remains constant while Peak 2 increase during the season, indicating returns near ice-snow (Peak 1) and ice-water (Peak 2) interface. (b) shows the similar increase in differences for Peak 2 and Peak 1 as a result of simulated ice thicknesses obtained with CLIMo (25% snow depth scenario).

Ice thicknesses derived using the methodology discussed in Section 3.2.3. using X- and Ku-band revealed excellent agreement to in-situ measurements averaged along the 100 m transect adjacent to UW-Scat field of view. The derived ice thickness values were averaged across the 21 - 60° incidence angle range, with an average standard deviation of 0.038 m and 0.044 m for X- and Ku-

band, respectively (represented by error bars in Figure 5-11). X- and Ku-band derived ice thicknesses produced RMSE of 0.053 and 0.050 m, with high R^2 of 0.955 and 0.964 respectively compared to in-situ measurements, with p-values less than 0.001 (Table 5-4). The minimum ice thickness that UW-Scat was able to resolve the ice-water interface was 0.4 m, observed on 28/11/2010, which was only observed by Ku-band. X-band was not able to resolve the ice-water interface when the ice thickness was ~0.4 m was likely due the inclusion of tubular bubbles within the ice volume that were shorter than the incident wavelength, resulting in specular reflection away from the sensor.

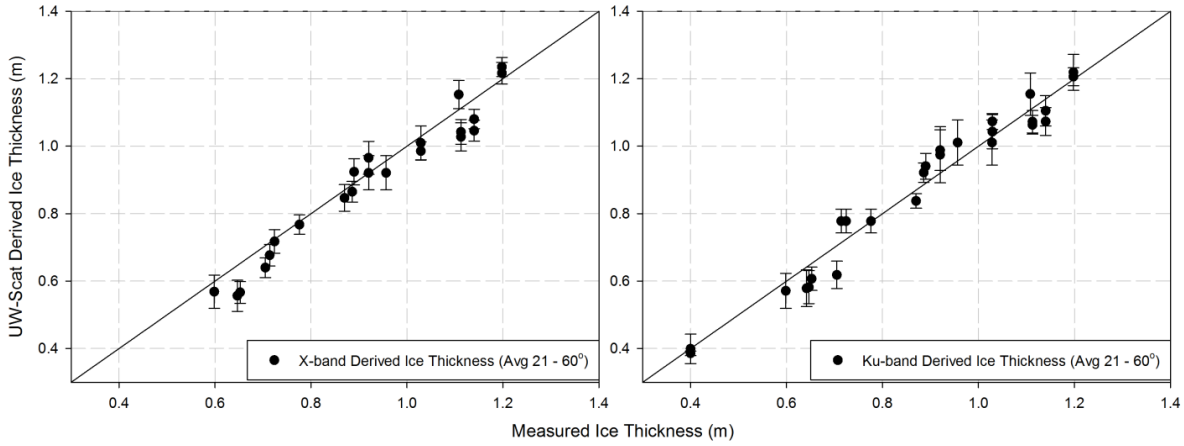

Figure 5-11: UW-Scat derived ice thickness at X- (left) and Ku-band (right) relative to in-situ measurements averaged over 100 m transect. Error bars are the standard deviation of derived ice thicknesses.

UW-Scat derived ice thickness showed agreement with the CLIMo 25% and 30% (not shown) snow depth scenario simulations and SWIP validation datasets (Figure 5-12). The CLIMo simulation ice thickness outputs indicate are consistently thinner for both X- and Ku-bands at thicknesses greater than 0.8 m, with a MBE of -0.013 and -0.035 m for the 25% scenario, and -0.54 and -0.076 m for the 30% snow depth scenario, respectively. The MBE at X-band was near 0 m for the 25 and 30% CLIMo simulations, whereas Figure 5-9 indicates that the modeled ice thickness should exhibit a negative MBE. The near 0 m MBE is due to a 0.2 m deviation (X-band derived = 0.61 m, CLIMO 25% = 0.81 m) at a roving site on 21/1/2011, where the formation of a thick snowpack (0.21 m) perturbed ice growth (0.65 m). CLIMo simulations did not reflect the anomalous observation point as snow depth observations were obtained from the Churchill weather station. However, the thinner ice at

the roving site was captured by UW-Scat observations accurately to within 0.04 m. Ku-band also exhibited a small negative MBE relative to the CLIMo 25% snow depth scenario simulation, influenced by the same positive outlier (Table 5-4). The 25% snow depth scenario also exhibited the lowest RMSE of CLIMo simulations for both X- and Ku-band (0.082 and 0.079m, respectively) compared to the 0 and 100% snow depth scenarios, which were unlikely to occur on the lake, especially later in the ice growth season.

Consistent with Figure 5-9, X- and Ku-band derived ice thicknesses were greater than SWIP observations. However, SWIP observations were also thinner than in-situ ice thickness measurements that were conducted adjacent to the scatterometer footprint (MBE = -0.102, -0.094 m at X- and Ku-band, respectively). The small negative MBE is likely also reduced by the overestimation caused by the outlier observed on 1/21/11. SWIP thickness estimation is only representative of total thickness at its static placement, which is likely the source of error when compared to lake-wide measurements.

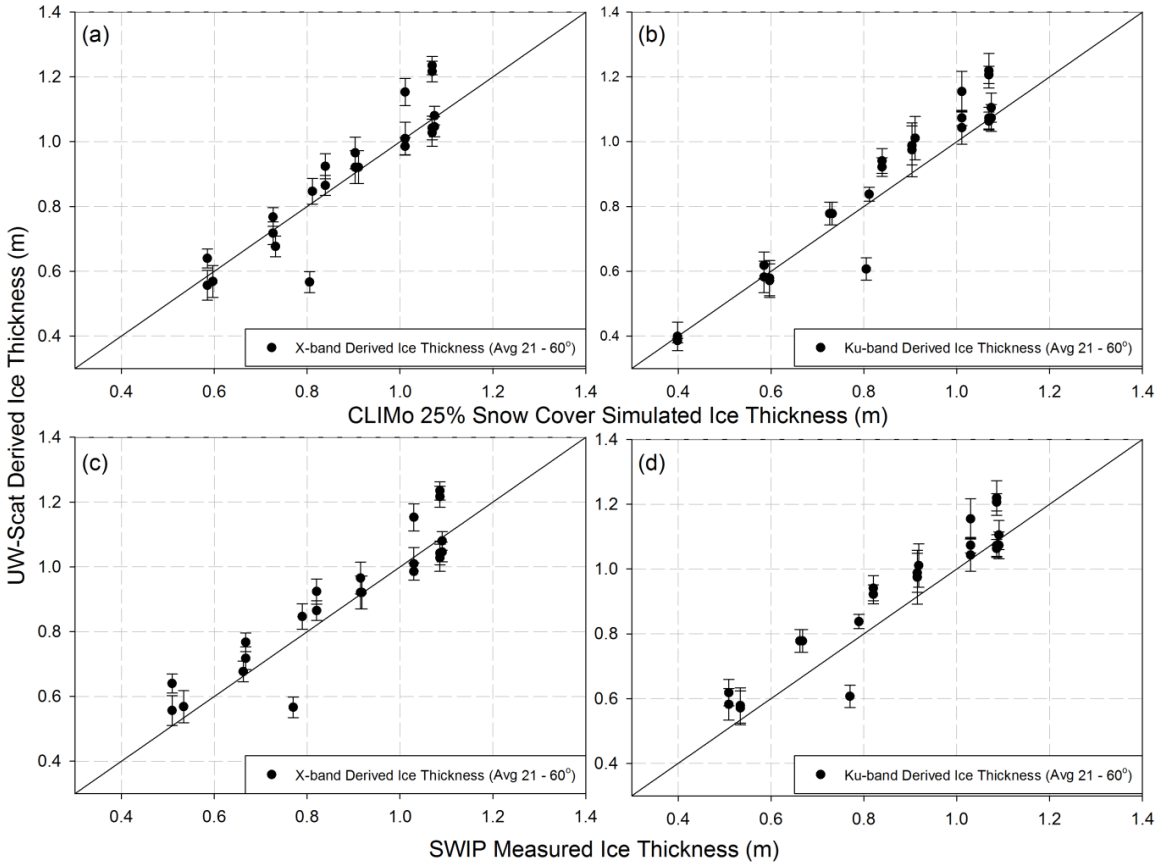

Figure 5-12: UW-Scat derived ice thickness at X- (a, c) and Ku-band (b, d) relative to CLIMo 25% snow depth simulation (a, b) and SWIP observations (c, d). Error bars are the standard deviation of derived ice thicknesses.

Table 5-4: X- and Ku-band derived ice thickness RMSE, MBE and R^2 relative to SWIP and CLIMo simulations using 0, 25, 30, and 100% snow depth scenarios. R^2 are not reported for CLIMo simulations because the statistical measure requires independent measurement, whereas CLIMo and UW-Scat derived ice thicknesses are dependent on external factors. All R^2 statistics are significant with p-values less than 0.001.

X-band

	n	R^2	RMSE (m)	MBE (m)
Measured Ice Thickness	22	0.955	0.053	0.050
SWIP Ice Thickness	22	0.865	0.082	-0.042
CLIMo 0% Snow depth	22	n/a	0.303	0.278
CLIMo 25% Snow depth	22	n/a	0.082	-0.013
CLIMo 30% Snow depth	22	n/a	0.107	-0.054
CLIMo 100% Snow depth	22	n/a	0.196	-0.150

Ku-band

	n	R^2	RMSE (m)	MBE (m)
Measured Ice Thickness	26	0.964	0.045	0.047
SWIP Ice Thickness	24	0.877	0.088	-0.087
CLIMo 0% Snow depth	26	n/a	0.258	0.243
CLIMo 25% Snow depth	26	n/a	0.079	-0.035
CLIMo 30% Snow depth	26	n/a	0.112	-0.076
CLIMo 100% Snow depth	26	n/a	0.211	-0.113

5.5 Discussion and Conclusion

There is very strong agreement between the in-situ measured and UW-Scat derived ice thicknesses at both X- and Ku-bands to within an RMSE of 0.053 and 0.045 m for X- and Ku-band, respectively. However, Ku-band derived ice thicknesses slightly better than X-band and produced superior R^2, RMSE and MBE, and was also capable of resolving thinner ice (0.4 m). Ku-band likely derives ice thickness with a greater degree of accuracy as a result of the shorter wavelength (17.4mm) compared to that of X-band (31mm) incident upon potential scatterers at or near the snow-ice and ice-water interface. The shorter wavelength may result in increased interaction with initial

tubular bubble formation near the ice/water interface, as well as the snowpack overlying the ice. Several studies have identified the sensitivity of Ku-band to terrestrial SWE variability (Yueh et al., 2009; King et al., 2013). Scatter caused by the snowpack at Ku-band would serve to increase the accuracy of the snow-ice interface target range, while remaining transparent at X-band.

CLIMo simulations using a snow depth scenario of 25% of that observed at the Churchill weather station produced ice thickness values to within an RMSE and MBE of 0.067 and -0.042 m compared to in-situ measurements with similarly low RMSE of 0.067 and 0.070 m and MBE of -0.025 and -0.048 for X- and Ku-band derived ice thicknesses, respectively. While local snow depth variability could not be ascertained with snow depth from point measurement, CLIMo outputs could be improved with increasingly accurate snow depth information (i.e. daily snow depth with evolving density or mass information). The use of fractional snow depth scenarios (0-100%) compared to terrestrial rather than on-ice snow introduces error into model outputs as snow density on the lake was also assumed.

This study extended laboratory analysis completed by Leconte et al., (2009) indicating that FMCWs with limited bandwidths are able to derive ice thickness for freshwater ice at non-normal incidence angles. UW-Scat X- and Ku-band FMCWs demonstrate the capability of off-nadir ground-based scatterometers to derive ice thickness values using multiple incidence angles over a range of 21 – 60° to within RMSE values of 0.053 and 0.088m for X- and Ku-bands, respectively when compared to in-situ measurements completed adjacent to the scatterometer footprint. UW-Scat-derived ice thicknesses also agreed with ice thickness simulations produced using a one-dimensional thermodynamic ice model (CLIMo) that was forced using meteorological inputs and snow depth from shoreline automated weather station (r = 0.927, RMSE = 0.045 m). The thinnest ice that was able to be resolved by UW-Scat was 0.54 and 0.39 m using X- and Ku-band, respectively. Multiple peaks within the scatterometer range able to be resolved for thinner ice, which is likely the result of increased sensitivity to smaller features near the ice-water interface due to the shorter incident wavelength. The sensitivity of deep snowpack overlying bubbled freshwater lake ice has not yet been evaluated using UW-Scat, and requires further observation. Additionally, the shape and variability in the range profiles observed at all sites require additional investigation to further understand the scattering response of physical parameters within the lake ice system.

5.6 Acknowledgements

This research was made possible with financial support from the European Space Agency (ESTEC Contracts No. 4000103590/11/NL/FF/fk and 4000106960/12/NL/BJ/lf) and the Natural Sciences and Engineering Research Council of Canada (NSERC) to C. Duguay, and G. Gunn. Logistics for field data collection was provided by the Churchill Northern Studies Centre. The authors would like to thank all those that assisted in field data collection, notably A. Silis, S. Howell, K. Kang, J. Oldham, and N. Svacina. UW-Scat was developed and manufactured by J. Mead at ProSensing, Inc. with funding by grants from the Canadian Foundation for Innovation and the Ontario Ministry of Research and Innovation to C. Duguay and R. Kelly.

Chapter 6

Examining Scattering Mechanisms within Bubbled Freshwater Lake Ice using a Time-Series of RADARSAT-2 (C-band) and UW-Scat (X-, Ku-band) Polarimetric Observations

6.1 Introduction

Lakes comprise 2% of globally available freshwater, and play a significant role in the biological, chemical and physical processes in the cold-regions water cycle (Brown and Duguay, 2010). The majority of lakes are located in the Northern hemisphere and comprise up to 40% of the landscape. The presence of lakes influences surface-atmosphere energy exchanges which modifies the surface radiative properties, affecting local and regional climate through thermal moderation (Rouse et al., 2008). Knowledge of the surface and thermal state of lakes is useful in numerical weather prediction or regional climate models for regions where lakes comprise a large portion of the landscape (Pour et al., 2014). Additionally, Arctic and sub-Arctic freshwater lake ice can be used as an indicator for change in climate, as Arctic regions have exhibited increased amplified warming compared to lower latitudes (Overland et al., 2014).

The number of manual lake ice monitoring stations within the Canadian Ice Database has dropped significantly since the late 1990s (Duguay et al., 2006). Existing stations are restricted to populated regions and accessible coastal areas, missing remote areas of the Arctic. Recent studies have indicated that the use of satellite microwave remote sensing can provide lake ice parameter observation including lake ice phenology (Howell et al., 2009), ice thickness (Jeffries et al., 1996; Duguay and Lafleur, 2003; Kang et al., 2010 and areas that are frozen to bed (Sellmann et al., 1975; Elachi et al., 1976; Weeks et al., 1981; Jeffries et al., 1994; Surdu et al., 2014). The use of active microwave has been identified as most suitable for the observation of lake ice in the Arctic as a result of its high spatial resolution compared to that of passive microwave sensors on the order of metres versus kilometers. Furthermore, microwave wavelengths are capable of penetrating through cloud and are independent of incoming solar radiation.

Recent developments in active microwave synthetic aperture radar (SAR) technology with systems like RADARSAT-2 or TerraSAR-X permit the use of quad-polarized acquisitions (VV, HH, HV, VH), phase information and the observation of the target scattering matrix that allow for the extraction of the contribution of scattering components within each ground pixel (Lee and Pottier,

2009). Earlier studies have attributed backscatter observed at the sensor from lake ice to be the result of double-bounce caused by single interaction of the signal with tubular bubbles within the ice volume and reflection off the high dielectric contrast at the ice-water interface (Elachi et al., 1976; Leconte and Klassen, 1991; Duguay et al., 2002). Single-acquisition L-band polarimetric decomposition results from (Engram et al., 2012; Engram et al., 2013) present polarimetric decomposition of the scattering matrix from large-scale oblate methane ebullition. Engram et al. (2012; 2013) indicate that surface bounce is the dominant scattering mechanism in several lakes on the Alaskan Coastal Plain and Northern Seward Peninsula, hypothesized to be influenced by surface roughness at the ice-water interface.

This paper presents a time-series of in-situ ground based X- and Ku-band observations collected during the 2009-2010 winter using a sled-borne scatterometer (UW-Scat) temporally coincident to spaceborne C-band RADARSAT-2 quad-polarized acquisitions to assess the scattering mechanism in tubular bubbled freshwater ice on Malcolm Ramsay Lake (near Churchill, Manitoba). Section 6.5 presents phase and backscatter observations for interaction near the snow-ice and ice-water interface observed using UW-Scat at four static sites that are related to in-situ snow and ice observations conducted adjacent to the scatterometer footprint. UW-Scat observations are supplemented by co-polarized phase difference observations using RADARSAT-2. Additionally, a time series of dominant scattering mechanisms is extracted using the Yamaguchi three-component polarimetric decomposition (Yamaguchi et al., 2006). This study presents the first time series analysis of polarimetric decompositions of freshwater lake ice using RADARSAT-2 for the purpose of examining the classic double-bounce scatter hypothesis in bubbled freshwater lake ice.

6.2 Background

Backscatter from lakes is dependent on a) the difference in permittivity properties of the media in the sensor field of view, and b) microwave interaction with scattering centers at media interfaces or within the snow or ice volume. In the case of lake ice, the sensor field of view observes a combination of water, freshwater ice, and snow (H_2O in liquid and solid states), and the interfaces between them. The complex relative permittivity of a medium (ε^*) is given by

$$\varepsilon^* = \varepsilon' + j\varepsilon'' \tag{6.1}$$

where ε' is real and represents the dielectric constant and ε'' is the dielectric loss, with j denoting that ε'' is the imaginary component. The relative permittivity of pure liquid water varies across the microwave region of the electromagnetic spectrum due to dependencies on temperature and

frequency, associated with Debye style dispersion (Ulaby et al., 1986). Therefore, the dielectric constant (ε') of pure liquid water at 0° C is ~90, ~40, and ~20, for C-, X, and Ku-bands respectively, with a high loss factor of approximately ε''= 36 across the C- to Ku-band range (Meissner and Wentz, 2004). Conversely, the highly-bonded molecular structure of solid-state H_2O results in a low-loss medium, where ε' has experimentally measured values of ε' =3.17 with negligible ε'' of 0.00065, and is independent of frequency and temperature across the microwave range (Lamb, 1946; Cumming, 1952).

The contrast in permittivity of water and ice influences the amount of radiation reflected (R) or transmitted (Γ) across the boundary layer, governed by Fresnel equations in (6.2 – 6.5), assuming the interface is smooth with respect to the incident wavelength. Transmission across the air-snow and snow-ice interface is quite high in both parallel and perpendicular polarizations, with ice being a low-loss medium. At the ice-water interface, the mismatch in dielectrics results in near-specular reflection.

$$R_{\perp} = \frac{\varepsilon_2^* cos\theta_1 - \varepsilon_1^* cos\theta_2}{\varepsilon_2^* cos\theta_1 + \varepsilon_1^* cos\theta_2} \tag{6.2}$$

$$R_{\parallel} = \frac{\varepsilon_1^* cos\theta_1 - \varepsilon_2^* cos\theta_2}{\varepsilon_1^* cos\theta_1 + \varepsilon_2^* cos\theta_2} \tag{6.3}$$

$$\Gamma = (1 - |R|) \tag{6.4}$$

where ε is the relative permittivity and θ is the incidence angle of the first ($_1$) and second ($_2$) medium within the propagation path of electromagnetic radiation.

6.2.1 Scattering Sources from Snow-Covered Lake Ice

The magnitude of the signal scattered back to the sensor from the surface is proportional to the surface roughness which is quantified by the root mean square (RMS) of height deviations from the surface mean (Woodhouse, 2006). As height deviations approach the size of the incident wavelength, the surface scatter becomes increasingly diffuse (incoherent), elevating backscatter observed at the sensor. Backscatter caused by surface roughness becomes pronounced when height deviations at the surface are greater than $\frac{\lambda}{32 \cos \theta_i}$, known as the Fraunhoffer criterion.

Gases are expelled into the water column during the ice formation process as ice growth responds to the negative heat deficit in the air overlying the lake. If the water column becomes super-saturated with dissolved gases, tubular/teardrop-like bubbles are incorporated into the ice volume parallel to the direction of congelation ice growth. The size and density of these bubbles are

dependent on gas concentration and ice growth rate (Bari and Hallet, 1974; Yoshimura et al., 2008). Several studies have identified tubular bubbles as the source of increased coherent backscatter over freshwater ice during the observation of single and winter time series of side-looking aperture radar (SLAR) (Elachi et al., 1976; Weeks et al., 1981) and synthetic aperture radar (SAR) (Kozlenko and Jeffries, 2000; Duguay et al., 2002; Surdu et al., 2014) observations. Recently, it has been suggested that the diameter and contrast in dielectrics presented by tubular bubbles in the ice volume is insufficient to induce a strong double-bounce mechanism, citing that the layer containing tubular bubbles is an anisotropic homogenous medium with modified permittivity parameters, through the effective medium theory (Atwood et al., *in press*). Instead it is proposed that backscatter is single bounce from the ice/water interface.

High-density spherical bubbles are occasionally observed in the volume of surface layers; the result of the formation of superimposed ice which is the result of a) ice nucleated during a snowfall on calm or turbulent water ("grey ice") or b) the refreezing of previously flooded surface snowpack through cracks In the ice, or from the shoreline when ice is depressed below the hydrostatic water line ("white ice") (Michel and Ramseier, 1971). The resultant ice types with spherical bubble inclusions of 0.5 – 1mm are identified as a source of depolarizing volume scatter (Nolan et al., 2002, Leconte et al., 2009).

Upon freezing to bed, the contrast in permittivity at the ice-water interface is reduced as the free-water is replaced by the ground medium with a much lower dielectric constant of $\varepsilon' = \sim 8.3$ (Shi and Dozier, 2000). The lower contrast in permittivity allows for increased transmission into the ground medium and ultimately a drop in backscatter at the sensor (Duguay et al., 2002; Duguay and Lafleur, 2003; Brown et al., 2010; Grunblatt and Atwood, 2013). An idealized scenario detailing the potential scattering mechanisms in bubbled freshwater lake ice is provided in Figure 6-1.

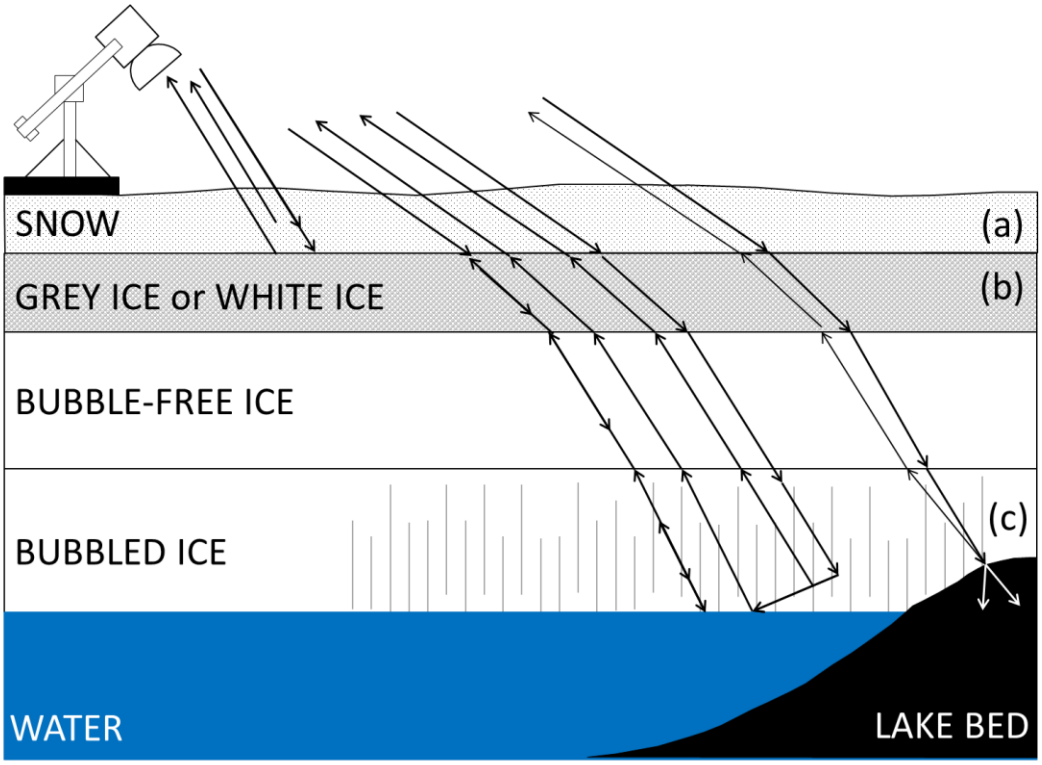

Figure 6-1: Idealized scattering mechanisms for floating and grounded bubbled freshwater lake ice. Potential scattering sources are (a) the overlying snowpack (volume scatter), (b) microbubbles within the superimposed surface "grey" or "white" ice (volume scatter), or (c) scatter off the ice-water interface or forward scatter off the tubular bubbles within the ice volume near the ice-water interface (surface roughness or double-bounce) (modified from Duguay et al., 2002).

6.2.2 Polarimetric Decomposition

There are two main categories of polarimetric decomposition; Coherent and Incoherent Target Decompositions. Coherent decompositions express the measured scattering matrix $[S]$ as a combination of polarized scattered waves from coherent targets, providing first-order estimates of the single-bounce, double-bounce and volume scatter mechanisms in a pixel (Lee and Pottier, 2009). Coherent decompositions are employed to study coherent targets within an observed pixel, with decompositions contributed by Pauli, Krogager, Cameron and Touzi (Krogager, 1990; Cameron et al., 1996; Rousi and Charbonneau, 2002). However, coherent decomposition algorithms ignore the noisy speckle typified by single look complex (SLC) SAR acquisitions, which can modify and otherwise

distort the physical properties of the target. Additionally, the use of coherent target decomposition is advantageous for the analysis of pure targets (i.e. man-made objects) of which the scattering response can be completely expressed through the measured scattering matrix $[S]$. Otherwise, the decomposition analysis of distributed scatterers must be conducted using incoherent decompositions (Lee and Pottier, 2009).

Incoherent polarimetric decompositions statistically characterize the complex scattering behaviour of naturally distributed targets through the use of the covariance or coherency matrix. The presence of additive (system) and multiplicative (speckle) noise inherent in SAR acquisitions is reduced by observing second order polarimetric representations represented by the 3 x 3 Hermitian average covariance $\langle[C]\rangle$ or coherency $\langle[T]\rangle$ matrices, which represent equivalent polarimetric information (An et al., 2010).

$$[T] = \begin{pmatrix} |S_{HH} + S_{VV}|^2 & \langle (S_{HH} + S_{VV})(S_{HH} - S_{VV})^* \rangle & 2\langle (S_{HH} + S_{VV}) S_{HV}^* \rangle \\ \langle (S_{HH} - S_{VV})(S_{HH} + S_{VV})^* \rangle & |S_{HH} - S_{VV}|^2 & 2\langle (S_{HH} - S_{VV}) S_{HV}^* \rangle \\ 2\langle S_{HV}(S_{HH} + S_{VV})^* \rangle & \sqrt{2} S_{VV} S_{HV}^* & 4\langle |S_{HV}|^2 \rangle \end{pmatrix} \quad (6.5)$$

where the superscript * represents the conjugate. The Freeman and Durden decomposition (41) models the $\langle[T]\rangle$ matrix to be composed of three scattering mechanisms: surface ($[T_{surface}]$), double-bounce$[T_{double}]$, and volume scatter ($[T_{volume}]$

$$[T] = P_s[T_{surface}] + P_d[T_{double}] + P_v[T_{volume}] \quad (6.6)$$

where P_s, P_d, andP_v are the power of each scattering component within the total power returned to the sensor (Touzi and Charbonneau, 2002). The surface component ($T_{surface}$) is modeled by a first-order Bragg scattering surface with zero depolarization, and in the case of smooth surfaces, negligible cross-polarization (Cloude, 2010). The double-bounce component (T_{double}) is modeled as a multiple scattering interaction from a dihedral corner reflector of surfaces with differing permittivity properties, whereby incident radiation undergoes Fresnel reflection at both horizontal and vertical interfaces. The volume scattering component (T_{volume}) is modeled as a cloud of dipole scatterers that utilizes a probability density function that prescribes the dipole orientation. The Freeman and Durden decomposition (Cloude, 2010) is extended by Yamaguchi et al. (2006) with an additional helix scattering component that identifies complex man-made urban targets (developed by Krogager and Freeman (1994)) and further modification of the orientation angle distribution of dipoles within the volume scattering component. In situations where the scene is composed of natural distributed targets, the helix component is negligible, and the Yamaguchi decomposition reverts to 3-component. The

resultant Freeman and Durden and Yamaguchi three-component decompositions yield similar results, therefore only the results from the Yamaguchi decomposition are presented below.

Few studies have conducted polarimetric decomposition for freshwater ice. Using a time series of RADARSAT-2 acquisitions under Pauli decomposition, (Van der Sanden and Drouin, 2011) observed the double-bounce component to produce the highest coefficient of determination (R^2) of many polarimetric parameters with river ice types, but did not report the associated power parameters. Conversely, Engram et al. (2012) and Engram et al. (2013) observed a positive correlation between L-band PALSAR surface-bounce component of the coherency matrix ($T11$) and density of large (0.01 – 1 m) methane ebullition bubbles for ice covered lakes in the Alaskan Coastal Plain (ACP) and the North Seward Peninsula (NSP). Values of the surface roughness component were the highest reported (-12 and -9 dB) compared to double-bounce (-20 and -17 dB) and volume scatter (-24 and -21 dB), for the ACP and NSP, respectively (Engram et al., 2012). Additionally, a drop in the surface bounce component was reported upon the lake freezing to bed (removing the high dielectric-contrast ice-water interface) (Engram et al., 2013). The increase in the surface bounce component relative to bubble density was inferred to be related to the modification ice surface roughness with the incorporation of bubbles at the ice-water interface.

6.3 Study Site

The experimental site for this study is Malcolm Ramsay Lake (formerly Lake 58), situated approximately 20 km east of Churchill, Manitoba (58.7221°N, 93.7845°W) in the Hudson Bay Lowlands region (Figure 6-2). The lake covers an area of approximately 2 km^2, with the lake bed comprised of patches of organics, sediment and rocks, and mean and maximum depth are 2.4 and 3.2m, respectively (Duguay and Lafleur, 2003). The region surrounding Malcolm Ramsay is located in the juncture of three ecological zones: tundra, tundra-boreal transition and boreal forest, which run parallel east-west along the coast (Scott et al., 1987). The region is relatively flat with a relatively high lake fraction (32%), with relief features the result of glacial deposits (Lafleur et al., 1997).

The annual mean temperature within the 1981-2010 climate average recorded at the Churchill airport weather station is -6.9 °C, with below-freezing monthly averages from October to May. The average temperature during the observation period of 1/10/2009 to 1/5/2010 was -11.7 °C, sufficient to maintain a dry snowpack or ice surface for the duration of radar acquisitions. The observation period exhibited warmer monthly averages compared to the 1981-2010 climate normal, an average of 4.7° C. Churchill, Manitoba and by extension, Malcolm Ramsay lake is situated on the south-western

shoreline of Hudson Bay, its situation resulting in sustained average wind speeds of 15.4 km/h during the observation period, influencing snowpack and ice development.

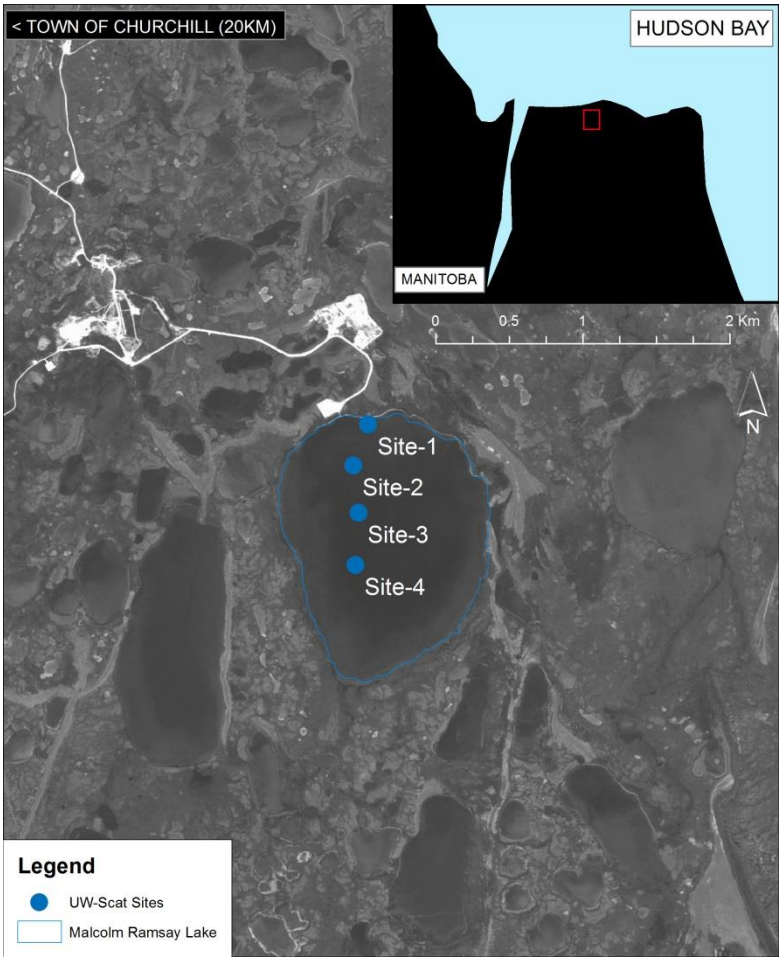

Figure 6-2: UW-Scat static observation sites on Malcolm Ramsay Lake, near Churchill, Manitoba, Canada.

6.4 Lake Ice Properties and Radar Observations

6.4.1 In-situ Snow and Ice Properties

In-situ snow depth, density and ice thickness observations were conducted along a 100 m transect adjacent to the fixed scatterometer footprint at 0° azimuth for four sites on Malcolm Ramsay Lake (Figure 6-2) from 15/11/2009 to 18/3/2010. Snow depth was measured every 0.5 m along the transect using a SnowHydro© Magnaprobe (Sturm and Holgrem, 1999). Ice thickness and surface types were measured every 25 m (Figure 6-3). Ice cores were extracted from within the scatterometer

footprint at the end of the observation period (4/4/2010) using an auger and ice saw. The depth of the bubbled layer shown in Figure 6-3 was recorded from the ice core, allowing for the inference of the date of bubble inclusions into the ice from prior measured ice thicknesses. A five meter transect of ten ice thickness measurements at the rear of the UW-Scat footprint perpendicular to the 0° azimuth of UW-Scat was also conducted at the end of the observation period at Sites 2 and 4 to obtain a rough estimate of large-scale surface roughness at the ice-water interface.

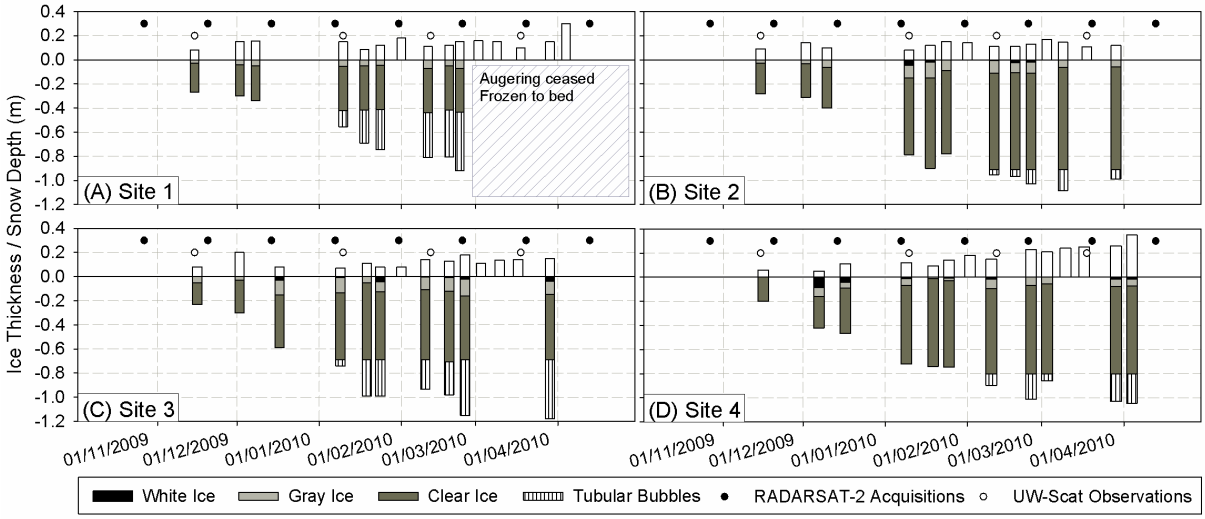

Figure 6-3: In-situ snow and ice properties for Sites 1 – 4 (A – D). Ice stratigraphy is derived from ice cores extracted at the end of the UW-Scat observation period (4/4/2010). Ice thickness values are averaged from measurements along the 100 m transect.

Traditional snow pits were also conducted adjacent to the scatterometer footprint within a "pit farm", which was located at the start of the 100 m transect, allowing for scatterometer observation of the natural variability of the lake ice system. Snow pit measurements were conducted according to (Fierz et al., 2009) and included snow stratigraphy, grain type, grain size, snow density, hardness and temperature profiles, with measurement parameters summarized in Table 6-1**.**

Snow and ice properties were observed at Static sites in Figure 6-2 as part of both intensive observation periods (IOPs), which were temporally coincident to UW-Scat observations, and during extended observation periods (EOPs), where information on snow and ice properties was collected to provide context between IOP observations. Additionally, the EOP snow and ice observations were conducted to provide context for RADARSAT-2 overpasses, which were more frequent than UW-Scat observations (Figure 6-3).

Table 6-1: Summary of snow and ice measurements collected in snow pit adjacent to scatterometer footprint

Snow			Ice		
Parameter	**Unit**	**Meas. Device**	**Parameter**	**Unit**	**Meas. Device**
Depth	m	SnowHydro© Magnaprobe (Sturm and Holgrem, 1999)	Thickness	m	10 cm ice auger
Density	kg/m^3	100 cm^3 density cutter/ ESC-30 snow core tube	Surface Types/ Thickness	m	Avalanche Probe
Grain size	mm	Sear grain size card (labelled 1-3 mm)	Layering (Core)	m	Kovaks© Mark II 9 cm Coring system
Hardness	Knife/ Pencil/ Finger/ Fist				
Temp	^0C	Digital Thermometer			

The snow conditions at Site 1 – 4 throughout the season were typified by a high density snow layer comprised of rounded grains (wind slab) (~400 kg/m^3) overlying a lower density snow layer with columnar grains (depth hoar) (~280 kg/m^3) which still maintained its hardness properties. This pattern was consistent across the lake for snowpacks of depths (>0.1 m), which was characteristic of slab-to-hoar snow classification found on tundra lakes exposed to sustained wind (Sturm and Liston, 2003). The deepest and densest snow was observed throughout the season at Site 4, with end-of-season depth and density of 0.18m and 389.22 kg/m^3, respectively.

The long-axis grain size of the depth hoar layers became larger from the beginning to end of the observation period from an average of 1.7 (17/11/2009) to 4 mm (3/3/2010) while the wind slab layer remained relatively consistent, ranging from 0.86 to 1.5 mm. The increase in long-axis grain size of the depth hoar layer is a result of the high thermal gradient within the snowpack. Average end-of-season snow depth across the four static observation sites was approximately 0.17 m, with local deviations in snow depth related to redistribution caused by sustained wind from the NW.

Ice thickness and stratigraphy varied depending on the relative location on Malcolm Ramsay Lake (e.g. proximity to shoreline, bathymetry), with a maximum observed thickness of 1.18 m at Site 3. In-situ observations indicated that Site 1 froze to bed prior to the 2/3/2010 observation when the auger struck bottom (soft sediment); future observations were abandoned. All sites observed exhibited a marked increase in tubular bubble inclusion near the ice-water interface, with an increase in bubble density closer to the ice-water interface dependent on the level of saturation of dissolved gas in the water beneath the ice (Figure 6-3). Observed tubular bubble inclusions typically appeared below a layer of completely clear (congelation) ice as inverted elongated teardrops, whereby the bubble origin was a semi-circle with a minimum and maximum diameter of ~1 mm and 5 mm, respectively. The semi-circle then reduced to a column or "tube" with a diameter of ~0.5mm and total bubble length of 5 mm to 20 mm. Ice-water interface root mean square (RMS) surface roughness was computed with values of 3.39 mm and 4.57 mm at Sites 2 and 4, respectively, using ten ice thickness measurements spaced approximately 1.5 m apart on a 15 m transect at the rear of the scatterometer footprint.

Tubular bubbles near the base of the ice volume became wider up to a diameter 2-3 mm at sites where bubbles were incorporated into the volume earlier in the season (Site 1: ice thickness – 0.44 m) compared to later in the season with diameters of 0.5mm (Site 2, ice thickness = 0.91m). Sites 1 and 3 (A, C in Figure 6-3) exhibit the development of tubular bubble inclusions much earlier than sites 2 and 4 (B, D) and therefore have a thicker bubbled layer, greater bubble density and larger tubular bubble diameters near the ice-water interface.

Surface ice types composed of high density spherical microbubbles (snow, grey ice) were observed at all sites, with minimum and maximum layer thicknesses of 0.05 and 0.11 m at Site 4 and Sites 2 and 3, respectively.

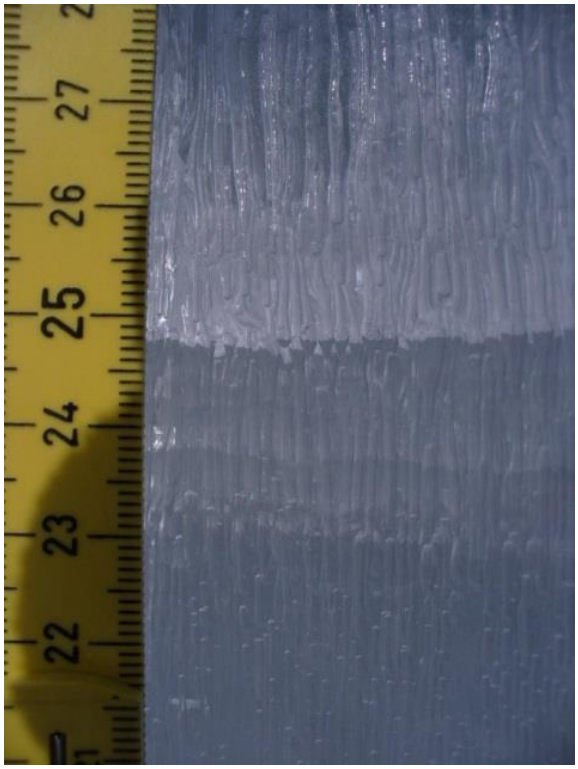

Figure 6-4: High density tubular bubble inclusions between 0.21 and 0.28 m from the bottom of ice core extracted from Site 1. The bubble length is >0.1 m, with a diameter 1.5 mm at terminus decreasing to 1mm at the "tube".

Meteorological observations were collected by an automated weather station on the north shoreline of Malcolm Ramsay Lake, including air temperature and wind speed/direction (shown in Figure 6-5). The observation period was typified by high wind events with sustained speeds of up to ~30 km/h, influencing the development of snow distribution and stratigraphy. Additionally, scatterometer and SAR acquisitions were collected in sub-freezing conditions with the exception of the late winter season (23/4/2010), when the final SAR acquisition observed melting snow and ice conditions.

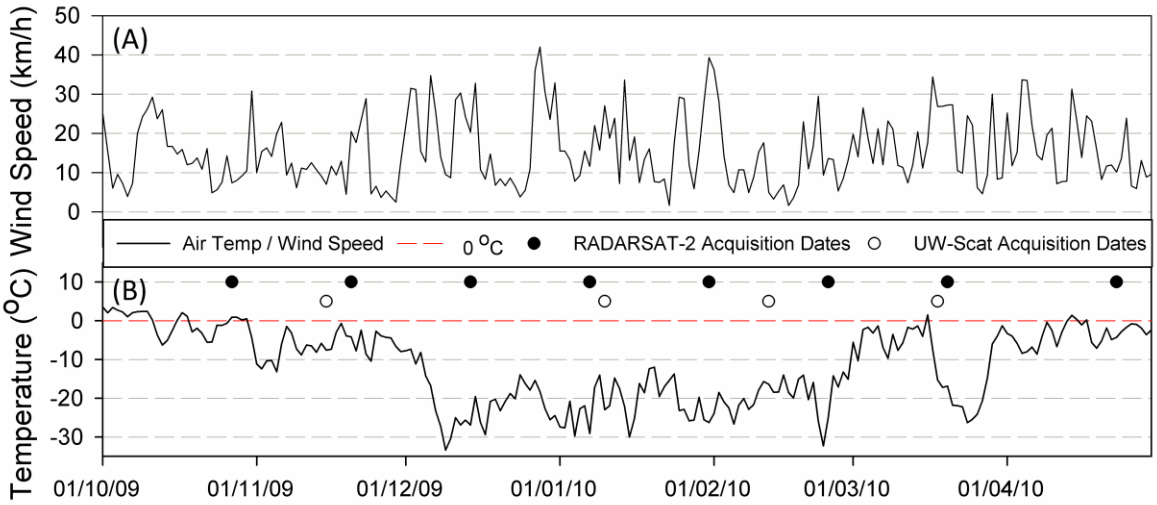

Figure 6-5: Meteorological station wind speed and air temperature collected on the north shoreline of Malcolm Ramsay Lake during the UW-Scat and SAR observation period.

6.5 UW-Scat Observations

Ground based scatterometer observations were collected using UW-Scat, which is comprised of two frequency-modulated continuous wave (FMCW) radars with center frequencies of 9.6 (X-band) and 17.2 GHz (Ku-band) (manufactured by ProSensing Inc.). UW-Scat operates in a switched transmit-receive mode, collecting fully polarimetric observations (VV, HH, VH, HV) and polarimetric parameters (ie. co-polarized phase difference). The FMCW radar head is mounted atop supports which are maneuvered by a Kipp and Zonen 2ap sun tracker across a 60° azimuth sweep at 3° intervals at an incidence angle range of 21 – 60°. Observations collected at incidence angles larger than 60° produced a marked drop in signal to noise ratio (SNR), precluding their incorporation into the study. Additional UW-Scat sensor information is provided in Table 6-2 with an extended sensor description and derivation of the normalized radar cross section (NRCS) provided in (King et al., 2013).

Table 6-2: UW-Scat Sensor Specifications

Parameter	X-band	Ku-band
Output Frequency (GHz)	9.35-9.85	16.95 - 17.45
Transmit Bandwidth (GHz)	0.5	0.5
Transmit Power (dB)	-11.8	-8.0
Range Resolution (m)	0.3	0.3
Cross-polarization isolation (dB)	>30	>30
Sensitivity/Noise Floor (dB m^2/m^2)	-50	-50
Antenna Beam width (°)	4.3	5.6
Transmit/Receive polarizations	VV/VH/HH	VV/VH/HH

6.5.1.1 Peak Return Isolation

Within the UW-Scat processing procedure, raw data blocks are transformed from the time to the range domain using a Fast Fourier Transform. A sky shot is obtained before each scan to estimate the range-dependent transmit leakage, and is coherently subtracted from range bins. Once the leakage removal is completed, the received signal power for all potential range profiles for co- and cross-polarized returns are averaged across the 60° azimuth at incidence angles determined by the initial scan. The procedure allows for manual selection of the peak signal return within range of the scatterometer, which varies according to the complexity of the target's geometry and permittivity properties. UW-Scat range resolution is influenced by the refractive index of the target (n_{ice}) and the bandwidth of the sensor (BW) in Hz (Marshall et al., 2007):

$$r_{min} = \frac{c}{(2n_{ice})(BW)} \tag{6.7}$$

where c is the speed of light (2.998 x 10^8 ms^{-1}). UW-Scat utilizes a BW of 500 MHz, resulting in minimum range resolution (r_{min}) of 0.17m in an ice medium, and 0.3m in air (King et al., 2013). The nominal range resolution implies that scattering interfaces in thick ice (> 0.4 m) will exhibit a discernable difference, delineating the range to the snow-ice and ice-water interface. The range profiles for an early and late winter season UW-Scat observation of Site 3 are shown in Figure 6-6 **Error! Reference source not found.**.

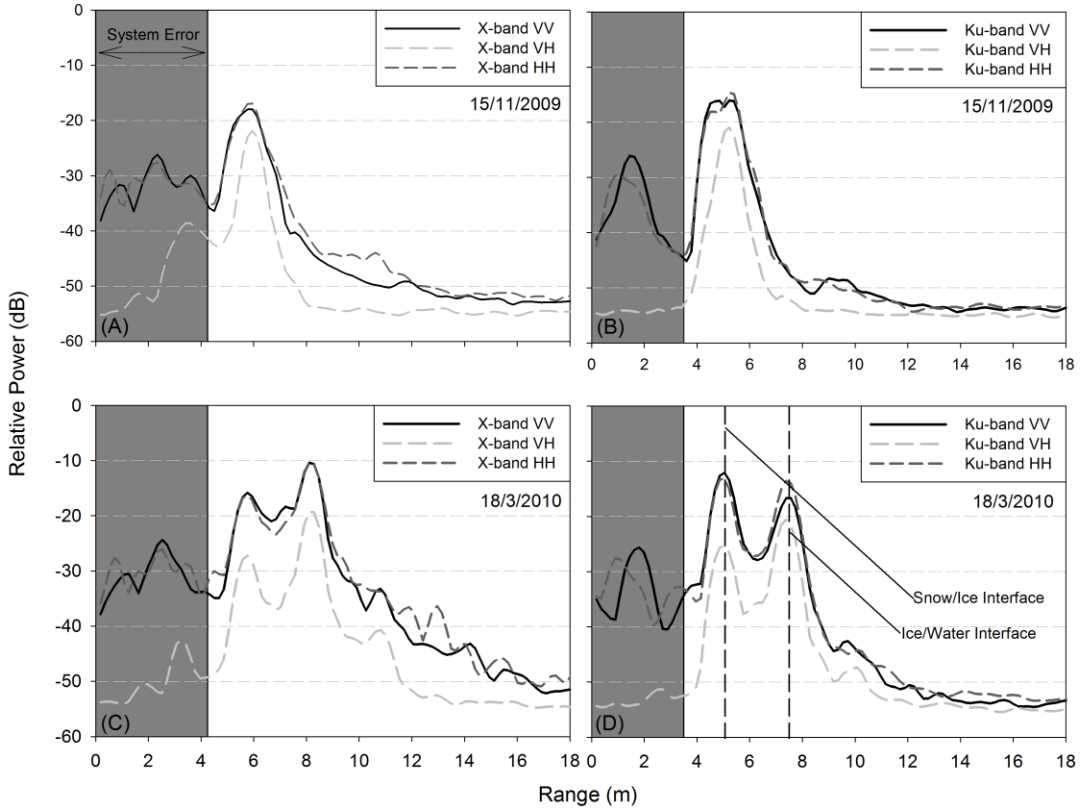

Figure 6-6: Relative power returned to UW-Scat at X- (A, C) and Ku-bands (B, D) for early (A, B) and late (C, D) winter season observations at Site 3 (39° incidence angle). Note that a single defined peak return is noticed in early observations (A, B) where ice thickness is 0.27 m, and two defined peak returns exist in late season observations when ice thickness is 1.18 m.

Snow and freshwater lake ice are relatively transmissive mediums due to the low contrast in permittivity at the air-snow and snow-ice interfaces ($\varepsilon'_{snow} = 1.5$, $\varepsilon'_{ice} = 3.17$) (Cumming, 1952). Microwave radiation incident upon snow and ice mediums therefore are largely transmitted across the interface and through snow and ice mediums to the ice-water interface, where a high contrast in permittivity is observed (ε'_{water} ~40 and ~20 for X- and Ku-bands, respectively). The contrast in permittivity results in high reflection of incident microwave radiation at the ice-water interface, according to Fresnel equations (assuming a flat surface) (Ulaby et al., 1986). The reflection of the signal at the ice-water interface was typically the dominant return in the scatterometer field of view.

The distance to the ice-water interface from the scatterometer increased as ice thickened, allowing for resolution of signal interactions at the ice-snow (P1) and ice-water (P2) interface in the

range profiles of both X- and Ku-band observations. The reflected component of backscatter from Peak 2 are previously hypothesized to be returned to the sensor via double-bounce mechanism caused by the incorporation of tubular bubbles into the ice volume parallel to the direction of ice growth (Jeffries and Morris, 1994; Duguay and Lafleur, 2003). Therefore, the distance (d_s) traveled by the incident microwave pulse within the ice volume (calculated difference in range of Peak 1 and 2 shown in Figure 6-6) should be equivalent to:

$$d_s = \frac{2d_{meas}}{\cos\theta} \tag{6.8}$$

where d_{meas} is the measured in-situ ice thickness in metres and θ is the incidence angle observed after adjusting for the refractive index of ice. Figure 6-7 shows the median peak difference derived from X- and Ku-bands (after adjusting for the speed of light in ice using Snell's law) compared to the calculated slant range using in-situ ice thickness measurements for all scatterometer observations observed on Malcolm Ramsay Lake. The derived two-way distance within the ice was nearly equivalent to in-situ observations, with coefficient of determination (R^2) of 0.79 and 0.90 for X- and Ku-bands, respectively.

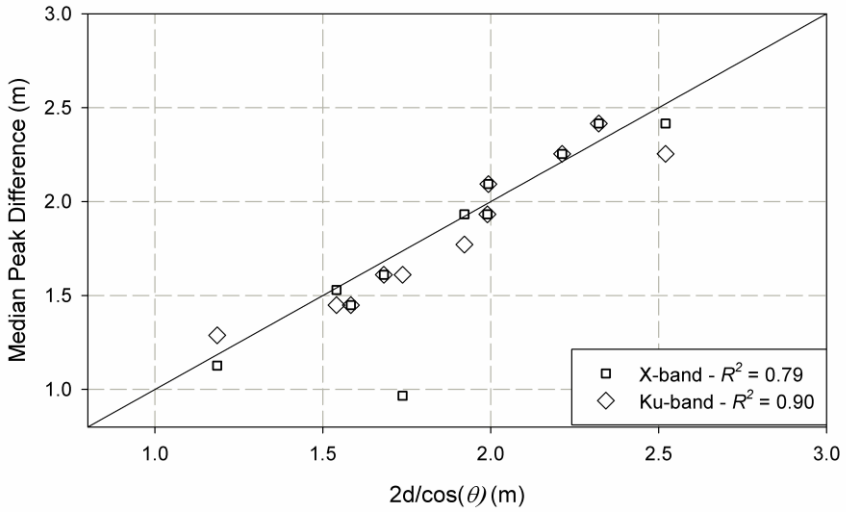

Figure 6-7: Verification of the assumption of interactions at the snow-ice and ice-water interface represented by Peak 1 and 2 in range. The Peak 2 – Peak 1 differences for X- (a) and Ku-band (b) tracked the calculated slant range from the refracted incident angle and measured ice thickness with a near 1:1 relationship.

Upon peak selection, the normalized radar cross section (NRCS) (σ°) is obtained through

$$\sigma^o = \frac{8\ln(2)R_t^2\sigma_c\cos(\phi_{inc})}{\pi R_c^4\theta_{3\,dB}^2}\left(\frac{\acute{P}_r}{\acute{P}_{rc}}\right) \tag{6.9}$$

where R_t is the target range, σ_c is the corner reflector's radar cross section, ϕ_{inc} is the incidence angle, R_c is the corner reflector range, $\theta_{3_{dB}}$ is the observing antenna's one-way half-power beamwidth, and $\acute{P}_r$ and $\acute{P}_{rc}$ are the recorded power for the scene and the corner reflector, respectively (King et al., 2013).

UW-Scat polarimetric parameters such as the co-polarized phase difference ($\Delta\phi_{HHVV}$) are obtained from the average covariance matrix representing the complex scattering amplitudes of a data blocks across an scan's azimuth for each incidence angle, represented by Equation (6.10)**,** with the derivation of $\Delta\phi_{HHVV}$ using Equation (6.11). The diagonal terms of the covariance matrix represent returned power at each of the polarizations and are real numbers, whereas the off-diagonal terms provide phase information and are complex numbers.

$$[C] = \left\langle \begin{bmatrix} S_{VV}S_{VV}^* & S_{VV}S_{VH}^* & S_{VV}S_{HV}^* & S_{VV}S_{HH}^* \\ S_{VH}S_{VV}^* & S_{VH}S_{VH}^* & S_{VH}S_{HV}^* & S_{VH}S_{HHH}^* \\ S_{HV}S_{VV}^* & S_{HV}S_{VH}^* & S_{HV}S_{HV}^* & S_{HV}S_{HH}^* \\ S_{HH}S_{VV}^* & S_{HH}S_{VH}^* & S_{HH}S_{HV}^* & S_{HH}S_{HH}^* \end{bmatrix} \right\rangle \tag{6.10}$$

$$\Delta\phi_{HHVV} = \tan^{-1}\left(\frac{\mathrm{Im}\langle S_{VV}S_{HH}^*\rangle}{\mathrm{Re}\langle S_{VV}S_{HH}^*\rangle}\right) \tag{6.11}$$

6.5.1.2 UW-Scat σ° Observations

Table 6-3 shows the σ° time series of X- and Ku-band for interactions near the snow-ice (Peak 1) and ice-water interface (Peak 2) for all sites observed on Malcolm Ramsay Lake. X and Ku-band Peak 1 σ° is high (-14 to -7 dB) at all sites where high density spherical microbubbles were observed within grey and white surface ice types, consistent with (Gunn et al., 2015). The exception is Site 4, where the lowest co-polarized Peak 1 σ° is observed at both X- and Ku-bands throughout the observation period, coincident with the thinnest recorded average surface ice types on Malcolm Ramsay Lake (0.05 m).

Table 6-3: Average UW-Scat σ° observations across a 39-45° range for X- and Ku-band at Sites 1 – 4. Co- (VV, HH) and cross-polarisation (VH) for interactions at Peak 1 (near snow-ice interface) and Peak 2 (ice-water interface).

		X-band						Ku-band					
		Peak 1			Peak 2			Peak 1			Peak 2		
	Date	VV	HH	VH	VV	HH	VH	VV	HH	VH	VV	HH	VH
Site 1	15/11/09	-13.09	-12.10	-22.60	n/a	n/a	n/a	-14.86	-11.94	-24.98	n/a	n/a	n/a
	10/01/10	-11.73	-12.27	-25.16	-14.21	-9.79	-19.11	-7.31	-8.17	-21.37	-14.42	-12.37	-22.63
	12/02/10	-9.06	-10.73	-25.53	-10.76	-8.84	-20.08	-6.84	-7.71	-19.73	-13.71	-11.62	-21.03
	18/3/10	-9.17	-11.03	-24.01	-19.58	-16.17	-27.34	-7.33	-8.14	-17.55	-26.38	-24.26	-33.06
Site 2	15/11/09	-14.75	-14.51	-22.16	n/a	n/a	n/a	-9.44	-8.08	-21.81	n/a	n/a	n/a
	10/01/10	-9.37	-10.22	-23.35	-12.33	-11.89	-18.29	-8.11	-8.72	-23.54	-16.39	-16.58	-21.60
	12/02/10	-11.27	-12.82	-27.84	-12.54	-14.56	-18.84	-10.18	-11.59	-21.15	-22.88	-20.24	-26.45
	18/3/10	-11.66	-12.61	-26.44	-10.02	-11.11	-18.89	-8.88	-9.03	-21.60	-13.37	-11.12	-17.97
Site 3	15/11/09	-15.76	-15.74	-23.04	n/a	n/a	n/a	-13.20	-10.92	-22.61	n/a	n/a	n/a
	10/01/10	-12.07	-13.86	-29.50	-8.85	-7.65	-17.01	-10.19	-11.34	-25.51	-8.58	-6.07	-18.36
	12/02/10	-10.05	-11.10	-27.42	-7.58	-5.76	-18.59	-10.91	-11.96	-23.75	-8.18	-5.48	-16.22
	18/3/10	-12.27	-12.83	-26.40	-6.91	-6.38	-15.96	-8.79	-9.73	-22.15	-10.27	-8.46	-16.12
Site 4	15/11/09	-18.99	-19.93	-30.61	n/a	n/a	n/a	-16.36	-15.30	-34.44	n/a	n/a	n/a
	10/01/10	-9.39	-10.62	-24.83	-12.93	-13.08	-28.58	-12.84	-12.73	-24.86	-19.88	-18.54	-30.63
	12/02/10	-13.58	-14.72	-28.67	-17.44	-17.44	-31.73	-11.47	-12.01	-22.75	-13.58	-12.07	-27.75
	18/3/10	-14.37	-14.52	-28.01	-10.47	-9.37	-25.42	-9.42	-10.02	-23.24	-9.18	-6.71	-21.45

Additionally, Peak 1 σ° at Ku-band is consistently higher than X-band for all sites, implying that media near the snow-ice interface scatters shorter wavelengths with greater efficiency. Two variables that are identified as potential contributors to σ° near the snow-ice interface are (a) the microbubbles in surface ice types (grey or white ice) and (b) the overlying snowpack (Leconte et al., 2009). Evidence suggests that the overlying snowpack is the cause for higher Ku-band backscatter based on Site 4, where Ku-band backscatter increased throughout the season coincident to increases in snow depth (and consistent surface ice type thicknesses), while X-band remained consistently low. However, correlation analysis of X- and Ku-band (VV, HH, VH) σ° does not provide statistical significance when comparing snow depth, surface ice type thickness or the summation of those variables to a layer of potential interaction near the snow-ice interface (snow depth + surface ice type thickness) due to the σ° variability over a small sample size (n = 12). When viewing each site individually, it is apparent that Ku-band VV σ° increases with increased complexity within the snow and ice volume near the snow-ice interface, consistent with scatterometer measurements of a snow removal experiment in (Gunn et al., 2015).

The longstanding double-bounce hypothesis infers that Peak 2 σ° interacts with the ice volume, specifically the observation of double-bounce caused by tubular bubbles within the ice and the ice-water interface. The sites observed exhibit increased σ° consistent with the double-bounce hypothesis, where high σ° is observed at X- and Ku-band Peak 2 for sites with thick bubbled ice layers (Sites 1, 3), and lower Peak 2 σ° observed at Sites where tubular bubble development occurred later in the season (Sites 2, 4). Additionally, upon freezing to bed X- and Ku-band Peak 2 σ° at Site 1 drops 8.8 and 12.7 dB (VV), and 7.3 and 12.6 dB (HH) respectively, consistent with the removal of the high contrast in permittivity at the ice-water interface.

An ideal dielectric dihedral inducing double-bounce will result in a co-pol phase change of nearly 180 degrees between horizontally and vertically polarized radiation. Similarly, an ideal surface bounce (or odd-bounce) exhibits a nearly 0° phase change between HH and VV (Cloude, 2010). Therefore, the expected HHVV phase difference ($\Delta\phi_{HHVV}$) calculated using Equation 11) for Peaks 1 and 2 for X- and Ku-band observations would be nearly +/- 180 degrees assuming double-bounce interaction near the ice-water interface. Figure 6-8 shows Peak 1 and Peak 2 frequency distribution of $\Delta\phi_{HHVV}$ for scans at an incidence angle range of 21 - 60° for all sites on Malcolm Ramsay Lake at peak ice thickness (18/3/2010). $\Delta\phi_{HHVV}$ values appear to be centered much closer to 0° than +/- 180° with median values of 0.8° and -21° (Peak 1), and -5.7° and -5.2° (Peak 2) at X- and Ku-bands, respectively (n =60). $\Delta\phi_{HHVV}$ centered near 0° indicates that the scattering mechanism near the ice-water interface may be independent of double-bounce scatter, and instead may be caused by scatter at the ice-water interface itself.

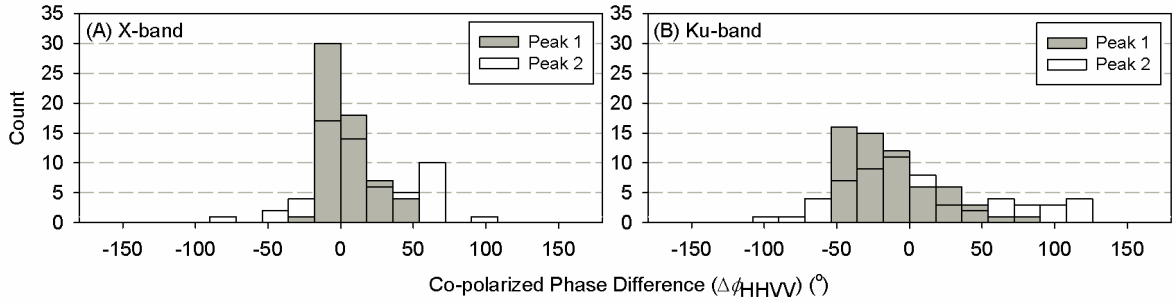

Figure 6-8: Co-polarized phase difference ($\Delta\phi_{HHVV}$) for all sites on Malcolm Ramsay Lake observed on 18/3/2010 (thick ice) for the first and second peak in range of the ground-based X- (A) and Ku-band (B) UW-Scat observations (21 - 60°).

6.5.2 RADARSAT-2 Acquisitions

A time-series of spaceborne C-band (5.4 GHz) SAR acquisitions were obtained using RADARSAT-2 Quad-pol Fine Beam Quad mode at multiple incidence angles (FQ1, FQ11 and FQ18) coincident with in-situ observations, with acquisition dates provided in Table 6-4. All RADARSAT-2 scenes were acquired using the same ascending pass and acquisition time with equivalent incidence angles for all FQ11 scenes. Radiometric and geometric calibration was performed using the Next ESA SAR Toolbox (NEST) version 5.1 with a 3 x 3 multilook, producing ground-range VV, HH, VH and HV σ° with a pixel size of 6.7m.

Co-polarized phase difference and polarimetric decomposition parameters derived using the Three-Component Yamaguchi method (Yamaguchi et al., 2005) were obtained using PolSARPro software (version 4.2). The coherency matrix (T3) was multi-looked (4x2) and exported to be geocoded to UTM zone 15N in MapReady (version 2.3). Once geocoded, the $\Delta\phi_{HHVV}$ was extracted from the multi-looked covariance matrix, and the Yamaguchi three-component polarimetric decomposition was performed, producing a pixel size of 22.4 m.

The geolocation of each image was refined in ArcMap 10.1 using a lateral translation using an affine transformation (no warping) due to the limited resolution of topographic data and satellite orbit information. Backscatter, phase and polarimetric decomposition parameters were extracted for a 50 x 50 m circular buffer of Sites 1 – 4, and on a lake-wide basis by a negative 50 m buffer of the lake shoreline to ensure the omission of shoreline contamination in the analysis.

Table 6-4: RADARSAT-2 Fine Beam Quad Mode acquisitions during 2009-2010 winter season. Average daily air temperature from an automated weather station located on the north shoreline of Malcolm Ramsay Lake is also provided.

Date	Time (UTC)	Ascending/ Descending	Beam Mode	Local Incidence Angle (°)	Average Daily Air Temperature (°C)
27/10/2009	23:49:20	A	FQ11	30.2 - 31.9	0.91
20/11/2009	23:49:21	A	FQ11	30.2 - 31.9	-4.19
14/12/2009	23:49:21	A	FQ11	30.2 - 31.9	-26.91
7/1/2010	23:49:19	A	FQ11	30.2 - 31.9	-29.13
31/1/2010	23:49:19	A	FQ11	30.2 - 31.9	-26.27
21/2/2010	23:36:52	A	FQ1	18.5 - 20.3	-15.93
24/2/2010	23:49:21	A	FQ11	30.2 - 31.9	-24.94
6/3/2010	23:57:41	A	FQ18	37.4 - 38.9	-6.9
20/3/2010	23:49:22	A	FQ11	30.2 - 31.9	-16.89
13/4/2010	23:49:23	A	FQ11	30.2 - 31.9	-0.24

6.5.2.1 RADARSAT-2 Backscatter

RADARSAT-2 σ° for the 50 m buffer at each UW-Scat observation (sites 1 – 4) is provided in Table 6-5, with a lake-wide spatial representation of the end-of-season conditions (20/3/2010) in Figure 6-9 A - C. The general trend of all sites is for VV and HH σ° to be very low in the beginning of the season (approximately -25 dB), and increase incrementally during ice growth to a maximum where σ° plateaus (-13 dB at Site 1). At the end of the observation period, σ° subsequently drops coincident to an increase in snow or ice moisture content when temperatures rise above 0° C (Figure 6-5). The pattern is similar to (Duguay et al., 2002; Jeffries et al., 2005) whereby σ° increases throughout the season, reaching a plateau for thick, bubbled ice prior to dropping upon the beginning of melt. The hypothesized scattering mechanism for a sharp σ° increase is attributed to tubular bubble inclusions. However, in this dataset a sharp σ° increase occurs on 20/11/2009, well before the inclusion of bubbles into the ice volume (10/1/2010 at Sites 1 and 3, 12/2/2010 at Sites 2 and 4). The sharp σ° increase of 5 – 6 dB from 27/10/2009 to 20/11/2009 in both VV and HH polarizations at all sites are coincident to increases in ice thickness of up to 0.3 m, similar to C-band HH σ° increases reported by Leconte et al. (2009) for thin ice (void of tubular bubbles) grown in a laboratory.

SAR σ° observations at Site 1 do not drop when it is deemed frozen to bed by 23/2/2010 (according to in-situ measurements). It is possible that the signal did not drop due to a) the soft

sediment being mixed with water, retaining contrast in permittivity and b) the spatial variability of areas that are frozen to bed or floating within the 50 m buffer that are not captured by the 15 x 20 m footprint of UW-Scat. An anomalous σ° departure is also noticed at Site 4, where VH σ° is much lower than other sites, with differences up to 7 dB. The drop in VH σ° is observed to be part of a larger feature on the lake where σ° observations approach the noise floor (-32.5 dB for Fine Beam Quad-Pol mode) (Figure 6-9 C). The feature persists for the duration of the observation period, indicating that VH σ° is not affected by tubular bubble inclusion. Site 4 exhibits thinner surface ice types than Sites 2 and 3, identifying spherical bubbles in white or grey ice as a potential source of depolarizing volume scatter. Additionally, the absence of thick surface ice type (0.07 m) layers at Site 4 does not result in lower σ° compared to Sites 2 – 3 where thicker surface ice type layers developed (0.11 and 0.15 m).

Table 6-5: Median (dB) and standard deviation (dB) of RADARSAT-2 σ° for pixels within a 50 m circular buffer of UW-Scat static sites on Malcolm Ramsay Lake.

		VV		HH		VH	
	Date	**Med**	**St. Dev**	**Med**	**St. Dev**	**Med**	**St. Dev**
Site 1	27/10/2009	-25.06	2.04	-25.35	2.08	-33.10	3.06
n= 333	20/11/2009	-20.90	2.26	-19.15	2.21	-29.45	2.54
	14/12/2009	-19.17	2.37	-17.94	2.79	-28.04	1.90
	7/1/2010	-18.44	2.95	-18.06	2.36	-26.49	2.36
	31/1/2010	-16.61	2.94	-15.34	2.31	-24.38	2.27
	24/2/2010	-13.65	3.67	-13.80	2.86	-23.73	2.52
	20/3/2010	-13.88	3.18	-13.05	2.24	-22.93	1.64
	23/4/2010	-19.30	2.62	-19.57	2.50	-30.25	2.27
Site 2	27/10/2009	-25.74	1.77	-24.87	1.57	-29.48	1.95
n= 340	20/11/2009	-17.27	2.56	-16.73	2.38	-20.85	2.18
	14/12/2009	-14.50	2.95	-13.92	2.49	-23.18	2.60
	7/1/2010	-13.18	2.38	-14.21	2.13	-22.35	2.56
	31/1/2010	-11.42	3.30	-11.64	2.95	-23.70	2.46
	24/2/2010	-14.58	4.10	-13.67	3.47	-25.13	2.16
	20/3/2010	-10.96	2.69	-10.74	2.42	-28.50	1.97
	23/4/2010	-14.33	2.23	-13.99	2.34	-33.52	1.96
Site 3	27/10/2009	-25.16	2.22	-25.95	1.89	-29.47	2.29
n= 341	20/11/2009	-19.54	2.06	-18.45	2.43	-20.41	1.99
	14/12/2009	-15.86	2.67	-14.51	2.79	-20.95	2.48
	7/1/2010	-13.04	2.71	-12.79	3.32	-21.53	2.63
	31/1/2010	-10.77	3.55	-10.49	2.80	-23.82	2.33
	24/2/2010	-11.33	3.04	-10.76	2.19	-26.09	2.72
	20/3/2010	-9.19	2.26	-9.03	2.33	-29.75	2.13
	23/4/2010	-13.25	2.02	-13.21	2.47	-33.84	2.08
Site 4	27/10/2009	-24.73	2.00	-25.01	1.86	-28.19	2.01
n= 338	20/11/2009	-18.77	3.70	-18.11	3.09	-26.79	2.19
	14/12/2009	-16.12	2.61	-15.92	2.56	-29.33	2.52
	7/1/2010	-14.53	3.19	-14.78	2.62	-29.88	2.20
	31/1/2010	-14.18	1.91	-14.28	2.11	-29.80	2.46
	24/2/2010	-13.30	2.17	-13.42	1.84	-31.29	2.43
	20/3/2010	-11.79	2.14	-11.63	1.86	-31.71	3.61
	23/4/2010	-14.21	2.10	-13.70	1.89	-33.65	1.82

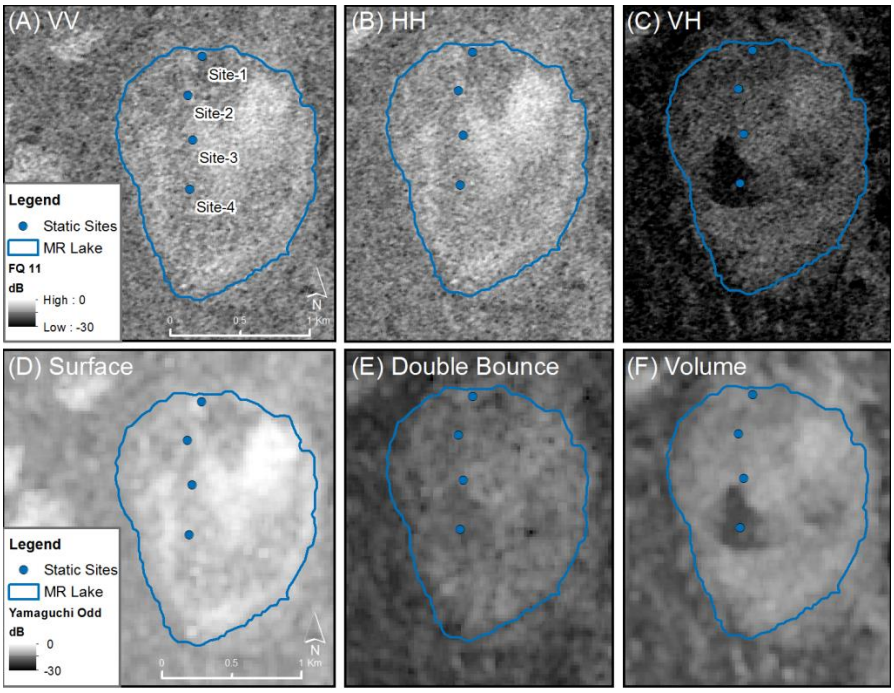

Figure 6-9: RADARSAT-2 σ° of Malcolm Ramsay Lake (VV (A), HH (B) and VH (C)) and Yamaguchi three component decomposition detailing the contribution from surface scatter (D), double-bounce (E) and volume scatter (F) for Malcolm Ramsay lake during peak ice thickness conditions prior to melt (20/3/2010). ***RADARSAT-2 Data and Product © MacDonald, Dettwiler and Associates Ltd. (2010) – All Rights Reserved***

Median co-polarized phase differences for the 50m buffer of Sites 1 – 4 and lake-wide pure-ice pixels indicate a dominant pattern whereby $\Delta\phi_{HHVV}$ is centered at approximately 0° for the majority of observations, with a maximum departure of 25.54° at Site 4 (n = 16) (Table 6-6). When observed at the lake scale, the median $\Delta\phi_{HHVV}$ is centered at 0° with a deviation of +/- 2.75° and has a much larger sample size than the 50m static site buffer (n = 3907). The dependence of $\Delta\phi_{HHVV}$ on incidence angle is also observed using multiple beam modes across an incidence angle range of 19.4° (FQ1), 31.4° (FQ11) and 38.4° (FQ18) acquired within a two week period when ice growth is minimal (0.06m growth at Site 2) (Figure 6-10). The frequency distribution of $\Delta\phi_{HHVV}$ across the incidence angle range is consistently unimodal and centered at approximately 0°, with median $\Delta\phi_{HHVV}$ at FQ1, FQ11 and FQ18 of 7.4°, 0.3°, and 2.98°, respectively.

Table 6-6: Median $\Delta\phi_{HHVV}$ (°) observed using RADARSAT-2 at snow and ice observation sites as well as lake-wide median values for pure-ice pixels within Malcolm Ramsay Lake.

Date	1	2	3	4	Lake-Wide Median
27/10/2009	8.21	-15.03	3.42	25.54	2.66
20/11/2009	-6.47	1.25	1.83	4.11	0.83
14/12/2009	-3.81	-1.15	2.23	0.86	-0.58
7/1/2010	-10.37	-4.88	-3.78	4.23	-2.74
31/1/2010	-1.66	-18.23	9.32	-5.77	-2.15
24/2/2010	-0.74	-2.87	6.32	1.73	0.30
20/3/2010	2.25	-3.92	12.00	2.59	2.71
13/4/2010	-13.09	-1.43	3.19	-1.47	0.88
n	16	16	16	16	3907

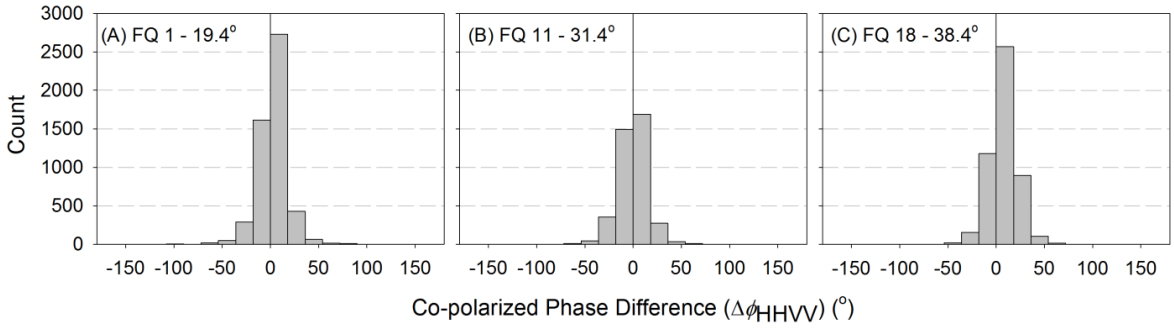

Figure 6-10: Lake-wide $\Delta\phi_{HHVV}$ for late- winter RADARSAT-2 acquisitions across an incidence angle range of 19.4 – 38.4° using FQ1, FQ11 and FQ18 beam modes during a two week period from 21/2/2010 – 6/3/2010.

6.5.2.2 RADARSAT-2 Polarimetric Decomposition

RADARSAT-2 polarimetric decomposition parameters are produced using the Yamaguchi three-component Decomposition. The relative proportion of odd bounce (surface), even bounce (double-bounce) and volume scatter to total σ° are shown in Figure 6-9 (D-F). The median values of the pixels within the 50 m footprint is provided in Table 6-7 in logarithmic scale (dB), with a graphical representation of the range of values at Sites 3 and 4 (those with contrasting snow/ice regimes) in Figure 6-11. Surface bounce is identified as the dominant scattering mechanism contributing to overall σ° across all static sites and is on average 10/14 times greater than the volume

scatter/double-bounce components, respectively. Volume scatter is identified as the second largest σ° source with the exception of Site 4, where low cross-polarized σ° is observed. Double-bounce scattering mechanism is consistently identified as the smallest σ° source, even at Site 3, where dense tubular bubbles were observed to be included into the ice volume as early as 9/1/2010 (according to ice core records). At Site 4, the volume scatter decomposition parameter is the lowest σ° contributor, which is spatially coincident to the thinnest layers of surface ice types containing spherical bubbles (0.05 m) compared to Sites 2 or 3 (0.11 m).

Table 6-7: Time series of median (*n* = 16) Yamaguchi three-Component Decomposition parameters for UW-Scat sites 1-4: Odd (Surface) bounce, Even (Double) bounce, and Volume scatter (represented in log scale (dB)).

	Odd (dB)				Double-bounce (dB)				Volume (dB)			
Site	1	2	3	4	1	2	3	4	1	2	3	4
27/10/2009	-15.33	-23.01	-21.80	-21.46	-22.01	-27.21	-26.48	-26.78	-15.10	-27.21	-27.45	-27.96
20/11/2009	-14.89	-13.36	-13.06	-15.61	-25.77	-25.45	-26.68	-26.78	-22.15	-20.92	-23.28	-21.58
14/12/2009	-10.34	-9.96	-10.02	-11.29	-20.86	-21.52	-21.25	-22.56	-17.57	-17.93	-18.86	-24.38
7/1/2010	-10.67	-9.87	-9.91	-9.59	-19.87	-19.87	-18.48	-20.56	-17.52	-16.46	-16.56	-23.10
31/1/2010	-10.84	-7.14	-5.30	-8.79	-19.32	-17.28	-15.77	-19.79	-16.02	-13.99	-12.51	-21.55
24/2/2010	-8.57	-10.50	-8.93	-7.72	-19.67	-19.00	-18.45	-21.22	-13.33	-15.00	-12.60	-21.84
30/3/2010	-7.06	-7.64	-6.48	-7.40	-16.84	-17.19	-15.73	-18.76	-14.88	-13.64	-13.22	-19.83
23/4/2010	-10.96	-9.14	-8.70	-8.48	-20.27	-21.80	-20.81	-21.46	-17.93	-22.04	-21.43	-20.78

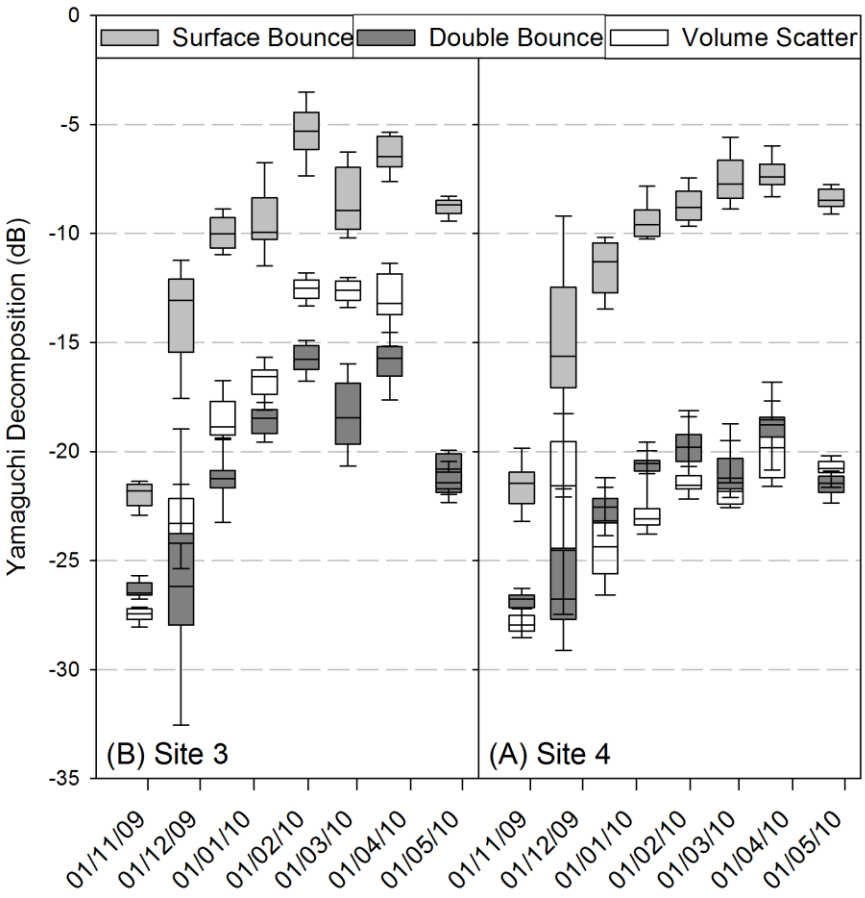

Figure 6-11: Time series and distribution (*n* = 16) of RADARSAT-2-derived Yamaguchi three-component decomposition parameters at Sites 3 and 4. Surface bounce is the dominant component of observed σ°.

The identification of surface bounce as the dominant contributor to backscatter is also prevalent when viewed at the lake-wide scale (Figure 6-12). The RADARSAT σ° increase noticed in Table 6-5 at each Static Site prior to the development of tubular bubbles in the ice volume is corroborated by the polarimetric decomposition, indicating that double-bounce caused by tubular bubble content is not the dominant scattering mechanism, consistent with (Engram et al., 2012; Engram et al., 2013) who used quad-pol L-band to identify relationships between ice-water interfaces that are roughened through methane ebullition. The surface bounce scattering component also increases throughout the season, indicating that roughness at the ice-water interface on Malcolm Ramsay Lake is increasing, returning more of the incident signal to the sensor, consistent with

(Atwood et al., *in press*). When observing RADARSAT-2 σ° at a lake-wide scale it is likely that areas of grounded ice are observed, especially later in the winter season, which would increase σ° variability as the high contrast in permittivity at the ice-water interface is removed. While an increase in standard deviation of returned power is not observed in Table 6-5 on a site by site basis, an increase in σ° variability is noticed in the surface bounce component when observed over the lake wide basis in Figure 6-12.

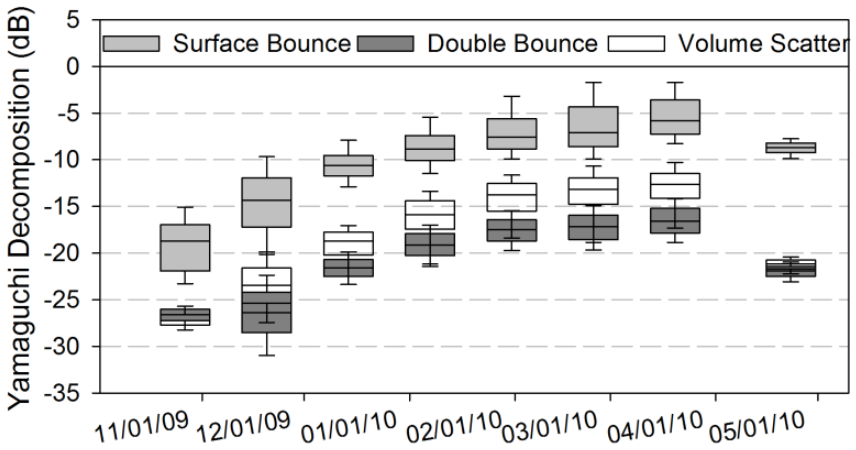

Figure 6-12: Time series and distribution (*n* = 3300) of RADARSAT-2-derived Yamaguchi 3-Component Decomposition parameters at lake-wide scale. Surface bounce is the dominant component of observed σ°, followed by volume scatter.

6.6 Discussion

The combination of UW-Scat/RADARSAT-2 co-polarized phase differences and polarimetric decomposition parameters provide evidence contrary to the hypothesized double-bounce scattering mechanism of (Sellmann et al., 1975; Elachi et al., 1976; Weeks et al., 1981; Jeffries and Morris, 1994; Duguay et al., 2002; Jeffries et al., 2005a). The co-polarized phase difference equalling near-zero degrees for both UW-Scat Peak 2 and RADARSAT-2 observations indicates that it is unlikely that double-bounce scatter is the primary scattering mechanism in lake ice, rather a surface bounce from the ice-water interface. Similarly, increases in the surface bounce component observed in the polarimetric decomposition time-series indicates that the scattering mechanism is caused by increasing roughness at the ice-water interface.

Upon primary investigation using UW-Scat the dominant scattering mechanism appears to be caused by double-bounce from tubular bubbles near the ice-water interface due to the difference in Peak 1 and 2 ranges being equivalent to the range to the snow-ice and ice-water interface. However, the two-way distance for double-bounce is equal to that of single-bounce off of a rough surface at the ice-water interface.

With the evidence provided by co-polarized phase difference and polarimetric decomposition derived from UW-Scat and RADARSAT-2, indicating that surface bounce is the dominant scattering mechanism, the cause of surface roughness at the ice-water interface must be addressed. Ice thickness is modified by the insulating properties of the surface snowpack. Snow redistribution and drifting is prevalent and quite variable on Malcolm Ramsay Lake, likely resulting in large-scale roughness at the ice-water interface. An additional contributing factor to surface roughness could also be the presence of tubular bubbles terminating at the ice-water interface. Observed bubble density increased with ice thickness, with the spherical portion of the tear drop terminus near or at the ice-water interface. The terminus also increases in diameter deeper in the ice volume, with diameters of 1 mm and 5 mm at higher and lower depths, respectively. Additionally, bubbles that have not been sealed within ice after ice has encroached beyond the bubble terminus protrude out the bottom of the ice-water interface, similar to observations conducted by (Inada et al., 2009]. The surface roughness is modified by the bubble protrusion as the high contrast in permittivity is maintained from the ice to the bubble. The bubble protrusion is observed at Site 4, where incomplete bubble inclusions in the ice are visible on the underside of the extracted ice core (Figure 6-13). An increase in density of bubble protrusions of up to 7 mm and more commonly at 4 to 6 mm could enhance the roughness at the ice-water interface, increasing surface bounce scatter throughout the observation period.

Furthermore, there appears to be a slight preference to HH scattering in UW-Scat when observing P2 (interaction near ice-water interface) and RADARSAT-2 acquisitions, however the co-polarization ratio ($\frac{\sigma_{HH}}{\sigma_{VV}}$) is near unity. As roughness increases, the co-polarization ratio will revert to 1, however the dihedral regime exists above 1. The slight preference to HH σ° at C-, X-, and Ku-bands indicates that HH exhibits some sensitivity to vertically oriented media within the ice volume (tubular bubbles), but the σ° intensity component caused by the double-bounce mechanism is orders of magnitude lower than surface bounce.

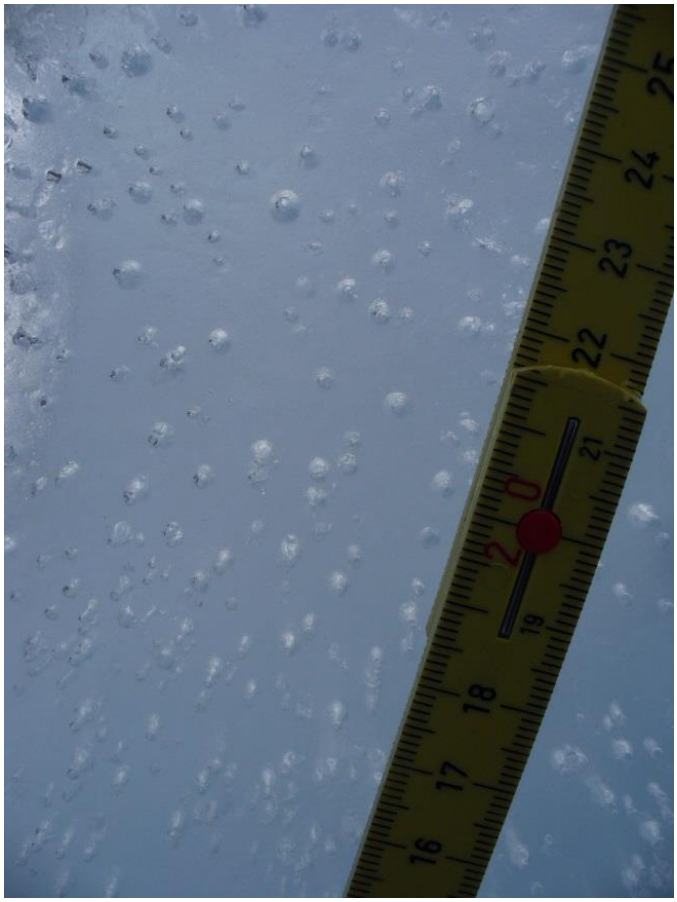

Figure 6-13: Tubular bubble inclusions with terminus breaching the ice-water interface of the underside of an extracted core at Site 4 on Malcolm Ramsay Lake (16/4/2010). Multiple bubble terminii diameters are observed at sizes of 4 to 6 mm.

The observations of this study indicate that the idealized scattering mechanisms in bubbled freshwater ice require updating. Firstly, the dominant return should be related to roughness at the ice-water interface. The mechanism by which the ice-water interface is modified is not discretely known, and is possibly caused by variable insulating properties of snow depth overlying the ice, and/or modification of the ice-water interface by bubble inclusion. The amount of backscatter caused by double-bounce must be reduced in the idealized scattering mechanisms for bubbled lake ice, as is shown by the co-polarized phase difference, polarimetric decomposition and co-polarized ratio. Therefore, an updated version of the idealized scattering mechanisms in lake ice is shown in Figure 6-14, whereby the double-bounce and volume scatter contribution to σ° observed at the sensor is much lower than surface bounce.

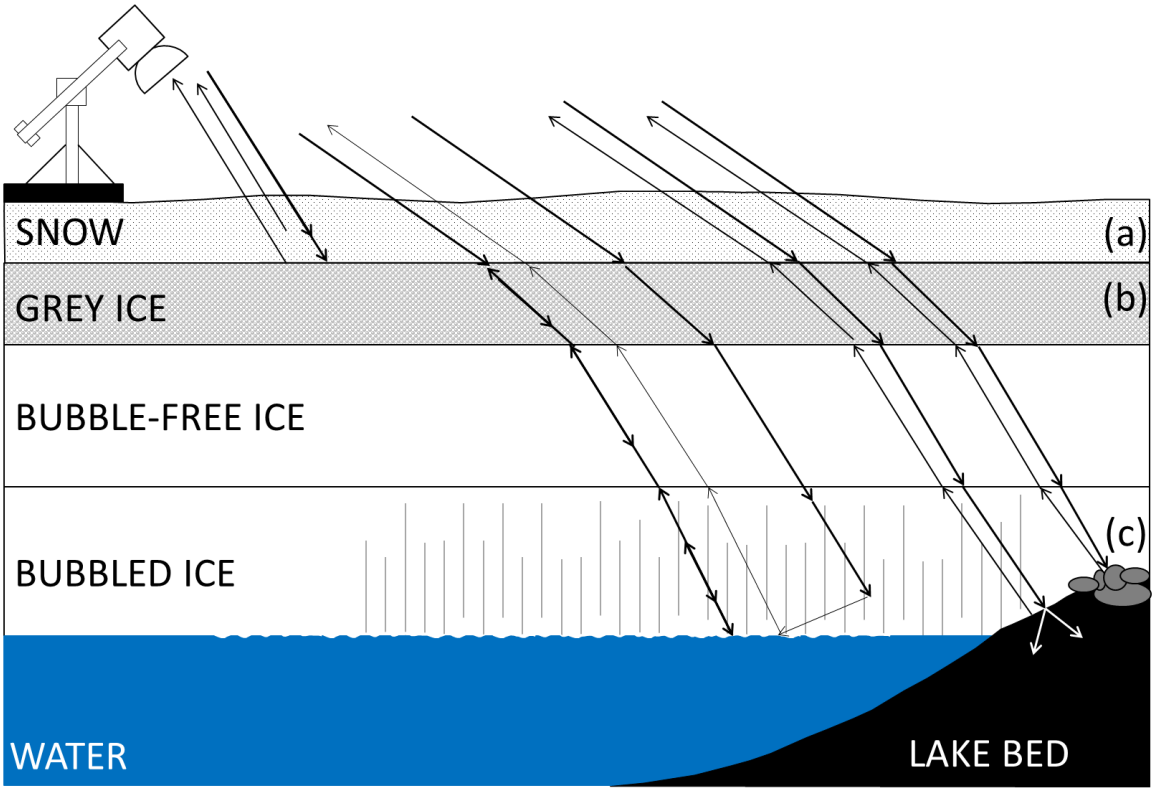

Figure 6-14: Updated contribution of scattering mechanisms to total backscatter as determined by Yamaguchi three-component decomposition. The surface bounce component is the dominant contribution for bubbled freshwater ice. Double-bounce and volume scatter contributions increased throughout the season but were several magnitudes lower than surface bounce.

6.7 Conclusion

The longstanding hypothesis suggesting σ° increases observed over a winter time-series are the result of forward double-bounce scatter caused by tubular bubble inclusions near the ice-water interface was tested using fully polarimetric scatterometer and SAR observations. Observations from the RADARSAT-2 time series indicates that σ° increases were observed well before the inclusion of tubular bubbles into the ice volume, suggesting the existence of an alternate scattering regime.

The phase information from both UW-Scat and RADARSAT-2 indicate that the co-polarized difference is centered at 0 degrees, and when observed on a lake-wide scale using RADARSAT-2 a maximum range of 2.74° is observed. Additionally, Yamaguchi three-component polarimetric decomposition results identified the dominant σ° as single bounce off the ice-water interface. Based on Fresnel reflection equations, the only mechanism that could provide single bounce at the ice-water

interface would be the increase in surface roughness or larger scale orientation of facets at the ice-water interface to produce a confluence of angles that would produce local mirror-like target geometry. However, the terminus of bubbles at the ice-water interface may increase surface roughness for thick ice cover resulting in an increase of the surface bounce component, indicating that σ° increases may still provide a proxy measure for bubbled versus bubble-free clear ice. The minor influence of tubular bubbles on overall σ° in ice is observed as slight HH preferential scattering, which indicates the presence of vertically oriented media.

As a measure of the validity of single bounce due to surface roughness at the ice-water interface, a crude metric of RMS surface roughness was computed using 10 ice thickness measurements within the UW-Scat footprint at two static sites, finding that the surface roughness was above the Fraunhoffer smooth criterion. Further research needs to be performed to provide a better characterization and quantification of the RMS surface roughness and the associated correlation length at the ice-water interface, with a focus on also preserving the orientation and position of bubbles directly beneath the ice to identify its contribution to overall interface roughness.

6.8 Acknowledgements

This research was made possible with financial support from the European Space Agency (ESTEC Contracts No. 4000103590/11/NL/FF/fk and 4000106960/12/NL/BJ/lf) and the Natural Sciences and Engineering Research Council of Canada (NSERC) to C. Duguay, and G. Gunn. Logistics for field data collection was provided by the Churchill Northern Studies Center. The authors would like to thank all those that assisted in field data collection, notably A. Silis, C. Derksen, A. Langlois, K. Kang, J. Oldham, A. Casey, B. Monpetit, and A. Royer. UW-Scat was developed and manufactured by J. Mead at ProSensing Inc. with funding from the Canadian Foundation for Innovation and the Ontario Ministry of Research and Innovation to C. Duguay and R. Kelly.

Chapter 7
General Conclusions

7.1 Overall Summary

The overall objective of this research was to further the understanding of scattering mechanisms for physical components of snow-covered freshwater lake ice within the microwave range of the electromagnetic spectrum. This work is not only a contribution to polarimetric remote sensing of the cryosphere, it also provides implications for retrieval of physical properties within the lake ice system. Furthering the understanding of microwave interaction in the ice, and potential for quantification of the associated lake ice components extends to other fields that are influenced by the presence/absence of ice cover, such as hydrology, biology and climatology. Chapter 1 provided the motivation and objectives of this research, which broadly stems from the decline in manual monitoring stations in remote sub-Arctic and Arctic regions.

Chapters 2 and 3 provided necessary background literature for the physical processes governing ice formation, and relevant radar principles for the remote observation of freshwater ice, respectively. Chapter 2 details the molecular structure of the ice crystal lattice, which has great implications for radar remote sensing. Chapter 3 presents electromagnetic and radar theory, the behaviour of microwaves in media with variable dielectric properties and the quantification metrics of the signal returned to the sensor, including backscatter, co-polarized phase difference and polarimetric decompositions.

The first analysis of a winter time series of UW-Scat X- and Ku-band backscatter observations for snow-covered freshwater lake ice on Malcolm Ramsay Lake was presented in Chapter 4. Additionally, the formulation and preliminary simulations (using in-situ snow and ice measurements) of a lake ice backscatter model using the dense media radiative transfer with quasi-crystalline approximation was presented. The key findings from Chapter 4 revolve mainly around the ability of UW-Scat to observe multiple peaks in range, providing evidence of signal interaction with targets near the ice-snow interface (snowpack, grey or white ice) and the ice-water interface (surface roughness, tubular bubble content). Based on the hypothesis of double-bounce from tubular bubbles presented in the literature from 1975 forward, interaction near the ice-water interface was surmised to be the result of double-bounce interaction.

Chapter 4 presented the isolation of unique scattering mechanisms from three static sites on Malcolm Ramsay Lake. Ku-band exhibited sensitivity to the overlying snowpack when removed from the scatterometer field of view with a backscatter reduction of 5.55, 6.17 and 7.96 dB for VV, HH, and VH for a snowpack of 0.235 m. X-band exhibited negligible backscatter departures with snow removal, which was a function of the longer wavelength penetrating through the snowpack. Sites with increasing complexity at the surface (grey surface ice types) resulted in backscatter increases of approximately 7 dB at X- and Ku-bands. The interaction near the ice-water interface was the dominant peak in range, with backscatter increases of approximately 10 – 12 dB (HH & VV) at X- and Ku-band coincident with the timing of tubular bubble development in the ice column. This interaction demonstrates issues in attempting to isolate backscatter sensitivity to the overlying snowpack, as the complexity of the evolving ice column introduces variable backscatter depending on the status of the bubble development and ice-water interface roughness. The lake ice backscatter model was useful in demonstrating the importance of including bubbles in freshwater ice simulations and the effect of the overlying snowpack into simulations. Using the ice-water interface roughness as a free parameter, the model performed well for snow covered ice with minimal surface ice types, with RMSE of 1.65 (VV) and 1.48 (VV) for X- and Ku-band, respectively.

Using the knowledge that multiple peaks in range related to interactions near the ice-snow and ice-water interfaces, Chapter 5 extended the laboratory observations of Leconte et al. (2009) by deriving ice thickness for freshwater ice at off-nadir angles. A time series of UW-Scat observations were obtained at static and roving sites coincident to in-situ ice thickness measurements which were used as validation. Once adjusted for the refractive index of ice and the slant range of the observed angle, the distance between peak returns for the ice-snow and ice-water interfaces at off-nadir angles of 21 - 60° agreed with in-situ ice thickness observations. Derived ice thicknesses were also compared to the upward looking SWIP and a one-dimensional thermodynamic ice model (CLIMo). Median ice thicknesses derived from UW-Scat X- and Ku-bands obtained ranges agreed well with in-situ measurements (R^2 = 0.955 and 0.964, RMSE = 0.053 and 0.045 m), SWIP (R^2 = 0.865 and 0.877, RMSE = 0.082 and 0.088 m) and CLIMo simulations that used 25% of the snowpack obtained from terrestrial weather stations (RMSE = 0.082 and 0.079 m). Ku-band was superior in delineating interfaces in range as a result of a shorter wavelength (17.4 mm) compared to X-band (31 mm), which increased the potential for interaction with smaller scatterers near the snow-ice or ice-water interface such as snow grains, spherical bubbles or shorter tubular bubbles. Chapter 5 presented the first field observations of ice thickness up to ~1.2 m using the range profiles of dual-frequency X- and Ku-band

observations at off-nadir angles. Additionally, Chapter 5 confirmed that the multiple peaks in range were the result of unique interaction with the ice-snow and ice-water interfaces.

Chapters 4 and 5 were written using the longstanding hypothesis of backscatter returned from the ice-water interface to be the result of double-bounce interaction from the tubular bubbles within the ice volume and reflection off the ice-water interface. However, in-situ ice cores extracted from static sites revealed that UW-Scat observed significant returns from the ice-water interface prior to the development of tubular bubbles at thicknesses < 0.5 m. Investigation of this phenomena lead to collaboration with Dr. Atwood at the Michigan Technological University: Research Institute and the publication of a research paper, presented in full in the Appendix. The study utilized several polarimetric datasets including PalSAR (L-band), RADARSAT-2 (C-band), TerraSAR-X (X-band) and UW-Scat (X-, Ku-band) in conjunction with the formulation of a numerical scattering model to investigate the dominant scattering mechanism within freshwater lakes and ponds in Arctic and sub-Arctic regions. UW-Scat observations confirmed that returns from within the ice volume interacted with the ice-water interface, and polarimetric decomposition of the satellite datasets suggested that the dominant scattering mechanism from the interface is single-bounce, rather than double-bounce. The identification of single-bounce scatter from the ice-water interface was also supported by a co-polarized phase difference centred at 0 ° obtained from satellite and UW-Scat observations. This study was the first to identify single-bounce scatter off the ice-water interface as the dominant scattering mechanism, a shift from the longstanding hypothesis of double-bounce off tubular bubble and the ice-water interface.

Building on the dominant single-bounce hypothesis presented in Appendix A, Chapter 6 presented a winter time series (2009-2010) of UW-Scat and RADARSAT-2 backscatter and phase observations of Malcolm Ramsay Lake, with polarimetric decomposition of RADARSAT-2 acquisitions. UW-Scat observations were consistent with Chapters 4 and 5 in identifying two dominant peaks within range of UW-Scat field of view associated with the snow-ice and ice-water interface, and that increases in backscatter occurred at the ice-water interface prior to the inclusion of tubular bubbles in the ice volume. The co-polarized phase difference of interactions near the ice-water interface for both UW-Scat and RADARSAT-2 observations centred at 0° for the duration of the time series, indicating that the scattering regime remained consistent for the entirety of the observation period. A Yamaguchi 3-component decomposition of the time series of RADARSAT-2 observations suggested that the dominant scattering mechanism to be single-bounce off the ice-water interface related to appreciable surface roughness or preferentially oriented facets. Lake ice thickness

observations and examination of the ice cores extracted adjacent to the scatterometer field of view indicated that two scales of roughness were present; a) small scale roughness related to the termination point of bubbles at the ice bottom, where a semi-sphere protrudes from the ice-water interface, and b) large scale roughness related to ice growth rate variability governed by the distribution of snow depth and surface ice types. This study enhances the hypothesis that the dominant scattering regime in bubbled freshwater lake ice is single-bounce from the ice-water interface, bolstered with evidence from modern fully polarimetric sensors.

7.2 Limitations

The most prominent limitation throughout this work is the lack of quantification of the ice-water interface. Surface roughness at boundary layers with high dielectric contrasts is of critical importance to model backscatter. Chapter 6 attempted to estimate the small scale roughness at the ice-water interface by measuring the diameter of bubbles at the termination point, but the large scale roughness is still unknown. Snow depth is highly variable on lakes due to the open exposure to aeolian forces, which serves to modify the conductive heat flux from the water to the atmosphere. Noted in Chapter 5, the range of CLIMo-simulated ice thicknesses from 0 – 100% of the reported terrestrial snowpack can lead to a range in ice thicknesses from approximately 0.9 to 1.5 m at the end of the observation period, a range of approximately 0.6 m. This large scale roughness is capable of forming mirror-like facets at the ice-water interface, resulting in the single-bounce scattering mechanism identified by polarimetric decomposition.

Concurrent to the issue of being unable to quantify roughness at the ice-water interface, the true date in which the ice freezes to bed is highly variable when observing using traditional means in the field. Once the bottom is struck while augering the ice, the site is declared “frozen-to-bed”, however if the bottom is comprised of saturated sediment, the radar observation may continue to identify an “ice-water interface” until the ground has sufficiently frozen.

A significant limitation regarding the collection of correlative datasets at static sites adjacent to the scatterometer footprint is that the observation of physical components of the lake ice system including snow depth, ice thickness and ice stratigraphy occur outside the actual field of view. While the extraction of the ice core within the scatterometer footprint provides an indication of ice growth at the ice bottom throughout the winter season, surface ice growth can occur at any time through pressure cracks or the snow depressing the ice beyond the hydrostatic water line. However, it was

deemed imperative to collect repeated observation of the same site(s) to capture the evolution of unique fields of view at static sites to provide an accurate perspective of the radar signature of ice and snow development at that site.

The quantification of backscatter from single components within the lake ice system (snow depth, surface ice types, ice thickness, etc.) is confounded by the complexity of the summation of physical components in the scatterometer and SAR field of view. Snow, grey ice and bubbled ice are all fairly transmissive media at microwave wavelengths. While scatter occurs within the volume of these layers, the quantification of any specific single layer requires accurate knowledge of the other layers. The presence, thickness, and roughness of these layers evolve continually during the winter season, resulting in increased complexity in modeling efforts.

The limitations of the sensors utilized in this thesis are generally grouped into available bandwidth and temporal resolution. The bandwidth of UW-Scat is 500 MHz, which roughly results in a range resolution of 0.3 m in a vacuum. Such a large range resolution influences the resolution and accuracy of the range to specific scattering centres identified by UW-Scat. The large range resolution also inhibited the delineation of unique scattering centres when separated by less than 0.4 m, restricting the minimum identified ice thickness to 0.4 m in Chapter 5, and the identification of interaction at or near multiple interfaces in all studies in the thesis. The temporal resolution of UW-Scat was influenced by factors external to this thesis, including alternate objectives within the Churchill area in 2009-2010, and 2010-2011, and the environment in which the equipment was being transported. The observation period was restricted to the frozen season, as the freeze-up and melt seasons were unable to be observed by UW-Scat because of un-safe ice or trail conditions. The temporal resolution of RADARSAT-2 was 24 days, in which a great deal of snow and ice evolution occurred. The temporal resolution is insufficient to capture the exact date of ice freezing to bed, but in the confines of Chapter 6, provided context for the scattering mechanisms driving the winter backscatter evolution.

7.3 Future Directions

This research using modern polarimetric decomposition produced evidence to the contrary of the longstanding hypothesis that the double-bounce scattering mechanism from tubular bubbles and the ice-water interface in freshwater lake ice. Instead, polarimetric decomposition suggests that the dominant scattering mechanism is single-bounce from the ice-water interface. This assertion requires

rigorous testing through scatterometer, SAR and in-situ observation, as well as the formulation of backscatter models. Moving forward, an imperative step to improve and validate backscatter models is to accurately describe and quantify the roughness at the ice-water interface. UW-Scat and RADARSAT-2 co-polarized phase difference and polarimetric decomposition results indicate that the ice-water interface is the dominant backscatter source, but does not indicate the dependence on roughness at small or large scales. Regarding future observations, small scale roughness could be recorded through the extraction of large sections of the ice and performing an exhaustive survey of the ice bottom roughness and tubular bubble diameters. The drawback with this method is the loss of the bubble formation protruding out of the ice bottom; the solution of which would require an underwater survey using an unmanned submersible sensor to map the underside of the ice cover, including bubble protrusions. Large scale roughness features can be obtained using ground penetrating radar, which has shown to resolve the ice bottom at a resolution as fine as 0.1 m (Barfoot et al., 2003).

Backscatter models can also be improved by improving the shape of the inclusion in the ice volume to vertical columns or tear drops, as the model presented in Chapter 4 enforced reciprocity, swapping the dielectric properties of the inclusion and the host media.

Finally, the snow removal experiments presented in Chapter 4 indicated Ku-band sensitivity to the presence of snowpack overlying the ice with a drop in backscatter upon removal. However, the sample size was not sufficient to perform statistical analysis or provide a quantification of the relative sensitivity of Ku-band to snow depth or snow water equivalent. Therefore, a snow-piling experiment should be conducted on new or clear ice to test the sensitivity of X- and Ku-band to variable snow depths. The piled snowpack may not emulate freshly fallen or wind-redistributed snow, but the viewing geometry and the roughness at the ice-water interface remains consistent, which is the more difficult variable to control. This experiment could be completed outdoor or in a cold laboratory, where ice formation processes are controlled. The effect of a thick snowpack on the accuracy of derived ice thicknesses should also be investigated, as it is currently unknown if the presence of a thick snowpack will confound the accuracy or the resolution/identification of the range to the ice-snow interface.

Appendix A
Microwave Backscatter from Arctic Lake Ice and Polarimetric Implications

Abstract— **Polarimetric SAR satellite and ground-based Ku- and X-band scatterometer measurements are used to explore the scattering mechanism for ice in shallow Arctic lakes, wherein strong radiometric responses are seen for floating ice and low returns are evident where the ice has grounded. Scatterometer measurements confirm that high backscatter is from the ice/water interface, while polarimetric decomposition suggests that the dominant scattering mechanism from that interface is single bounce. Using Fresnel Equations, a simple model for surface bounce from the ice/water interface is proposed and its predictions are supported by experimental parameters such as co-pol phase difference, co-pol ratio, and the results of rigorous numerical modeling. Despite early research suggesting double bounce scattering from columnar air bubbles and the ice/water interface as the dominant scattering mechanism in shallow lakes, this research strongly supports a single bounce model.**

I. Introduction

Lakes and ponds are a characteristic feature of the Arctic landscape, accounting for more than 24% of the area on Alaska's North Slope coastal plain alone (Zhang et al., 1999). With growing concern for ecosystem changes due to climate change, the thermodynamic status of lakes and change in lake phenology take on greater research interest. Recent research has shown the role of lakes in thawing permafrost (Lin et al., 2010), supporting ebullition of greenhouse gases such as methane (Walter et al., 2006), and serving as an indicator of regional climate change through their changes in size and vegetative content (Roach et al., 2011). The characterization of lake bathymetry through optical remote sensing has been long demonstrated (Lyzenga et al., 2006). However the limitations of optical remote sensing in the face of cloud cover and polar darkness in the Arctic are well-established. Synthetic Aperture Radar (SAR) offers obvious advantages for year-round monitoring of lakes, with observations available independent of solar illumination and weather.

In the mid-1970s, researchers used Side Looking Airborne Radars (Sellmann et al., 1975; Elachi et al., 1976; Weeks et al., 1978; Mellor, 1982) to explore the response of lake ice to microwaves using

X- and L-bands. Since then, a number of satellite SAR missions, such as ERS-1/2, RADARSAT-1, and ALOS PALSAR have provided a wealth of archival data that can be used to explore lake ice evolution over more than two decades. The longevity of these observations will be further expanded via missions such as ALOS-II, Sentinel-1A/B, RADARSAT-2, and RADARSAT Constellation. Thus, SAR observations are an invaluable resource in understanding the response of lake ice to climate change (Surdu et al., 2014).

Polarimetric SAR systems such as ALOS (L-band), RADARSAT-2 (C-band), and TerraSAR-X (X-band) offer the best possibility for characterizing lakes and lake ice. The addition of multiple polarizations and phase yield the target scattering matrix from which one can extract the contributing scattering mechanism for each pixel on the ground. Early researchers, cognizant of the structure of shallow lake ice, with its distinctive layer of columnar air inclusions, have long ascribed the strong backscatter from floating ice to a double bounce scattering mechanism (Jeffries et al., 1993; Wakabayashi et al., 1993; Jeffries et al., 1994). However, a recent study (Engram et al., 2013) employing polarimetric SAR suggests that the scattering from lakes with methane ebullition is single bounce from the lake ice/water interface. To date, there has been no clear reconciliation of the widely-accepted double bounce explanation with contrary PolSAR observations of more recent work. The intent of this paper is to resolve this uncertainty by exploring lake ice in Alaska and the Canadian sub-Arctic using polarimetric satellite and ground-based radar from Ku- to L-band. In addition, numerical modeling is used to confirm the conclusions drawn from the empirical data.

II. Background

Figure A-1 shows two ERS-2 acquisitions of frozen lakes on the Barrow Peninsula of Alaska, acquired in January and February of 2009. The red ovals serve to highlight lakes which transitioned from bright to dark. This behaviour is observed for many of the shallower lakes in the region, which exhibit reduction in backscatter as the lake ice thickens through the winter and grounds to the underlying sediment. Other lakes, seen as dark in the figure, were even shallower and had grounded earlier in the season. This effect has been noted by numerous researchers (Sellmann et al., 1975; Elachi et al., 1976; Weeks et al., 1978; Mellor, 1982; Jeffries et al., 1994). The proposed mechanism (Elachi et al., 1976; Weeks et al., 1978) is that the ice/water interface at the bottom of the lake ice offers a very large dielectric mismatch, which results in strong microwave reflection. However for lakes with shallow bathymetry, the ice grounds to the underlying sediment as it thickens through the winter season. Once this occurs, the smaller dielectric discontinuity between ice and frozen sediment

results in the transmission of radar energy into the lake bottom, resulting in a 10-12 dB drop in backscatter as noted by (Jeffries et al., 1993).

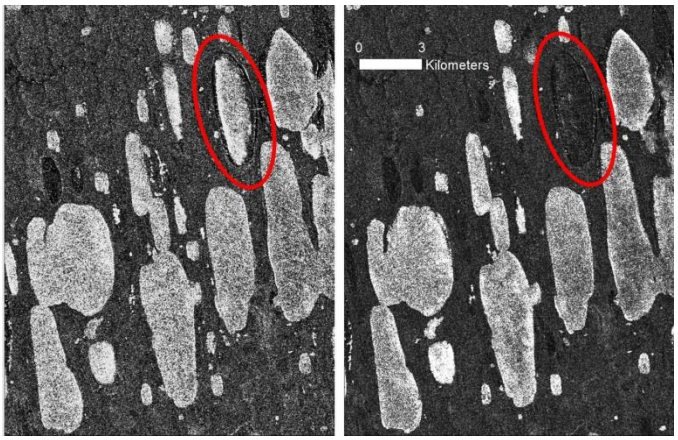

Figure A-1: ERS C-band images acquired on 10 January (left) and 14 February (right) of 2009, show changes in radiometry as ice grounds to the bottom of the lake.

Besides being a useful indicator of the presence of liquid water, the effect of grounded ice provides a rudimentary technique for determining lake bathymetry. With knowledge of degree-days and a model of ice growth, researchers have mapped lake depths (Mellor, 1982; Jeffries et al., 1996; Duguay & Lafleur, 2003). Low radar return means those portions of the lake have water depth less than that of the current ice thickness. Thus by monitoring the grounding line as seen in SAR, bathymetry contours can be mapped through the winter season. In a recent investigation, (Grunblatt & Atwood, 2014) used ERS-2 imagery from April 2009 to map all the lakes of the North Slope of Alaska with depths less than 1.6m (the mean March ice thickness) and depths greater than that amount.

A key structural element in lake ice is the presence of columnar gas inclusions, often referred to as tubular, elongated, or needle-like bubbles. In some lakes with decomposition of biological detritus or lakes residing on thawing permafrost, large methane bubbles form in the ice. These bubbles tend to be large (on the order of 10 cm) and are usually oblate. However, on the North Slope of Alaska and the Canadian sub-Arctic near Churchill, a more common occurrence is the presence of vertically-oriented columnar bubbles, as seen in Figure A-2 and described by (Weeks et al., 1978; Weeks et al., 1981). These bubbles are observed to be on the order of millimeters in width and approximately 5-10 cm in height. The hypothesis first put forward by (Weeks et al., 1978) suggests that as the water of shallow lakes freeze, the dissolved gasses in the water are driven to super-

saturation and precipitate into bubbles at specific points on a rough lake floor. These precipitation points feed a steady stream of bubbles and are incorporated into the ice volume during freezing. The upper portion of the ice column is commonly found to be clear of bubble inclusions, while the lower half is seen to contain a dense layer of columnar bubbles. This suggests that the dissolved gasses do not reach saturation until midway through the growth process.

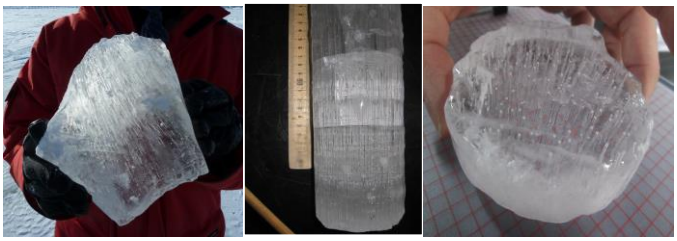

Figure A-2: Image of lake ice with vertically-oriented columnar bubbles acquired near Barrow, Alaska in March 2012 (left), and ice cores taken from Malcom Ramsay Lake, near Churchill, Canada, in March 2011 (middle), and Sitidgi Lake, near Inuvik, Canada, in April 2013 (right).

Many of the explanations for high backscatter from floating ice have been attributed to double bounce from columnar bubbles (Jeffries et al., 1993; Wakabayashi et al., 1993; Matsuoka et al., 1999). This mechanism is similar to the double bounce scattering observed in forests and analytically explained by Lin & Sarabandi (1995). As illustrated in Figure A-3, the refracted microwaves in the ice are assumed to forward-scatter off the bubbles in the plane of incidence and reflect off the ice/water interface to retro-reflect back to the radar source. This mechanism explains strong backscatter return as long as the ice/water interface remains intact. While seemingly consistent with ice structure, this explanation has yet to be confirmed with a full polarimetric model capable of simulating the measurements of current full-polarization SAR satellites.

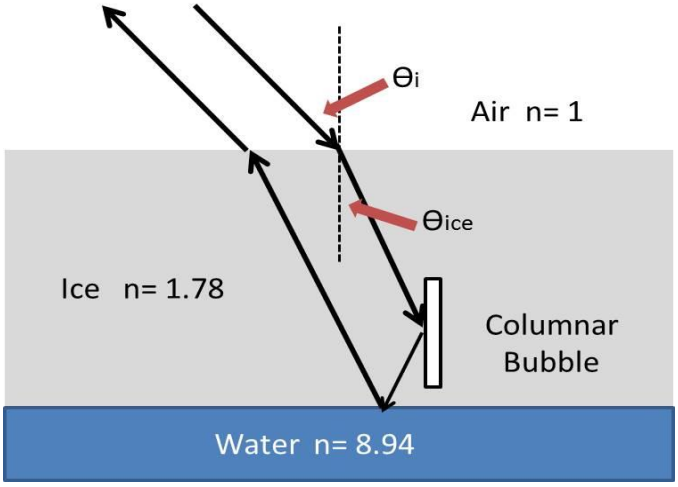

Figure A-3: Schematic showing ice-refracted microwaves bouncing off bubble and ice/water interface, consistent with (Jeffries et al., 1993; Wakabayashi et al., 1993; Matsuoka et al., 1999).

Most studies quantitatively addressing scattering from ice have relied upon single polarization radar (Jeffries et al., 1994; Wakabayashi et al., 1993; Matsuoka et al., 1999; Duguay et al., 2002). However more recent SAR systems such as L-band ALOS PALSAR and C-band RADARSAT-2, as well as a broad range of airborne systems, provide full-polarization radiometry and the potential to deepen our understanding of the underlying scattering mechanisms (Boerner, 2007). The diagonal elements of the Pauli matrix (Lee & Pottier, 2009) provide good first-order estimations for the scattering mechanisms of double bounce, single bounce, and volume scattering. However, with the increased use of polarimetric SAR systems, a number of model-based incoherent target decompositions (Freeman & Durden, 1998; van Zyl et al., 2011; Touzi, 2007; Yamaguchi et al., 2005) have been developed that offer better representations of the underlying scattering mechanisms for various land cover types. The authors explored several of these, but since they all yield similar values, only the results from the Yamaguchi 3-component decomposition (Yamaguchi et al., 2005) are presented here.

Figure A-4 shows a RADARSAT-2 acquisition for the Barrow Peninsula of Alaska, with several lakes containing floating ice highlighted in red. The associated histogram shows the relative proportions of Single Bounce, Double Bounce, and Volume Scattering decomposition for both C-band RADARSAT-2 and L-band ALOS PALSAR produced using the Yamaguchi 3-component decomposition. For both bands, the decomposition shows that more than 70% of the backscattered power resides in Single (Surface) Bounce. This polarimetric decomposition presents somewhat

contrary evidence to the generally accepted double-bounce theory related to the presence of columnar bubbles. In considering the accepted double bounce model, one must either explain the mischaracterization of the double scattering mechanism by all decomposition methods or accept that the scattering is due to another mechanism

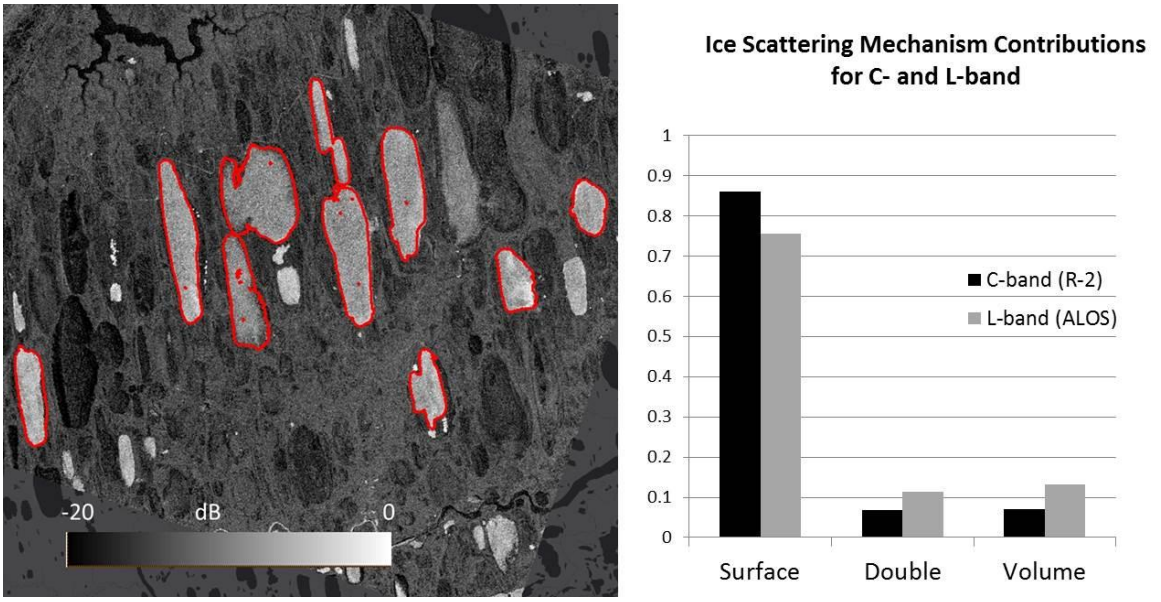

Figure A-4: RADARSAT-2 HH image acquired on 26 March, 2012 (left) with selected examples of floating ice (outlined in red). Histogram on right shows proportions of Surface Bounce, Double Bounce, and Volume Scattering from the Yamaguchi 3-component decomposition of the selected ice for both C-and L-band SAR.

In this paper, microwave scattering from floating ice is investigated in detail, with the goal of investigating whether the dominant mechanism is double bounce off columnar air bubbles or single bounce off the ice/water interface. Section III provides critical background by confirming experimentally that the backscatter signal from floating ice comes dominantly from the ice/water interface. Section IV investigates the predictions from published backscatter models and proposes a simple scattering model in which bubbles play no critical role in the strong radiometric response of floating ice. Instead both polarizations simply refract into the ice where they undergo reflection from a rough ice/water interface and are strongly reflected back to the source. Section V supports the proposed single bounce with experimental results from X-band, C-band, and L-band satellite data, as well as ground-based, X- and Ku-band scatterometer data. Section VI describes a numerical model that confirms that columnar bubbles have little impact upon C-band backscatter. Finally, the results

and implications of this for PolSAR are discussed in Section VII, and conclusions are offered in Section VIII.

III. Experimental Confirmation of Bounce from Ice-Water Interface

SAR backscatter from floating lake ice can come from a variety of sources: snow, "grey" or snow ice on the surface, entrapped bubbles, a rough ice/water interface, or double bounce from columnar bubbles and the ice/water interface. Literature suggests that the high reflectance from floating ice is attributable to the ice/water interface. In this section we look at an experiment that confirms that the backscatter from floating lake ice is dominated by microwaves reflecting off the ice/water interface, either through double bounce involving columnar air bubbles or through direct scattering off a rough surface.

Ground-based measurements of lake ice were performed at Malcolm Ramsay Lake, Canada. The University of Waterloo scatterometer (UW-Scat) was used to perform measurements in both X-band and Ku-band. The system is comprised of two standalone Frequency Modulated Continuous Wave (FMCW) radars centered at X- (9.6 GHz) and Ku-band (17.2 GHz) with a bandwidth of 500 MHz and a range resolution of 30 cm. Each observation consisted of a succession of azimuthal sweeps from a near range incidence angle of 21 degrees to a far range incidence angle of 60 degrees. For each azimuthal sweep, a single averaged Covariance Matrix was calculated. This matrix, in turn, provides information on the amplitude and phase of co-pol and cross-pol elements. A further description of UW-Scat is provided in (King et al., 2013).

Figure A-5 shows power versus range plots for X-band and Ku-band scatterometer measurements obtained at 39 degrees from floating lake ice that was measured to be approximately 1.2 m thick. It was hypothesized that first peak (at about 6m range) is associated with surface reflection from the top of the ice surface and that the larger peak (at about 8m range) is associated with reflection from the bottom (at the ice/water interface). In both instances, the bottom reflection is seen to be approximately 5dB greater than the reflection from the top surface, confirming that the ice/water interface plays the dominant role in backscatter from floating lake ice.

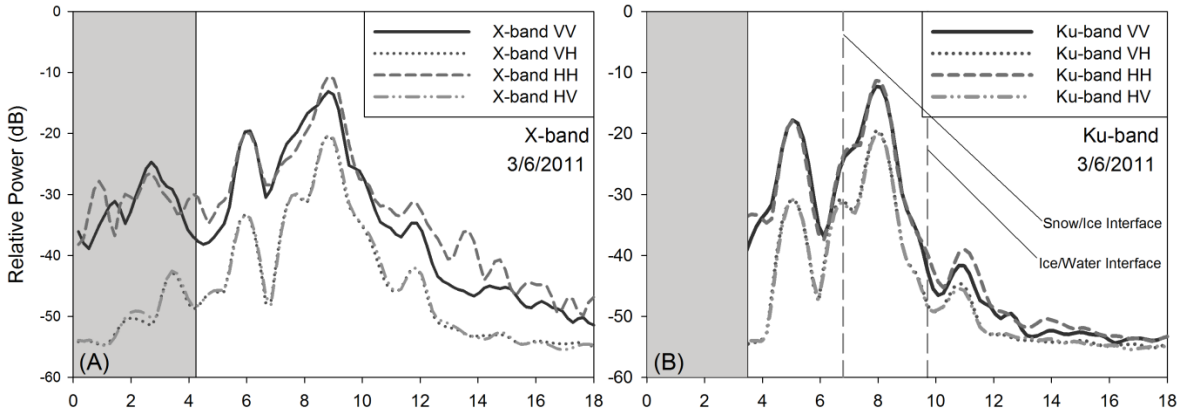

Figure A-5: Scatterometer power plots for X-band (left) and Ku-band (right) for each of four polarizations. The peak at a range of approximately 6 m is assumed to be associated with reflection from the ice surface, whereas the peak at a range of approximately 8m is considered to be a reflection from the bottom of the lake ice.

The separation of the peaks should reflect the difference in travel time between the surface bounce and bottom bounce paths. With knowledge of the refractive index and a set of measurements of the peak separation for each incidence angle, it becomes possible to compute the thickness of the ice. Note that whether the scattering mechanism is double bounce or surface bounce from the ice/water interface, the time delay will be the same. That is, the scattering plane of both scattering mechanisms lies at the ice/water interface. The reason for this is that the range for double bounce from a dihedral is the same as the range to the bottom corner of the dihedral. Calling the refractive index of the ice, n, the separation between peaks, R_{12}, is related to the additional range in the ice, R_{ice}, by:

$$R_{ice} = R_{12}/n \tag{1}$$

From Snell's Law, the angle of incidence in the ice, θ_{ice}, is related to the incidence angle of the scatterometer, θ_i, by:

$$\theta_{ice} = \sin^{-1}(\sin\theta_i/n) \tag{2}$$

Then from simple trigonometry, the ice thickness, d, can be related to the peak separation, R_{12}, by:

$$R_{12} = 2nd/\cos(\theta_{ice}) \quad (3)$$

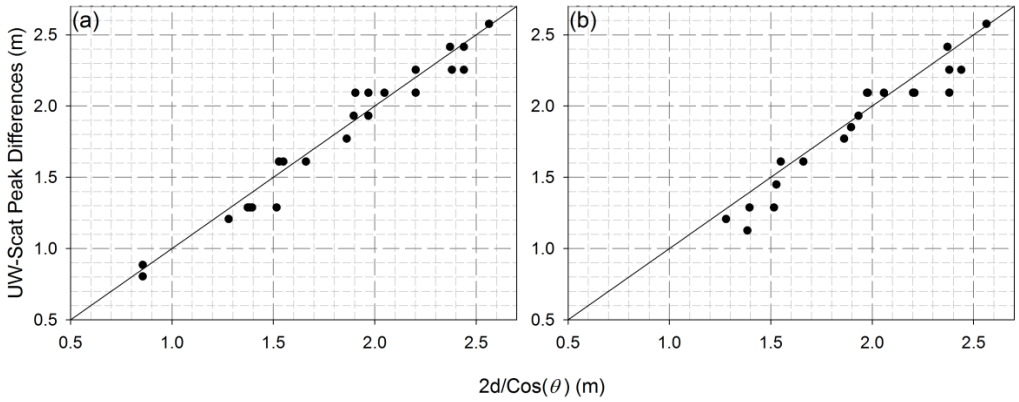

Figure A-6: Plots showing high agreement between measured and computed ranges, based on the assumption of reflection off the bottom of the ice, for Ku-band (left) and X-band (right).

Figure A-6 shows plots of measured versus computed slant range of the signal within the ice for X-band and Ku-band at three static sites that were visited throughout the winter season, and 11 roving sites sampled randomly across Malcom Ramsay Lake near Churchill, Manitoba. The coefficients of determination (R^2) are 0.98 for Ku-band and 0.95 for X-band, indicating excellent agreement with modelled data. While these results cannot differentiate between double bounce and surface bounce, they do confirm that the dominant microwave backscatter energy comes from the bottom of the ice with a range that depends largely on viewing geometry.

IV. Published Simulations and Proposed Wave Propagation Model

Several models have been developed to explain the backscatter from lake and river ice. In addition, other modelers have addressed scattering from dielectric targets of a suitable size scale to shed light on the expected behaviour of microwaves impinging on columnar air inclusions in frozen lake ice. Each of these will be examined and particular attention will be given to model predictions that can be tested with current or future available data.

In modeling ERS-1 backscatter from lake ice, (Wakabayashi et al., 1993) developed a model that assumed a smooth, planar ice structure consisting of bubble inclusions. The permittivity of the ice is assumed to be a "two-phase" mixture of air and ice. Air inclusions are considered to be 2mm spheres and 1mm x 5cm cylinders. Simulation showed a difference of 7.5 dB between floating and grounded ice; differing from the 10-12dB observations of Jeffries et al., (1996). In addition, the

simulations showed an increase in backscatter with increases in columnar bubble layer thickness. However, when simulation used the actual conditions of ice at 11 lake sites, the simulated backscatter was shown to be 5.5 dB lower than that observed in ERS-1 data. This suggests that double bounce from a smooth ice/water interface fails to explain the observed high backscatter from floating ice.

Matsuoka et al., (1999) developed a model for X, C, and L-band backscatter from 0.5 cm oblate bubbles in a lake in Hokaido, Japan. The incoherent model assumed that all interfaces were smooth and that scattering is determined by angle dependent Mie theory. It predicted that X-band backscatter is slightly greater than C-band, and 6 to 20 dB greater than L-band backscatter, dependent on incidence angle. In addition, it suggested that the co-pol ratio of HH/VV is unity for X-band and C-band, but grows from unity for L-band as the incidence angle is increased from 10 to 60 degrees. This simulation suggests that the bubbles play a critical role in backscatter and offers testable hypotheses for polarimetric SAR. However, the dimension and physical shape of the Hokaido lake bubbles differ significantly from the columnar bubbles in the current study (i.e. 0.5cm oblate bubbles versus 1mm x 15 cm columnar bubbles).

In another study, Gherboudj et al., (2007, 2010) described a simulation for backscatter from river ice containing columnar ice, frazil ice, and snow ice. Using Radiative Transfer theory (doubling matrix theory) with rough ice interfaces, the authors investigated the role of ice surface roughness and columnar air inclusions in the columnar ice. Backscatter from the ice/water interface was shown to dominate the top return by 5-10 dB, exhibiting over a 8 dB increase as the bottom roughness was increased from $K\sigma = 0.15$ to 0.5. In addition, the model showed backscatter increasing with increasing volume fraction and thickness of columnar air inclusions; the proposed explanation being both volume scattering and volume/boundary double bounce. In all cases, VV backscatter was about 1.5dB greater than HH, with both polarizations having decreased backscatter with increasing incidence angle. Using ice structure data for 10 samples from the Athabascan River and the assumption that the river ice bottom was smooth as a result of flow erosion, single-pol Radarsat-1 (HH) data was found to agree with simulations within 2dB.

The suggested role of columnar bubbles in the models described above raises questions about the details of microwave scattering from air inclusions in ice. In a 1988 paper (Karam et al., 1988), microwave scattering from a dielectric with one dimension much smaller than the wavelength was considered. For the case of a dielectric cylinder, Rayleigh, Generalized Rayleigh-Gans, and an infinite length cylinder approximation were modeled and compared. At broadside angle to the cylinder, all three approaches yielded identical results. However when multiple incidence angles and wavelengths

were considered, the infinite cylinder approximation worked best. For cylinders of arbitrary cross section at oblique incidence, comprehensive formulations are provided in (Sarabandi & Senior, 1990; Stiles and Sarabandi, 1996). For modelling vegetation with a dielectric of 9.6 and a variety of ka (where k equals wavenumber and a equals the cylinder radius) values between 0.1 and 0.4, all backscatter cross sections were found to be less than -15dB, significantly lower than the -6dB that characterizes floating ice. Considering that the dielectric mismatch between ice and air is less than that between air and vegetation, and that scattering from bubbles is far off broadside incidence where backscatter is maximum, scattering from air inclusions appears to be of the wrong magnitude to explain the observed lake backscatter.

If bubbles cannot produce sufficient backscatter to explain the high reflectance of lake ice, what effect do they have? For wavelengths that are 10x the dimensions of inclusions, effective medium theory should apply. In such conditions, it is shown that the random volume can be approximated by an anisotropic homogeneous medium. In fact for columnar inclusions, the effective medium is uniaxial with a diagonal permittivity tensor whose elements are given by (Srabandi, 1990):

$$\varepsilon_z = f + (1 - f)\epsilon_{ice} \tag{4}$$

$$\epsilon_x = \epsilon_y = \left(1 - \sqrt{f}\right)\epsilon_{ice} + \frac{\sqrt{f}\,\epsilon_{ice}}{\sqrt{f}\,\epsilon_{ice} + \left(1 - \sqrt{f}\right)} \tag{5}$$

where f is the surface fraction of air bubbles to ice. Horizontally polarized incident waves "see" ϵ_x and ϵ_y which are very close to ϵ_{ice}, while the smaller dielectric ϵ_z is observed by a vertically polarized wave.

Figure A-7 schematically depicts the proposed single bounce from the ice/water interface. Incident microwaves undergo refraction into the ice where they propagate to the bubble layer where further slight refraction may occur. Those microwaves within a resolution cell that are retro-reflected to the source have undergone a perpendicular reflection from an appropriately oriented facet on the bottom of the lake ice. This assumption is consistent with geometric optics approximation for rough surface, especially considering the fact that the refracted incident wave corresponds to low incidence angle on the ice/water interface. Clearly, this model assumes a degree of faceting on the ice bottom to permit back-reflection for microwaves with a wide variety of incidence angles. This will be discussed in greater detail in Section V.

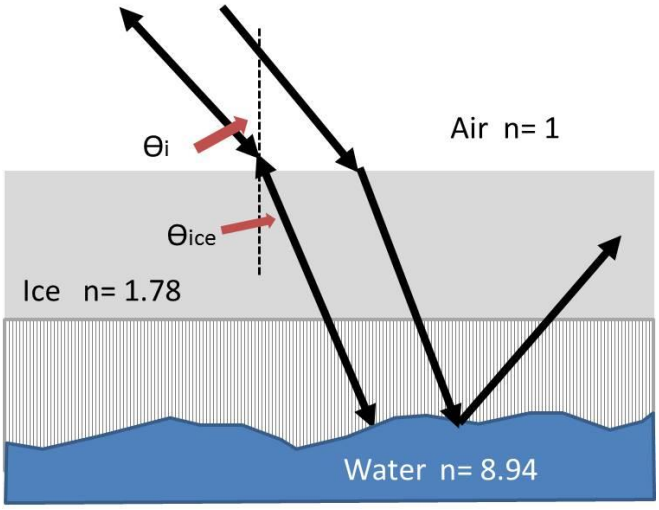

Figure A-7: Schematic showing ice-refracted microwaves bouncing off perpendicularly oriented facets on the bottom of the lake ice. Columnar bubbles in lower half of ice are assumed to have only refractory effect upon microwaves

*

This model assumes no significant role for surface snow, consistent with the findings of other researchers (Wakabayashi et al., 1993; Matsuoka et al., 1995; Gherboudj et al., 2010). Ignoring the possible modification of the bulk refractive index of the bubble-containing ice, Fresnel's Equations can be used to determine the backscattered amplitudes for horizontal and vertical polarization. In this model, microwaves in the ice are assumed to impinge perpendicularly upon the ice/water interface, and thus both polarizations experience the same reflectance, R, which is given by:

$$|R| = \frac{n_{water} - n}{n_{water} + n} \tag{6}$$

where n is the refractive index of the ice. The total backscatter reflectance will be the product of 1) the transmission from air to ice, 2) the reflectance from the bottom of the ice, and 3) the transmission from ice to air. Assuming that the microwaves reflect off perpendicular facets on the bottom of the ice, the backscatter amplitudes for HH and VV can be expressed as follows, using the standard Fresnel Equations:

$$BS_{hh} \sim \left[\frac{2\cos\theta_i}{\cos\theta_i + \sqrt{n^2 - \sin^2\theta_i}}\right] * \left[\frac{n_{water} - n}{n_{water} + n}\right] * \left[\frac{2n\cos\theta_r}{n\cos\theta_r + \sqrt{1 - n^2\sin^2\theta_r}}\right] \tag{7}$$

$$BS_{vv} \sim \left[\frac{2n\cos\theta_i}{n^2\cos\theta_i + \sqrt{n^2 - \sin^2\theta_i}}\right] * \left[\frac{n_{water} - n}{n_{water} + n}\right] * \left[\frac{2n\cos\theta_r}{\cos\theta_r + n\sqrt{1 - n^2\sin^2\theta_r}}\right] \quad (8)$$

where θ_i is the SAR incidence angle and θ_r is the refracted angle within the ice, computed as:

$$\theta_r = \sin^{-1}\left[\frac{\sin\theta_i}{n}\right] \quad (9)$$

Figure 8 plots σ^0_{hh} and σ^0_{vv} (arbitrarily scaled) as a function of incidence angle. For small incidence angles, the two polarizations are seen to be very similar in magnitude. But as the incidence angle approaches the air-to-ice Brewster angle of 60.7 degrees, the VV backscatter increases since more energy couples into the ice from the air. The horizontal polarization drops off because it experiences more specular reflection from the surface.

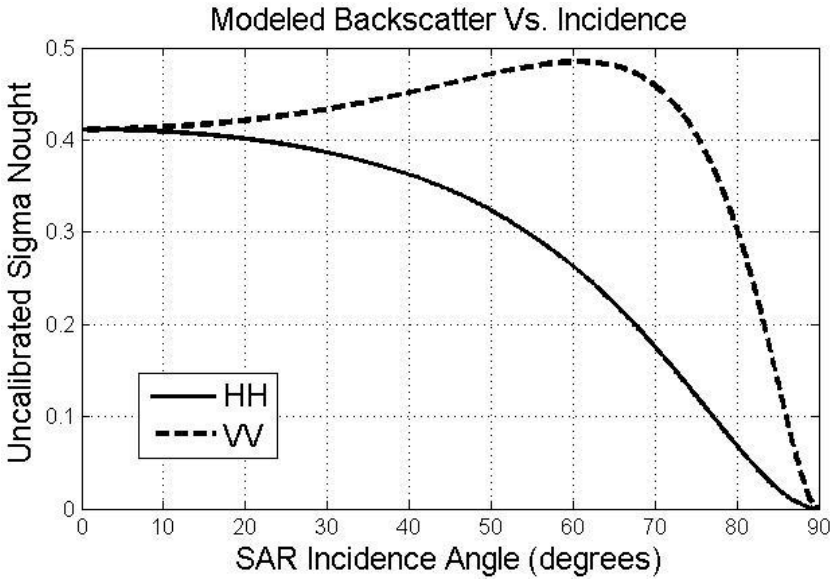

Figure A-8: Backscatter intensity calculated from Fresnel Equations for HH and VV polarizations, assuming ice-refracted microwaves reflect from perpendicular facets on bottom of lake ice.

In the simplified results of Figure A-8, there were no detailed assumptions made about bottom roughness; but simply the assumption that reflective facets exist. This assumption is consistent with Ashton's (1986) description of ripples and dunes on the underside of lake and river ice. Realistically, the reflected power will be less than that suggested in Figure A-8. Deviations from prediction will depend upon the actual statistics of the bottom roughness and may be subtly influenced by

polarimetric differences in the effective refractive index of the bubbles. This simple model leads to several predictions that can be tested using current or future datasets:

- This model requires that the lake ice bottom be rough. The existence of strong backscatter from floating lake ice with a flat, smooth ice/water interface would rule out this single bounce model.
- The coherent co-pol phase difference (Sarabandi, 1992) should be equal to two-way transmission coefficient phase difference at the air/ice interface. A double bounce model would require additional phase differences corresponding to specular scattering off of columnar bubbles and reflection off of water/ice interface.
- The co-pol ratio (HH/VV) for all bands should be close to unity for small incidence angles and decrease with increasing incidence angle. Note that the Matsuoka model (Matsuoka et al., 1999) suggested that the L-band co-pol ratio grows with incidence angle and that the Gherboudj model (Gherboudj et al., 2010) shows a non-unity co-pol ratio even for small incidence angles

V. Satellite and In-situ Results

From Fresnel's equations, double bounce from a dielectric dihedral can be shown to introduce a near-180 degree phase change between horizontal and vertical polarizations. Similarly, the Fresnel equations predict a near-0 degree phase change between HH and VV for reflection from a dielectric surface. Thus the Pauli term, HH-VV, becomes large for double bounce while the Pauli term, HH+VV, becomes large for surface bounce. From this it is clear that the co-pol phase difference (CPD), which equals the phase difference between HH and VV is a telling indicator for whether a land cover class is dominated by double bounce or surface bounce.

As noted above, it is useful to investigate the CPD, which can be extracted from the multi-looked Covariance Matrix:

$$\begin{vmatrix} HH\,HH^* & HH\,HV^* & HH\,VV^* \\ HV\,HH^* & HV\,HV^* & HV\,VV^* \\ VV\,HH^* & VV\,HV^* & VV\,VV^* \end{vmatrix}$$

The diagonal terms of the covariance matrix are real and represent power in each of the polarizations. The off-diagonal terms, however, are complex and provide phase information that can be used to better understand the scattering mechanisms.

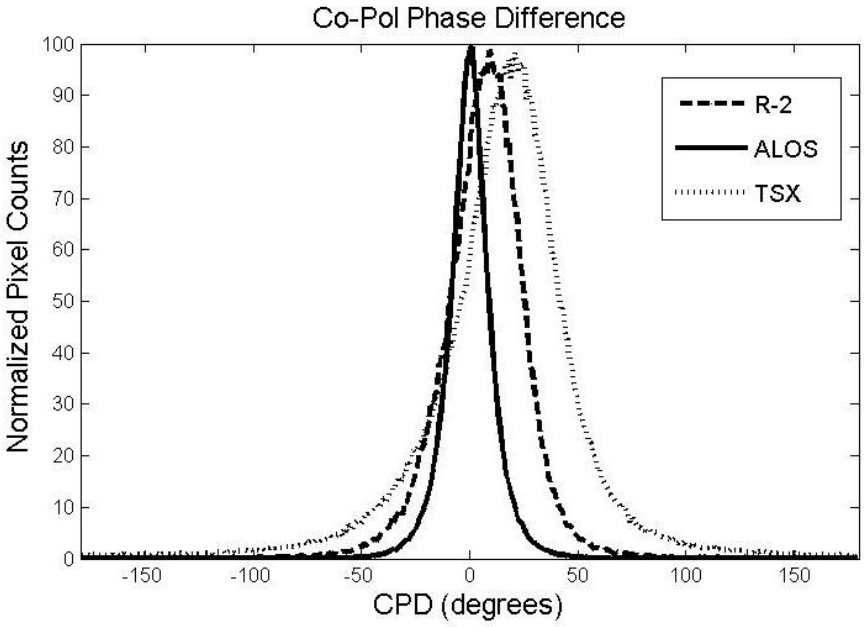

Figure A-9: Histograms showing co-pol phase differences for X-band TerraSAR-X (22 March 2013), C-band RADARSAT-2 (26 March 2012), and L-band ALOS PALSAR (13 March 2009), for floating lake ice on the North Slope of Alaska.

Figure A-9 shows histograms of the CPD extracted from the HHVV* term of the multilooked covariance matrices for a dual-pol TerraSAR-X image acquired on March 22, 2013, a quad-pol RADARSAT-2 FQ10 image acquired on March 26, 2012, and a quad-pol ALOS PALSAR PLR image collected on March 13, 2009. In all three cases, the CPD histogram peak centers are seen to be near-zero (less than or equal to 18 degrees). It is noted that the probability density function (pdf) of the co-pol phase difference can directly be obtained from the average covariance matrix (Sarabandi, 1992). This near-zero phase is consistent with the earlier observation that both C- and L-band decompositions indicate a surface bounce scattering mechanism. It would be notable if such consistent phase results existed over such a broad range of wavelengths (3 cm to 23 cm) if double bounce scattering were occurring off the vertical air bubbles in the ice.

In addition to the phase results, additional evidence for a surface bounce scattering mechanism is found in an investigation of co-pol ratio (HH/VV). As noted in the previous section, the

co-pol intensity ratio is expected to be approximately unity for the incidence angles that characterize spaceborne SAR systems (23 degrees for ALOS PALSAR and 30 degrees for RADARSAT-2). Using the same selected lakes shown in Figure 4, all co-pol ratios are seen to be near unity in Table A-1 below:

Table A-1: POLARARIMETRIC CHARACTERISTICS (CO-POLARIZED PHASE DIFFERENCE (CPD) AND CO-POLARIZED RATIO) OF LAKE ICE FOR TERRASAR-X, RADARSAT-2, AND ALOS PALSAR.

Satellite	Incidence (deg)	CPD Peak (deg)	Co-pol Ratio (HH/VV)
ALOS PALSAR	23.8	0.0	0.97
TerraSAR-X	28.3	15.1	1.22
TerraSAR-X	33.8	18.2	1.27
Radarsat-2	30.0	6.4	1.04

For the small ice samples collected in Barrow, Alaska and shown in Figure A-2, the bottom of the ice was found to be off horizontal by approximately 15-20 degrees. Means did not exist for examining the extent to which the remainder of the lake had a modulated surface, but it should not be presumed that our choice of excavation location was unique. Research performed by (Arcone et al., 1997), using a FM-CW radar in 1997 saw ice thickness fluctuations on the scale of 25 cm over a lake transect in Prudhoe, Alaska. As the presence of tilted facets is a necessary requirement for the proposed bottom bounce, there is a clear need to better characterize the bottom surface of Arctic lake ice. Until direct evidence can be presented, circumstantial evidence can be put forward.

It is possible that lake bottom surface roughness can be discerned when observing the incidence angle dependence of SAR backscatter. The polarimetric SAR data acquired over the North Slope of Alaska is not available in a broad range of incidence angles. However a large archive of single-pol RADARSAT-1 data exists for the Canadian sub-Arctic. Focusing on the region near Churchill, Canada, σ^0_{HH}values for Malcom Ramsay lake were examined as a function of incidence angle, using a set of twenty one March images, representing ST1, ST2 ST3, ST4, ST5, ST6, and ST7 acquisition modes. These modes span incidence angles from 20 to 49 degrees, which using Snell's Law correspond to incidence angles of 11 to 25 degrees within the ice. Figure A-10 shows Malcom Ramsay Lake, highlighted, as well as a plot of the incidence angle dependence. A significant roll-off

with incidence angle is seen. This result is consistent with an undulating lake bottom in which there are many more normal facets at 11 degrees than at 25 degrees.

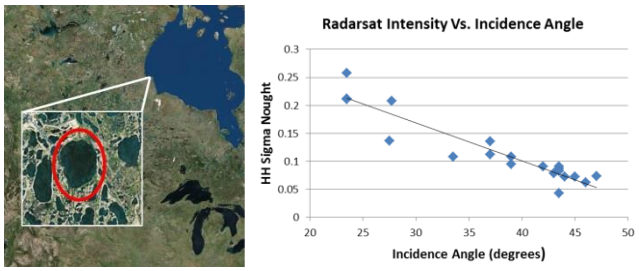

Figure A-10: Image at left shows Malcolm Ramsay Lake near Churchill, Canada used in the evaluation of incidence angle dependence. Plot on right shows lake ice σ^0_{HH} versus incidence angle.

VI. Numerical Model Results

In the last section polarimetric data either indicated or was consistent with surface bounce being the dominant scattering mechanism for lake ice. In this section, a numerical scattering model is used to directly test whether double bounce from bubbles occurs at all. The numerical model is an exact solution for the propagation and scattering of microwaves through a heterogeneous medium composed of a layer of ice with and without the columnar bubbles over a water surface. The formulation is based on the finite element method with periodic boundary conditions on two lateral directions (x and y directions). To examine whether columnar bubbles can contribute to scattering four scenarios are considered: 1) a layer of planar ice slab of 15cm thick over water, 2) a layer of planar ice with columnar air bubbles having radius of 1.5mm, height of 8cm, and spacing 10mm on average, 3) the same ice layer with a small roughness (rms height 5mm, and correlation length 50mm) at the ice water boundary, and 4) the ice layer with the same roughness as scenario 3 and the same bubble inclusions as scenario 2.

In these simulations, the water and ice complex permittivity values of εwater = 73 – 18j and εice = 3.17-0.001j are chosen respectively. Also a plane wave excitation at 5.4 GHz (C-band) and incidence angle of 30 degrees is selected. Figure A-11a –d show the bistatic scattering from each of the four aforementioned scenarios in order. Comparing simulation results for scenarios 1 and 2 it is obvious that the bubbles do not generate scattering to any level measurable by this simulation. The signal level in the backscatter direction is within the numerical noise (50 dB lower than the specular reflection). Scenario 3 shows that even small roughness can generate backscatter significantly higher

than numerical noise floor (by 20 dB or more). Comparing scenarios 3 and 4, it is observed that the two levels of bistatic scattering are remarkably similar. This indicates that the columnar air bubbles do not contribute to scattering significantly. It is noted that at higher frequencies where the spacing between air bubbles become electrically larger, scattering from air bubbles could increase.

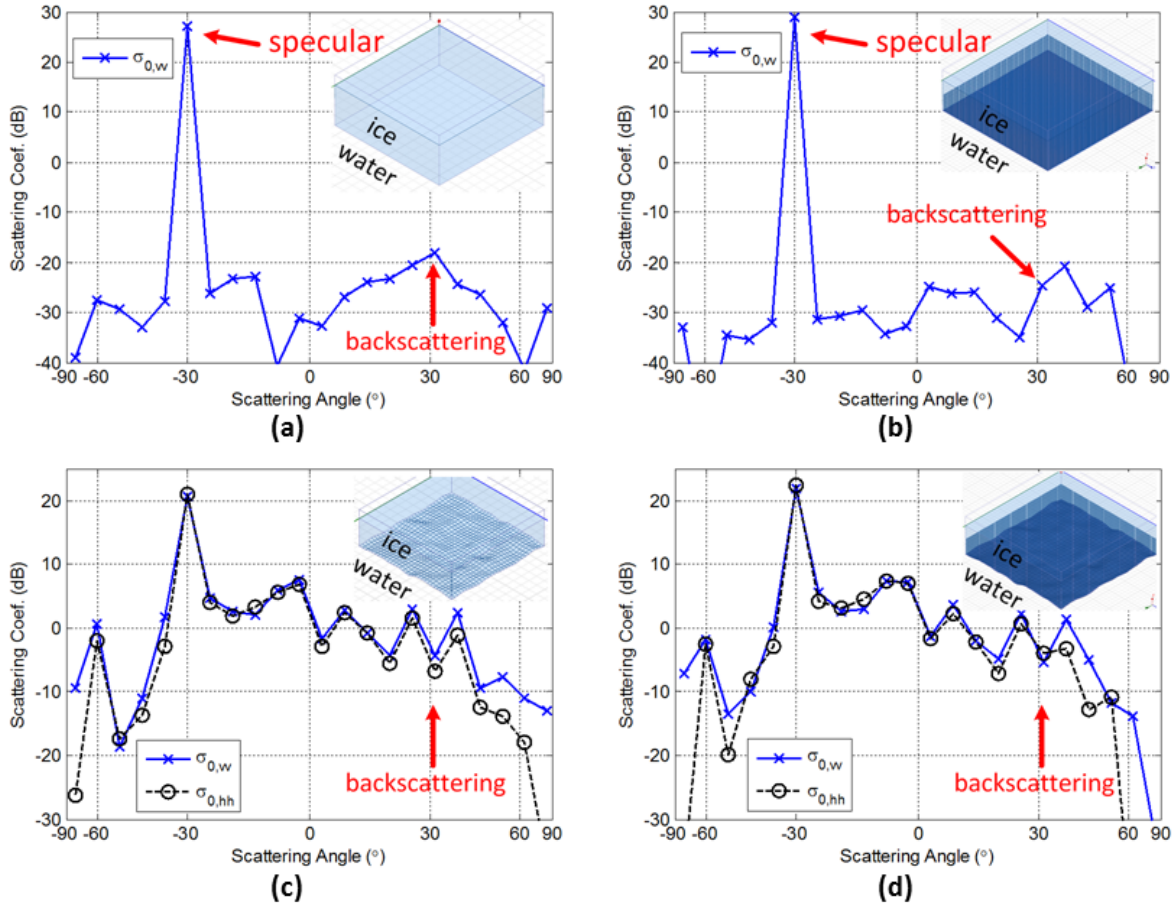

Figure A-11: Scattering simulation for an ice layer over water. (a) planar ice layer over water shows only specular reflection. (b) planar ice layer with columnar air bubbles also shows only specular reflection (Note: backscatter direction is indicated by the red arrow). (c) same ice layer with small roughness at the ice water boundary shows significant non-specular scattering. (d) ice layer with small roughness and columnar bubbles showing identical non-specular scattering as in case c.

VII. Discussion

As noted in Section II and further confirmed with CPD in Section V, polarimetric analysis indicates surface bounce at the ice/water interface as the dominant scattering mechanism. For double bounce to be true, one has to assume that the CPD is anomalous. But no such alternate mechanism has been modeled and confirmed. Next, the scattering of microwaves from columnar air bubbles should be strongly dependent upon the relative proportions of the bubble radius and the wavelength of the microwaves. However, X-band, C-band, and L-band all produce similar near-zero degree CPD, equal to the predicted answer for an alternative model of surface bounce from the ice/water interface. Circumstances by which a double bounce model could produce a co-pol ratio near unity (for small incidence angle) are difficult to resolve. Unlike the surface bounce case, in which the bubbles only serve to present bulk (birefringent) characteristics, microwaves in the double bounce model must scatter off the columnar bubbles along a dihedral trajectory. In scattering from cylinders, the parallel (VV) electric field couples much more strongly with the cylinders than the perpendicular (HH) electric field. Moreover, whereas the HH polarization response is independent of incidence angle, the VV dependence can vary by tens of dB (Ruck et al., 1970). Having the co-pol ratio equal near-unity over a range of wavelengths from 3 to 23 cm, and a range of incidence angles from 23 to 46 degrees, would be quite surprising for double bounce. The absence of this dependence is perhaps the strongest argument against scattering from columnar bubbles.

While a modulated ice bottom is a necessary condition for the surface bounce model, it does not in itself preclude the possibility of double bounce. Ice with spatially varying thickness can still support double bounce in that numerous horizontal facets would exist to serve as dihedral planes for reflecting microwaves back to the source. However, we would not expect to see the rapid roll-off in power as a function of incidence angle. No matter how the incidence angle changes, a dihedral double bounce is still dependent upon the same horizontal facets to reflect the energy back to the source. Thus the four-fold loss of power in going from an incidence angle of 20 to 49 degrees would not be expected.

VIII. Conclusion

As noted in the Introduction, all polarimetric decompositions lead to floating ice backscatter as having a surface bounce scattering mechanism. Rather than accept this decomposition at face value, a plane wave model was developed to provide testable hypotheses. The model ignores snow on the surface and gas bubbles within the body of the ice (the latter choice based on the assumption that the

bubbles only serve to perturb the refractive index). The key forecasts of this model are 1) a CPD equal to 0 degrees, 2) a HH/VV ratio approximately equal to unity, and 3) the requirement that the bottom surface be modulated with facets tilting over a broad range of angles.

From a variety of experiments with satellites and scatterometers, the CPD was found to be within 19 degrees of zero for TerraSAR-X, RADARSAT-2, and ALOS; and the co-pol ratio (HH/VV) was found to be within 3 dB of the simulated value for all incidence angles and all bands explored. Moreover, both interferometric coherence and power versus incidence angle measurements point to the probability of angular facets being a characteristic of the lakes examined in this study and possibly other regions in the Arctic. Last, a rigorous simulation with a coherent numerical model was unable to show any significant impact of bubbles upon the lake ice backscatter, except for what one would expect from their contribution to modulating the effective refractive index of the ice. In sum, the results of this study seem to offer overwhelming evidence that the long-held belief in the role of double bounce from columnar bubbles is incorrect.

Since the proposed model is dependent upon the lakes with high backscatter having a rough ice bottom surface, further research should be performed to confirm the roughness of the ice/water interface. With sound measurements of roughness and coherence length, it will be possible to perform more rigorous modeling of microwave response as a function of wavelength and incidence angle.

References

Adams, W. P. 1976. Diversity of Lake Cover and its Implications. *Musk-Ox*, 181: 86-98.

Albert, M., Shuman, C., Courville, Z., Bauer, R., Fahnestock, M., and Scambos, T. 2004. Extreme firn metamorphism: impact of decades of vapor transport on near-surface firn at a low-accumulation glazed site on the East Antarctic plateau. *Annals of Glaciology*, 39(1): 73-78.

Albert, M. D., Lee, Y. J., Ewe, H. T., and Church, H. T. 2012. Multilayer model formulation and analysis of radar backscattering from sea ice. *Progress in Electromagnetics Research,* 128: 267-290.

Ambach, W., and Denoth, A. 1980. The dielectric behavior of snow: A study versus liquid water content. *Presented at NASA Workshop on the Microwave Remote Sensing of Snowpack Properties*, Fort Collins, CO, NASA CP-2153.

An, W., Cui, Y., and Yang, J. 2010. Three-component model-based decomposition for polarimetric SAR data. *IEEE Transactions on Geoscience and Remote Sensing*, 48(6): 2732-2739.

Arcone, S. A., Yankielun, N. E., and Chacho, N. E. Jr. 1997. Reflection profiling of arctic lake ice using microwave FM-CW radar. *IEEE Transactions on Geoscience and Remote Sensing*, 35(2): 436-443.

Arp, C. D., Jones, B. M., Lu, Z., and Whitman, M. S. 2012. Shifting balance of thermokarst lake ice regimes across the Arctic Coastal Plain of northern Alaska. *Geophysical Research Letters*, 39: L16503.

Ashton, G. D. 1986. River and Lake Ice Engineering. *Water Resources Publications*, Book Crafters, Inc., Michigan, USA.

Atwood, D., Gunn, G. E., Roussi, C., Wu, J., Duguay, C., and Sarabandi, K. *in press*. Microwave backscatter from Arctic lake ice and polarimetric implications. *IEEE Transactions on Geoscience and Remote Sensing*, TGRS-2014-01296.

Barber, D. G. 2005. Microwave remote sensing, sea ice and arctic climate. *La Physique au Canada*, 61: 105-111.

Barfoot, T. D., D'Eleuterio, G. M. T., and Annan, P. 2003. Subsurface Surveying by a Rover Equipped with Ground-Penetrating Radar. *International conference on Intelligent Robotics and Systems*, Las Vegas, October, 2003.

Bari, S. A., and Hallet, J. 1974. Nucleation and growth of bubbles at an ice-water interface. *Journal of Glaciology*, 13: 489-520.

Barns, R. L., and Laudise, R. A. 1985. Size and perfection of crystals in lake ice. *Journal of Crystal Growth*, 71: 104-110.

Bello, R. L., and Smith, J. D. 1990. The effect of weather variability on the energy balance of a lake in the Hudson Bay Lowlands, Canada. *Arctic Alpine Research*, 22: 98-107.

Bernier, P. 1987. Microwave remote sensing of snowpack properties: potential and limitations. *Nordic Hydrology*, 18(1): 1-20.

Bengtsson, L. 1986. Spatial variability of lake ice covers, *Geographiska Annaler*, 68A(1-2): 113-121.

Boerner, W.M. 2007. Introduction to Synthetic Aperture Radar (SAR) Polarimetry, *Wexford College Press*.

Brown, L. C., and Duguay, C. R. 2010. The response and role of ice cover in lake-climate interactions. *Progress in Physical Geography*, *34*(5): 671-704.

Brown, L. C., and Duguay, C. R. 2011a. A comparison of simulated and measured lake ice thickness using a shallow water ice profiler. *Hydrological Processes*, 25(19): 2932- 2941.

Brown, L. C., and Duguay, C. R. 2011b. The fate of lake ice in the North American Arctic. *The Cryosphere*, 5(4): 869–892.

Brown, R. S., Duguay, C., Mueller, R., Moulton, L., Doucette, P., and Tagestad, J. 2010. Use of synthetic aperture radar (SAR) to identify and characterize overwintering areas of fish in ice-covered arctic rivers: a demonstration with broad whitefish and their habitats in the Sagavanirktok River, Alaska. *Transactions of the American Fisheries Society*, 139(6): 1711–1722.

Cable, J. W., Kovacs, J. M., Shang, J., and Jiao X. 2014. Multi-temporal polarimetric RADARSAT-2 for land cover monitoring in Northeastern Ontario, Canada. *Remote Sensing*, 6:, 2372–2392.

Cameron, W. L., Youssef, N. N., and Leung, L. K. 1996. Simulated polarimetric signatures of primitive geometrical shapes. *IEEE Transactions on Geoscience Remote Sensing*, 34(3): 793-803.

Carte, A. E. 1961. Air Bubbles in Ice. *Proceedings of the Physical Society*, 77: 757-768.

Cloude, S. R., and Pottier, E. 1996. A review of target decomposition theorems in radar polarimetry. *IEEE Transactions on Geoscience Remote Sensing*, 34: 498–518.

Cloude, S. R. 2010. Polarisation. *Oxford University Press*, New York, N.Y. 453 pp.

Cook, T.L. and Bradley, R.S. 2010. An analysis of past and future changes in the ice cover of two High-Arctic lakes based on synthetic aperture radar (SAR) and Landsat imagery. *Arctic, Antarctic, and Alpine Research* 42: 9-18.

Cumming, W. A. 1952. The Dielectric Properties of Ice and Snow at 3.2 Centimeters. *Journal of Applied Physics*, *23*(7): 768-773.

Debye, P. 1929. Polar Molecules. *Chemical Catalog Company*, New York, N.Y. 172 pp.

Derksen, C., Silis, A., Sturm, M., Holmgren, J., Liston, G. E., Huntington, H., and Solie, D. 2009. Northwest Territories and Nunavut Snow Characteristics from a Subarctic Traverse: Implications for Passive Microwave Remote Sensing. *Journal of Hydrometeorology*, *10*(2): 448-463.

Duguay, C. R., Pultz, T. J., Lafleur, P. M., and Drai, D. 2002. RADARSAT backscatter characteristics of ice growing on shallow sub-Arctic lakes, Churchill, Manitoba, Canada. *Hydrological Processes*, *16*(8): 1631-1644.

Duguay, C. R., and Lafleur, P. M. 2003. Determining depth and ice thickness of shallow sub-Arctic lakes using space-borne optical and SAR data. *International Journal of Remote Sensing*, 24(3): 475-489.

Duguay, C.R., Flato, G.M., Jeffries, M.O., Ménard, P., Morris, K. and Rouse, W. R. 2003. Ice-cover variability on shallow lakes at high latitudes: model simulations and observations. *Hydrological Processes*, 17: 3465-3483.

Duguay, C R., Prowse, T. D., Bonsal, B. R., Brown, R. D., Lacroix, M. P., and Ménard, P. 2006. Recent trends in Canadian lake ice cover. *Hydrological Processes*, 20(4): 781–801.

Ebert, E. and Curry, J. 1993. An intermediate one-dimensional thermodynamic sea ice model for investigating ice-atmosphere interactions. *Journal of Geophysical Research*, 98(C6): 10085-10109.

Elachi, C., Bryan, M., and Weeks, W. 1976. Imaging radar observations of frozen Arctic lakes. *Remote Sensing of Environment*, 5: 169–175.

Ellison, W. J., Lamkaouchi, K., and Moreau, J-M. 1996. Water: A dielectric reference. *Journal of Molecular Liquids*, 68: 171-279.

Engram, M., Anthony, K. W., Meyer, F. J., and Grosse G. 2012. Synthetic aperture radar (SAR) backscatter response from methane ebullition bubbles trapped by thermokarst lake ice. *Canadian Journal of Remote Sensing*, 38(6): 667–682.

Engram, M., Anthony, K. W., Meyer, F. J., and Grosse, G. 2013. Characterization of L-band synthetic aperture radar (SAR) backscatter from floating and grounded thermokarst lake ice in Arctic Alaska. *Cryosphere*, 7: 1741–1752.

Evans, S. 1965. Dielectric properties of snow and ice – a review. *Journal of Glaciology*, 5: 773-792.

Fierz, C., Armstrong, R. L., Durand, Y., Etchevers, P., Greene, E., McClung, D. M., Nishimura, K., Satyawali, P. K., and Sokratov S. A. 2009. The international classification for seasonal snow on the ground. *Tech. Doc. Hydrol.*, International Hydrology Programme, UNESCO, Paris.

Flato, G.M., and Brown, R.D. 1996. Variability and climate sensitivity of landfast Arctic sea ice. *Journal of Geophysical Research*, 101(C10): 25767-25777.

Fletcher, N. H. 1970. The Chemical Physics of Ice. *Cambridge University Press*, London, New York, 271 pp.

Freeman, A., Durden, S. L. 1998. A three-component scattering model for polarimetric SAR data. *IEEE Transactions on Geoscience Remote Sensing*, 36(3): 963–973.

Fröhlich, H. 1949. Theory of Dielectrics – Dielectric Constant and Dielectric Loss. In *Monographs on the physicals and chemistry of materials*, Eds. Jackson, W., Fröhlich, H., and Mott, N. F. Oxford University Press, Toronto.

Fujita, S., Mae, S., Matsuoka, T. 1993. Dielectric anisotropy in ice Ih at 9.7 GHz. *Annals of Glaciology*, 17: 276 – 280.

Fung, K. 1994. Microwave Scattering and Emission Models and Their Applications. *Arctech House*, Boston, MA.

Gherboudj, I., Bernier, M., and Leconte, R. 2010. A backscatter modeling for river ice: Analysis and numerical results. *IEEE Transactions on Geoscience and Remote Sensing*, 48(4): 1788 – 1798.

Geldsetzer, T., Mead, J. B., Yackel, J. J., Scharien, R. K., and Howell S. E. L. 2007. Surface-based polarimetric C-band scatterometer for field measurements of sea ice. *IEEE Transactions on Geoscience Remote Sensing*, 45(11): 3405-3416.

Gherboudj, I., Bernier, M., and Leconte. R. 2007. Validation of a backscatter model of a river ice covers using Radarsat-1 images. *IEEE Geoscience and Remote Sensing Symposium, 2007.*

Gherboudj, I., Bernier, M., and Leconte. R. 2010. A backscatter modeling for river ice: Analysis and numerical results. *IEEE Transactions on Geoscience Remote Sensing*, 48(4): 1788-1798.

Gogineni, S., Prasad, S., Moore, R. K., Grenfell, T. C., Barber, D. G., Digby, S., and Drinkwater, M. 1992. The effects of freeze-up and melt processes on microwave signatures. in *Microwave Remote Sensing of Sea Ice*, *Geophysical Monogram Series 68*, Ed. Carsey, F. D.: 329-341.

Gow, A., 1986. Orientation textures in ice sheets of quietly frozen lakes. *Journal of Crystal Growth*, 74: 247–258.

Grunblatt, J., and Atwood, D. 2013. Mapping lakes for winter liquid water availability using SAR on the North Slope of Alaska. *International Journal of Applied Earth Observation*, 27(A): 63-69.

Gunn, G. E., Brogioni, M., Duguay, C., Macelloni, G., Kasurak, A., and King, J. 2015. Observation and modeling of X- and Ku-band backscatter of snow-covered freshwater lake ice. *IEEE Journal of Selected Topics in Applied Earth Observations and Remote Sensing*, DOI:10.1109/JSTARS.2015.2420411.

Haijiang, W., Qijonh, H., and Yiming, P. 2009. Polarization decomposition with S and T matrix of a PolSAR image. *ICCCAS 2009. International Conference on Communications, Circuits and Systems,* 530-532.

Hajnsek, I., Jagdhuber, T., Schon, H. and Papathanassiou, K. P. 2009. Potential of estimating soil moisture under vegetation cover by means of PolSAR. *IEEE Transactions on Geoscience Remote Sensing*, 47(2): 442–454.

Hall, D. K., Fagre, D. B., Klasner, F., Linehaugh, G., and Liston, G. E. 1994. Analysis of ERS-1 synthetic aperture radar data of frozen lakes in northern Montana and implications for climate studies. *Journal of Geophysical Research*, 99: 22473-22482.

Hallikainen, M., Ulaby, F., and Abdelrazik, M. 1986. Dielectric properties of snow in the 3 to 37 GHz range. *IEEE Transactions on Antennas and Propagation*, 34(11): 1329-1340.

Heron, R. & Woo, M. K. 1994. Decay of a high Arctic lake-ice cover: observations and modelling. *Journal of Glaciology*, 40(135): 283 – 292.

Hirose, T., Kapfer, M., Bennett, J., Cott, P., Manson, G., and Solomon, S. 2008. Bottomfast Ice Mapping and the Measurement of Ice Thickness on Tundra Lakes Using C-Band Synthetic Aperture Radar Remote Sensing. *JAWRA Journal of the American Water Resources Association*, *44*(2): 285-292.

Hobbs, P. V. 1974. Ice Physics. *Oxford University Press*, Ely House, London W. 837 pp.

Howell, S. E. L., Brown, L. C., Kang, K.-K., and Duguay, C. R. 2009. Variability in ice phenology on Great Bear Lake and Great Slave Lake, Northwest Territories, Canada, from SeaWinds/QuikSCAT: 2000–2006. *Remote Sensing of Environment*, 113(4): 816–834.

Iliescu, D., Baker, I. 2007. The structure and mechanical properties of river and lake ice. *Cold Regions Science and Technology*, 48: 202–217.

Inada, T., Hatakeyama, T., and Takemura, F. 2009. Gas-storage ice grown from water containing microbubbles. *International Journal of Refrigeration*, *32*(3): 462–471.

Jeffries, M.O., Wakabayashi, H., and Weeks, W. F. 1993. ERS-1 SAR backscatter changes associated with ice growing on shallow lakes in Arctic Alaska. *IEEE Geoscience and Remote Sensing Symposium, IGARSS'93: Better Understanding of Earth Environment*.

Jeffries, M. O., Morris, K., Weeks, W. F., and Wakabayashi, H. 1994. Structural and stratigraphic features and ERS-1 synthetic aperture radar backscatter characteristics of ice growing on shallow lakes in NW Alaska, winter 1991-1992. *Journal of Geophysical Research*, 99(C11): 22459 – 22472.

Jeffries, M. Morris, K. and Liston, G. 1996. A method to determine lake depth and water availability on the North Slope of Alaska with spaceborne imaging radar and numerical ice growth modelling. *Arctic*, 49(4): 367–374.

Jeffries, M.O., Morris K., and Duguay, C. R. 2005a. Lake ice growth and decay in central Alaska, USA: observations and computer simulations compared. *Annals of Glaciology*, 40: 1-5.

Jeffries, M., Morris, K., and Kozlenko, N. 2005b. Ice characteristics and processes, and remote sensing of frozen rivers and lakes. In *Remote Sensing in Northern Hydrology: measuring environmental change*, 63-90

Jeffries, M. O., and Morris, K. 2006. Instantaneous daytime conductive heat flow through snow on lake ice in Alaska, *Hydrological Processes*, 20(4): 803–815.

Kang, K. K., Duguay, C. R., Howell, S. E. L., Derksen, C. P., and Kelly, R. E. J. 2010. Sensitivity of AMSR-E Brightness Temperatures to the Seasonal Evolution of Lake Ice Thickness. *IEEE Transactions on Geoscience and Remote Sensing Letters*, 7(4): 751-755.

Kang, K. K., Duguay, C. R., and Howell, S. E. L. 2012. Estimating ice phenology on large northern lakes from AMSR-E: algorithm development and application to Great Bear Lake and Great Slave Lake, Canada. *The Cryosphere*, 6(2): 235-254.

Kang, K.-K., Duguay, C. R., Lemmetyinen, J., and Gel, Y. 2014. Estimation of ice thickness on large northern lakes from AMSR-E brightness temperature measurements. *Remote Sensing of Environment*, 150: 1–19.

Karam, M.A. Fung, A.K. and Antar, Y. M. M. 1988. Electromagnetic wave scattering from some vegetation samples. *IEEE Transactions on Geoscience and Remote Sensing*, 26(6): 799-808.

Key, J., Drinkwater, M., and Ukita, J. 2007. IGOS Cryosphere Theme Report. *WMO/TD* 1405: 100 pp.

Kheyrollah Pour, H., Duguay, C.R., Martynov, A., and Brown, L. C. 2012. Simulation of surface temperature and ice cover of large northern lakes with 1-D models: A comparison with MODIS satellite data and in situ measurements, *Tellus Series A: Dynamic Meteorology and Oceanography* ,64: 17614, DOI: 10.3402/tellusa.v64i0.17614.

Kheyrollah Pour, H., Rontu, L., Duguay, C., Eerola, K., and Kourzeneva, E. 2014. Impact of satellite-based lake surface observations on the initial state of HIRLAM. Part II: Analysis of lake surface temperature and ice cover. *Tellus A*, 66: 21395.

King, J., Kelly, R., Kasurak, A., Duguay, C., Gunn G., and Mead, J. B., 2013. UW-Scat: A ground-based dual-frequency scatterometer for observation of snow properties. *IEEE Transactions on Geoscience and Remote Sensing Letters*, 10(3): 528–532.

Kontu, A., Kemppainen, S., Lemmetyinen, J., Pulliainen, J., and Hallikainen, M. 2008. Determination of snow emission on lake ice from airborne passive microwave measurements. *Geoscience and Remote Sensing Symposium, 2008, IGARSS 2008. IEEE International*, 4(4): 1046-1049.

Kozlenko, N., and Jeffries, M. O. 2000. Bathymetric Mapping of Shallow Water in Thaw Lakes on the North Slope of Alaska with Spaceborne Imaging Radar. *Arctic*, 53(3): 306 – 316.

Krogager, E. 1990. A new decomposition of the radar target scattering matrix. *Electronics Letters*, 26(18): 1525-1526.

Krogager, E., and Freeman, A. 1994. Three component break-downs of scattering matrices for radar target identification and classification. in *Proceedings PIERS '94*, Noordwijk, The Netherlands, 391.

Krogager, E., and Czyz, Z. H. 1995. Properties of the sphere, diplane, helix decomposition," in *Proceedings of 3rd International Workshop on Radar Polarimetry (JIPR'95)*, IRESTE, Univ. Nantes, France, 106-114.

LaChapelle, E. R. 1969. Field guide to snow crystals. *University of Washington Press*, Seattle and London.

Ladd, M.F.C. 1998. Introduction to Physical Chemistry. *Cambridge University Press*, Cambrdige, New York, 513 pp.

Lafleur, P., Wurtele A., and Duguay, C. 1997. Spatial and temporal variations in surface albedo of a subarctic landscape using surface-based measurements and remote sensing. *Arctic and Alpine. Research*, 29(3): 261–269.

Lamb, J. 1946. Measurements of the dielectric properties of ice. *Transactions of the Faraday Society*, 42(A): 238-44.

Latifovic, R., and Pouliot, D. 2007. Analysis of climate change impacts on lake ice phenology in Canada using the historical satellite data record. *Remote Sensing of Environment*, 106(4): 492-507.

Leconte, R., and Klassen, P. D. 1991. Lake and river ice investigations in northern Manitoba using airborne SAR imagery. *Arctic*, *44:* 153-163.

Leconte, R., Daly, S., Gauthier, Y., Yankielun, N., Berube, F., and Bernier, M. 2009. A controlled experiment to retrieve freshwater ice characteristics from an FM-CW radar system. *Cold Regions Science and Technology*, 55(2): 212–220.

Lee J-S., and Pottier, E. 2009. Introduction to the Polarimetric Target Decomposition Concept. in Polarimetric Radar Imaging: From Basics to Applications, Boca Raton, FL: CRC, pp. 214-215.

Lenormand, F., Duguay, C. R., and Gauthier, R. 2002. Development of a historical ice database for the study of climate change in New England. *Hydrological Processes*, 16: 3707 – 3722.

Leppäranta, M., and Kosloff, P. 2000. The Structure and Thickness of Lake Pääjärvi. *Geophysica*, 36(1-2): 233-248.

Liang, D., Xu, X., Tsang, L., Andreadis, K. M., and Josberger, E. G. 2008. The effects of layers in dry snow on its passive microwave emission using dense media radiative transfer theory based on the quasicrystalline approximation (QCA/DMRT). *IEEE Transactions on Geoscience and Remote Sensing*, 46(11): 3663–3671.

Liang, D., Tsang, L., Yueh, S., Xu, X. 2008. Modeling Active Microwave Remote Sensing of Multilayer Dry Snow using Dense Media Radiative Transfer Theory. *IEEE 2008 International Geoscience and Remote Sensing Symposium. IGARSS'08*, 3: III-39.

Libbrecht, K. G. 2005. The physics of snow crystals. *Reports on Progress in Physics*, 68: 855-895.

Lin, Y.C., and Sarabandi, K. 1995. Electromagnetic Scattering Model for a Tree Trunk Above a Tilted Ground Plane. *IEEE Transactions on Geoscience and Remote Sensing*, 33(4): 1063-1070.

Lin, Z., Niu, F., Xu, Z., Xu, J., and Wang, P. 2010. Thermal regime of a thermokarst lake and its influence on permafrost, Beiluhe Basin, Qinghai-Tibet Plateau. Permafrost and Periglacial Processes. 21(4): 315-324.

Lindenschmidt, K. E. 2010. Measuring Ice Thicknesses along the Red River in Canada Using RADARSAT-2 Satellite Imagery. *Journal of Water Resource and Protection*, *2*(11): 923-933.

Lyzenga, D.R., Malinas, N. P., and Tanis, F. J. 2006. Multispectral bathymetry using a simple physically based algorithm. *IEEE Transactions on Geoscience and Remote Sensing*, 44(8): 2251-2259.

Lorrain, P., Corson, D. R., and Lorrain, F. 1998. Electromagnetic Fields and Waves. Third Edition. W. H. *Freeman and Company*, New York. 754 pp.

Magnuson, J. J., Robertson D. M., Benson, B. J., Wynne, R. H., Livingstone, D, M., Arai, T., Assel, R. A., Barry, R. G., Card, V., Kuusisto, E., Granin, N. G., Prowse, T. D., Stewart, K. M., Vuglinski, V. S. 2000. Historical trends in lake and river ice cover in the Northern Hemisphere. *Science*, 289: 1743 – 1746.

Marko, J. R., Fissel, D. B., and Jasek, M. 2006. Recent developments in ice and water column profiling technology. In *Proceedings from the 18th IAHR Ice Symposium 2006*, Sapporo, Japan. 8 pp.

Marshall, H.P., Schneebeli, M., and Koh, G. 2007. Snow stratigraphy measurements with high-frequency FMCW radar: Comparison with snow micro-penetrometer. *Cold Regions Science and Technology*, 47(1–2): 108–117.

Martynov, A., Sushama, L., Laprise, R., Winger, K., and Dugas, B. 2012. Interactive lakes in the Canadian Regional Climate Model, version 5: the role of lakes in the regional climate of North America, *Tellus Series A: Dynamic Meteorology and Oceanography* 64, 16226.

Mätzler, C., Schanda, E., and Good, W. 1982. Towards the definition of optimum sensor specifications for microwave remote sensing of snow *IEEE Transactions on Geoscience and Remote Sensing*, GE-20(1): 57–66.

Mätzler, C. 1987. Applications of the interaction of microwaves with the natural snow cover. *Remote sensing reviews*, 2(2): 259–387.

Mätzler, C., and Wegmüller, U. 1987. Dielectric properties of fresh-water ice at microwave frequencies. *Journal of Physics D: Applied Physics*, 20(April): 1623-1630.

Mätzler, C. (2006). Thermal Microwave Radiation: Applications for Remote Sensing (Eds. Mätzler, C., Rosenkranz, P.W., Battaglia, A., Wigneron J. P.) *IET Electromagnetic Waves Series* Volume 52, Institute of Engineering and Technology, Stevenage, U.K..

Matzuoka, T., Fujita, S., Morishima, S., and Mae, S. 1997a. Precise measurement of dielectric anisotropy in ice Ih at 39 GHz. *Journal of Applied Physics*, 81(5): 2344-2348.

Matsuoka, T., Uratsuka, S., Takahashi, A., Kobayashi, T., Satake, M., Nadai, A., Umehara, T., Wakabayashi, H., and Nishio, F. 1999. A backscattering model for bubbles in lake ice and comparisons with satellite and airborne SAR data. *IEEE 1999 International Geoscience and Remote Sensing Symposium IGARSS'99 (Cat. No.99CH36293)*, 1: 107–109.

Maykut, G. A., and Untersteiner, N. 1971. Some results from a time-dependent, thermodynamical model of sea ice. *Journal of Geophysical Research*, 76(6): 1550 – 1575.

Maykut, G. A. 2008. Large-scale heat exchange and ice production in the Central Arctic. *Journal of Geophysical Research*, 87(C10): 7971 – 7984.

Meissner, T., and Wentz, F. J. 2004. The complex dielectric constant of pure and sea water from microwave satellite observations. *IEEE Transactions on Geoscience and Remote Sensing*, 42(9): 1836–1849.

Melling, H. 2012. Sea-Ice Observation: Advances and Challenges. in *Arctic Climate Change*, Eds. Lemke P., and Jacobi, H.-W. , Dordrecht: Springer Netherlands, 43: 27–115.

Mellor, J. C. 1982. Bathymetry of Alaskan arctic lakes: A key to resource inventory with remote-sensing methods (No. DOE/EV/70009-T2). Alaska Univ., Fairbanks (USA). *Institute of Marine Science*.

Mellor, J. 1994. ERS-1 SAR use to determine lake depths in Arctic and sub-Arctic regions. In *Proceedings of the Second ERS-1 Symposium – Space at the Service of our Environment, 11-13 October 1993*, Hamburg, Germany, Special Publication 361, Paris: European Space Agency, 1141-1146.

Ménard, P., Duguay, C.R., Flato, G.M., Rouse, W. R. 2002. Simulation of ice phenology on Great Slave Lake, Northwest Territories, Canada. *Hydrological Processes*, 16: 3691-3706.

Mendez, J., Hinzman, L. D., and Kane, D. L. 1998. Evapotranspiration from a wetland complex on the Arctic coastal plain of Alaska. *Nordic Hydrology*, 29: 303–330.

Michel, B. and Ramseier, R. O. 1971. Classification of River and Lake Ice. *Canadian Geotechnical Journal*, 8(1): 36-45.

Morris, K., Jeffries, M. O., and Weeks, W. F. 1995. Ice processes and growth history on Arctic and sub-Arctic lakes using ERS-1 SAR data. *Polar Record*, 31(177): 115-128.

Morris, K., Jeffries, M. and Duguay, C. 2005. Model simulation of the effects of climate variability and change on lake ice in central Alaska, USA. *Annals of Glaciology*, 40: 113-118.

Morrison, K., Rott, H., Nagler, T., Rebhan, H., and Wursteisen, P. 2007. The SARALPS-2007 measurement campaign on Xand Ku-Band Backscatter of snow. *IEEE International Geoscience and Remote Sensing Symposium 2007*, 1207-1210.

Mueller, D.R., Van Hove, P., Antoniades, D., Jeffries, M.O., and Vincent, W. F. 2009. High Arctic lakes as sentinel ecosystems: Cascading regime shifts in climate, ice cover, and mixing. *Limnology and Oceanography* , 54: 2371–2385.

Muller-Stoffels, M., Langhorne, P. J., Petrich, C. and Kempema, E. W. 2009. Preferred crystal orientation in freshwater ice. *Cold Regions Science and Technology*, 56: 1-9.

Nghiem, S. V. Kwok, R., Yueh, S. H. and Drinkwater, M. R. 1995. Polarimetric signatures of sea ice 1. Theoretical Model" *Journal of Geophysical Research,* 100(C7): 13665 – 13679.

Nghiem, S. V., Leshkevich, G. A., and Kwok, R. 1998. Shipborne scatterometer measurements of Great Lakes Ice. *5th International Conference on Remote Sensing for Marine and Coastal Environments, San Diego, California.*

Nolan, M., Liston, G., Prokein, P., Brigham-Grette, J., Sharpton, V. L., and Huntzinger, R. 2002. Analysis of lake ice dynamics and morphology on Lake El'gygytgyn, NE Siberia, using synthetic aperture radar (SAR) and Landsat. *Journal of Geophysical Research*, *108*(D2): 1-12.

Onstott, R. G., Moore, R. K., Gogineni, S., and Delker, C. Four years of low-altitude sea ice broad-band backscatter measurements. *Ocean Engineering*, OE-7(1): 44–50.

Oh, Y., Sarabandi, K., and Ulaby, F. T. 2002. Semi-empirical model of the ensemble averaged differential Mueller matrix for microwave backscattering from bare soil surfaces. *IEEE Transactions on Geoscience and Remote Sensing*, 40: 1348–1355.

Overland, J. E., Hanna, E., Hanssen-Bauer, I., Kim, S. J., Walsh, J., Wang, M., and Bhatt, U. S. 2014. Air Temperature, in *Arctic Report Card, 2014*. Eds. Jeffries, M. O., Richter-Menge, J., and Overland, J. E. *http://www.arctic.noaa.gov/reportcard*.

Petrenko, V. F. 1993a. Structure of Ordinary Ice I_h, Part I: Ideal Structure of Ice. *Report No. 93-25, U.S. Army Corps of Engineers, Cold Regions Research and Engineering Laboratory*, Hanov, NH.

Petrenko, V. F. 1993b. Electrical Properties of Ice. *Report No.93-20, U.S. Army Corps of Engineers, Cold Regions Research and Engineering Laboratory*, Hanov, NH.

Petrenko, V. F., and Whitworth, R. W. 1994. Structure of Ordinary Ice I_h, Part II: Defects in Ice, Volume 1: Point Defects. *Report No.94-4, U.S. Army Corps of Engineers, Cold Regions Research and Engineering Laboratory*, Hanover, NH.

Petrenko, V. F., and Whitworth, R. W. 1999. The Physics of Ice. *Oxford University Press,* Oxford.

Petrich, C., and Eicken, H. 2010. Growth, Structure and Properties of Sea Ice. In *Sea Ice, Second Edition* (Eds. Thomas D. N. and Dieckmann G. S.), Wiley-Blackwell, Oxford, UK.

Polder, D., and van Santeen, J. 1946. The effective permeability of mixtures of solids. *Physica, 12*(5): 257–271.

Prowse, T., Furgal, C., Chouinard, R., Melling, H., Milburn, D., Smith, S. L. 2009. Implications of Climate Change for Economic Development in Northern Canada: Energy, Resource, and Transportation Sectors. *Ambio*, 38(5): 272 -281.

Prowse, T., Alfredsen, K., Beltaos, S., Bonsal, B., Duguay, C., Korhola, A., McNamara, J., Vincent, W. F., Vuglinsky, V., and Weyhenmeyer, A. 2011. Arctic freshwater ice and its climatic role. *Ambio*, 40(S1): 46-52.

Redmund, Q. P., and Long, D. G. Large-scale inverse Ku-band backscatter modeling of sea ice. *IEEE Transactions on Geoscience and Remote Sensing*, 41(8):1821 – 1833.

Roach, J., Griffith, B., Verbyla, D., and Jones, J. 2011. Mechanisms influencing changes in lake area in Alaskan boreal forest. *Global Change Biology*, 17(8): 2567-2583.

Rouse, W. R., Blanken, P. D., Duguay, C. R., Oswald, C. J., and Schertzer, W. M. 2008. Climate-lake interactions. in *Cold Region Atmospheric and Hydrologic Studies: The Mackenzie GEWEX Experience*, no. 2, M. K. Woo, ed. Berlin, Heidelberg: Springer, 139-160.

Royer, G, M. 1973. The Dielectric properties of ice, snow and water at microwave frequencies and the measurement of the thickness of ice and snow layers with radar. *Communications Research Centre- Department of Communications*, CRC-Report 1242, Ottawa, Canada.

Ruck, G.T., Barrick, D. E., Stewart, W. D., and Kirshbaum, C. K. 1970. Radar cross section handbook, vol. 1. *Plenum*, New York and London.

Sarabandi, K. 1990. Simulation of a Periodic Dielectric Corrugation with an Equivalent Anisotropic layer. *International Journal of Infrared and Millimeter Waves*, 11(11): 1303-1321.

Sarabandi, K., and Senior, T.B.A. 1990. Low Frequency Scattering from Cylindrical Structures at Oblique Incidence. IEEE *Transactions on Geoscience and Remote Sensing*,28(5): 879-885

Sarabandi, K. 1992. Derivation of Phase Statistics from the Mueller Matrix. *Radio Science*, 27(5): 553-560.

Scott, P. A., Bentley, C. V., Fayle, D. C. F., and Hansell, R. I. C. 1987. Crown forms and shoot elongation of white spruce at the treeline, Churchill, Manitoba, Canada. *Arctic and Alpine Research*, 19(2): 175-186.

Sellmann, P., Weeks, W. F., and Campbell, W. J. 1975. Use of side-looking airborne radar to determine lake depth on the Alaskan North Slope. *CRREL-SR-230. Cold Regions Research and Engineering Lab, Hanover, N.H.*.

Serreze, M. C., Holland, M. M., and Stroeve, J. 2007. Perspectives on the Arctic's shrinking sea-ice cover. *Science*, 315: 1533–1536.

Shi, J., and Dozier, J. 2000. Estimation of snow water equivalence using SIR-C/X-SAR. I. Inferring snow density and subsurface properties. *IEEE Transactions on Geoscience and Remote Sensing*, 38(6): 2465-2474.

Shi, J., Yueh, S., and Cline, D. 2003. On estimation of snow water equivalence using L-band and Ku-band radar. *IGARSS 2003. 2003 IEEE International Geoscience and Remote Sensing Symposium. Proceedings (IEEE Cat. No.03CH37477), 00*(C), 845-847.

Shumskii, P. 1964. Principles of Structural Glaciology. *Dover Publications*, Inc. New York.

Sobiech, J. and Dierking, W. 2013. Observing lake- and river-ice decay with SAR: advantages and limitations of the unsupervised k-means classification approach. *Annals of Glaciology,* 54: 65-72.

Stiles J.M., and Sarabandi, K. 1996. A Scattering Model for Thin Dielectric Cylinders of Arbitrary Cross-Section and Electrical Length. *IEEE Transactions on Antennas and Propagation*, 44(2) 260-266.

Stiles, W., and Ulaby, F. T. 1980. Dielectric properties of snow. *Journal of Geophysical Research, 85*(C2), 1037-1044.

Sturm, M., Holmgren, J., and Liston, G. E. 1995. A seasonal snow cover classification system for local to global applications. *Journal of Climate*, 8(5): 1261-1283.

Sturm, M., and Benson, C. S. 1997. Vapor transport, grain growth and depth-hoar development in the subarctic snow. *Journal of Glaciology,* 43(143) 7-12.

Sturm, M., Holmgren, J., König, M., and Morris, K. 1997. The thermal conductivity of seasonal snow. *Journal of Glaciology*, 43(143): 26–41.

Sturm, M., and Holmgren, J. A. 1999. Self-recording snow depth probe" *U.S. Patent 5864059 A.*

Sturm, M., and Liston, G. E. 2003. The snow cover on lakes of the Arctic Coastal Plain of Alaska, U.S.A. *Journal of Glaciology, 49*(166): 370-380.

Sturm, M., and Wainwright, F. 2010. Snow Distribution in the Taiga and Heat Flow. *Arctic*, *24*(2): 145-152.

Surdu, C., Duguay, C. R., Brown, L. C., and Fernández Prieto, D. 2014. Response of ice cover on shallow Arctic lakes of the North Slope of Alaska to contemporary climate conditions (1950-2011): Radar remote sensing and numerical modeling data analysis. *The Cryosphere*, 8: 167-180.

Svacina, N. A., Duguay, C.R., and Brown, L.C. 2014. Modelled and satellite-derived surface albedo of lake ice - Part I: Evaluation of the albedo parameterization scheme of the Canadian Lake Ice Model. *Hydrological Processes*, 28: 4550–4561, DOI: 10.1002/hyp.10253.

Tinga, W. R. 1973. Generalized approach to multiphase dielectric mixture theory. *Journal of Applied Physics*, *44*(9): 3897.

Tiuri, M. E., Sihvola, A. H., Nyfors, E. G., and Hallikainen, M. T. 1984. The Complex Dielectric Constant of Snow at Microwave Frequencies. *IEEE Journal of Oceanic Engineering*, GE-9(5): 377-382.

Tjuatja, S., Fung, A. K., and Bredow, J. 1992. A scattering model for snow- covered sea ice. *IEEE Trans. Geosci. Remote Sens*., vol. 30, no. 4, pp. 804–810, 1992.

Touzi, R., and Charbonneau, F., Characterization of target symmetric scattering using polarimetric SARs, *IEEE Transaction on Geoscience Remote Sensing*, 40(11), 2507-2516, November 2002.

R. Touzi, "Target scattering decomposition in terms of roll-invariant target parameters." *IEEE Transactions on Geoscience and Remote Sensing*, 45(1): 73-84.

Tsang, L., and Kong. J. 2001. Scattering of Electromagnetic Waves: Advanced Topics. *New York, John Wiley and Sons, Inc*.

Tsang, L., Pan, J., Liang, D., Li, Z., Cline, D. W., and Tan, Y. 2007. Modeling active microwave remote sensing of snow using dense media radiative transfer (DMRT) theory with multiple-scattering effects," *IEEE Transaction on Geoscience Remote Sensing*, 45(4): 990–1004.

Ulaby, F. T., and Stiles, W. H. 1980. The Active and Passive Microwave Response to Snow Parameters 2. Water Equivalent of Dry Snow. *Journal of Geophysical Research*, 85(C2): 1045-1049.

Ulaby, F. T., Moore, R. K., Fung, A. K. 1982a. Microwave Remote Sensing: Active and Passive. Volume I: Microwave Remote Sensing Fundamentals and Radiometry. *Addison-Wesley Publishing Company*, Norwood, MA.

Ulaby, F. T., Moore, R. K., Fung, A. K. 1982b. Microwave Remote Sensing: Active and Passive. Volume II: Radar Remote Sensing and Surface Scattering and Emission Theory. *Addison-Wesley Publishing Company*, Norwood, MA.

Ulaby, F., Moore, R., and Fung, A. 1986. Microwave Remote Sensing: Active and Passive. Volume II: Radar Remote Sensing and Surface Scattering Emission Theory. *Addison-Wesley Pub Co.*, Reading, Mass.

Ulaby, F. T., Held, D., Donson, M. C., McDonald, K. C., and Senior, T. B. A. 1987. Relating Polaization Phase Difference of SAR Signals to Scene Properties. *IEEE Transactions on Geoscience and Remote Sensing*, GE-25(1): 83–92.

Ulaby, F. T., and van Zyl, J. J. 1990. Wave Properties and Polarization. In *Radar Polarimetry for Geoscience Applications*, Eds, Ulaby, F. T., and Elachi, C. Artech House, Inc. Norwood, MA.

Van der Sanden, J. J., and Drouin, H. 2011. Satellite SAR Observations of River Ice Cover: A RADARSAT-2 (C-band) and ALOS PALSAR (L-band) Comparison, *CGU HS committee on River Ice Processes and the Environment, 16th Workshop on River Ice*, 179–197.

Von Hippel, A. 1988. The Dielectric Relaxation Spectra of Water, Ice, and Aqueous Solutions, and their Interpretation. 3. Proton Organization and Proton Transfer in Ice. *IEEE Transactions on Electrical Insulation*, 23(5): 825 – 840.

Wakabayashi, H., Jeffries, M. O., and Weeeks, W. F. 1993. C-band backscatter from ice on shallow tundra lakes: Observation and modelling. *In Proceedings of the 1st ERS-1 Symposium – Space at the Service of Our Environment*, 333 – 337.

Wakabayashi, H., Jeffries, M. and Weeks, W. 1994. C band backscatter variation and modelling for lake ice in northern Alaska. *Journal of Japanese Remote Sensing,* 18(220): 220–229.

Walsh, J. E., Overland, J. E., Groisman, P. Y., and Rudolf, B. 2011. Chapter 2: Arctic climate: Recent variations. *Snow, Water, Ice andPermafrost in the Arctic (SWIPA) Oslo, Arctic Monitoring and Assessment Programme (AMAP).*

Walter, K.M., Zimov, S.A., Chanton, J.P., Verbyla, D., and Chapin, F. S. 2006. Methane bubbling from Siberian thaw lakes as a positive feedback to climate warming. *Nature*, 443(7107) 71-75.

Walter, K. M., Engram, M., Duguay, C. R., Jeffries, M. O., and Chapin, F. S. 2008. The potential use of synthetic aperture radar for estimating methane ebullition from arctic lakes. *Journal of the American Water Resources Association*, 44(2): 305–315.

Weber, F., Nixon, D., and Hurley, J. 2003. Semi-automated classification of river ice types on the Peace River using RADARSAT-1 synthetic aperture radar (SAR) imagery. *Canadian Journal of Civil Engineering* 30(1): 11–27.

Weeks, W. F., Fountain, A. G., Regions, U. S. A. C., Bryan, L., and Elachi, C. 1978. Differences in Radar Return From Ice-Covered North Slope Lakes. *Journal of Geophysical Research*, 83(8): 4069-4073.

Weeks, W. F., Gow, A. J., and Schertler, R. J. 1981. Ground-truth observations of ice-covered North Slope lakes imaged by radar. *Cold Regions Research and Engineering Lab, Hanover, NH*., no. CRREL-81-19.

Weeks, W. F., and Ackley, S. F. 1982. The Growth, Structure and Properties of Sea Ice. *Cold Regions Research and Engineering Lab, Hanover, NH.* No. CRREL-82-1.

Wdowinski, S., Amelung, F., Miralles-Wilhelm, F., Dixon, T. H., and Carande R. 2004. Space-based measurements of sheet-flow characteristics in the Everglades wetland, Florida, *Geophysical Research Letters*, 31(15).

Woodhouse, I. H. 2006. Introduction to Remote Sensing. *Taylor and Francis.* Boca Raton, Florida.

Van Zyl, J. J., Arii, M., and Yunjim, K. 2011. Model-based decomposition of polarimetric SAR covariance matrices constrained for nonnegative eigenvalues. *IEEE Transaction on Geoscience Remote Sensing*, 49(9): 3452-3459.

Vant, M. R., Gray, R. B., Ramseier, R. O., and Makios, V. 1974. Dielectric properties of fresh and sea ice at 10 and 35 GHz. *Journal of Applied Physics*, 45(11): 4712-4717.

Vavrus, S.J., Wynne, R.H., and Foley, J.A. 1996. Measuring the sensitivity of southern Wisconsin lake ice to climate variations and lake depth using a numerical model. *Limnology and Oceanography*, 41: 822-831.

Verman, R. 2012. Polarimetric decomposition based on general characterization of scattering from urban areas and multiple component scattering model. Ph.D. Thesis, *University of Twente*.

Yajima, Y., Yamaguchi, Y., Sato, R., Yamada, H., and Boerner, W.-M. 2008. POLSAR image analysis of wetlands using a modified four-component scattering power decomposition. *IEEE Transaction on Geoscience Remote Sensing*, 46(6): 1667–1673.

Yamaguchi, Y., Moriyama, T., Ishido, M., and Yamada, H. 2005. Four-component scattering model for polarimetric SAR image decomposition. *IEEE Transaction on Geoscience Remote Sensing*, 43(8): 1699-1706.

Yamaguchi, Y., Yajima, Y., and Yamada, H. 2006. A four-component decomposition of POLSAR images based on the coherency matrix. *IEEE Geoscience on Remote Sensing Letters*, 3(3): 292-296.

Yankielun, N. E., Ferrick, M. G., & Weyrick, P. B. 1992. Development of an airborne millimeter-wave FM-CW radar for mapping river ice. *Canadian Journal of Civil Engineering*, 20(6): 1057-1064.

Yen, Y. 1962. Effective Thermal Conductivity of Ventilated Snow. *Journal of Geophysical Research*, 67(3): 1091–1098.

Yoshimura, K., Inada, T., and Koyama, S. 2008. Growth of spherical and cylindrical oxygen bubbles at an ice−water interface. *Crystal Growth and Design*, 8(7) 2108–2115.

Yueh, S. H., Dinardo, S. J., Akgiray, A., West, R., Cline, D. W., and Elder, K. 2009. Airborne Ku-Band Polarimetric Radar Remote Sensing of Terrestrial Snow Cover. *IEEE Transactions on Geoscience and Remote Sensing*, 47(10): 3347-3364.

Zhang, T., Barry, R.G., Knowles, K., Heginbottom, J.A., and Brown, J. 1999. Statistics and characteristics of permafrost and ground-ice distribution in the Northern Hemisphere. *Polar Geography*, 23(2): 132-154.